



**HAL**  
open science

# Somatic cells enhance the oocyte developmental potential through cytoplasmic protrusions

Flora Crozet

► **To cite this version:**

Flora Crozet. Somatic cells enhance the oocyte developmental potential through cytoplasmic protrusions. Cellular Biology. Sorbonne Université, 2021. English. NNT : 2021SORUS166 . tel-04204267

**HAL Id: tel-04204267**

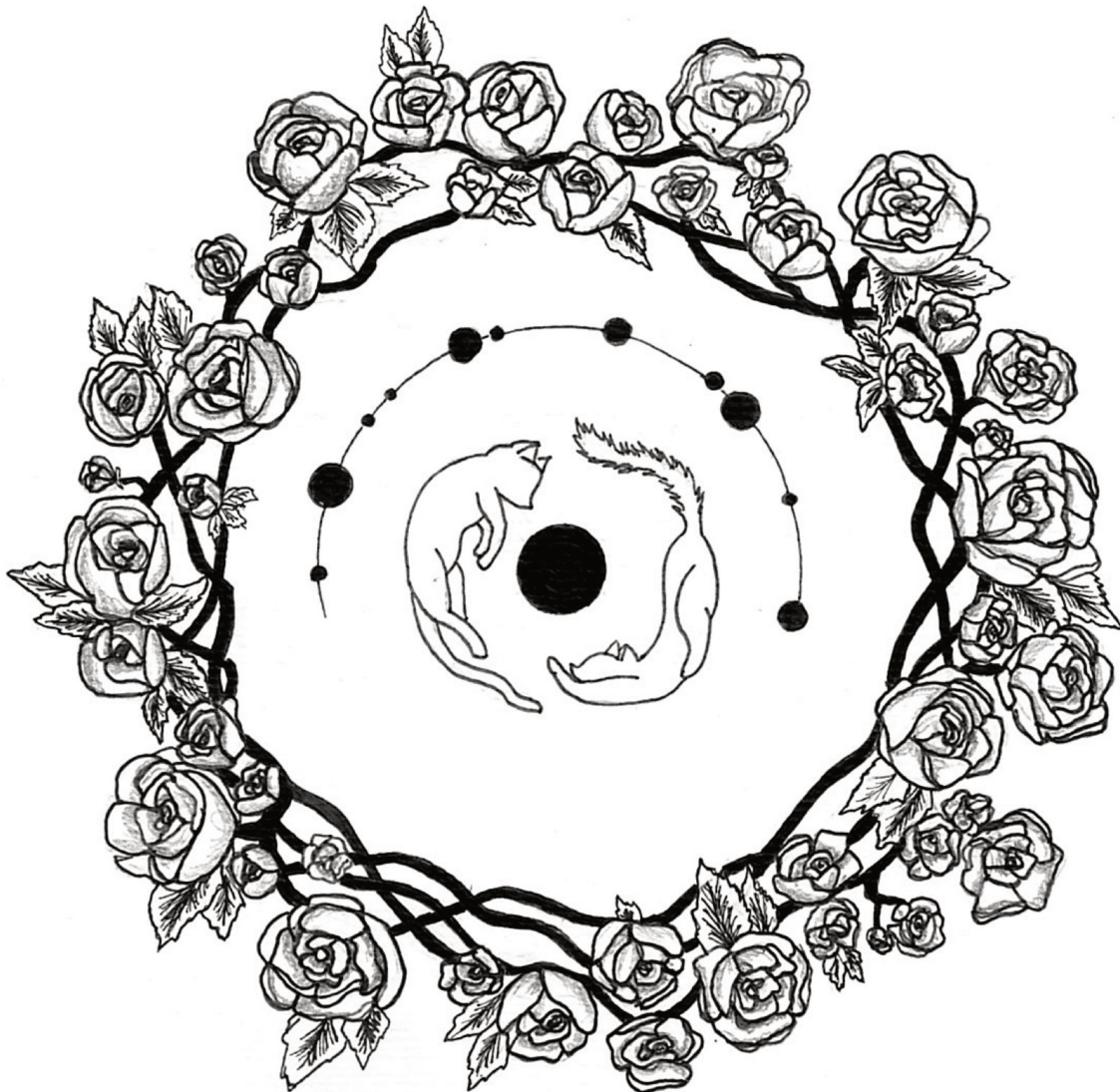
**<https://theses.hal.science/tel-04204267>**

Submitted on 12 Sep 2023

**HAL** is a multi-disciplinary open access archive for the deposit and dissemination of scientific research documents, whether they are published or not. The documents may come from teaching and research institutions in France or abroad, or from public or private research centers.

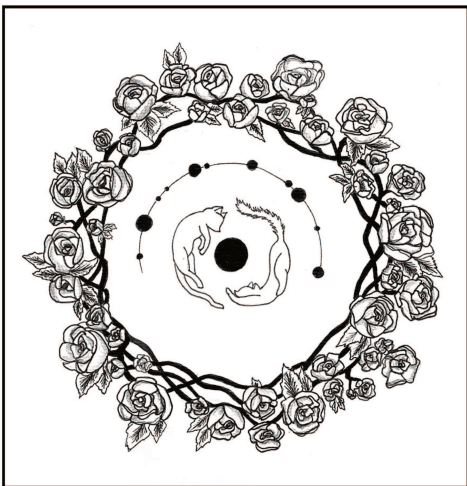
L'archive ouverte pluridisciplinaire **HAL**, est destinée au dépôt et à la diffusion de documents scientifiques de niveau recherche, publiés ou non, émanant des établissements d'enseignement et de recherche français ou étrangers, des laboratoires publics ou privés.

# **Somatic cells enhance the oocyte developmental potential through cytoplasmic protrusions**



**By Flora CROZET**

**Supervised by Marie-Emilie TERRET**



Drawing of a cumulus-oocyte complex kindly made by Adrien Eichmuller



COLLÈGE  
DE FRANCE  
—1530—



## Sorbonne Université

Ecole doctorale Complexité du Vivant ED515

*Equipe Oocyte Mechanics and Morphogenesis, CIRB, UMR 7241/ U1050, Collège de France*

# Somatic cells enhance the oocyte developmental potential through cytoplasmic protrusions

Par **Flora CROZET**

Thèse de doctorat de Biologie Cellulaire

Dirigée par **Marie-Emilie TERRET**

Présentée et soutenue publiquement le 10 septembre 2021

Devant un jury composé de :

**Katja WASSMANN**  
**Suzanne MADGWICK**  
**Peter LENART**  
**Céline GUIGON**  
**Stéphane ROMERO**  
**Hugh CLARKE**  
**Marie-Hélène VERLHAC**  
**Marie-Emilie TERRET**

Président du jury  
Rapporteur  
Rapporteur  
Examineur  
Examineur  
Membre invité  
Membre invité  
Directrice de thèse

# Remerciements

**Suzanne Madgwick and Peter Lenart**, thank you for reviewing the following manuscript and for your feedback. **Katja Wassmann, Suzanne Madgwick, Peter Lenart, Céline Guigon, Stéphane Romero and Hugh Clarke**, thank you very much for agreeing to be part of my thesis jury. Thank you for examining it, thank you for your time and for reviewing the manuscript and the defense.

**Véronique, Evelyne Fischer et Stéphane Romero**, merci d'avoir constitué mon comité de thèse. Merci d'avoir suivi l'avancement de ma thèse et merci pour vos retours constructifs.

**Marie-Emilie** : Je tiens à te remercier pour beaucoup de raisons. La liste est longue et je vais essayer de la rendre digne de tout ce que tu m'as apporté pendant ma thèse. Merci de m'avoir formée scientifiquement. Tu m'as enseigné une vision de la Science que je trouve belle et qui m'a servie, et me servira, de référence à plusieurs occasions. Ton respect pour le matériel biologique, ton intégrité, et ton ouverture d'esprit sont à mes yeux les plus belles et inspirantes valeurs professionnelles qu'on puisse avoir et que tu possèdes. Merci pour toutes les discussions scientifiques que nous avons eues et qui m'ont aidées à me construire professionnellement. La discussion est facile avec toi, constructive, et sans jugement. Je te remercie aussi de m'avoir fait confiance et donné beaucoup de libertés : notamment d'arriver et de partir du labo aux horaires de mon choix, d'organiser mes journées et les manips à ma convenance, et surtout, de m'avoir permis d'écrire les deux articles de ma thèse. Je t'en suis reconnaissante. Je te remercie aussi du fond du cœur d'avoir été à mon écoute et de m'avoir soutenue moralement. Tu as une analyse psychologique des gens impressionnante, ce qui fait que tu es souvent de très bons conseils. Merci d'avoir analysé les données quand je ne pouvais pas le faire. Tu n'étais pas obligée de le faire, mais tu as quand même pris de ton temps pour m'aider. Cela représente beaucoup pour moi. En bref, merci d'avoir été ma directrice de thèse. Tu es non seulement une grande scientifique, mais une personne bienveillante, et j'ai eu beaucoup de chance d'apprendre auprès de toi.

**Marie-Hélène** : Je te remercie de m'avoir accueillie au laboratoire et de m'avoir conseillée. J'ai beaucoup apprécié nos discussions scientifiques et sociétales, et j'aime bien ta vision de la vie. Elle est, à mes yeux, beaucoup plus pragmatique et directe que la mienne, ça fait du bien ! Comme pour Marie-Emilie, tu as été une source d'inspiration pour moi sur le plan professionnel et humain. J'ai eu de la chance d'avoir été formée par deux brillantes scientifiques, humaines et attentionnées. Notamment, j'admire ta force, ta persévérance, ton enthousiasme pour la Science et ton souci de la justice. Ton jugement a toujours compté pour moi, et m'a aussi intimidée, dans le bon sens, et j'y accorde une grande valeur. Je trouve aussi que tu proposes des idées originales et novatrices, que très peu de personnes auraient imaginées. En ce sens, je te trouve très créative. Tu m'as appris à être le plus *straight to the point* possible lors

des présentations de résultats, et j'essaye de l'être autant que possible. Je trouve ça important de te le dire. Merci pour tout Marie-Hélène !

**Hugh Clarke** : Thank you for collaborating with us. Thank you for your feedback and advice on the TZP project and for always kindly answering our questions about follicular growth. Thank you for inviting us to your lab and for the tour of Montreal. It was a really nice trip.

**Christelle et Adrien** : Un grand merci à tous les deux ! Vous êtes deux rayons de soleil au labo. J'ai passé de super moments grâce à vous, à rire et à déconner. Merci d'avoir été là pour moi dans les bons, comme les mauvais moments. La vie au labo avec vous va énormément me manquer, et je garderai un très beau souvenir des années que nous avons passées tous les trois. Mais, chut c'est secret... ;)

**Christelle** : Chrichri, co-présidente de la Christaflore, merci beaucoup d'avoir été ma voisine de labo. Tu as été à mes côtés pendant toute la durée de ma thèse, et cela va me faire bizarre de ne plus te voir quotidiennement. J'ai pris l'habitude des matins à nous raconter notre vie de la veille, ou encore à échanger nos avis sur les séries. Tous ces moments ont été simples et agréables, et mis bout à bout, ils constituent une part importante de ma vie de thèse. Je voudrais aussi te remercier de m'avoir toujours conseillée avec justesse, notamment lorsque j'écrivais un mail compliqué, ou lorsque j'avais besoin d'aide avec les règles de sécurité d'une manip. Ta maturité, ta rigueur et ton empathie font de toi une personne avec qui il est agréable d'être. J'ai été honorée d'être ta collègue, et je suis heureuse d'avoir passé ces moments à tes côtés.

**Adrien** : Dridri, je te promets que tu ne ressembles pas à l'affreux animal que nous avons mis un temps sur la porte d'entrée. Tu es gentil, attentif, et toujours prêt à aider les autres. J'ai beaucoup apprécié la vie au labo à tes côtés. Nous avons discuté de beaucoup de sujets ensemble, certains sérieux, d'autres très, très peu sérieux ! Tu es aussi un exemple pour moi : tu t'affirmes, tu suis ton instinct et tes goûts, et tu n'as pas peur du jugement des autres. J'aimerais avoir la moitié de ta force. Merci encore pour toutes les fois où tu m'as proposé ton aide, que ce soit lié ou non aux manips. Tu es naturellement altruiste et généreux, et je suis heureuse de te connaître.

**Gaëlle** : Merci beaucoup d'avoir partagé des instants de pur non-sens avec moi, comme renommer les zones du CIRB, c'était fun ! Je garderai en tête tous les bons moments passés avec toi, de la Gaëlli (mon passeport est toujours valide) aux eaux internationales. Merci aussi de m'avoir appris à distinguer les pierres précieuses (émeraude = vert, saphir = bleu). Je te souhaite d'avoir le plus beau citron ever, qu'il pousse en ta présence, et qu'il te rende fière ;). Plus sérieusement, je te souhaite le meilleur pour ta vie professionnelle future, mais aussi personnelle. Je prendrai grand plaisir à te revoir en tant qu'ancienne collègue, et maintenant amie.

**Adel** : Merci pour les pauses café/clope que nous avons partagées ensemble. J'ai beaucoup aimé discuter avec toi et débattre des sujets polémiques du moment. Tu es quelqu'un de fin, cultivé, qui maîtrise beaucoup de sujets, et c'est toujours enrichissant

de discuter avec toi. Merci aussi de m'avoir aidée avec toute la partie transcriptomique de ma thèse, je n'aurais pas pu monter le graphique RNA-Seq sans toi. Sinon, j'espère que tu recroiseras la route du plus beau pigeon du monde, tu le mérites !

**Maria** : Tu m'as fait beaucoup rire ! J'ai apprécié nos allers et retours à la cantine, notamment à critiquer mansplaining. Je dois dire que la cantine va me manquer pour ça, certainement pas pour la bouffe, mais pour ces moments qu'on a passés ensemble. Je te remercie pour ta gentillesse et ton empathie. Je te souhaite le meilleur dans ton nouvel appart avec ta puce qui arrive sous peu ! Je suis ravie pour toi.

**Isma** : Je te remercie de m'avoir accompagnée pendant la première partie de ma thèse. Tu as été une référence pour moi et un exemple à suivre, et je te trouve brillante scientifiquement et dans la vie de tous les jours. Je te remercie de m'avoir invitée à faire de l'escalade. Au final, ce sport n'est pas fait pour moi, mais j'ai aimé passer ces moments avec toi. J'ai beaucoup apprécié nos afterworks à jouer du rock et les musiques que tu composais. Tu as du talent pour ça.

**Elvira** : We did not spend much time together in the lab, and I apologize for that. I liked our hikes, with Nochka running around. She is so full of energy! I also liked our afterworks. We should have done them more often because they were really nice. I wish you all the best professionally and personally.

**Lucie et Rose** : Je vous connais depuis peu de temps, mais même si nous n'avons pas passé beaucoup de temps ensemble, je suis contente de vous avoir rencontrées. Je trouve que vous apportez beaucoup de choses nouvelles au labo. Merci **Lucie** pour tes gestes d'attention (comme cacher des chocolats dans nos bureaux). Tu es aussi la reine de l'astuce, et je suis sûre qu'on apprend beaucoup de choses pratiques à tes côtés. **Rose**, je te souhaite de t'éclater dans ce que tu fais. Je serai curieuse et intéressée de lire l'aboutissement de ton projet, comme le tien **Lucie**.

**Anne-Marie, Despoina and Noemi** : It was nice to see you always happy and motivated in the corridors. You brought a nice dynamic to the lab. I wish you all the best for your theses and future work. Enjoy it !

Merci beaucoup à l'ensemble de **l'équipe Selimi** pour votre bonne humeur, vos sourires et votre soutien. En particulier, merci à **Maëla, Mélanie, Maxime et Shayan**.

**Maxime** : Merci beaucoup pour nos parties d'échecs ! C'était agréable d'apprendre à y jouer (même si je ne suis pas très bonne), et aussi de passer ces moments avec toi. Merci d'avoir été là lors des moments compliqués. Ça m'a fait du bien de te parler et de vider mon sac quand j'en avais besoin. J'espère te revoir bientôt !

**Shayan** : Thank you for everything ! For your time, your empathy, our discussions. You are a truly nice person. Thank you for your cooking (despite what you say, it is good!). I look forward to discussing more movies and books with you.

Un grand merci à **la plateforme imagerie du CIRB. Tristan et Julien**, merci pour votre aide et vos conseils. Grâce à vous nous avons de super images de TZPs !

Un grand merci également à **la plateforme animalerie, l'équipe de la laverie et l'équipe de gestion du CIRB**. Sans vous je n'aurais pas pu réaliser ma thèse.

**Véronique et Jean-Antoine** : Merci **Véronique** de m'avoir encadrée lors de mon tout premier stage. Tu m'as présenté la vie en laboratoire, et c'est à la suite de ce stage que j'ai eu envie de faire une thèse. Tu m'as aussi mise en contact avec Marie-Emilie, sans toi je n'aurais jamais réalisé cette thèse. Merci d'avoir fait partie de mon comité de thèse et d'avoir été à mon écoute. J'espère que tout va pour le mieux pour toi et Vincent. Merci **Jean-Antoine** pour ta gentillesse et le temps que tu m'as accordé pendant mon stage de M1, et aussi pendant ma thèse aux meetings du cytoskeleton club. C'est un plaisir de discuter avec toi.

**Caro** : Merci de faire partie de ma vie depuis toutes ces années ! On a muri et traversé des grandes étapes de vie ensemble. J'ai l'impression de te connaître depuis toujours. Je repense à tous nos moments d'amitié et de déconnade (Gertrude !), et j'espère que pleins d'autres nous attendent encore. Merci d'être là quand je ne vais pas bien, merci de me conseiller, merci pour tous les bons moments. J'espère t'apporter tout cela en retour.

**Aurore** : Merci d'être toujours là pour moi, de me soutenir, d'être un repère d'équilibre. Tu es d'une grande générosité et à l'écoute des autres, et j'ai beaucoup de chance d'être ton amie. Je souhaite que ça dure pour toujours. Après ma soutenance, je suis prête à ce que tu m'apprennes à coudre, si tu en as toujours envie !

**Florian** : J'aime beaucoup nos moments one VS one : les restos, cinés, et discussions autour d'une bouteille de vin et d'une pizza. Merci d'avoir été là pour moi pendant la traversée de ma thèse. Avec toi je peux parler de tout et c'est facile de déconner. C'est vrai que parfois on s'engueule, mais c'est normal entre amis, et d'ailleurs ça ne dure jamais longtemps ;) . Merci !

**Anne-Laure** : Je nous revois toutes les deux à parler de nos études. On se doutait bien que ça allait être long, et aujourd'hui, on s'approche toutes les deux de la fin ! Il faudra fêter ça dignement ! Même si on se voit moins, je suis contente de te savoir heureuse dans le Nord avec Guillaume. Tu m'invites quand tu veux et je débarque !

**Graciela et JB** : Merci pour les soirées passées ensemble. J'ai hâte de refaire ça bientôt ! **Graciela**, tu me fais rire avec tes plantes ! **JB**, la prochaine fois qu'on se voit, j'ai bien envie d'apprendre à faire des cocktails comme ceux que tu as fait à la soirée d'anniversaire de Graciela !

**Djamila, Noémie et Ulduz:** Thank you girls for all the good times we spent together! Merci **Djamila** de m'avoir invitée à tes journées barbecue, et merci pour tous les autres moments de glotonnerie partagés ensemble. Ta bonne humeur fait toujours plaisir à voir. **Noémie**, je me souviendrai toujours de ton discours devant la télé extérieure de l'institut à Roscoff. Tu m'as fait énormément rire. **Ulduz**, it has been a long time since we have seen each other, I hope that everything is going fine in your life.

**Rostyslav and Camilo :** Thank you for always bringing joy when we hang out.

**Xingming :** I am glad I met you a year and a half ago now! I like hanging out with you, discovering new places to eat. I am sorry I have not shown you much of Paris, and I promise I will make it up to you.

**Gianluca :** Tu resteras une personne qui a compté pour moi et je te dois beaucoup. Merci d'avoir cuisiné et partagé de délicieux plats avec moi. Tu es un excellent cuisinier, et aussi un très bon musicien. Même si on se voit moins aujourd'hui, j'ai toujours plaisir à passer du temps avec toi. Tu es l'une des personnes les plus gentilles et attentionnées que je connaisse. Merci d'avoir été présent pour moi.

**Papy, Mamy, Pascal, Dominique, Agnès, Thibault, Ariane, Simon, Rodolphe, Colin et Gabriel :** Je suis heureuse de faire partie d'une famille soudée, qui prend plaisir à se retrouver et à passer du temps ensemble. C'est une chance, merci !

**Guillaume :** Je suis contente que tu sois avec Agathe et je suis heureuse de te connaître. J'ai hâte que tu me fasses goûter ta version du Flé-mmard et que tu m'apprennes quelques morceaux à la guitare, si tu es d'accord !

**Hector :** Merci d'être le meilleur des chats, tu es mon fils de cœur.

**Papa, maman, et Agathe :** Vous êtes la raison pour laquelle j'ai eu une enfance heureuse. Je vous aime.

**Papa :** Merci de m'avoir accueillie chez toi pendant une grande partie de la rédaction de ma thèse. Je t'en suis reconnaissante. Merci pour les repas, nos ballades et soirées ciné ! J'en garderai un très bon souvenir. Je reviendrai chez toi avec grand plaisir, mais cette fois pour y passer des vacances !

**Maman :** Merci de m'avoir soutenue et motivée pendant la dernière partie de la rédaction de ma thèse. Tu es une personne bienveillante et tu mérites le meilleur. J'espère un jour avoir au moins la moitié de ton empathie. Je serai toujours là pour toi.

**Agathe :** Je devrais t'appeler et prendre de tes nouvelles plus souvent, c'est mon erreur, et il faut que je change ça. Tu es toujours de bons conseils, et je te remercie de m'aider à voir la vie sous un bel angle. Merci d'être ma grande sœur, avec tout ce que cela implique.

*My thesis years represent and will remain a singular period of my life, with many ups and downs, joyful moments and others, sadder. It was an intense professional and personal experience, where scientific training was mixed with personal development. It confronted me with my limits, sometimes brutally, sometimes in a subtler way. In essence, it was an initiatory journey during which I received directly or indirectly beautiful values of life, qualities that could not have been taught to me as effectively if I had not engaged in this path. The rigor, logic and open-mindedness that Science requires, and brings in return, are part of these values. This experience has helped me to build and mature. For this, I would like to thank all the people who shared my daily life these last four years and who contributed to this study: Marie-Emilie, Marie-Hélène, Christelle, Adrien, Adel, Gaëlle, Maria, Isma and the whole Terret-Verlhac team. You have trained me, given me your time, helped me analyze data, made me laugh, supported me emotionally, made me taste (and drink) a lot of good things, and most of all, made sure that today, I have a positive overall view of my thesis. Merci.*

# Preface

This manuscript will present two studies conducted in the mouse oocyte through the prism of Myosin-X, a molecular motor having the dual interest of being involved in the formation of filopodia and in the positioning of division spindles in several cellular models.

My initial thesis project, which will be the first one addressed in the Results section (although presented last in the introduction), follows on from studies conducted in the lab on spindle positioning in the mouse oocyte. In essence, it remains to be established how F-actin, which plays a critical role in spindle positioning in this model, transmits pulling forces to the microtubule spindle of the first meiotic division to position it in the oocyte. Myosin-X emerged as an interesting candidate for mediating this process due to its known involvement in spindle positioning in several mitotic cells, and its potential to bind to F-actin and microtubules. To determine whether Myosin-X plays a role in spindle positioning in the mouse oocyte, we generated what we thought was a conditional knockout of Myosin-X in oocytes using the *Zp3-Cre loxP* system. It turned out that we had in fact generated a total knockout of Myosin-X because of the retention of the neomycin selection cassette, whose promoter interfered with Myosin-X expression in all mouse cell types.

With a total knockout in hand, we coincidentally observed that oocytes from Myosin-X null mice displayed a reduced density of contacts with somatic cells. These contacts are cellular protrusions established by somatic cells that surround the oocyte during its development. The role of these protrusions in oocyte development has been indirectly addressed, but requires further study. Since we generated oocytes with reduced density of somatic protrusions, we decided to study the role of these structures in oocyte quality, focusing on the ability of these oocytes to support meiotic maturation. My second thesis project was born, and is now the main subject of this manuscript.

We subsequently generated a true conditional knockout of Myosin-X in oocytes by removing the neomycin selection cassette. This allowed us to complete my first thesis project, the results of which ruled out a role for Myosin-X in spindle positioning in the mouse oocyte. Importantly, Myosin-X in the oocyte is not required for female fertility. Hence, we were able to attribute the defects we observed in full knockout

oocytes to the somatic depletion of Myosin-X and the resulting decrease in somatic contact density. In this regard, my two thesis projects crossed over, the former benefiting the latter. The discovery that we had a full knockout strain and the subsequent launch of my second thesis project occurred relatively soon after I joined the lab, so we were able to bounce back easily. I am glad events turned out this way, and I enjoyed working on two separate projects.

The introduction of this manuscript will be organized into three parts. The first one briefly introduces the mammalian oocyte and the two major stages of its *post-partum* development, oocyte growth and meiotic maturation. The second chapter focuses on the interaction between the oocyte and somatic cells with an emphasis on direct contacts during oocyte growth. Finally, the last chapter briefly presents the mechanisms by which the mouse oocyte positions its spindle before anaphase of the first meiotic division. For each chapter, where I have written paragraphs based on reviews, these are cited at the end of the relevant paragraph as follows:

- Review.

# Table of content

<b>Abbreviations</b>	p.1
<b>INTRODUCTION</b>	p.3
<b>Chapter I: Introducing the oocyte, the female germ cell</b>	p.4
<b>I) Production of the oocyte pool: the fundamental basis of female fertility</b>	p.6
1) <u>Oocyte fetal development: germ cell entry into meiosis</u>	p.6
2) <u>Primordial follicles formation: enclosing the oocyte in a somatic environment</u>	p.7
<b>II) Oocyte and follicular growth: shaping the developmental potential of the oocyte</b>	p.8
1) <u>Overview of the growth phase: preparing the oocyte for future meiotic divisions and embryogenesis</u>	p.8
2) <u>Activation of primordial follicles and preantral growth</u>	p.9
3) <u>Antral follicle growth</u>	p.10
<b>III) Meiotic divisions: extrusion of half of the oocyte DNA content while preserving the maternal stores</b>	p.12
1) <u>Overview of meiotic divisions: becoming haploid in an altruistic way</u>	p.12
2) <u>Competence to resume meiosis and release from prophase I arrest</u>	p.13
3) <u>Summary of the main features of meiotic maturation</u>	p.14
3.1- <i>Off-centering and segregation of homologous chromosomes</i>	p.14
3.2- <i>Organelle reorganization and translational regulation/degradation of maternal transcripts</i>	p.15
<b>Concluding remarks</b>	p.16
<b>Chapter II: Oocyte-somatic cell interaction during oogenesis</b>	p.17
<b>I) Overview of oocyte-somatic cell interaction during oogenesis</b>	p.19
<b>II) Oocyte-somatic cell interaction in primordial and early growing follicles: an unconstrained dialogue</b>	p.20

<b>III) Oocyte-somatic cell interaction with a defined <i>zona pellucida</i>: an impeded but persistent dialogue</b>	<b>p.21</b>
1) <u>The <i>zona pellucida</i>, the extracellular layer surrounding the oocyte</u>	p.21
2) <u>Transzonal projection, a mean to maintain intercellular contact</u>	p.23
2.1- <i>Overview</i>	p.23
2.2- <i>TZP structure and dynamics</i>	p.23
➤ <i>A filopodia-like protrusion</i>	
➤ <i>TZP dynamics during oogenesis</i>	
2.3- <i>TZP-mediated interactions: meeting the needs of the oocyte</i>	p.27
➤ <i>Cell-cell adhesion</i>	
➤ <i>Gap junction coupling</i>	
➤ <i>Exchange of extracellular vesicles</i>	
2.4- <i>Opening to broader perspectives</i>	p.30
➤ <i>Disease impact on TZP-mediated communication</i>	
➤ <i>Age impact on TZPs</i>	
➤ <i>Exclusively somatic? Protrusions of oocyte origin</i>	
<b>IV) Oocyte-neighboring cell interaction in non-mammals</b>	<b>p.32</b>
1) <u>The case of the <i>Drosophila</i> oocyte: multiple interactions with different cell types</u>	p.32
2) <u>The case of the <i>C. elegans</i> oocyte: use of somatic cells for timely resumption of meiosis</u>	p.34
<b>Concluding remarks</b>	<b>p.35</b>
 <b>Chapter III: Preserving a nutrient-rich cytoplasm through spindle off-centering</b>	 <b>p.36</b>
<b>I) Spindle positioning in the absence of cortical cues and centrioles</b>	<b>p.38</b>
<b>II) Two F-actin networks cooperate to off-center the meiosis I spindle</b>	<b>p.39</b>
1) <u>A straight cytoplasmic network surrounds the spindle and connects it to the cortex</u>	p.39
2) <u>A branched subcortical network provides cortical softness to enhance spindle migration</u>	p.40
<b>III) Myosin-X, a possible mediator of spindle off-centering forces?</b>	<b>p.41</b>
<b>Concluding remarks</b>	<b>p.43</b>

## RESULTS p.44

**Article #1: Myosin-X is dispensable for spindle morphogenesis and positioning in the mouse oocyte p.45**

**Article #2: Granulosa cells enhance the oocyte developmental potential through transzonal projections p.47**

## DISCUSSION p.49

**I) TZP-deprived oocytes reach canonical size p.51**

- 1) TZP density reduction and oocyte size in the literature p.51
- 2) Oocyte-directed compensation for increased nutrient uptake? p.54

**II) Possible effects of TZPs on *zona pellucida* integrity p.55**

- 1) Impaired *zona pellucida* due to altered expression/secretion of its component proteins? p.55
- 2) Impaired *zona pellucida* due to lack of matrix degradation by TZPs? p.55

**III) Origins of metaphase I arrest in some TZP-deprived oocytes p.56**

- 1) Alteration of oocyte lipid content? p.57
- 2) Unregulated oocyte  $pH_i$  during growth? p.58
- 3) Indirect cause of an altered transcriptome? p.59
  - 3.1- *Somatic regulation of the oocyte transcriptome through TZP-mediated transfer of RNA?* p.59
  - 3.2- *Impaired MPF regulation in *Myo10*<sup>-/-</sup> full oocytes?* p.60

**Concluding remarks p.61**

## REFERENCES p.62

## ANNEXES p.76

# Abbreviations

- **Akr1b3**: aldo-keto reductase family 1, member B3
- **cAMP**: cyclic adenosine monophosphate
- **cGMP**: cyclic guanosine monophosphate
- **COC**: cumulus-oocyte complex
- **dpc**: days *post-coitum*
- **dpp**: days *post-partum*
- **EPAB**: Embryonic poly(A)-binding protein
- **EU**: 5-ethynyl uridine
- **FABP3**: Fatty acid-binding protein 3
- **F-actin**: filamentous actin
- **FDR**: false discovery rate correction
- **FERM**: band 4.1/ezrin/radixin/moesin
- **FSH**: Follicle stimulating hormone
- **GDF-9**: Growth differentiation factor-9
- **GO**: gene ontology
- **GOC**: granulosa-oocyte complex
- **IQ**: IQ motifs
- **LH**: Luteinizing hormone
- **lincRNA**: long intergenic non-coding RNA
- **MII**: meiosis II
- **miRNA**: microRNA precursors
- **MPF**: maturation promoting factor
- **Mt-tRNA**: transfer RNA located in the mitochondrial genome
- **MYO10**: Myosin-X
- **MyTH4**: myosin tail homology 4
- **NEBD**: nuclear envelope breakdown
- **Oser1**: oxidative stress responsive serine rich 1
- **P adj**: adjusted P value with false discovery rate
- **PB**: polar body
- **PBE**: polar body extrusion

- **PGC:** primordial germ cell
- **PH:** pleckstrin homology domains
- **pHi:** intracellular pH
- **ROS:** reactive oxygen species
- **SAH:** single  $\alpha$ -helix
- **SiR-act:** SiR-actin
- **SiR-tub:** SiR-tubulin
- **TEC:** to be experimentally confirmed
- **TNT:** tunneling nanotube
- **TUB:** Tubulin
- **TZP:** transzonal projection
- **ZP:** *zona pellucida*
- **ZP1-4:** Zona pellucida glycoprotein 1, 2, 3 or 4.

# **INTRODUCTION**

# **Chapter I: Introducing the oocyte, the female germ cell**

*The following is a general introduction to the oocyte, its biological function as a germ cell, and the acquisition of its developmental potential, a prerequisite for the generation of a good quality embryo. This section serves as a background to the main topic of this thesis, i.e. the oocyte-somatic cell interaction during oocyte development. The different stages of oogenesis and folliculogenesis will therefore be briefly introduced, but not detailed. If you are interested in learning more about these processes, I recommend reading the reviews listed at the end of the paragraphs, or the following books, which I used to write some chapters in this section:*

- *Biology and pathology of the oocyte: its role in fertility and reproductive medicine. (2003). (A. Trounson, & R. Gosden, Eds.). Cambridge University Press.*
- *Oogenesis: the universal process. (2010). (M-H. Verlhac, & A. Villeneuve, Eds.). John Wiley & Sons, Ltd.*

Organisms that rely on sexual reproduction for species propagation produce germ cells to generate genetically new individuals. Germ cells include the oocyte for females and the spermatozoon for males, and are unique in that they change from a diploid to a haploid state during their formation process. Subsequent fertilization of the oocyte by the spermatozoon restores the cell diploid content and leads to the formation of a single totipotent cell, the zygote. The ability of the zygote-derived embryo to develop into a healthy offspring is closely related to the quality of the oocyte, also known as the oocyte developmental potential. This potential is acquired after the oocyte has undergone two developmental stages: a growth phase, during which it stores macromolecules critical for embryogenesis, and a maturation process, accompanied by the extrusion of half of its DNA content. Oocyte production is, in its basal state, subject to developmental errors that increase with the age of the mother and are a potential cause of impaired fertility or congenital disease in the prospective offspring. Further knowledge of how the oocyte acquires its developmental competence is valuable not only for basic research but also for clinical purposes. Decreased fertility due to poor oocyte quality or altered oocyte development leads to the use of assisted reproductive technology to conceive. The chances of success of these technologies are low and a current societal challenge is to increase their efficiency by, in particular, improving *in vitro* recapitulation of the critical steps of oocyte development.

## **I) Production of the oocyte pool: the fundamental basis of female fertility**

### 1) Oocyte fetal development: germ cell entry into meiosis

Mammalian oocytes are produced in the ovary during fetal life from primordial germ cells (PGC) that have undergone several cycles of mitotic proliferation. The germ cells are called oocytes when they enter meiosis. This process consists of two successive cell divisions (meiosis I and II) with a single step of DNA replication, a meiotic feature that leads to the reduction of the cell DNA content by half. During fetal life, oocytes develop until the diplotene stage of prophase I where they arrest with pre-condensed pairs of homologous chromosomes that have undergone genetic

recombination. Oocytes remain arrested at this stage until meiosis resumes in post-pubertal mammals, upon hormonal stimulation. It is therefore in a quiescent state that oocytes spend most of their life, a state that can last up to several months in mice and decades in humans.

Since it is thought that germ cells no longer enter meiosis after the birth of female mammals, individuals are born with a limited number of resting oocytes that constitutes their only reproductive pool. This lack of germ cell renewal after birth is a characteristic of female reproduction, as spermatozoa are produced continuously throughout the life of male individuals. For sexually mature females, this implies that they rely on long-lived germ cells to reproduce and that their oocyte pool is depleted during each reproductive cycle, making the pool size critical for fertility.

- Byskov and Nielsen 2003
- Combes 2010

## 2) Primordial follicles formation: enclosing the oocyte in a somatic environment

The fetal oocyte undergoes the early stages of prophase I not isolated but surrounded by neighboring oocytes in a progressively disrupted syncytium-like nest, which results from earlier mitotic divisions with incomplete cytokinesis. Once the nest breaks down, the individualized oocytes get surrounded by a single layer of somatic cells termed pregranulosa cells (Fig.1 A). This event occurs during embryogenesis in humans and during the perinatal period in rodents. The coupling of the oocyte and pregranulosa cells marks the formation of the primordial follicle, the fundamental unit of the ovary that contains the quiescent oocyte. Importantly, it initiates a close intercellular dialogue between the oocyte and the somatic cells, and bidirectional communication between the two cell types is essential for proper oocyte development. Somatic embedding is maintained for most of the remaining development of the oocyte. When the oocyte leaves its quiescent state to grow, the somatic cells accompany it in this process by proliferating and differentiating in a process called follicular growth.

- Skinner 2005
- O'Connell and Pepling 2021

## **II) Oocyte and follicular growth: shaping the developmental potential of the oocyte**

### **1) Overview of the growth phase: preparing the oocyte for future meiotic divisions and embryogenesis**

The oocyte enclosed in the primordial follicle is incompetent to resume meiosis, to be fertilized and therefore to generate an offspring. To do so, it must first undergo morphological and cytoplasmic changes in a process termed oocyte growth. During this process, which lasts about 2-3 weeks in mice and several months in humans, the size of the oocyte increases from a diameter of ~ 15  $\mu\text{m}$  to ~ 80  $\mu\text{m}$  in mice and from ~ 30  $\mu\text{m}$  to ~ 120  $\mu\text{m}$  in humans.

One of the most prominent feature of growth is the substantial storage in the oocyte of proteins and transcripts required for future development (Fig.1 A). Importantly, the oocyte becomes transcriptionally silent at the end of growth and no longer synthesizes transcripts during subsequent meiotic divisions (Fig.1 B). Additionally, the early embryo depends on stored maternal RNAs to develop until zygote genome activation, which occurs predominantly at the 2-cell embryonic stage in mice. Storage of transcript during oocyte growth is therefore critical not only for subsequent meiotic divisions, but also for early embryogenesis (Clarke 2012, Conti and Franciosi 2018).

Another critical aspect of the growth phase is the ultrastructural change in oocyte organelles, particularly mitochondria (Wassarman and Josefowicz 1978), which may reflect an increased metabolic activity of the oocyte during this time period. Therefore, the oocyte growth process can be viewed as a marathon for the oocyte to provide enough energy and macromolecular content to the embryo for optimal development.

## 2) Activation of primordial follicles and preantral growth

As mentioned earlier, the primordial follicle is the basic unit from which each oocyte competent to be fertilized originates. Once the follicular pool is constituted, resting follicles enter growth (also called initial recruitment or follicle activation) in a continuous manner until the pool is severely depleted. Pool exhaustion, which results either from follicle entering growth or from follicle degeneration by atresia, marks the end of female reproductive life and the entry into menopause.

The factors that trigger follicle activation are still poorly understood. However, it is proposed that the activation is regulated by a combination of autocrine and paracrine factors, inhibitory and activating, coming from the oocyte and surrounding somatic cells. Importantly, it is suggested that oocyte growth is triggered by intercellular communication between the oocyte and the granulosa cells.

The onset of growth is marked by the exit of the oocyte from quiescence and by the mitotic proliferation of the surrounding somatic cells, which change from a squamous to a cuboidal shape. Follicles are termed primary when the oocytes are surrounded by a single layer of cuboidal granulosa cells. At this stage, glycoproteins start to assemble into filaments to form the *zona pellucida*, an extracellular layer surrounding the oocyte (Wassarman and Litscher 2018, see Chapter II, paragraph III.1). As the granulosa cells continue to proliferate, they accumulate in several layers around the growing oocyte. The follicle is termed secondary. Another type of somatic cell enters in the follicle constitution at this period, the theca cell. Theca cells notably contribute to follicular development by providing steroid precursors to the granulosa cells that they surround and structural support to the follicle (Young and McNeilly 2010). Note that since this thesis investigates oocyte-somatic cell communication through direct contact and that theca cells are not adjacent to the oocyte, I will not focus on this type of somatic cell in the rest of the manuscript.

- Faddy and Gosden 2003
- Oktem and Urman 2010
- El-Hayek and Clarke 2016
- Clarke 2018

### 3) Antral follicle growth

As the follicle continues to expand with additional layers of granulosa cells surrounding the growing oocyte, a fluid-filled chamber called the antrum appears between the granulosa cells. The antrum segregates the granulosa cells into two differentiated subpopulations (Fig.1 A). The first population of granulosa cells (called cumulus cells) is adjacent to the oocyte with which it constitutes a sub-complex termed the cumulus-oocyte complex (COC). The COC is of particular interest to this study as it represents the only site in the antral follicle where direct oocyte-somatic cell communication occurs. The other population of granulosa cells is located on the follicle wall, the cells are called mural granulosa cells and are notably characterized by their steroid production.

At the antral stage, follicles are dependent on Follicle stimulating hormone (FSH) to further grow. Upon FSH stimulation, only a few antral follicles continue to grow, while the majority undergo degeneration by atresia. This selection process corresponds to the second follicle recruitment and occurs cyclically in sexually mature organisms. Only a minority of antral follicles therefore continue growth and among this cohort, depending if the species is mono- (human) or poly- (mouse) ovulating, only one or a few follicles classified as dominant are selected to resume meiosis and undergo ovulation.

- Faddy and Gosden 2003
- Oktem and Urman 2010
- El-Hayek and Clarke 2016
- Clarke 2018

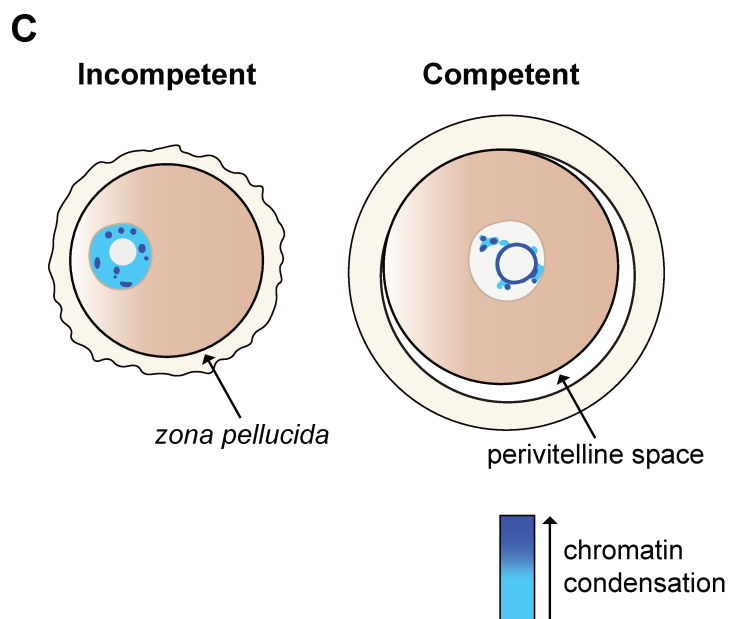
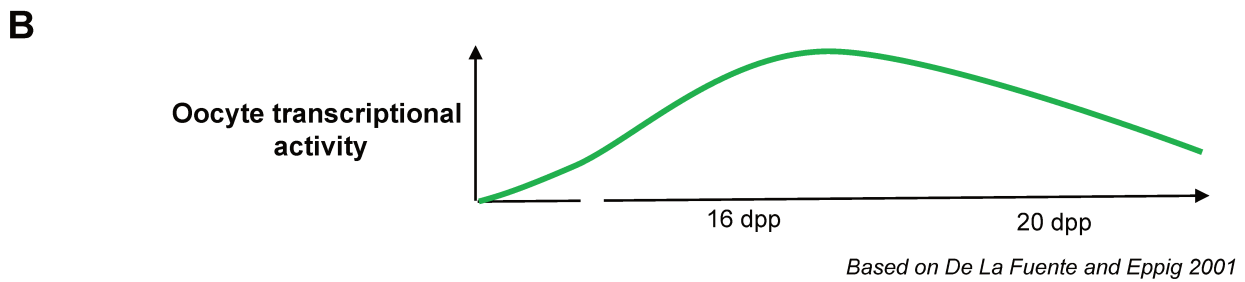
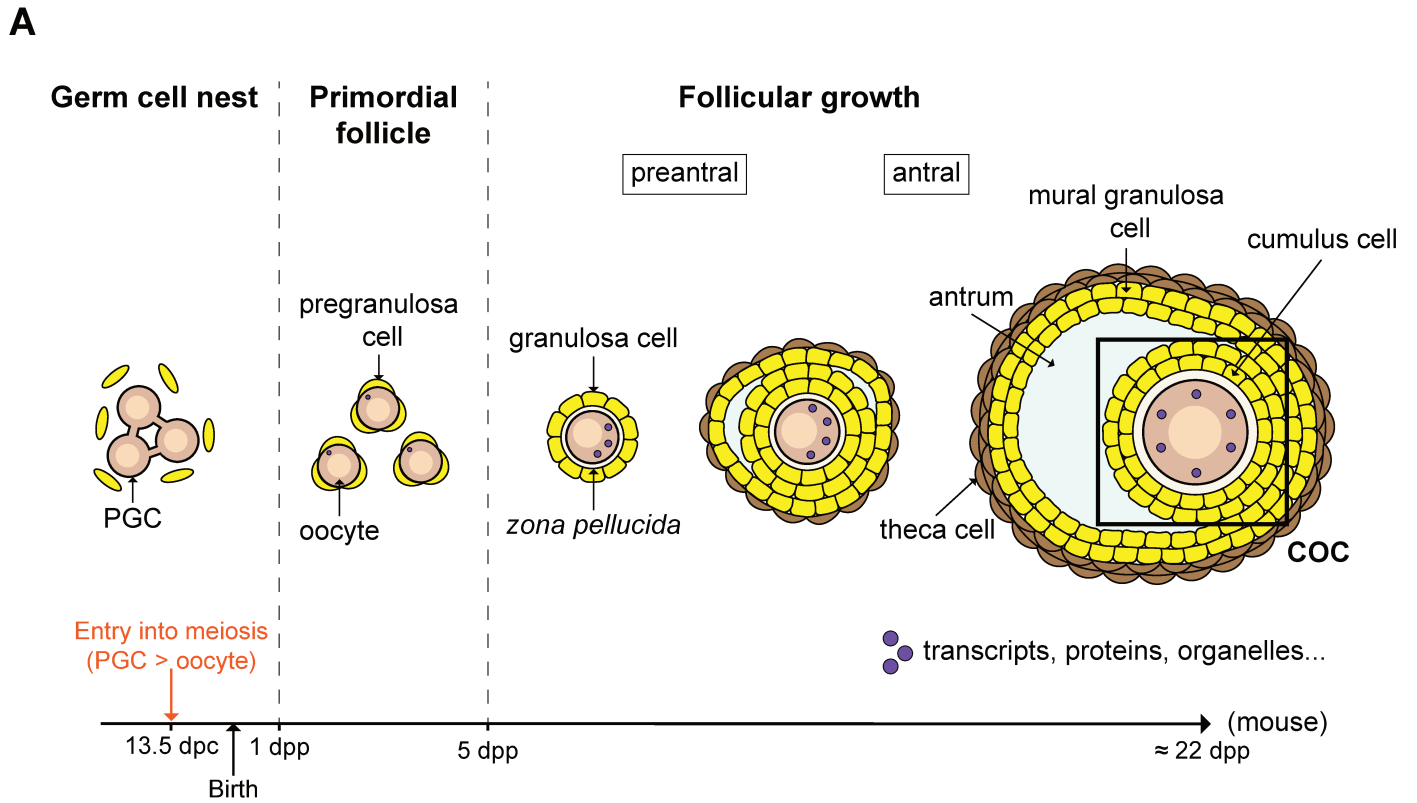


**Figure 1: Development of the mouse oocyte arrested in prophase I.** **A)** Schematic of fetal oocyte development and follicular growth. PGC stands for primordial germ cell, dpc days *post-coitum*, dpp days *post-partum* and COC cumulus-oocyte complex. **B)** Graph of global transcriptional activity of the oocyte during growth. **C)** Schematics depicting some of the morphological criteria that we used to characterize an “incompetent” (left) and “competent” (right) oocyte before meiosis resumption at the antral stage.

### **III) Meiotic divisions: extrusion of half of the oocyte DNA content while preserving the maternal stores**

#### 1) Overview of meiotic divisions: becoming haploid in an altruistic way

At the end of growth, the oocyte has developed into a large cell with a remodeled cytoplasm, rich in nutrients and macromolecules. The oocyte still contains the paternal and maternal chromosomes. To fulfill its biological fate, i.e. to provide an offspring to the individual who carries it, it must become haploid. The oocyte achieves this goal after two successive divisions (meiosis I and II) without a DNA replication step in between. It undergoes a process termed meiotic maturation marked by a series of nuclear and cytoplasmic remodeling that lasts ~12 hours in mice and ~ 36 hours in humans (Fig. 2). Meiotic maturation extends from the resumption of meiosis, where the oocyte had paused in prophase I, to metaphase II. At this stage, the oocyte experiences its second meiotic arrest until fertilization, caused by the encounter with a spermatozoon, which triggers the resumption and exit of the second meiotic division. Of note, fertilization does not take place in the ovary but in the fallopian tube, where the oocyte is delivered after its release from the follicle during ovulation in metaphase II. Therefore, ovulation signs the end of the embedding of the oocyte in the follicle (Fig. 2).

The oocyte loses half of its DNA content with numerous constraints. One of these constraints is to implement a strategy to off-center the chromosomes to ensure asymmetric divisions in size. The asymmetry of cell divisions limits the loss of oocyte reserve at each division. Each meiotic division therefore releases a small cell of derisory size compared to that of the oocyte, called polar body. This is part of a

perspective, which can be qualified anthropomorphically as “altruistic”, which allows the embryo to receive the greatest number of macromolecules and organelles necessary for its development.

## 2) Competence to resume meiosis and release from prophase I arrest

The ability of the oocyte arrested at the diplotene stage of prophase I to resume meiosis, also known as meiotic competence, is acquired at the antral stage and is positively correlated with oocyte size (Sorensen and Wassarman 1976). Importantly, the oocyte nucleus is subject to changes while reaching meiotic competence. It is relocated from an eccentric to a centric position in the oocyte (Fig. 1C). This process is mediated by F-actin and is accompanied by a reshaping of the oocyte transcriptome that correlates with the acquisition of its developmental potential (Almonacid 2015, Almonacid 2019). In addition, the chromatin of the oocyte undergoes large-scale remodeling throughout the progression of the antral stage and progressively shifts from a predominantly decondensed configuration in the nucleoplasm to a condensed configuration primarily surrounding the nucleolus (Fig.1 C). This period of gradually condensed chromatin corresponds to that of global transcriptional silencing of the oocyte, which precedes the resumption of meiosis (Fig.1 B).

A competent oocyte can be identified *in vitro* by its ability to spontaneously resume meiosis when released from the follicle. This illustrates the involvement of the surrounding somatic cells in the control of maturation entry. When the oocyte becomes meiotically competent, the interaction with somatic cells blocks meiosis resumption to further enhance oocyte developmental competence. Indeed, the ability of the oocyte to resume meiosis and its competence to complete meiotic maturation are acquired in temporally decoupled manner (Sorensen and Wassarman 1976). Somatic prevention of premature meiotic resumption relies on sending inhibitory signals to the oocyte that maintain a high level of cyclic adenosine monophosphate (cAMP) in the oocyte. Somatic inhibitory inputs cease after a surge of Luteinizing hormone (LH), which leads to a cascade of intercellular communication involving both mural and cumulus cells. The latter results in a decreased in the amount of cAMP in the oocyte, activation of the maturation promoting factor (MPF), and ultimately the resumption of meiosis.

In this study, we used different morphological criteria to classify oocytes as “incompetent” or “competent” to support meiotic maturation (i.e., meiosis resumption and extrusion of the first polar body). This classification is based on the presence or absence of a visible perivitelline space (i.e., the space between the oocyte and the *zona pellucida*), the granularity of the outer border of the *zona pellucida* and the subcellular position of the oocyte nucleus (Fig.1 C).

- Albertini 2003
- Luciano 2012
- Coticchio 2015

### 3) Summary of the main features of meiotic maturation

#### *3.1- Off-centering and segregation of homologous chromosomes*

The resumption of meiosis is marked by the rupture of the nuclear envelope (NEBD), which is followed by the compaction of chromosomes into individualized bivalents. Homologous chromosomes congress and align on the spindle equatorial plane during a long prometaphase/metaphase and then separate into two batches, one of which is extruded in the first polar body (Mihajlović and FitzHarris 2018, Fig. 2). The first meiotic division, qualified as reductional, yields a haploid oocyte. It is followed by an equational division of mitotic type which leads to the separation of sister chromatids after fertilization.

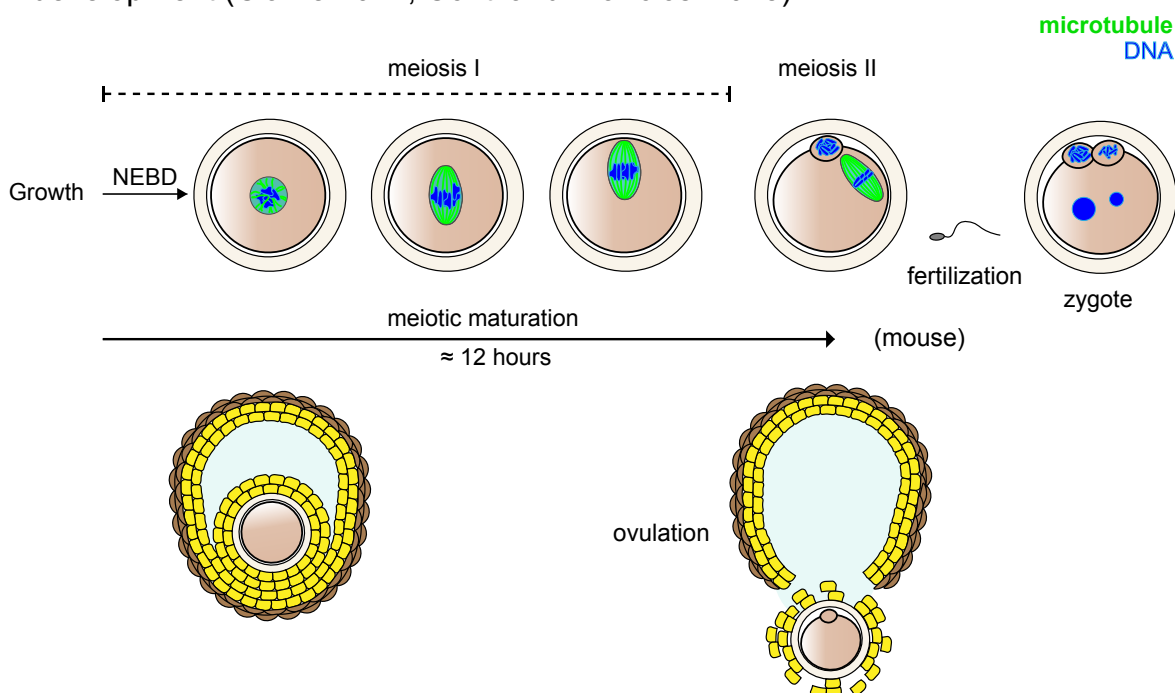
To align and segregate homologous chromosomes during meiosis I, a division spindle, distinct in shape from most of its mitotic counterparts, is assembled in a centriole-free context (Bennabi 2016, Mihajlović and FitzHarris 2018). Centrioles are indeed degraded in many mammalian oocytes prior to meiotic divisions (Szollosi 1972, for mouse oocytes). Subsequently, the spindle migrates from the center of the oocyte, where it has bipolarized, to the cell cortex by a process engaging filamentous actin (F-actin) (Chaigne 2017). Spindle off-centering underlies the asymmetric division in size of the oocyte and the retention of a large cytoplasm for embryogenesis, a feature positively correlated with oocyte developmental potential (Kyogoku 2017). As spindle

positioning is atypical in the maturing mouse oocyte, mainly because it is performed without centrioles, this process will be discussed in more detail in Chapter III.

### 3.2- *Organelle reorganization and translational regulation/degradation of maternal transcripts*

As meiotic maturation proceeds, the oocyte undergoes changes in the distribution or morphology of many of its organelles, including endoplasmic reticuli, golgi apparatus and mitochondria. This remodeling is believed critical for the acquisition of the developmental potential of the oocyte (Coticchio 2015, Conti and Franciosi 2018). In particular, the spindle of the first meiotic division migrates to the cortex surrounded by mitochondria in the mouse. This mitochondria distribution is considered valuable in providing a localized energy supply to the maturing oocyte.

Meiotic maturation is also marked by the timely translational activation of dormant transcripts previously accumulated during growth. This activation occurs in a context of transcriptional repression and is required for proper maturation progression. In addition, meiotic maturation is a period of degradation of maternal transcripts, which, together with translational activation, appears to be a prerequisite for the completion of the oocyte-to-embryo transition and for the embryo to use its own genome for further development (Clarke 2012, Conti and Franciosi 2018).



Adapted from Verlhac and Terret 2016

**Figure 2: Meiotic divisions of the mouse oocyte.** Schematic of oocyte meiotic maturation and fertilization. NEBD stands for nuclear envelope breakdown.

## **Concluding remarks**

The mammalian oocyte is an unconventional cell in that it can remain dormant for a significant period of the female's life, then expand drastically, and finally become haploid after a process involving two asymmetric divisions. The quality of the oocyte, determined by its ability to generate a well-constituted embryo, depends on the correct completion of these sequential steps. Numerous studies have been carried out to decipher the main cellular and molecular actors involved in the key processes of oocyte development. A major objective of this research is to gain a solid knowledge on the latter in order to bring new fundamental advances on why oocyte formation generates a basal rate of bad quality oocytes. This scientific knowledge could be exploited in more applied contexts, such as the modulation and improvement of oocyte culture conditions to increase the rate of success of assisted reproductive technologies. In particular, an important line of study is to determine the extent to which the oocyte relies on somatic cells for proper development. Indeed, the oocyte is engaged in a two-way dialogue with the surrounding granulosa cells as it develops, and this dialogue is critical for adequate follicular growth and oogenesis.

# **Chapter II: Oocyte- somatic cell interaction during oogenesis**

*This section provides an overview of the interaction between the oocyte and somatic cells during mammalian oogenesis, with an emphasis on direct dialogue during follicular growth. The fact that this chapter is the main section of this thesis is the result of two fortuitous elements; the retention of a selection cassette in a conditional knockout and the realization of a non-routine immunostaining protocol in the lab. These two elements initiated my main thesis project and can therefore be considered as “tartes Tatin” in a scientific background. I would like to thank Marie-Emilie for trusting me enough to let me dock and discover the field of follicular growth.*

Cells in the body communicate with each other for a variety of purposes, including spatial orientation, proliferation, or adoption of a specific fate. These communications can take place when cells are physically distant from each other, or conversely, require direct cellular contact. Among the various cellular complexes present in mammals, the ovarian follicle is a site of intense cellular communication, involving not only different cell types, but also various means of dialogue. The timely coordination of these intercellular exchanges is crucial for the proper development of the oocyte, and by extension, for the generation of a good quality embryo.

Among the different communications established between the oocyte and the somatic cells, that by direct contact is particularly interesting for this study as it represents the main mode of communication used by the granulosa cells to send developmental inputs to the oocyte. The emergence of the *zona pellucida* at an early stage of follicular growth challenges the maintenance of this direct dialogue, as it spatially separates the oocyte from surrounding granulosa cells. One strategy implemented to maintain the direct dialogue between the oocyte and somatic cells is the elaboration by the granulosa cells of filopodia-like protrusions to connect to the oocyte membrane. Although the dynamics of these structures remains to be further studied, several of their mediated communications have been identified as important to the developmental potential of the oocyte. Importantly, the oocyte regulates the formation of these somatic protrusions and therefore acts as a coordinator of somatic input release for its proper development.

## **I) Overview of oocyte-somatic cell interaction during oogenesis**

The oocyte grows and matures enclosed by the granulosa cells which participate in the acquisition of its developmental potential. The need for a close coupling between these two cell types for oocyte development is nowadays well established. It has been notably evidenced by the *in vitro* culture of oocytes with altered association with granulosa cells (Eppig 1979, Ge 2008). Oocytes cocultured with, but not enclosed in, granulosa cells failed to grow properly compared to cultured granulosa cell-enclosed oocytes (Eppig 1979). In addition, oocytes devoid of somatic cells showed impaired *in vitro* maturation that was improved by coculture with cumulus cells (Ge 2008).

The bidirectional communication between the two cell types coordinates critical biological processes of the oocyte. This communication is the basis of the oocyte dependence on the granulosa cells for development. Oocyte-somatic communications during growth consist of a well-orchestrated combination of paracrine signaling, gap junction coupling, and possibly extracellular vesicle exchange. The role of these communications in the follicle has been the subject of numerous studies and has been notably investigated by oocyte denudation (Haghighat and Van Winkle 1990, De La Fuente and Eppig 2001, Eppig 2005, FitzHarris and Baltz 2006, Macaulay 2014, Macaulay 2016), oocyectomy (Eppig 2005, Sugiura 2005, El-Hayek 2018), chimeric cell reaggregation (Eppig 2002), use of chemical uncouplers (Haghighat and Van Winkle 1990, FitzHarris and Baltz 2006, Norris 2009, Luciano 2011), targeted gene deletions (Dong 1996, Carabatsos 1998, Simon 1997, Zhang 2021) and siRNA (El-Hayek 2018). Note that this list is not exhaustive.

Through intercellular communication, somatic cells participate in oocyte metabolic activity (Biggers 1967, Donahue and Stern 1968, Haghighat and Van Winkle 1990, Eppig 2005), control the timely resumption of meiosis (Norris 2009), and modulate large-scale chromatin remodeling and global RNA synthesis in the oocyte (De La Fuente and Eppig 2001, Luciano 2011). In turn, the oocyte, primarily by secreting factors, modulates granulosa cell differentiation and proliferation for adequate follicle growth (Dong 1996, Carabatsos 1998, Eppig 2002).

- Kidder and Vanderhyden 2010
- El-Hayek and Clarke 2016
- Clarke 2018
- Da Broi 2018
- Alam and Miyano 2019

## **II) Oocyte-somatic cell interaction in primordial and early growing follicles: an unconstrained dialogue**

From the primordial stage to early follicular growth, the granulosa cells are positioned adjacent to the oocyte without being separated by a defined layer of extracellular matrix (Fig. 3 B). This promiscuity between the two cell types is conducive

to intercellular dialogue, which is thought critical for oocyte survival and growth activation.

Among the dialogue between the oocyte and somatic cells identified in dormant or early growing follicles, paracrine factors secreted by granulosa cells and the oocyte activate signaling pathways in the corresponding cell type. Notably, the expression of Kit ligand by pregranulosa cells activates Kit signaling in the oocyte, which most likely contributes to activation of oocyte growth (Kidder and Vanderhyden 2010, El-Hayek and Clarke 2016, Clarke 2018). In addition, gap junctions are proposed to be located at the interface between the oocyte and granulosa cells in early growing follicles, and cytoplasmic protrusions of granulosa cells have been identified by electron microscopy in human primordial and primary follicles (Motta 1994, Makabe 2006). These protrusions increase in number as the follicle enters into growth and the *zona pellucida* starts to be deposited, and contact the oocyte membrane.

The interaction between the oocyte and somatic cells in dormant and early growing follicles is the initiation of a communication that will be maintained for the rest of the oocyte growth. However, the progressive formation of the *zona pellucida* from the primary stage spatially isolates the oocyte in the follicle. It represents a physical constraint that must be overcome to maintain oocyte-somatic cell dialogue and to further shape oocyte quality.

### **III) Oocyte-somatic cell interaction with a defined *zona pellucida*: an impeded but persistent dialogue**

#### **1) The *zona pellucida*, the extracellular layer surrounding the oocyte**

The *zona pellucida* is the extracellular matrix that surrounds the oocyte and embryo from early follicular growth to the end of preimplantation development. This coat is similar to the vitelline envelope found in non-mammalian organisms, such as fish and amphibians. The *zona pellucida* plays a role in follicular growth (Rankin 2001), fertilization, and embryo protection during preimplantation development, making it a critical element for fertility (Liu 1996, Rankin 1996, Rankin 1999, Ranking 2001).

In most mammals, the *zona pellucida* is composed of four Zona pellucida glycoproteins (ZP1-4), with the exception of the mouse, which does not express ZP4.

These proteins are secreted by both the oocyte and the granulosa cells during follicular growth (with the further exception of the mouse and other rodents in which only the oocyte expresses matrix glycoproteins).

In the mouse, the *zona pellucida* is constituted by ZP1 interconnected fibrils composed of ZP2 and ZP3 heterodimers (Fig. 3 A). During early follicular growth, the fibrils are first deposited in patches between the oocyte and the granulosa cells, and gradually join to form a defined matrix layer that completely surrounds the oocyte (Fig. 3 B). As growth proceeds, the *zona pellucida* thickens and pushes the granulosa cell bodies away from the oocyte. Nevertheless, direct communication between the two cell types, essential for the developmental potential of the oocyte, is maintained by numerous somatic protrusions that cross the extracellular matrix.

- Wassarman and Litscher 2018
- Litscher and Wassarman 2020
- Moros-Nicolás 2021

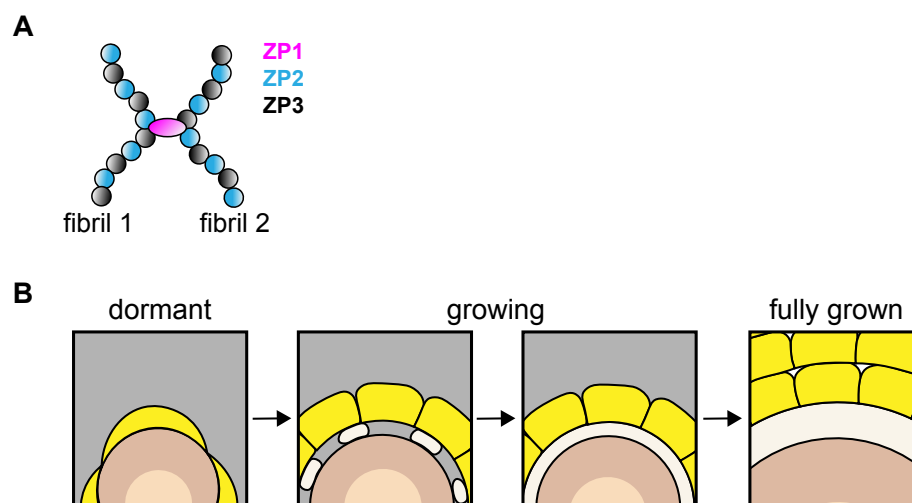


**Figure 3: The *zona pellucida* in the mouse ovarian follicle. A)** Schematic of two fibrils of ZP2-ZP3 dimers cross-linked by ZP1. **B)** Schematic of *zona pellucida* formation and thickening during follicular growth. Images show dormant (left), growing (middle), and fully-grown (right) follicles.

## 2) Transzonal projection, a mean to maintain intercellular contact

### 2.1- Overview

To maintain close contact with the oocyte as the *zona pellucida* is gradually deposited between the two cell types, granulosa cells elaborate cytoplasmic protrusions that cross the matrix and contact the oocyte membrane (Albertini and Rider 1994, Motta 1994, Makabe 2006, Baena and Terasaki 2019). These protrusions are called transzonal projections (TZPs) owing to their localization in the extracellular matrix.

TZPs are well conserved in mammals and have been notably identified in horse, pig, monkey, goat, guinea pig, rat (Albertini and Rider 1994), cow (Macaulay 2014, Macaulay 2016, Del Collado 2017), mouse (Simon 1997, Carabatsos 1998, Combelles 2004, Mora 2012, McGinnis and Kinsey 2015, Lowther 2017, El-Hayek 2018, Baena and Terasaki 2019, Abbassi 2021, Zhang 2021) and human (Motta 1994, Makabe 2006).

Due to the presence of adherens junctions at their tips (Mora 2012, Baena and Terasaki 2019, Abbassi 2021), it is proposed that TZPs play a role in cell-cell adhesion in the follicle. Importantly, they mediate intercellular signaling and exchange of nutrients and macromolecules between somatic cells and the oocyte. Hence, cellular and molecular properties of TZPs make them a pivotal element in oocyte-somatic cell dialogue.

- Albertini 2001
- Clarke 2018

### 2.2- TZP structure and dynamics

#### ➤ *A filopodia-like protrusion*

In addition to their snake-like appearance, TZPs share structural features with filopodia (Gallop 2020) and other cytoplasmic protrusions that enable intercellular contact, such as tunneling nanotubes (TNTs) (Yamashita 2018, Zurzolo 2021). The

main common feature of these protrusions is that they have an actin-rich backbone (Fig. 4 A, B). Some TZPs also contain tubulin (Albertini and Rider 1994, Combelles 2004, El-Hayek 2018), although they represent a minority in the overall TZP population. Knowledge about the morphology and structure of TZPs has mainly been obtained by electron microscopy (Anderson and Albertini 1976, Albertini and Rider 1994, Motta 1994, Simon 1997, Makabe 2006, Mora 2012, Macaulay 2014, Macaulay 2016, Baena and Terasaki 2019), and by fluorescence and confocal microscopy (Albertini and Rider 1994, Carabatsos 1998, Combelles 2004, Mora 2012, Macaulay 2014, Macaulay 2016, McGinnis and Kinsey 2015, Lowther 2017, Del Collado 2017, El-Hayek 2018, Abbassi 2021, Zhang 2021) using primarily phalloidin to label F-actin rich TZPs.

A study in mice demonstrated that in addition to being actin-rich, TZPs also contain other structural components present in filopodia (El-Hayek 2018, Fig. 4 A). These include DAAM1 and fascin, a formin and an actin-bundling protein respectively (Gallop 2020), known to be involved in filopodia formation and integrity. El-Hayek and colleagues showed that TZPs may also contain the molecular motor Myosin-X (MYO10) (Berg 2000, Kerber and Cheney 2011), which accumulates in foci at the granulosa cell membrane facing the oocyte. Of note, MYO10 has been shown to be involved in the formation of filopodia (Berg 2002, Bohil 2006, Heimsath 2017), and also that of TNTs (Gousset 2013). It is proposed that MYO10 initiates filopodia formation by converging F-actin into parallel bundles (Fig. 4 A) and elongates it by providing cargo proteins involved in filopodia growth (Kerber and Cheney 2011). In particular, it is suggested that the MYO10 dimer moves on actin bundles, with larger step sizes and higher velocity than on single actin filaments, a peculiarity that would be valuable in promoting filopodia formation (Ropars 2016). The role of MYO10 in TZPs remains to be determined. Nevertheless, the possible localization of MYO10 to TZPs and its role as a filopodia promoter make it a prime candidate to alter the integrity of TZPs to better understand the significance of these protrusions for oocyte development. This will be addressed in the Results section.

### ➤ *TZP dynamics during oogenesis*

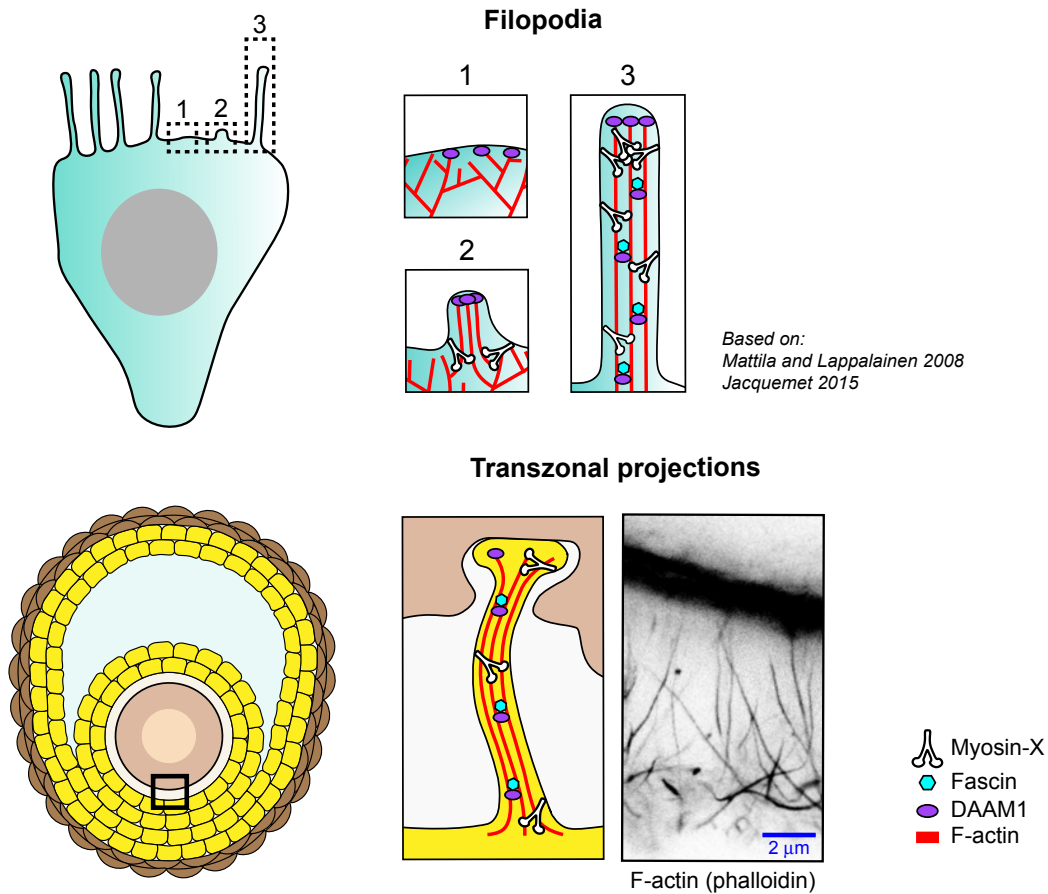
One aspect of TZPs that remains to be further deciphered is their dynamics, including their formation and retraction during oocyte development. This latter aspect is difficult to access as it is technically challenging to monitor TZPs in the follicle by live microscopy. Nevertheless, there is increasing evidence to suggest that, like filopodia, TZPs are dynamic structures.

Electron, fluorescence and confocal microscopy images have shown that TZPs not only vary in morphology, but also increase in number during oocyte growth, and undergo significant retraction during meiotic maturation to disconnect from the oocyte (Motta 1994, Makabe 2006, El-Hayek 2018, Macaulay 2014, Abbassi 2021). Mirroring these dynamics, the ability of granulosa cells to establish new protrusions during oocyte growth has been demonstrated by chimeric reaggregation of oocytes and granulosa cells isolated from respectively wild-type and transgenic mice expressing a membrane-targeted fluorescent protein. After chimeric cell reaggregation, newly formed TZPs from membrane-labeled granulosa cells were evidenced to make contact with wild-type oocytes, indicating the establishment of new intercellular contacts (El-Hayek 2018). In addition, a recent study using serial section electron microscopy showed that most TZPs in the mouse antral follicle do not contact the oocyte (Baena and Terasaki 2019). This may reflect the ability of TZPs to dynamically form and retract during follicular growth, intermittently establishing and interrupting communication with the oocyte.

Interestingly, the ability of granulosa cells to establish new protrusions during oocyte growth is regulated by external factors. Among these, Growth differentiation factor-9 (GDF-9), a factor secreted by the oocyte, and FSH, the gonadotropin involved in antral follicular growth, modulate the extent of somatic contact received by the oocyte by respectively enhancing (Carabatsos 1998, El-Hayek 2018, Zhang 2021) or reducing TZP density (Albertini 2001, Combelles 2004). In the case of GDF-9, its role as a modulator of TZP density is likely achieved by regulating the mRNA quantity of TZP structural components in granulosa cells, including that of MYO10 (El-Hayek 2018). Hence, the ability of granulosa cells to elaborate or retract TZPs in response to external factors, including those from the oocyte, allows for the timely adjustment of oocyte-somatic cell contacts for optimal follicular growth.

- Albertini 2001
- Clarke 2018

**A**



**B**

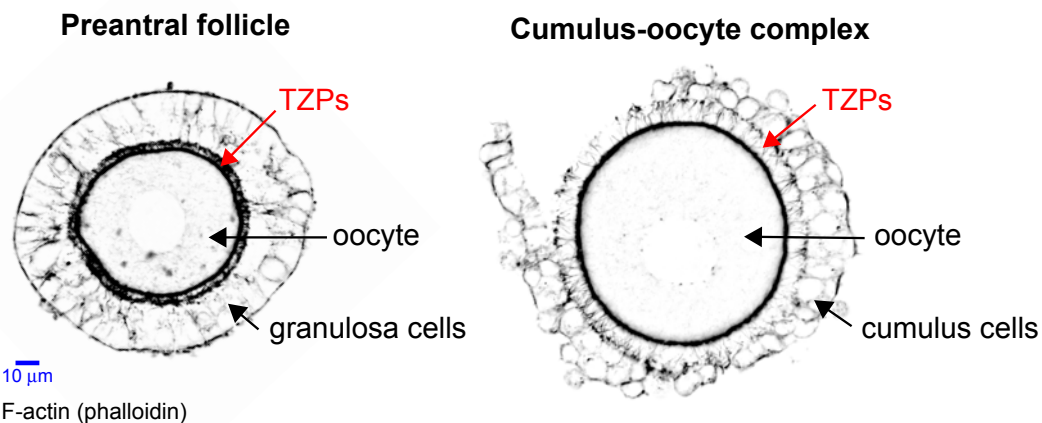


**Figure 4: Transzonal projections (TZPs) connect granulosa cells to the oocyte.**

**A)** Schematics of a forming filopodium in a cultured cell (top) and a TZP in a mammalian ovarian follicle (bottom). STED microscopy image of TZPs stained with

phalloidin to label F-actin in a fully-grown mouse oocyte (bottom right). Credits Julien Dumont, CIRB imaging facility. **B)** Spinning disk images of a mouse preantral follicle (left) and a mouse cumulus-oocyte complex (right) stained with phalloidin to label F-actin.

### *2.3- TZP-mediated interactions: meeting the needs of the oocyte*

#### *➤ Cell-cell adhesion*

By virtue of adherens junctions located at the interface between TZPs and the oocyte membrane (Mora 2012, Baena and Terasaki 2019, Abbassi 2021), it is proposed that TZPs maintain a stable connection between the oocyte and surrounding granulosa cells. At this interface, adherens junctions include N-cadherin on the TZP side, and E-cadherin on the oocyte side (Fig. 5 A).

Consistent with a role for TZPs in intercellular connection, TZP disruption in mice lacking Embryonic poly(A)-binding protein (EPAB) correlates with cumulus cells that are loosely associated with oocytes after isolation of COCs from follicles (Lowther and Mehlmann 2015, Lowther 2017). However, a direct role of TZPs in this process cannot be attributed, as EPAB is a post-transcriptional regulator that binds to poly(A) tails whose depletion may have caused other oocyte defects not necessarily attributable to the decrease in TZP density. In addition, loose contact between the oocyte and granulosa cells correlated with TZP retraction has been observed in growing follicles upon destabilization of cadherins following calcium depletion (Mora 2012). Again, caution should be exercised regarding the direct role of TZPs in this intercellular contact, as calcium depletion may also have altered the adherens junctions between granulosa cells. Nevertheless, it is highly suggested that TZPs provide granulosa cells with an anchor point to the oocyte. This anchoring may be necessary to maintain a robust intercellular complex, and therefore ensure efficient communication between the oocyte and the granulosa cells.

### ➤ *Gap junction coupling*

One of the most critical intercellular interaction enabled by TZPs is the exchange of nutrients and signaling molecules between granulosa cells and the oocyte. This exchange is mediated by gap junctions located at the interface between the TZP and the oocyte membrane (Anderson and Albertini 1976, Simon 1997, Fig. 5 A, B). Gap junctions are integral to oocyte development, as mice deficient in Connexin 37, the major connexin composing the oocyte-granulosa cell gap junction, yield oocytes that are smaller than controls and are incompetent to resume meiosis (Simon 1997).

TZP-oocyte gap junctions participate in a variety of biological processes in the follicle. This includes metabolic cooperativity between the oocyte and granulosa cells that allows somatic cells to fulfill the energy needs of the oocyte. In essence, the oocyte is not self-sufficient in several respects; it cannot use glucose as an energy source for meiotic maturation (Biggers 1967, Donahue and Stern 1968) and has a limited uptake of amino acids (Haghighat and Van Winkle 1990, Eppig 2005). To remedy this, the oocyte relies on granulosa cells from which it draws metabolites at the appropriate time during development (Biggers 1967, Donahue and Stern 1968, Haghighat and Van Winkle 1990, Eppig 2005). Gap junctions mediate this metabolite sharing, most likely by transferring amino acids (Haghighat and Van Winkle 1990) and energy substrates, such as pyruvate, from the granulosa cells to the oocyte (Fig. 5 B).

In addition to providing somatic nutrients to the oocyte, TZPs regulate the level of cAMP in the oocyte through gap junctions. This regulation is instrumental in keeping the oocyte arrested in prophase I and preventing an untimely resumption of meiosis. In short, gap junction mediated-transfer of cyclic guanosine monophosphate (cGMP) from the granulosa cells to the oocyte maintains a high level of oocyte cAMP, which prevents MPF activation and meiosis resumption (Norris 2009, Fig. 5 B). Also through the possible regulation of oocyte cAMP level, junctional coupling between the oocyte and granulosa cells is required for the gradual chromatin compaction and transcriptional silencing of the oocyte, which is associated with the meiotic and developmental competence of the oocyte (Luciano 2011).

- Kidder and Vanderhyden 2010
- El-Hayek and Clarke 2016
- Clarke 2018

- Da Broi 2018
- Alam and Miyano 2019

➤ *Exchange of extracellular vesicles*

In addition to metabolically coupling granulosa cells and the oocyte, it has been proposed in cattle that TZPs also mediate the exchange of extracellular vesicles between the two cell types (Macaulay 2014). This synaptic-type of communication, as suggested by the authors, would allow the transfer of macromolecules, and possibly organelles, from one type of cell to the other, which cannot be achieved by gap junctions. Indeed, gap junctions permit the transfer of molecules smaller than 1 kDa, which excludes large macromolecules. Hence, our understanding of the diversity of signals exchanged between the two cell types would be taken to a higher molecular scale. In particular, it has been shown that transcripts, such as mRNAs, transit along the TZP and are transferred to the oocyte, where they are likely translated by the oocyte machinery (Macaulay 2014, Macaulay 2016). These observations lead to the attractive concept that somatic cells may participate in the oocyte transcriptome on which the embryo may rely for development. At present, whether somatic transcripts are transferred through extracellular vesicles is a conjuncture that remains to be substantiated.

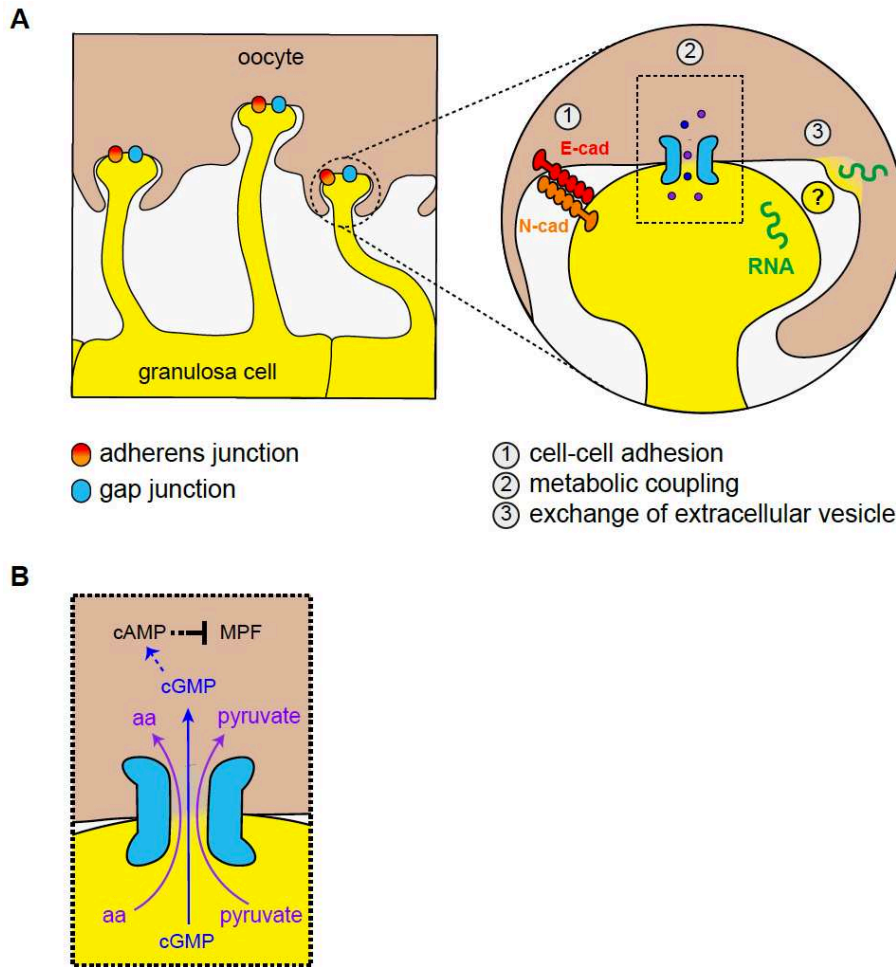


**Figure 5: TZP-mediated interactions in the ovarian follicle. A)** Schematics of TZPs making adherens and gap junctions with the oocyte. E-cad stands for E-cadherin and N-cad for N-cadherin. **B)** Magnification of the rectangle in A) representing a gap junction at the oocyte-TZP interface. MPF stands for maturation promoting factor, cAMP for cyclic adenosine monophosphate, cGMP for cyclic guanosine monophosphate, and aa for amino acid.

#### 2.4- Opening to broader perspectives

##### ➤ Disease impact on TZP-mediated communication

The study of TZP-mediated interactions in pathological contexts, such as diabetes, could be crucial to the ethology of disease-related fertility disorders. Of note, maternal diabetes is associated with impaired oocyte maturation, defects in embryonic

development, and poorer reproductive outcome (Wang and Moley 2010). In a type I diabetic mouse model (Ratchford 2008), gap junction communication between cumulus cells and the oocyte is reduced. Likely contributing to the decrease in cell coupling, the expression of Connexin 37, the predominant connexin composing the gap junction between the oocyte and somatic cells, is reduced in the oocyte of diabetic mice compared to non-diabetic mice. Alteration of the TZP-oocyte gap junction in the pathological context of diabetes could lead to defects in oocyte development, which could partly explain the link between this disease and impaired female fertility.

➤ *Age impact on TZPs*

The ability of granulosa cells to elaborate or maintain TZPs has been shown to decrease with maternal age in mice (El-Hayek 2018). When comparing the number of TZPs between two mice of different ages, this number was lower in the older mouse. In addition, El-Hayek and colleagues identified in granulosa cells of aged mice a decrease in the RNA quantity of some structural components of TZPs, including MYO10, compared to younger mice. This decrease could account for the difficulty that aged granulosa cells have in assembling or maintaining contacts with the oocyte. It is worth noting that maternal age correlates negatively with oocyte quality, and by extension, with female fertility. Since TZPs may participate in shaping oocyte quality, the latest findings in mice provide new perspectives into the role that TZP density may play in age-related decline in fertility.

➤ *Exclusively somatic? Protrusions of oocyte origin*

A most recent study in mice attractively documented that microvilli elaborated by the oocyte traverse the *zona pellucida* in growing follicles, as do the somatic TZPs (Zhang 2021). These oocyte protrusions, called “mushroom-like” microvilli by the authors owing to their bubble-like end, form a less dense ensemble than TZPs. Nonetheless, they contribute to follicular growth and female fertility. Interestingly, the loss of these microvilli, due to the deletion in the oocyte of a gene involved in microvilli formation, results in delayed oocyte and follicle growth and leads to female subfertility. To explain these phenotypes, the authors propose that oocyte microvilli mediate the

release of factors, such as GDF-9, in the vicinity of granulosa cells, thereby coordinating granulosa cell proliferation and function.

Although oocyte protrusions do not appear to contact granulosa cells, their location in the *zona pellucida* and their probable involvement in oocyte-somatic cell dialogue make them resemble transzonal projections. As the authors point out, these local elongations of the oocyte illustrate the ability of the oocyte to respond to the constraint of the *zona pellucida* in order to enhance the dialogue with the granulosa cells.

In light of the three TZP-mediated interactions presented above, the TZP structure serves several functions within the follicle, from a putative role in cell-cell adhesion to mediating the oocyte-somatic cell dialogue. This protrusion appears to be a crucial element in the manufacture of an oocyte capable of producing a good quality embryo.

#### **IV) Oocyte-neighboring cell interaction in non-mammals**

We have just seen that most mammals set up cellular protrusions within the ovarian follicle, mainly somatic, to establish the dialogue between the oocyte and the surrounding somatic cells. What about the strategy used in non-mammalian organisms to enable oocyte development? This final section focuses on two non-mammalian models that rely on intercellular communication for oocyte development, namely *Drosophila* and *C.elegans*.

##### **1) The case of the *Drosophila* oocyte: multiple interactions with different cell types**

A particular feature of *Drosophila* oogenesis is that the oocyte develops adjacent to two types of cells: nurse cells and follicle cells (Fig. 6 A). The nurse cells are germline cells that form a cyst with the oocyte following cell divisions without complete cytokinesis. The oocyte is located adjacent to them on its anterior side. The follicle cells, like the granulosa cells, are somatic and border the remaining oocyte surface. Intercellular interactions between the oocyte and neighboring cells play not

only a role in oocyte polarization, defining the embryonic axes, but also promote oocyte growth. Like its mammalian counterpart during meiotic maturation, the *Drosophila* oocyte is primarily transcriptionally inactive during its growth and therefore depends notably on neighboring cells to develop, which supply macromolecules.

The nurse cells, as their name indicates, have a nutritive role for the oocyte. They provide it with organelles and transcripts through ring canals, which are cytoplasmic bridges linking the germ cells in the cyst. As proposed by Macaulay and colleagues, this exogenous contribution to the oocyte transcriptome could also be found in the bovine oocyte, possibly mediated by extracellular vesicles (Macaulay 2014, Macaulay 2016).

An interesting type of interaction between follicle cells and the oocyte is that which occurs during vitellogenesis. The follicle cells provide yolk proteins to the oocyte by exocytosis, which is a source of nutrients for embryogenesis. It is noteworthy that the follicle cells and the oocyte establish microvilli at their extracellular interface. However, it remains to be established whether the microvilli of both cell types allow for intercellular exchange of yolk proteins by contact. Nevertheless, the authors of the review cited below suggest that these protrusions may indeed be the site of communication by direct contact or, as suggested by Zhang and colleagues in mouse oocytes (Zhang 2021), deliver local factors to overcome the distance between the two cell types. As proposed by Antel and Inaba, the microvilli established by follicle cells and the *Drosophila* oocyte are reminiscent of TZPs. Indeed, at this stage of *Drosophila* oogenesis, the vitelline bodies, which are granules that will later assemble to form the vitelline membrane, are localized between the two cell types and may represent an obstacle to intercellular exchange, as does the *zona pellucida*. Like TZPs, the microvilli of the follicle cell and oocyte could counteract this obstruction and reduce the dialogue distance between the two cell types.

Therefore, like mammalian oocytes, the *Drosophila* oocyte depends on cellular interactions with neighboring cells, in this case from two different cell origins, in order to develop optimally.

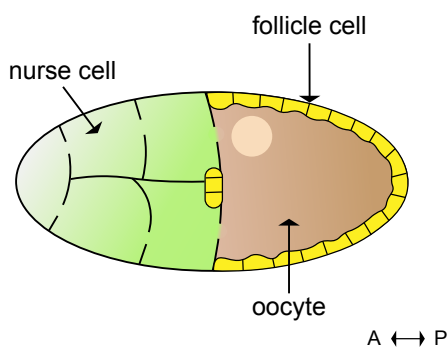
- Antel and Inaba 2020

## 2) The case of the *C. elegans* oocyte: use of somatic cells for timely resumption of meiosis

The *C. elegans* oocyte develops adjacent to somatic cells called sheath cells (Fig. 6 B). Like cumulus cells in the mammalian follicle, sheath cells are involved in regulating the resumption of meiosis of the prophase I arrested oocyte. Sheath cells allow for the timely resumption of meiosis, which is triggered by the presence of sperm that secretes the major sperm protein, a protein that acts similarly to LH in mammals. Interestingly, as in mammals, regulation of meiosis resumption is based on G-protein and protein kinase A signaling, which in the case of *C. elegans* occurs in the sheath cells but would not be required in the oocyte. Importantly, inhibition of premature meiotic maturation is mediated by gap junctions at the interface between sheath cells and the oocyte. Therefore, as pointed out by the authors of the reviews cited below, the control of meiosis resumption is a rather conserved mechanism, which involves somatic-oocyte dialogue by direct contacts.

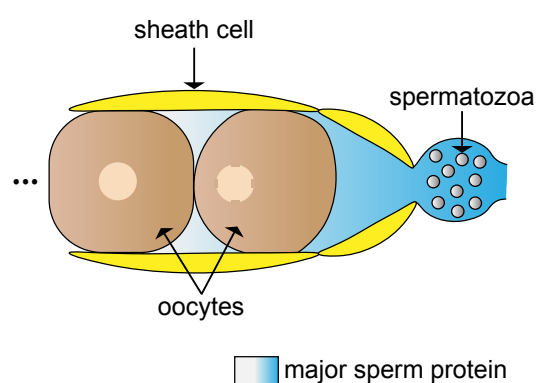
- Kim 2013
- Huelgas-Morales and Greenstein 2018

**A**  
***Drosophila* oocyte and neighboring cells**



Adapted from Antel and Inaba 2020

**B**  
***C. elegans* oocytes and sheath cells**



Adapted from:  
Kim 2013  
Huelgas-Morales and Greenstein 2018

**Figure 6: *Drosophila* and *C. elegans* oocytes and their neighboring cells. A)** Schematic of a *Drosophila* egg chamber. A and P stands for anterior and posterior, respectively. **B)** Schematic of the proximal part of a *C. elegans* hermaphrodite gonad.

## Concluding remarks

In mammals, as in non-mammalian organisms, neighboring cells help the oocyte to fulfill its biological purpose of ensuring an offspring for its carrier. In the mammalian follicle, the granulosa cells and the oocyte have a common goal, namely that the oocyte stores the nutrients necessary for embryogenesis in a coordinated manner during its development. Under the control of the oocyte, the granulosa cells integrate and address the changing needs of the oocyte despite the intrusion of the *zona pellucida* between the two cell types. In spite of the latter, transzonal projections not only provide metabolic coupling between the oocyte and somatic cells, but also ensure that the oocyte resumes meiosis timely with optimal developmental competence.

Like the oocyte, granulosa cells are subject to aging and project or maintain their cellular protrusions less efficiently as the female advances in age. As there is increasing evidence that TZPs are critical to oocyte development, a decrease in their density may compromise oocyte quality. Therefore, oocyte defects caused exogenously by a decrease in TZP numbers would be in addition to those inherent to the oocyte also triggered by female aging. Importantly, the time of conception of the childbearing generation has changed from previous decades and tends to be postponed until later in life, especially when career goals have been met. This implies that more women are facing age-related fertility issues when they intend to conceive. For this reason, but also for basic research, there is a growing need to better understand the involvement of TZPs in oocyte development.

By being assisted by granulosa cells, the oocyte has stored a significant amount of nutrients during its growth. Its next challenge is to conserve them for embryogenesis during the last step of its development, that is meiotic maturation. During this period, the oocyte timely implements mechanisms to generate asymmetric divisions in size, a strategy to retain most of the maternal stores in the oocyte.

# **Chapter III: Preserving a nutrient-rich cytoplasm through spindle off- centering**

*In this final introductory chapter, I will briefly discuss the strategy employed by mouse oocytes to off-center their division spindle prior to anaphase of meiosis I. I will also succinctly review the role of Myosin-X in spindle positioning in other models, and discuss why we considered it as an interesting candidate to mediate spindle off-centering forces in the mouse oocyte.*

*This chapter may seem out of place after discussing oocyte growth and oocyte-somatic cell interaction, and I apologize if the transition is a bit abrupt. This reflects the chance I had during my thesis to work on two seemingly distinct topics. However, it could be said that oocyte growth and spindle off-centering have in common that they provide the embryo with optimal nutrient content for its development. I am glad that I was able to study both of these topics, and I would even say that it helped me to have a more integrated view of Science. In this regard, each of my two thesis projects has pulled the other up.*

With the assistance of the granulosa cells, the oocyte has increased in size and accumulated nutrient reserves during its growth that must be conserved to support early embryogenesis. Upon resuming meiosis, the oocyte faces a paradox. To become haploid, it must shed half of its DNA content, yet each meiotic division inevitably results in a loss of cytoplasm and, by extension, of nutrients required for embryo development. To solve this issue, the mammalian oocyte implements a spindle off-centering strategy that allows the oocyte to perform two asymmetric divisions in size. In this regard, chromosomes are extruded with limited loss of cytoplasm in the polar bodies. In mammalian oocytes, spindle positioning involves molecular mechanisms that differ from those of most somatic cells. Importantly, if not properly coordinated, spindle off-centering in the mouse oocyte can trigger chromosome misalignment prior to anaphase and lead to aneuploidy, a defect associated with decreased pregnancy success and congenital diseases.

### **I) Spindle positioning in the absence of cortical cues and centrioles**

In mouse oocytes, the spindle of meiosis I is first assembled in the cell center at the former nucleus location and migrates to the cortex once bipolarized in a process that lasts about 2.5 hours (Verlhac 2000). Unlike many somatic cells, the oocyte lacks cortical cues as it reengages in cell division. Consequently, spindle positioning is not predefined by the cortex, but rather depends on the subcentral site of the oocyte where the spindle has assembled, and on the orientation of the spindle pole axis (Verlhac 2000). Indeed, the spindle is formed in the central region of the oocyte, but not at its perfect geometrical center, with one pole closer to the cortex than the other (referred to as leading pole). The axis of migration is defined by the two spindle poles and the spindle travels along this axis towards the closest cortical site.

In addition, many mammalian oocytes, including those of the mouse (Szollosi 1972), undergo meiotic maturation devoid of centrioles. As a result, oocytes do not nucleate astral microtubules, which play a critical role in mitotic spindle orientation and positioning in most somatic cells (di Pietro 2016, Théry 2005, Toyoshima and Nishida 2007, Woolner and Papalopulu 2012, Fig. 7 A). In essence, astral microtubules, nucleated by centrosomes containing centrioles forming the spindle poles, anchor the mitotic spindle to the cell cortex and exert forces that allow adequate spindle

positioning. Notably, in many somatic cells, astral microtubules transmit pulling forces to the centrosomes. This microtubule-mediated traction derives from force-generating proteins localized at particular sites in the cortex (di Pietro 2016). In mammalian oocytes, F-actin substitutes for astral microtubules to anchor and position the spindle to the cell cortex (Fig. 7 B). Treatment of mouse oocytes with F-actin-destabilizing drugs prevents spindle migration, whereas treatment with microtubule-destabilizing drugs is not detrimental to chromosome off-centering (Longo and Chen 1985, Van Blerkom and Bell 1986, Verlhac 2000, Azoury 2008). In mouse oocytes, the F-actin that drives spindle migration derives from two distinct networks nucleated in a timely manner during meiotic maturation. These two networks, although elaborated by distinct nucleators and different in their architecture, work synergistically to transmit pulling forces to the spindle and therefore underlie the first asymmetric division of the oocyte.

## **II) Two F-actin networks cooperate to off-center the meiosis I spindle**

### **1) A straight cytoplasmic network surrounds the spindle and connects it to the cortex**

Of the two F-actin networks involved in spindle off-centering in mouse oocytes, one is nucleated in the cytoplasm by the straight F-actin nucleators Formin-2 (Leader 2002, Dumont 2007a, Azoury 2008, Schuh and Ellenberg 2008) and Spire1, 2 (Pfender 2011). This network connects the spindle to the cortex. In this regard, cytoplasmic F-actin could be considered as the functional analogue of astral microtubules. Importantly, a subsection of this network encapsulates and infiltrates the spindle (Azoury 2008, Schuh and Ellenberg 2008), forming a structure referred to as the F-actin cage (Fig. 7 B). The F-actin cage is the site of force transmission from the F-actin to the spindle microtubules, and is therefore the scene of interplay between the two cytoskeleton elements.

The pulling forces that drive spindle migration are generated by the Myosin-II molecular motor located at the poles of the spindle/F-actin cage (Schuh and Ellenberg 2008, Bennabi 2020, Fig. 7 B). The initiation of spindle migration is enabled by the slightly off-center assembly of the spindle in the oocyte (Verlhac 2000) and its initial pushing (Li 2008, Yi 2013, Duan 2020), which likely results in one pole being closer

and thus better connected to the cortex than the other (Schuh and Ellenberg 2008). It is proposed that this imbalance in spindle anchoring leads to Myosin-II located at the leading spindle pole to have a greater amount of F-actin substrate than Myosin-II at the opposite pole, thereby triggering spindle migration. Once initiated, spindle migration is not achieved without the intervention of a second F-actin network that reinforces the imbalance of pulling forces at the spindle poles.

## 2) A branched subcortical network provides cortical softness to enhance spindle migration

The second F-actin network involved in spindle migration in the mouse oocyte is progressively nucleated by the Arp2/3 complex after NEBD (detectable 3 hours later) and forms a subcortical thickening (Chaigne 2013, Chaigne 2015, Fig. 7 B). This network triggers a decrease in cell cortical tension by dislodging Myosin-II from the cortex. In essence, the cortical tension of the oocyte decreases during meiotic maturation (Larson 2010, Chaigne 2013) and accommodates spindle migration when encompassed within a defined range of forces. Indeed, cortical tension outside this range impedes asymmetric oocyte division (Chaigne 2013, Chaigne 2015). It is proposed that lowered cortical tension and a resulting softer cortex may facilitate the penetration of cytoplasmic F-actin into the cortex for increased spindle anchorage. This may also promote the extraction of filaments from the cortex to provide more substrates for Myosin-II located at the leading spindle pole (Chaigne 2015). Hence, subcortical F-actin and the resulting decrease in cortical tension of the oocyte may increase pulling forces in an anisotropic way at the leading spindle pole to enhance spindle migration (Chaigne 2013, Chaigne 2015).

Interestingly, an excessive drop in cortical tension mediated by subcortical F-actin increases the risk of chromosome misalignment before anaphase I (Bennabi 2020). In this regard, spindle off-centering places the oocyte in an already paradoxical situation during maturation. Indeed, the mechanisms that allow the oocyte to reconcile the extrusion of its genetic material with the limitation of cytoplasmic loss is potentially generative of aneuploidy if implemented incorrectly.

Summarily, spindle positioning in the mouse oocyte requires an interplay between cytoskeletal elements at two levels: between cytoplasmic and subcortical F-actin, and between cytoplasmic F-actin and spindle microtubules. The latter interplay deserves further study, as it remains to be determined how the F-actin cage transmits pulling forces to the spindle. A candidate protein for this process is Myosin-X, a molecular motor with unconventional binding properties.

### **III) Myosin-X, a possible mediator of spindle off-centering forces?**

We have briefly introduced MYO10 in the previous chapter by mentioning its involvement in the formation of filopodia and possibly transzonal projections, making it a potential contributor to the establishment or maintenance of oocyte-somatic cell contacts. Interestingly, MYO10 has also been identified as a coordinator of spindle positioning in dividing cells.

MYO10 is an unconventional myosin with myosin tail homology 4 (MyTH4) and band 4.1/ezrin/radixin/moesin (FERM) domains (Berg 2000, Fig. 7 C). MYO10 binds to F-actin with its motor domain located at the protein head. Importantly, its tail-located MyTH4 domain allows it to bind directly to microtubules (Weber 2004, Hirano 2011). This latter feature yields the attractive concept that MYO10 may connect F-actin to microtubules, and thereby promote interplay between the two cytoskeletal elements.

MYO10 has been documented to be involved in spindle assembly and integrity maintenance in *Xenopus* oocytes (Weber 2004) and embryos (Woolner 2008). Importantly, it is instrumental in proper spindle anchoring, positioning and orientation in several mitotic cells (Toyoshima and Nishida 2007, Kwon 2015, Woolner 2008, Woolner and Papalopulu 2012, Liu 2012). Notably, in cultured human cells, MYO10 is necessary for spindle orientation parallel to the substrate plane (Toyoshima and Nishida 2007). In addition, MYO10 directs centrosomes towards “clouds” of subcortical F-actin and retraction fibers (Kwon 2015, Fig. 7 A). In *Xenopus* embryo epithelial cells, MYO10 is engaged in correct spindle movement within the cell (Woolner 2008) and spindle positioning on the apical-basal axis (Woolner and Papalopulu 2012).

MYO10 ability to bind to F-actin and microtubules, and previous documentations of its role in spindle positioning in several models, make it an interesting candidate for mediating force transmission from cytoplasmic F-actin to spindle microtubules in the

mouse oocyte. For these reasons, the first project of this thesis was to test whether MYO10 plays a role in the first asymmetric division of the mouse oocyte, the results of which are presented in the first part of the Results section.

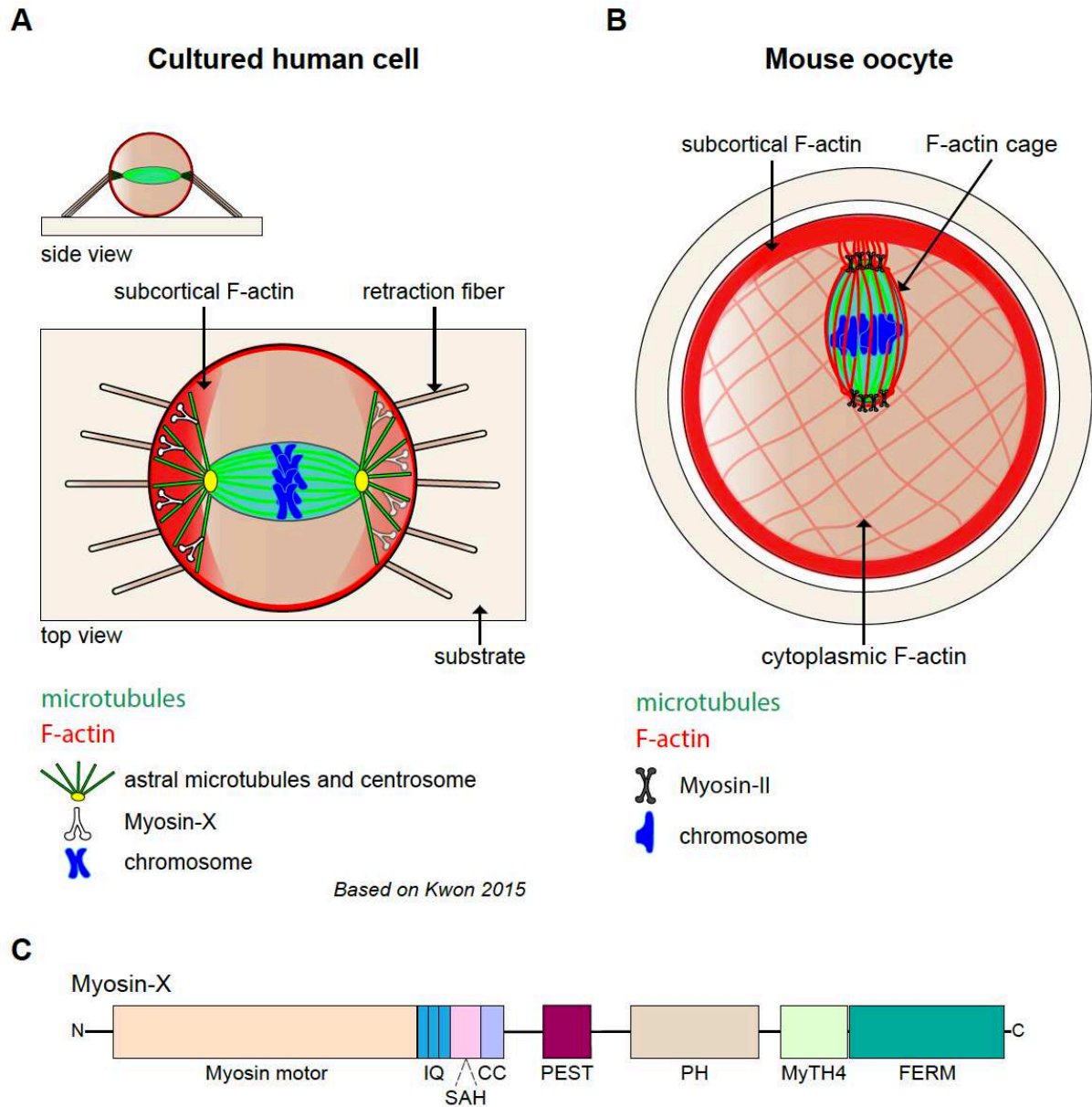


**Figure 7: Mechanisms of spindle positioning in metaphase cells. A)** Schematics of a cultured human cell, side view (upper image) and top view at the equatorial plane of the cell (lower image). **B)** Schematic of a mouse oocyte. **C)** Schematic of the Myosin-X protein (partially based on UniProt database for mouse). IQ stands for IQ motifs, SAH for single  $\alpha$ -helix, CC for coiled-coil, PH for pleckstrin homology domains, MyTH4 for myosin tail homology 4, and FERM for band 4.1/ezrin/radixin/moesin.

## Concluding remarks

After a quiescent phase of variable duration, followed by a period of expansion and reserve accumulation, the oocyte completes its development by reconciling the loss of diploidy with the retention of a nutrient-rich cytoplasm. Each step of *post-partum* oocyte development, namely oocyte growth and meiotic maturation, must be properly coordinated to ensure a high developmental potential of the oocyte. Interestingly, while granulosa cells play a critical role in coordinating oocyte growth, spindle positioning during meiosis I is inherent to the oocyte. Although spindle off-centering in mammalian oocytes is indirectly initiated by exogenous factors triggering meiosis resumption, it is not predetermined by external determinants, as pointed out by the authors of the articles cited above. In support of this last argument, spindle positioning is studied in the lab in *in vitro* maturing oocytes devoid of granulosa cells.

It is therefore interesting to note the ability of the oocyte to undergo spindle off-centering/asymmetric division without extracellular contribution. However, it should be considered that this may only be an apparent autonomy. Indeed, although asymmetric oocyte division can be achieved in the absence of granulosa cells during *in vitro* maturation, somatic cells may contribute to the completion of this process indirectly by interacting with the oocyte, upstream, during oocyte growth. The latter is the subject of the main article of this thesis and will be discussed in the second part of the Results section. In this respect, the role of granulosa cells during oogenesis could be simplistically summarized as accompanying and coordinating the acquisition of developmental autonomy of the oocyte, allowing it to dispose of the molecular content necessary to efficiently sustain meiotic maturation and embryogenesis.

# RESULTS

# **Article #1:**

**Myosin-X is dispensable for  
spindle morphogenesis and positioning  
in the mouse oocyte**

*Attached is the manuscript of the first study of this thesis published in Development in April 2021. Referring to several dividing cell models in which Myosin-X plays a major role in spindle positioning, we investigated the possible involvement of this molecular motor in spindle morphogenesis and off-centering in the mouse oocyte. We generated a mouse strain conditionally depleted of MYO10 in oocytes and assessed meiosis I spindle assembly and positioning by live spinning disk imaging throughout meiotic maturation. We first demonstrated that MYO10 is not enriched at the meiosis I spindle. Importantly, targeted deletion of the Myo10 gene does not impair spindle assembly and off-centering, or female fertility. These results support a non-essential role for MYO10 in the first asymmetric division of the oocyte. Although we close the door on a function for MYO10 in mediating the transmission of F-actin forces to spindle microtubules, this study may be useful to further investigate other candidates for linking F-actin to the spindle in the mouse oocyte*

## RESEARCH ARTICLE

# Myosin-X is dispensable for spindle morphogenesis and positioning in the mouse oocyte

Flora Crozet, Christelle Da Silva, Marie-Hélène Verlhac\* and Marie-Emilie Terret\*

## ABSTRACT

Off-center spindle positioning in mammalian oocytes enables asymmetric divisions in size, which are important for subsequent embryogenesis. The migration of the meiosis I spindle from the oocyte center to its cortex is mediated by F-actin. Specifically, an F-actin cage surrounds the microtubule spindle and applies forces to it. To better understand how F-actin transmits forces to the spindle, we studied a potential direct link between F-actin and microtubules. For this, we tested the implication of myosin-X, a known F-actin and microtubule binder involved in spindle morphogenesis and/or positioning in somatic cells, amphibian oocytes and embryos. Using a mouse strain conditionally invalidated for myosin-X in oocytes and by live-cell imaging, we show that myosin-X is not localized on the spindle, and is dispensable for spindle and F-actin assembly. It is not required for force transmission as spindle migration and chromosome alignment occur normally. More broadly, myosin-X is dispensable for oocyte developmental potential and female fertility. We therefore exclude a role for myosin-X in transmitting F-actin-mediated forces to the spindle, opening new perspectives regarding this mechanism in mouse oocytes, which differ from most mitotic cells.

**KEY WORDS:** Myosin-X, Mouse oocyte, Spindle positioning, F-actin

## INTRODUCTION

Spindle positioning is key for the development of eukaryotic organisms as it defines the geometry of cell division. It can trigger either redundancy or divergence of fate between daughter cells, following a symmetric versus an asymmetric division (for reviews, see Morin and Bellaïche, 2011; Di Pietro et al., 2016). Owing to their two successive asymmetric divisions in size (meiosis I and II), mammalian oocytes are relevant models for studying spindle off-centering mechanisms. In meiosis I, it is a process that has not yet been fully deciphered, consisting of the migration of the spindle from the cell center to the cortex (Verlhac et al., 2000). The asymmetric divisions of the oocyte provide the prospective mother with one big egg and two tiny polar bodies, a discrepancy in size that is important for keeping the largest proportion of maternal stores needed for embryogenesis in the fertilizable egg (Kyogoku and Kitajima, 2017).

CIRB, Collège de France, UMR7241/U1050, 75005 Paris, France.

\*Authors for correspondence (marie-helene.verlhac@college-de-france.fr; marie-emilie.terret@college-de-france.fr)

 M.-H.V., 0000-0001-8377-9010; M.-E.T., 0000-0001-5843-925X

This is an Open Access article distributed under the terms of the Creative Commons Attribution License (<https://creativecommons.org/licenses/by/4.0>), which permits unrestricted use, distribution and reproduction in any medium provided that the original work is properly attributed.

Handling Editor: Haruhiko Koseki

Received 14 December 2020; Accepted 2 March 2021

As with most mitotic cells (Morin and Bellaïche, 2011; Di Pietro et al., 2016), spindle positioning in mammalian oocytes relies on cortical inputs and forces applied to the spindle, and hence depends on the cell mechanical properties. Pioneering studies in murine oocytes have highlighted the importance of tight regulation of cortical mechanics to properly transmit forces to the spindle, enabling an asymmetric division in size and a good oocyte quality (Chaigne et al., 2013, 2015; Bennabi et al., 2020). Cortical mechanics is a very good predictor of oocyte developmental potential in humans and mice (Yanez et al., 2016). Strikingly, a weakened transmission of forces in extra-soft engineered oocytes prevents spindle off-centering (Chaigne et al., 2015) and induces chromosome misalignment, causing aneuploidy (Bennabi et al., 2020). The forces applied to mouse oocyte spindles are mediated by filamentous actin (F-actin) bypassing the absence of canonical centrosomes and the consequent lack of astral microtubules (Szollosi et al., 1972; Longo and Chen, 1985), which are the main effectors of spindle positioning in mitotic cells (Théry et al., 2005; Toyoshima and Nishida, 2007; Fink et al., 2011; Morin and Bellaïche, 2011; Woolner and Papalopulu, 2012; Kwon et al., 2015; Di Pietro et al., 2016). A dynamic cytoplasmic F-actin network, including an actin-cage surrounding the spindle (Azoury et al., 2008; Schuh and Ellenberg, 2008; Chaigne et al., 2013, 2015; Mogessie and Schuh, 2017), is polymerized by the straight actin nucleators formin 2 (Leader et al., 2002; Dumont et al., 2007a; Azoury et al., 2008; Schuh and Ellenberg, 2008), spire 1 and spire 2 (Pfender et al., 2011). It anchors the spindle to the cortex and off-centers it through myosin II-generated pulling forces at spindle poles (Schuh and Ellenberg, 2008; Chaigne et al., 2013; Bennabi et al., 2020). A subcortical Arp2/3-dependent F-actin network (Chaigne et al., 2013, 2015), progressively nucleated after nuclear envelope breakdown (NEBD), remodels cortical properties by chasing myosin II from the cortex, resulting in lower cortical tension (Larson et al., 2010; Chaigne et al., 2013, 2015). Working in synergy with the cytoplasmic F-actin, the subcortical F-actin network increases an imbalance of pulling forces at the spindle poles (Chaigne et al., 2015). This imbalance first originates from the slightly off-center assembly of the spindle before the onset of migration (Verlhac et al., 2000) and its initial pushing (Li et al., 2008; Yi et al., 2013; Duan et al., 2020), resulting in one pole closer to the cortex (the leading pole). Following cortex softening, this imbalance of forces is further amplified by the cytoplasmic F-actin-mediated stretching of the subcortical F-actin towards the leading spindle pole, likely providing spindle-localized myosin II with greater substrate and accelerating spindle migration (Chaigne et al., 2015).

Although the cytoplasmic F-actin involvement in coupling cortical mechanics to spindle off-centering is well established in mouse oocytes, how it directly transmits forces to the spindle remains elusive. Intriguingly, the actin cage perfectly surrounds the microtubule spindle and numerous actin filaments penetrate it

(Azoury et al., 2008; Schuh and Ellenberg, 2008; Mogessie and Schuh, 2017), suggesting a possible inter-cytoskeleton crosstalk at the spindle. Moreover, artificial F-actin enrichment at the meiotic spindles in murine eggs increases the bundling of microtubules and affects their dynamics (Mogessie and Schuh, 2017), supporting the ability of F-actin to transmit mechanical constraints to the microtubules and suggesting a spindle-localized F-actin/microtubule crosslinker in mouse oocytes. In this study, we addressed the role of a known F-actin and microtubule binder, the unconventional myosin-X (MYO10), in this process. MYO10 is a MyTH4-FERM myosin (myosin tail homology 4 - band 4.1, ezrin, radixin, moesin) (Berg et al., 2000; Hirano et al., 2011) capable of binding both to F-actin via its head motor domain (Homma et al., 2001) and to microtubules via its MyTH4-FERM domain (Weber et al., 2004; Hirano et al., 2011). Numerous studies have highlighted MYO10 involvement in spindle dynamics, orientation and positioning in mitotic cells (Toyoshima and Nishida, 2007; Woolner et al., 2008; Liu et al., 2012; Woolner and Papalopulu, 2012; Kwon et al., 2015; Sandquist et al., 2016, 2018). It has also been involved in nuclear anchoring and spindle rotation in *Xenopus* oocytes (Weber et al., 2004), as well as in spindle morphogenesis and integrity in *Xenopus* oocytes and embryos (Weber et al., 2004; Woolner et al., 2008; Sandquist et al., 2016). We therefore investigated whether MYO10 directly links F-actin to spindle microtubules in mouse oocytes and thus participates in spindle off-centering. We took advantage of the *Cre-loxP* system to generate a mouse strain conditionally invalidated for MYO10 in oocytes and assessed spindle morphogenesis and positioning in oocytes lacking MYO10, as well as their subsequent developmental capacity. Our results show that MYO10 is present in mouse oocytes but not enriched at the spindle in meiosis I. Importantly, MYO10 is dispensable for actin organization, spindle morphogenesis and positioning in oocytes, and more generally not essential for female fertility.

## RESULTS

### MYO10 does not localize to the meiosis I spindles

If MYO10 crosslinks F-actin to microtubules in mouse oocytes, it might be enriched at the spindle. In several models, MYO10 was detected at both mitotic and meiotic spindles (Weber et al., 2004; Woolner et al., 2008; Woolner and Papalopulu, 2012; Sandquist et al., 2016, 2018; Briño-Enríquez et al., 2017; So et al., 2019), and more specifically often accumulated at spindle pole regions in the vicinity of cortical/spindle F-actin (Weber et al., 2004; Woolner et al., 2008). Contrary to what was previously described in mouse oocytes (Briño-Enríquez et al., 2017; So et al., 2019), we did not detect by immunofluorescence any endogenous MYO10 accumulation at the meiosis I spindles (Fig. 1A). We quantified MYO10 spindle enrichment by measuring the ratio of the spindle and cytoplasmic MYO10 fluorescence intensities. This ratio was close to 1 (Fig. 1B left,  $1.05 \pm 0.06$ ), showing that endogenous MYO10 is not enriched at the spindle. In addition, no specific labeling of MYO10 in the cytoplasm was observed, with a signal that was mostly diffuse. In previous articles (Briño-Enríquez et al., 2017; So et al., 2019), the authors used different antibodies and immunostaining protocols than ours, which could explain the different localizations observed between their studies and ours. However, these studies were not intended to address the role of myosin-X in oocytes, so the specificity of their staining was not tested on oocytes depleted for myosin-X (genetically or using siRNA) as we do here. Indeed, our MYO10 antibody was further validated in our mouse strain conditionally invalidated for MYO10

in oocytes (*Myo10*<sup>-/-</sup>, see Materials and Methods and Fig. 1E-H). We observed a decrease in the intensity of MYO10 labeling in both mid-grown *Myo10*<sup>-/-</sup> oocytes enclosed in an environment of otherwise wild-type granulosa cells and fully grown *Myo10*<sup>-/-</sup> oocytes compared with their respective controls (Fig. 1G). This intensity was fivefold lower in the cytoplasm of *Myo10*<sup>-/-</sup> oocytes than in controls at NEBD+6 h (Fig. 1G, lower images and quantification in H; control,  $0.75 \pm 0.13$ ; *Myo10*<sup>-/-</sup>,  $0.15 \pm 0.02$ ). Conversely, we detected MYO10 in the wild-type granulosa cells surrounding *Myo10*<sup>-/-</sup> oocytes at mid-growth, as in those surrounding control oocytes of the same stage (Fig. 1G, upper images). This further confirms the specificity of the MYO10 antibody and also shows the efficiency of our genetic approach that allowed the specific depletion of MYO10 in oocytes from the mid-growth stage of their development. In parallel, we microinjected exogenous MYO10 tagged with GFP (GFP-MYO10) into prophase I oocytes and monitored its localization throughout meiosis I. Similar to endogenous MYO10, GFP-MYO10 was not enriched at the meiosis I spindles (Fig. 1B, right, C and Movie 1; ratio of spindle and cytoplasmic GFP-MYO10 fluorescence intensities of  $0.99 \pm 0.05$ ) or at any other cytoplasmic location. Supporting the robustness of our MYO10 detection tools, we observed that both endogenous and exogenous MYO10 (Fig. 1D, left and right, respectively) accumulated in foci in the vicinity of the oocyte cortex, a pattern of localization consistent with previous studies in somatic cells (Berg et al., 2000; Liu et al., 2012; Kwon et al., 2015). To conclude, and in contrast to other models, MYO10 is present in mouse oocytes but is not enriched at the spindle.

### Spindle morphogenesis is normal in MYO10 depleted oocytes

MYO10 plays a role in spindle morphogenesis and integrity in various models. MYO10 disruption, using morpholino oligonucleotide-based approaches, dominant-negative constructs or neutralizing antibodies, alters spindle assembly in *Xenopus* oocytes (Weber et al., 2004), and triggers both spindle lengthening (Woolner et al., 2008; Woolner and Papalopulu, 2012) and pole fragmentation (Woolner et al., 2008; Sandquist et al., 2016) in *Xenopus* embryos. In somatic cells, however, spindle length (Toyoshima and Nishida, 2007; Liu et al., 2012) and pole integrity (Kwon et al., 2015) are normal when MYO10 is knocked down. In murine oocytes, spindle morphogenesis starts with the formation of a microtubule ball assembled around the chromosomes following NEBD that progressively bipolarizes (Schuh and Ellenberg, 2007; Dumont et al., 2007b; Kitajima et al., 2011; Bennabi et al., 2016). We followed spindle morphogenesis using live spinning disk microscopy during meiosis I in control and *Myo10*<sup>-/-</sup> oocytes incubated with SiR-tubulin to label the microtubules. Both the bipolarization timing of meiosis I spindles (Fig. 2A,B; control  $3.64 \pm 1.17$  h, *Myo10*<sup>-/-</sup>  $3.69 \pm 0.70$  h; Movie 2), their inter-polar length and width 30 min before polar body extrusion (Fig. 2C,D; control,  $31.02 \pm 3.82$   $\mu\text{m}$ ; *Myo10*<sup>-/-</sup>,  $29.54 \pm 2.49$   $\mu\text{m}$  for spindle length; control,  $15.59 \pm 0.56$   $\mu\text{m}$ ; *Myo10*<sup>-/-</sup>,  $15.41 \pm 0.51$   $\mu\text{m}$  for spindle width) were not significantly different between control and *Myo10*<sup>-/-</sup> oocytes. MYO10 therefore does not play a role in spindle morphogenesis and integrity in mouse oocytes.

### F-actin is properly organized in MYO10-depleted oocytes

Owing to the role of MYO10 in actin organization in *Xenopus* oocytes and somatic cells (Weber et al., 2004; Toyoshima and Nishida, 2007), we also assessed the integrity of the cytoplasmic F-actin in *Myo10*<sup>-/-</sup> oocytes by immunofluorescence in fixed cells

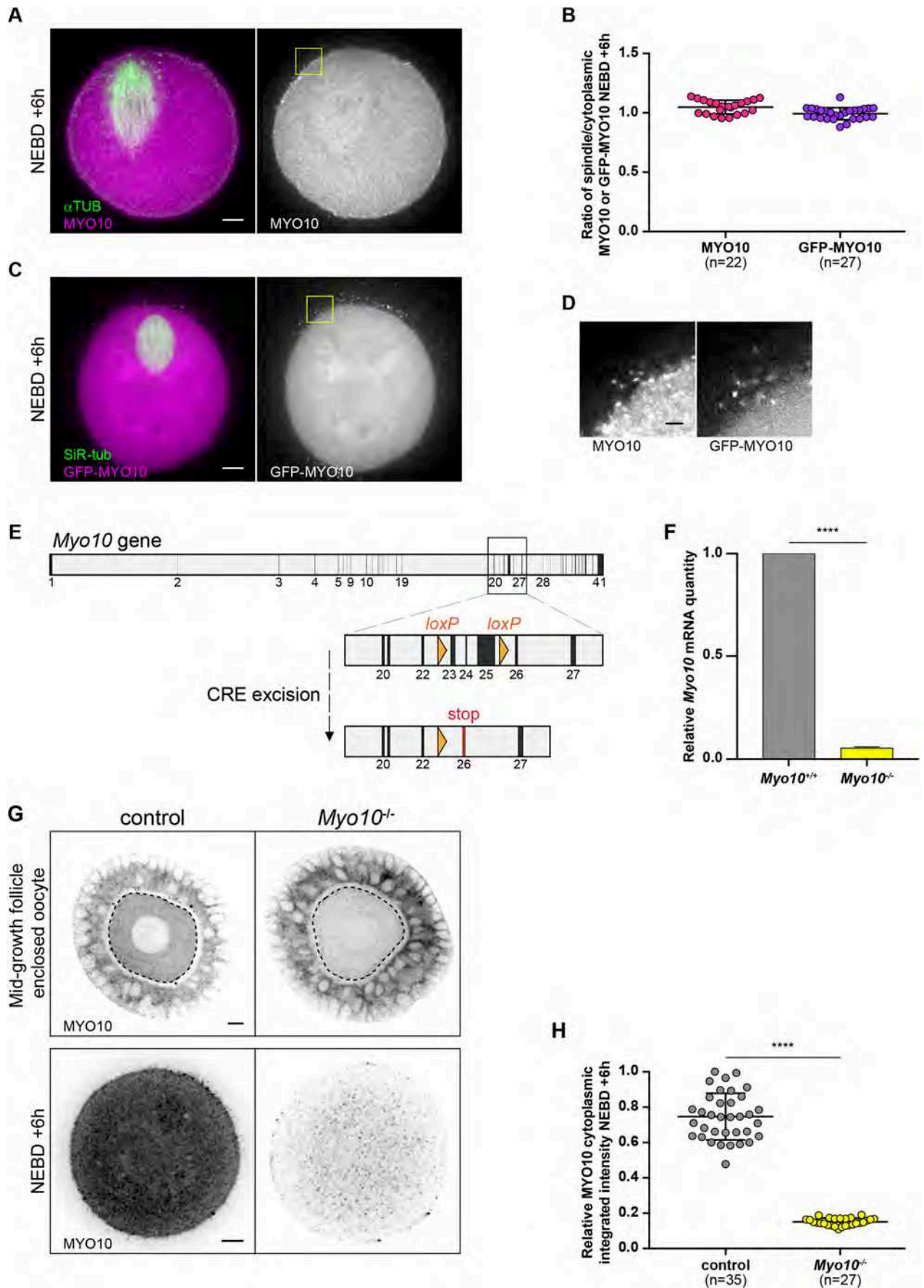


Fig. 1. See next page for legend.

**Fig. 1. MYO10 does not accumulate at the meiosis I spindles.** (A) Confocal spinning disk images of an oocyte fixed at NEBD+6 h stained for  $\alpha$ -tubulin ( $\alpha$ TUB) and myosin-X (MYO10). Left, merge of  $\alpha$ TUB (green) and MYO10 (magenta) staining. Right, MYO10 staining only. Scale bar: 10  $\mu$ m. (B) Scatter plot representing the ratio of spindle and cytoplasmic MYO10 fluorescence intensities at NEBD+6 h in fixed oocytes labeled with MYO10 and  $\alpha$ TUB (pink), and in live oocytes expressing GFP-MYO10 and incubated with SiR-tubulin (purple).  $n$  is the number of oocytes analyzed. Data are from three (fixed oocytes) and two (live oocytes) independent experiments. Data are mean and s.d. with individual data points plotted. (C) Confocal spinning disk images of an oocyte at NEBD+6 h microinjected with GFP-MYO10 and incubated with SiR-tubulin (SiR-tub) to label the microtubules. Left, merge of SiR-tub (green) and GFP-MYO10 (magenta) staining. Right, GFP-MYO10 staining only. Scale bar: 10  $\mu$ m. (D) Confocal spinning disk images showing cortical/membrane foci of endogenous (left) and exogenous (right) MYO10. Images corresponding to the areas outlined with yellow squares in A and C. Scale bar: 2  $\mu$ m. (E) *Cre-loxP*-mediated depletion of MYO10 in oocytes. The *Myo10* gene with exons in black and introns in gray based on the Ensembl database. *loxP* sites, shown as orange triangles, flank exons 23 to 25. *Zp3*-mediated CRE expression in oocytes allows *Myo10* excision at the *loxP* sites. The depletion of exons 23-25 leads to a frame-shift and the appearance of a stop codon at exon 26. (F) Bar chart representing *Myo10* mRNA levels in *Myo10*<sup>-/-</sup> oocytes (from *Myo10*<sup>lox1/lox</sup>; *Cre*<sup>+</sup> female mice, yellow) relative to *Myo10*<sup>+/+</sup> oocytes (from *Myo10*<sup>lox1/lox</sup>; *Cre*<sup>-</sup> female mice, gray). *Myo10*<sup>+/+</sup> normalized mean=1. *Myo10*<sup>-/-</sup> normalized mean=0.05±0.005 (normalized s.e.m.). RT-qPCRs were performed on two biological replicates using 30 oocytes for each condition from two females; two technical replicates were carried out. The statistical significance of the differences was assessed with a two-tailed unpaired *t*-test, \*\*\*\**P*<0.0001. Error bar for the *Myo10*<sup>-/-</sup> group represents s.e.m. (G) Confocal spinning disk images of fixed oocytes at mid-growth surrounded by granulosa cells (granulosa-oocyte complexes, upper images) and fully grown oocytes fixed at NEBD+6 h (lower images) stained for MYO10. Controls are on the left and *Myo10*<sup>-/-</sup> oocytes on the right. The black dotted lines delimit the oocytes in the complexes. The images show the equatorial plane of the oocytes. Scale bars: 10  $\mu$ m. (H) Scatter plots of the relative integrated intensities of cytoplasmic MYO10 labeling observed at NEBD+6 h in control (gray) and *Myo10*<sup>-/-</sup> (yellow) oocytes.  $n$  is the number of oocytes analyzed. Data are from three independent experiments. Data are mean±s.d. with individual data points plotted. The statistical significance of the differences was assessed with a two-tailed unpaired *t*-test with Welch's correction, \*\*\*\**P*<0.0001.

using phalloidin staining (Fig. 2E, upper images) and in live oocytes microinjected with the F-actin probe GFP-UtrCH (Fig. 2E, lower images). The cytoplasmic F-actin meshes were not altered in meiosis I *Myo10*<sup>-/-</sup> oocytes, as evidenced by a cytoplasmic F-actin intensity not significantly different from controls (Fig. 2E, upper images, F; control, 0.85±0.08; *Myo10*<sup>-/-</sup>, 0.82±0.11). The actin cages enclosing the meiosis I spindles were also properly shaped in *Myo10*<sup>-/-</sup> oocytes (Fig. 2E, lower images), arguing that MYO10 does not play a role in assembling such structures. In addition, we assessed the integrity of the subcortical F-actin network, which mediates spindle positioning through cortex softening, in GFP-UtrCH-injected *Myo10*<sup>-/-</sup> oocytes. No defects in the subcortical F-actin network were observed in such a MYO10 depletion context, as indicated by a thickness comparable with controls at NEBD+7 h in *Myo10*<sup>-/-</sup> oocytes (Fig. 2G,H; control, 3.32±0.32  $\mu$ m; *Myo10*<sup>-/-</sup>, 3.40±0.25  $\mu$ m). Interestingly, the lack of impact of MYO10 depletion on F-actin networks is consistent with earlier studies and is not specific to mouse oocytes. Subcortical F-actin is not affected by MYO10 knockdown in terms of assembly and cellular localization in somatic cells (Kwon et al., 2015), nor are the F-actin cables surrounding the spindle in *Xenopus* embryos (Woolner et al., 2008).

### The spindle migrates in MYO10 depleted oocytes

In different studies, conducted in a wide variety of models ranging from *Xenopus* oocytes, epithelia to somatic cells, MYO10 was

described as being required for proper spindle movement in the cell (Weber et al., 2004; Toyoshima and Nishida, 2007; Woolner et al., 2008; Woolner and Papalopulu, 2012; Liu et al., 2012; Kwon et al., 2015; Sandquist et al., 2016, 2018). Interestingly, MYO10 and F-actin disruption leads to similar defects in spindle orientation in mammalian cells (Toyoshima and Nishida, 2007; Kwon et al., 2015) and aberrant cortical anchoring in *Xenopus* embryos (Woolner et al., 2008), suggesting that they work synergistically in such processes. In mouse oocytes, F-actin disruption impairs spindle migration in meiosis I (Longo and Chen, 1985; Verlhac et al., 2000). We thus analyzed spindle positioning in MYO10-depleted oocytes in order to assess whether MYO10 transmits forces to the spindle. We followed the spindle migration by live spinning disk microscopy during meiosis I in control and *Myo10*<sup>-/-</sup> oocytes incubated with SiR-tubulin to label the microtubules. Unlike the latter models, spindle positioning was unaltered by MYO10 depletion in mouse oocytes (Fig. 3A,B; Movie 3). Spindle migration and cortical positioning, assessed by measuring the distance between the cortex and the leading spindle pole 30 min before polar body extrusion (Fig. 3B; control, 6.35±3.52  $\mu$ m; *Myo10*<sup>-/-</sup>, 4.65±2.58  $\mu$ m), were not significantly different between control and *Myo10*<sup>-/-</sup> oocytes. In addition, we examined the cortical position of the spindle in metaphase II-arrested oocytes by live spinning disk microscopy (Fig. 3C). The majority of the arrested control (97.56%) and MYO10 depleted (97.22%) oocytes showed an off-centered meiosis II (MII) spindle 7 h after polar body extrusion (Fig. 3D). These results show that MYO10 does not play a role in the cortical positioning of the meiotic spindles in mouse oocytes.

### Chromosomes are well aligned in MYO10 depleted oocytes

A weakened transmission of forces to the spindle has no effect on spindle morphogenesis but alters meiosis I chromosome alignment in mouse oocytes engineered to become extra soft (Bennabi et al., 2020). We thus assessed chromosome behavior in *Myo10*<sup>-/-</sup> oocytes, testing whether MYO10 depletion might affect force transmission, if not to the spindle, at least to the chromosomes. We microinjected control and *Myo10*<sup>-/-</sup> oocytes with H2B-RFP to label their chromosomes, incubated them with SiR-tubulin to label the microtubules and followed them by live spinning disk microscopy before polar body extrusion. We observed no defects in the alignment or segregation of meiosis I chromosomes in *Myo10*<sup>-/-</sup> oocytes (Fig. 3E,F; Movie 4). Chromosome alignment was evaluated 30 min before anaphase by framing all chromosomes in a single rectangle (referred to as the bounding box as in Bennabi et al., 2020) and by measuring the bounding box height (Fig. 3F, upper chart; control, 12.44±2.81  $\mu$ m; *Myo10*<sup>-/-</sup>, 12.12±2.66  $\mu$ m) and width (Fig. 3F, lower chart; control, 16.04±0.98  $\mu$ m; *Myo10*<sup>-/-</sup>, 16.24±1.59  $\mu$ m). Consistent with our observations on spindle assembly (Fig. 2C,D), bounding box values were not significantly different between the two conditions. Our results show that MYO10 does not transmit forces from the actin cage to the meiotic spindle by crosslinking F-actin and spindle microtubules.

### Mice lacking MYO10 in their oocytes are fertile

Even though MYO10 was dispensable for spindle positioning, we nevertheless tested whether it was required for meiotic divisions (from NEBD to meiosis II) and more broadly for oocyte developmental potential. We monitored meiotic divisions of *Myo10*<sup>-/-</sup> oocytes with a focus on the timing of polar body extrusion, as MYO10 disruption has been previously reported to extend metaphase duration in *Xenopus* embryos (Woolner et al.,

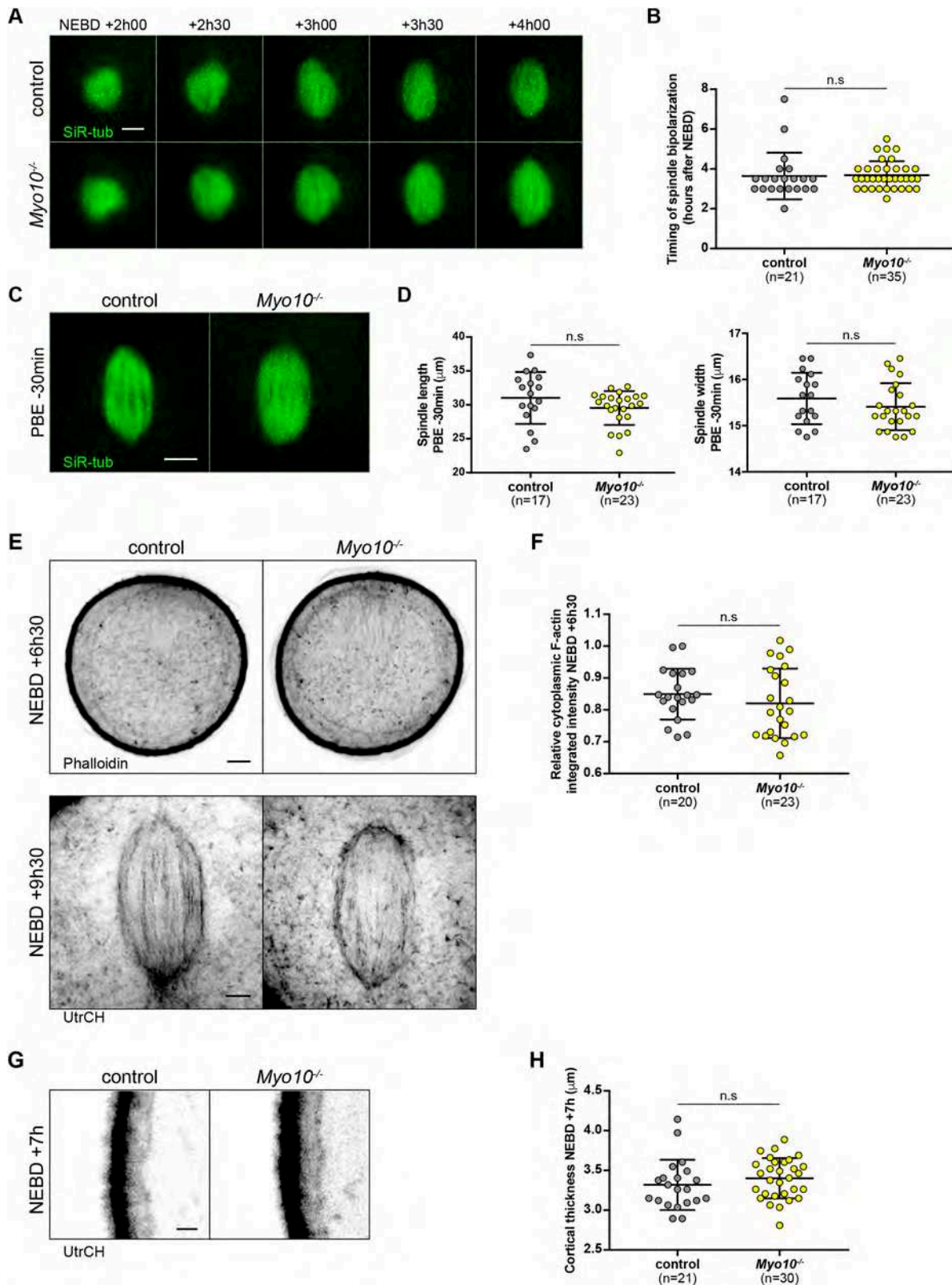


**Fig. 2.** See next page for legend.

2008; Sandquist et al., 2016, 2018). The kinetics and completion of meiosis I were comparable with controls in *Myo10<sup>-/-</sup>* oocytes (Fig. 4A-D; Movie 5). Both NEBD timing (Fig. 4A,B; control,  $1.19 \pm 0.45$  h; *Myo10<sup>-/-</sup>*,  $1.23 \pm 0.40$  h) and polar body extrusion

timing (Fig. 4A,C; control,  $7.88 \pm 0.82$  h; *Myo10<sup>-/-</sup>*,  $7.94 \pm 1.15$  h) were comparable between control and *Myo10<sup>-/-</sup>* oocytes. No significant difference in the rate of first polar body extrusion was measured between the two conditions (Fig. 4D; control, 79.71% of

**Fig. 2. Meiosis I spindles and F-actin networks are properly formed in *Myo10*<sup>-/-</sup> oocytes.** (A) Stills from time-lapse spinning disk movies showing microtubules labeled with SiR-tub (green) forming a ball that progressively bipolarizes to form the meiosis I spindle in a control (upper images) and a *Myo10*<sup>-/-</sup> (lower images) oocyte. Scale bar: 10  $\mu$ m. (B) Scatter plots of the timings of spindle bipolarization (hours after NEBD) in control (gray) and *Myo10*<sup>-/-</sup> (yellow) oocytes. *n* is the number of oocytes analyzed. Data are from three independent experiments (mean $\pm$ s.d. with individual data points plotted). The statistical significance of the differences was assessed with a two-tailed Mann-Whitney test,  $P=0.2948$ . (C) Confocal spinning disk images of a control (left) and a *Myo10*<sup>-/-</sup> (right) spindle 30 min before polar body extrusion (PBE) labeled with SiR-tub (green). Scale bar: 10  $\mu$ m. (D) Scatter plots of spindle length (left chart) and width (right chart) 30 min before PBE in control (gray) and *Myo10*<sup>-/-</sup> (yellow) oocytes. *n* is the number of oocytes analyzed. Data are from five independent experiments (mean $\pm$ s.d. with individual data points plotted). The statistical significance of the differences was assessed with a two-tailed unpaired *t*-test,  $P=0.2995$  for the width. (E) The upper images are oocytes fixed at NEBD+6 h30 showing cytoplasmic F-actin meshes labeled with phalloidin. The images correspond to the equatorial plane of the oocytes. Left, control; right, *Myo10*<sup>-/-</sup>. Scale bar: 10  $\mu$ m. The lower images are confocal spinning disk images of oocytes at NEBD+9 h30 microinjected with GFP-UtrCH (UtrCH) showing actin cages in control (left) and *Myo10*<sup>-/-</sup> (right) oocytes. Scale bar: 5  $\mu$ m. (F) Scatter plots of the relative integrated cytoplasmic intensity from the labeling with phalloidin at NEBD+6 h30 in control (gray) and *Myo10*<sup>-/-</sup> (yellow) oocytes. *n* is the number of oocytes analyzed. Data are from four independent experiments (mean $\pm$ s.d. with individual data points plotted). The statistical significance of the differences was assessed with a two-tailed unpaired *t*-test,  $P=0.3315$ . (G) Confocal spinning disk images focused on the equatorial plane cortex of a control (left) and a *Myo10*<sup>-/-</sup> (right) oocyte microinjected with UtrCH at NEBD+7 h. Scale bar: 2  $\mu$ m. (H) Scatter plots of the measure of cortex thickness at NEBD+7 h in control (gray) and *Myo10*<sup>-/-</sup> (yellow) oocytes. *n* is the number of oocytes analyzed. Data are from two independent experiments (mean $\pm$ s.d. with individual data points plotted). The statistical significance of the differences was assessed with a two-tailed Mann-Whitney test,  $P=0.1322$ .

meiosis II oocytes; *Myo10*<sup>-/-</sup>, 81.18% of meiosis II oocytes), supporting the lack of MYO10 involvement in oocyte division.

We also determined the reproductive potential of mice producing *Myo10*<sup>-/-</sup> oocytes by mating *Myo10*<sup>fllox/fllox</sup>; *Cre*<sup>+</sup> females with control males. The number of pups per litter derived from *Myo10*<sup>fllox/fllox</sup>; *Cre*<sup>+</sup> mice was comparable with the *Myo10*<sup>fllox/fllox</sup>; *Cre*<sup>-</sup> derived litters (Fig. 4E; *Myo10*<sup>fllox/fllox</sup>; *Cre*<sup>-</sup>, 6.75 $\pm$ 2.32 pups; *Myo10*<sup>fllox/fllox</sup>; *Cre*<sup>+</sup>, 6.43 $\pm$ 1.91 pups), arguing that MYO10 is not essential for the developmental potential of the oocyte and for female fertility.

## DISCUSSION

Contrary to what has been described in several models of mitotic cells and in amphibian oocytes, MYO10 is dispensable for spindle assembly and positioning in murine oocytes. These discrepancies could be explained by oocyte specific features that differ from most mitotic cells. In particular, their huge volume, their lack of centrioles and their absence of external cues and cell polarity at NEBD impose alternative mechanisms for spindle morphogenesis and positioning. Importantly, microtubules are not involved in spindle off-centering and mouse oocytes lack astral microtubules present in centriole-containing mitotic cells, potentially explaining why MYO10 is not essential in this model. Indeed, MYO10 involvement in mitotic spindle positioning is likely achieved via astral microtubules, through their pulling toward retraction fibers and the regulation of their dynamics/cortical interaction in somatic cells (Kwon et al., 2015) and their asymmetric distribution at the apical cell surface in *Xenopus* embryos (Woolner and Papalopulu, 2012). Moreover, nuclear anchoring in *Xenopus* oocytes, regulated by MYO10, is a microtubule-dependent process (Weber et al., 2004). Interestingly, unlike mitotic spindles (Woolner et al., 2008;

Fink et al., 2011; Woolner and Papalopulu, 2012; Kwon et al., 2015; Sandquist et al., 2016, 2018) and *Xenopus* oocytes (Weber et al., 2004), the meiosis I spindle in mouse oocytes does not undergo oscillatory movements or rotation during metaphase. Instead, the spindle migrates in a straight manner to the closest cortex along its long axis (Verlhac et al., 2000). Spindle rotation/oscillatory movements in mitotic cells (Woolner et al., 2008; Kwon et al., 2015; Sandquist et al., 2016, 2018) and *Xenopus* oocytes (Weber et al., 2004) involve MYO10. In essence, a role for MYO10 in setting up the cell division plane has so far been described mainly for the microtubule-dependent positioning of chromosome-containing structures and in spindle rotation/oscillation during metaphase, two events that do not take place in murine meiosis I oocytes. Another possibility that could explain the differences between mouse oocytes and other models is the architecture of the cytoplasmic actin-cage surrounding the spindle, which is made of linear F-actin, as opposed to the branched subcortical F-actin likely cooperating with MYO10 to position the mitotic spindles in somatic cells (Mitsushima et al., 2010; Fink et al., 2011; Kwon et al., 2015). We can thus speculate that like myosin II, the activity of which depends on the architecture of actin networks (Reymann et al., 2012), MYO10 function could differ depending on the type of F-actin meshes, preferentially crosslinking branched F-actin to microtubules in the cytoplasm.

The lack of involvement of MYO10 in spindle migration argues for another mechanism at work in transmitting forces to the spindle in murine oocytes. This mechanism could rely on another direct actin-microtubule crosslinker; MYO7a, MYO7b and MYO15a, the other mammalian myosins known to have a MyTH4-FERM domain (which could enable them to bind directly to microtubules), have not been confirmed to be expressed at the protein level in human ovaries (Human Protein Atlas database). In addition, no study to our knowledge has pointed out their prospective function in crosslinking F-actin to microtubules, nor their involvement in spindle integrity and positioning, as they are mostly studied for their functions in actin-rich protrusions (for a review, see Weck et al., 2017). Alternatively, microtubule-based motors could be good candidates for linking the actin-cage to the meiotic spindle. Two spindle and cortex-localized kinesins, NabKin and KIF14, also colocalize with actin in *Xenopus* oocytes and human somatic cells, and are able to bind F-actin in *in vitro* assays (Samwer et al., 2013). Besides motor proteins, other direct and indirect F-actin/microtubule crosslinkers have been identified as being involved in different cellular functions and could as well be at work in meiotic spindle migration (for a review, see Dogterom and Koenderink, 2019). In addition, cytoplasmic F-actin function in spindle off-centering could depend on F-actin direct binding to chromosomes. This hypothesis is supported by the presence of F-actin aggregates accumulated in chromosomal regions oriented towards the closest cortex in nocodazole-treated mouse oocytes (Azoury et al., 2008) and by the ability of F-actin to off-center the chromosomes in such a microtubule disrupted context (Verlhac et al., 2000; Leader et al., 2002; Azoury et al., 2008).

Spindle off-centering in the murine oocyte is thus an atypical process implemented to conciliate the discard of half of the oocyte DNA content with the preservation of a rich cytoplasm enabling the egg to fulfill its developmental purpose. Deciphering how this process is orchestrated and, more specifically, how forces are transmitted from the cortex to the spindle is of significant public health interest, as defects in force transmission could trigger chromosome misalignment and subsequent egg aneuploidy (Bennabi et al., 2020) – the main cause of female infertility (Gruhn et al., 2019).

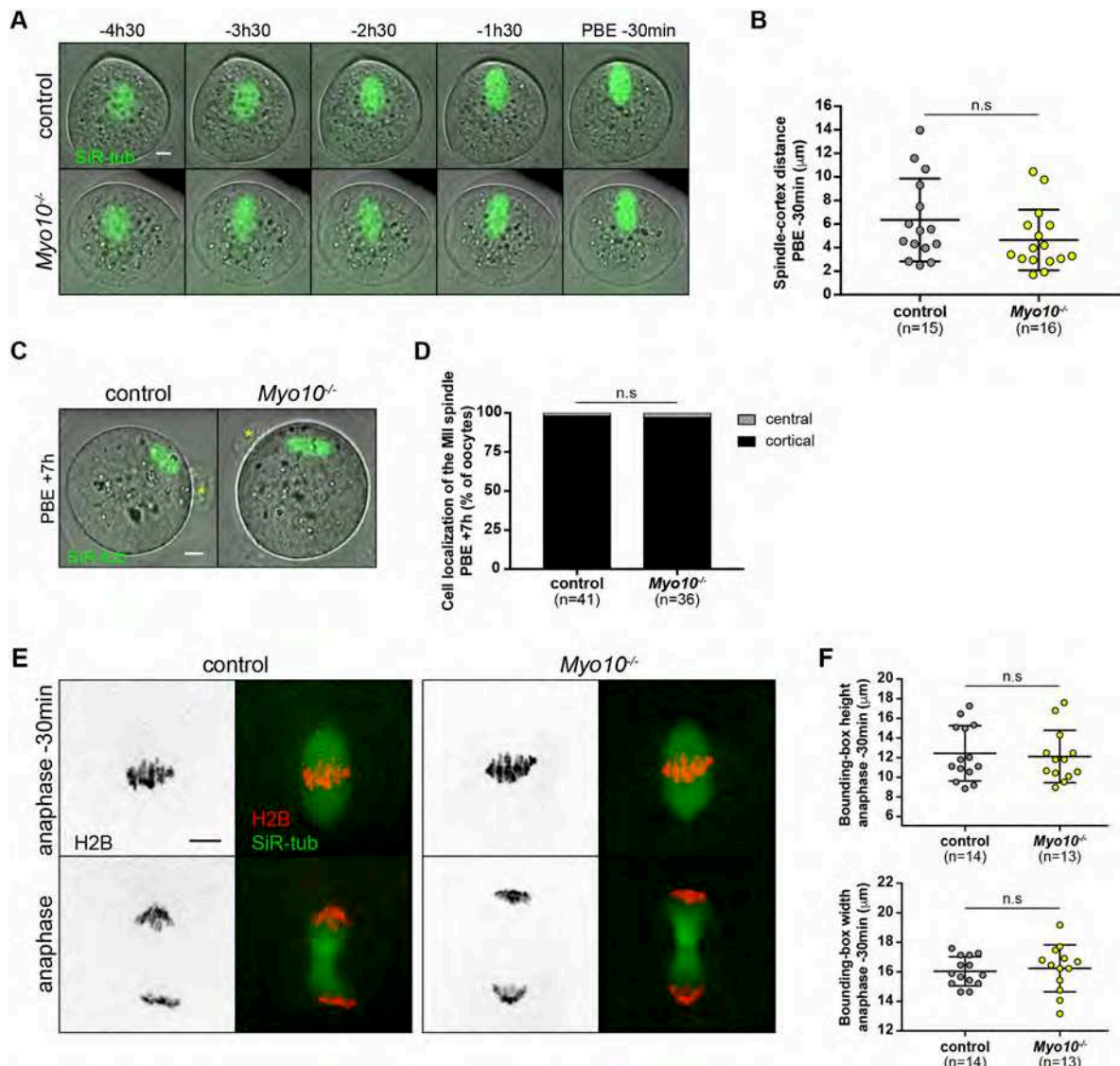


**Fig. 3. Force transmission to the spindle and chromosomes is unaffected by MYO10 depletion.** (A) Stills from time-lapse spinning disk movies showing meiosis I spindles labeled with SiR-tub (green) merged to their corresponding bright-field images. Control oocyte in upper images, *Myo10*<sup>-/-</sup> in lower images. Scale bar: 10 µm. (B) Scatter plots of the distance between the leading spindle pole and the cortex 30 min before polar body extrusion (PBE) in control (gray) and *Myo10*<sup>-/-</sup> (yellow) oocytes. *n* is the number of oocytes analyzed. Data are from five independent experiments (mean±s.d. with individual data points plotted). The statistical significance of the differences was assessed with a two-tailed unpaired *t*-test, *P*=0.1332. (C) Confocal spinning disk images showing the meiosis II spindles 7 h after the first polar body extrusion (PBE) labeled with SiR-tub (green) and merged to their corresponding bright-field images. The control oocyte is on the left; the *Myo10*<sup>-/-</sup> oocyte on the right. The yellow asterisks indicate the first polar bodies. Scale bar: 10 µm. (D) Stacked bars of the cell localization of the meiosis II (MII) spindles as a percentage of the oocytes. Gray indicates the meiosis II spindles centrally located in the metaphase II-arrested oocytes; black indicates the meiosis II spindles anchored to the cortex. *n* is the number of oocytes analyzed. The data are from seven independent experiments. The statistical significance of the differences was assessed with a two-sided Fisher's exact test, *P*>0.9999. (E) Stills from time-lapse spinning disk movies showing meiosis I chromosome alignment (upper images, 30 min before anaphase) and segregation (lower images, anaphase) in control (left panel) and *Myo10*<sup>-/-</sup> (right panel) oocytes. Oocytes were microinjected with H2B-RFP (H2B, black or red) and incubated with SiR-tub (green). Scale bar: 10 µm. (F) Scatter plots of the height (upper chart) and the width (lower chart) of the bounding boxes framing the chromosomes 30 min before anaphase in control (gray) and *Myo10*<sup>-/-</sup> (yellow) oocytes. *n* is the number of oocytes analyzed. Data are from three independent experiments (mean±s.d. with individual data points plotted). The statistical significance of the differences was assessed with a two-tailed unpaired *t*-test, *P*=0.7601 for the height and *P*=0.6903 for the width.

## MATERIALS AND METHODS

### Mouse strains and genotyping

*Myo10*<sup>vt/flox</sup> mice were generated by geneOway by inserting two *loxP* sites into the C57BL/6N mice genome in intronic sequences flanking exons 23 to 25 (according to Ensembl database) of the *Myo10* endogenous locus (Fig. 1E). This line was further crossed with *FLPo* mice [B6.129S4-Gt(ROSA)26Sor<sup>tm2(FLP\*)Sor/J</sup>] to allow excision of the Neo cassettes flanked by FRT sites (mice obtained from the Jackson Laboratory). The resulting line was crossed with *Zp3-Cre* mice available in the lab to create

the final mouse strain conditionally invalidated for myosin-X in oocytes. *loxP*-insertion sites were selected to prevent expression of the MYO10 isoform 1 (F8VQB6-1, referred to as full-length MYO10, FL-myo10) and isoform 2 (F8VQB6-2, referred to as headless MYO10, Hdl-myo10, Sousa et al., 2006). To detect *Flp*-mediated excision of the Neo cassettes flanked by FRT sites, the following PCR primers were used: 5'-ACA GCC CAT ATC ACT GTC TAG AGA CCC ATT-3', 5'-ATC GCC TTC TAT CGC CTT GAC G-3' and 5'-GAG GAT CCA GAC TTG GAC CCG GTC-3'. To detect *Cre*-mediated excision at the *Myo10* locus, the following PCR

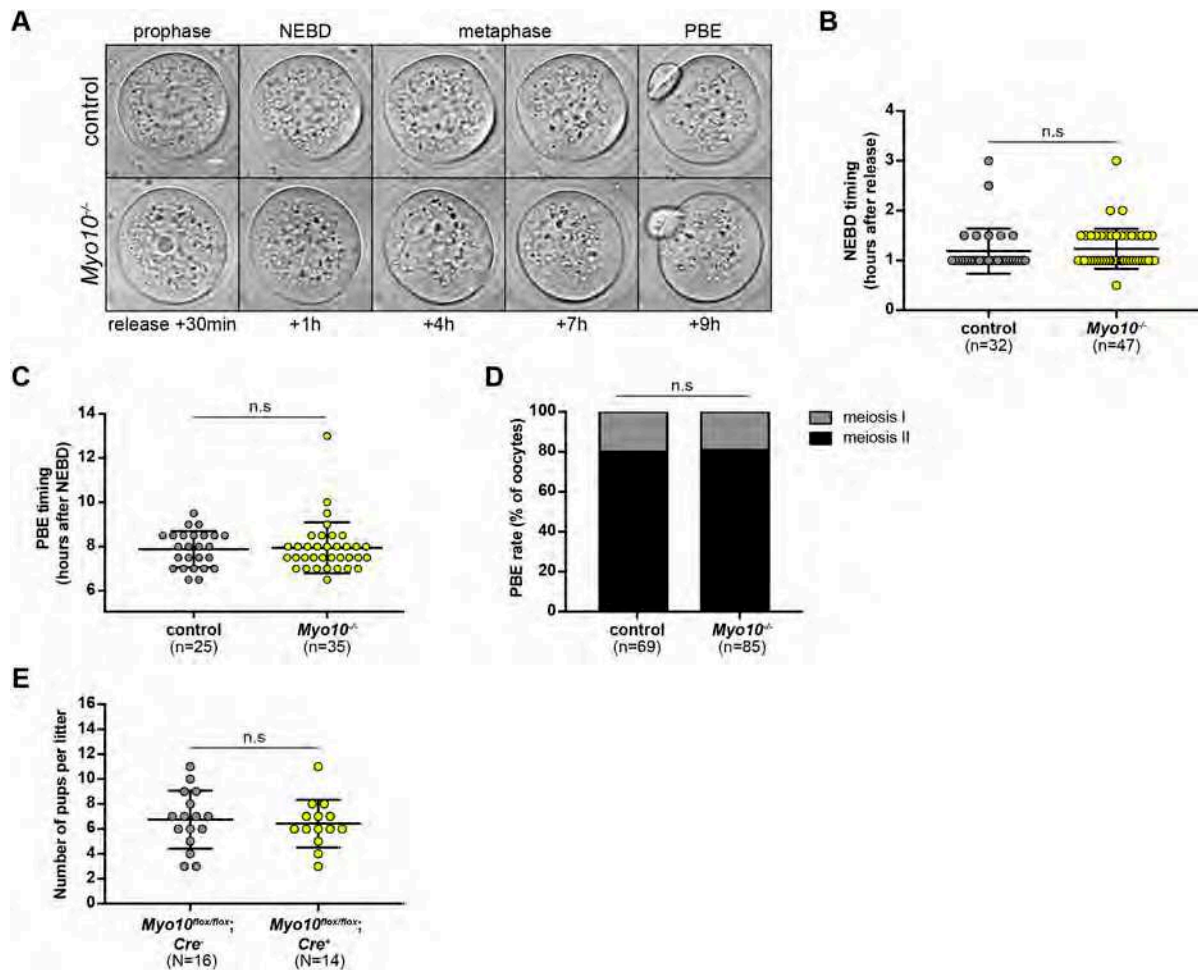


**Fig. 4. MYO10 is dispensable for oocyte developmental potential and female fertility.** (A) Stills from time-lapse spinning disk movies of a control (upper images) and a *Myo10*<sup>-/-</sup> oocyte (lower images) starting 30 min after release of the prophase block until polar body extrusion (PBE). Scale bar: 10  $\mu$ m. (B) Scatter-plot of NEBD timing (hours after release) of control (gray) and *Myo10*<sup>-/-</sup> (yellow) oocytes. *n* is the number of oocytes analyzed. Data are from three independent experiments (mean $\pm$ s.d. with individual data points plotted). The statistical significance of the differences was assessed with a two-tailed Mann-Whitney test, *P*=0.2275. (C) Scatter plot of polar body extrusion (PBE) timing (hours after NEBD) of control (gray) and *Myo10*<sup>-/-</sup> (yellow) oocytes. *n* is the number of oocytes analyzed. Data are from three independent experiments (mean $\pm$ s.d. with individual data points plotted). The statistical significance of the differences was assessed with a two-tailed Mann-Whitney test, *P*=0.6907. (D) Stacked bars of the rate of polar body extrusion (PBE) as a percentage of oocytes. Gray, oocytes arrested in meiosis I that have not extruded a polar body; black, oocytes that have extruded a polar body and are arrested in meiosis II. *n* is the number of oocytes analyzed. Data are from three independent experiments. The statistical significance of the differences was assessed with a two-sided Fisher's exact test, *P*=0.8404. (E) Scatter plots of the number of pups per litter from *Myo10*<sup>flox/flox</sup>; *Cre*<sup>-</sup> female mice (control, gray) and *Myo10*<sup>flox/flox</sup>; *Cre*<sup>+</sup> female mice (carrying *Myo10*<sup>-/-</sup> oocytes, yellow). *N* is the number of litters analyzed, from four (*Myo10*<sup>flox/flox</sup>; *Cre*<sup>-</sup>) and five (*Myo10*<sup>flox/flox</sup>; *Cre*<sup>+</sup>) independent couplings. Data are mean $\pm$ s.d. with individual data points plotted. The statistical significance of the differences was assessed with a two-tailed unpaired *t*-test, *P*=0.6848.

primers were used: for the *Cre*, 5'-GCG GTC TGG CAG TAA AAA CTA TC-3' and 5'-GTG AAA CAG CAT TGC TGT CAC TT-3'; and for the *Myo10*, 5'-ACC CCA GTA CTT GTT CAT ACA TCC TAT ATC CTA CA-3', 5'-GAC TAC ACC ATT CTG AAT GTG CCT GAT CTC-3' and 5'-GAG TAT CTG CCA TCT TGT CCC TAA AGG TGG-3'. Control oocytes were collected from *Myo10*<sup>w<sup>t</sup>/flox</sup>; *Cre*<sup>+</sup>, *Myo10*<sup>w<sup>t</sup>/flox</sup>; *Cre*<sup>-</sup>, *Myo10*<sup>flox/flox</sup>; *Cre*<sup>-</sup> and *Myo10* <sup>$\Delta$ /flox</sup>; *Cre*<sup>-</sup> mice, and *Myo10*<sup>-/-</sup> oocytes from *Myo10*<sup>flox/flox</sup>; *Cre*<sup>+</sup> and *Myo10* <sup>$\Delta$ /flox</sup>; *Cre*<sup>+</sup> mice.

#### Oocyte collection, culture and cRNA microinjection

Oocytes were collected from 2- to 5-month-old female mice following ovaries shredding (Verlhac et al., 1994) in a M2+BSA medium supplemented with milirinine (1  $\mu$ M, Reis et al., 2006) to maintain them in prophase I arrest. For live cell imaging, oocytes were microinjected with cRNAs using an Eppendorf Femtojet microinjector and were left expressing protein fusions in prophase I for 30–45 min (H2B-RFP and GFP-UtrCH) or 1 h (GFP-MYO10) before being transferred into a M2+BSA milirinine-free medium to trigger meiosis resumption. Oocyte culture and live cell imaging were performed under oil at 37°C.

#### Plasmids and *in vitro* transcription of cRNA

The following constructs were used: pCS2+ GFP-Myosin10(MYO10) (a gift from Nicolas Plachta, University of Pennsylvania, PA, USA), pspe3-GFP-UtrCH (Azoury et al., 2008) and pRN3-Histone(H2B)-RFP (Tsurumi et al., 2004). Plasmids were linearized with proper restriction enzymes and subsequently *in vitro* transcribed using the T3 or SP6 mMESSAGE mMACHINE (Ambion, AM1348 and 1340) transcription kits. The resulting cRNAs were purified using the RNeasy Mini Kit (Qiagen, 74104) and were centrifuged for 90 min at 4°C before being microinjected into the cytoplasm of prophase I-arrested oocytes.

#### RNA extraction and RT-qPCR

Total RNA was extracted from 30 freshly collected oocytes (*Myo10*<sup>+/+</sup> from *Myo10*<sup>flox/flox</sup>; *Cre*<sup>-</sup> mice and *Myo10*<sup>-/-</sup> from *Myo10*<sup>flox/flox</sup>; *Cre*<sup>+</sup> mice) using the RNeasy Micro Total RNA Isolation Kit (ThermoFisher, AM1931). Oocytes were washed three times in PBS, resuspended in lysis buffer, frozen in liquid nitrogen and conserved at -80°C for 1 h. After unfreezing, RNA extraction was carried out following the manufacturer's instructions. RNA was eluted twice in 10  $\mu$ l elution buffer and samples were

treated with DNase I. For reverse transcription, iScript Reverse Transcription Supermix (Bio-Rad, Ref. 1708840) was used following the manufacturer's instructions. The cDNA was then used for quantitative PCR using SsoAdvanced Universal SYBR Green Supermix (Bio-Rad, Ref. 1725270) and CFX-96 (Bio-Rad) with the primer pairs listed below. Levels were calculated using the 2- $\Delta\Delta C_T$ . Mean and s.e.m. were both normalized relative to *Myo10*<sup>+/-</sup>. *Myo10* mRNA quantity was normalized to *Gadph*. The following primers were used: *Myo10*, 5'-GGC ACG AAA GCA ATA TAG AAA GG-3' and 5'-CTT CTG GAA CAC GAT GGC TG-3', *Gadph*, 5'-TGG AGA AAC CTG CCA AGT ATG-3' and 5'-GGT CCT CAG TGT AGC CCA AG-3'.

### Immunostaining

Fully grown oocytes were freed from their zona pellucida in acid Tyrode before fixation. Granulosa-oocyte complexes (GOCs) and fully grown oocytes were fixed on gelatin and polylysine-treated coverslips.

For F-actin and  $\alpha$ -tubulin staining, fully grown oocytes were fixed for 30 min at 37°C in PBS, EGTA (pH 7, 50 mM), HEPES (pH 7, 100 mM) and MgSO<sub>4</sub> (10 mM) buffer supplemented with 2% formaldehyde (methanol free) and 0.2% Triton X-100 (Schuh and Ellenberg, 2008). Oocytes were washed and permeabilized overnight at 4°C in PBS and 0.1% Triton X-100. Blocking (30 min) and antibody incubation (primary, 1 h 30 min; secondary, 1 h) were carried out the next day at room temperature in PBS, 0.1% Triton X-100 and 3% BSA. Washes between and after the primary and secondary antibody incubations were carried out in PBS and 0.1% Tween 20.  $\alpha$ -Tubulin staining is not shown in Fig. 2E.

For MYO10 and  $\alpha$ -tubulin staining, fully grown oocytes were fixed for 30 min at 37°C in PBS and 4% paraformaldehyde, and washed in PBS overnight at 4°C. Oocytes were permeabilized the next day in PBS and 0.5% Triton X-100 for 10 min, and washed subsequently in PBS and in PBS/0.1% Tween 20. Blocking (30 min) and antibody incubation (primary, 1 h 30 min; secondary, 1 h) were carried out at room temperature in PBS, 0.1% Tween 20 and 3% BSA. Washes between and after the primary and secondary antibody incubations were carried out in PBS/0.1% Tween 20.

GOCs were fixed for 30 min at 37°C in PBS, EGTA (pH 7, 50 mM), HEPES (pH 7, 100 mM) and MgSO<sub>4</sub> (10 mM) buffer supplemented with 0.3% formaldehyde (methanol free) and 2% Triton X-100, and washed in PBS overnight at 4°C. GOCs were permeabilized again the next day in PBS and 0.5% Triton X-100 for 10 min, and washed subsequently in PBS and PBS/0.1% Tween 20. Blocking (30 min) and antibody incubation (primary, 1 h 30 min; secondary, 1 h) were carried out at room temperature in PBS, 0.1% Tween 20 and 3% BSA. Washes between and after the primary and secondary antibody incubations were carried out in PBS/0.1% Tween 20.

Fully grown oocytes and GOCs were mounted on 0.25 mm or 0.50 mm thick slide wells, respectively, filled with Vectashield Antifade Mounting Medium with DAPI (Vector Laboratories, H-1200). We used rabbit anti-MYO10 (Sigma-Aldrich, HPA024223; 1:200) and mouse anti- $\alpha$ -tubulin ( $\alpha$ TUB, Sigma-Aldrich, T8203; 1:200) primary antibodies. We used Cy3-conjugated anti-rabbit (Jackson ImmunoResearch, 11-165-152; 1:150), Cy3-conjugated anti-mouse (Jackson ImmunoResearch, 715-165-151; 1:150) and Alexa Fluor 488-conjugated anti-mouse (Invitrogen, A21121; 1:150) secondary antibodies. To label F-actin, fully grown oocytes and GOCs (not shown in Fig. 1G for GOCs) were incubated with Alexa Fluor 488-conjugated phalloidin (Invitrogen, A12379; 10 U/ml) for 1 h concomitantly with secondary antibody incubation.

### Fixed and live imaging

Spinning disk images and movies were acquired using a Plan-APO 40 $\times$ /1.25 NA objective on a Leica DMI6000B microscope enclosed in a thermostatic chamber (Life Imaging Service) equipped with a Retiga 3 CCD camera (iQImaging) coupled to a Sutter filter wheel (Roper Scientific) and a Yokogawa CSU-X1-M1 spinning disk. Metamorph software (Universal Imaging) was used to collect data.

### Image analysis

MYO10 spindle enrichment was quantified by measuring the ratio of the spindle and cytoplasmic MYO10 fluorescence intensities in fixed oocytes

labeled with MYO10 and  $\alpha$ -tubulin at NEBD+6 h, and in live oocytes expressing GFP-MYO10 and incubated with SiR-tubulin (from prophase I, SiR-tub, Spirochrome, SC006; 100 nM) at NEBD+6 h. Background subtraction and intensity measurements were made using Metamorph software. Spindle and cytoplasmic integrated fluorescence intensities were measured randomly four times in each compartment (spindle and cytoplasm) per oocyte using the same circle ROI of 17  $\mu$ m<sup>2</sup>. Measurements were taken on one focal plane containing the spindle.

MYO10 cytoplasmic intensity was measured on fixed oocytes labeled with MYO10 at NEBD+6 h. F-actin cytoplasmic intensity was measured on fixed oocytes labeled with phalloidin at NEBD+6 h 30 min. Background subtraction and intensity measurements were carried out using Metamorph software. The integrated intensity was measured on the equatorial plane of the oocytes in the same ellipsoidal ROI encompassing the oocyte cytoplasm (MYO10 ellipse=3776.29  $\mu$ m<sup>2</sup>, F-actin ellipse=2869.04  $\mu$ m<sup>2</sup>). Intensity values were then normalized to the highest control value.

Spindle inter-polar distance, spindle width and spindle-cortex distance in meiosis I were measured manually using Metamorph software 30 min before polar body extrusion on live oocytes incubated with SiR-tub (100 nM). Only spindles parallel to the observation plane were measured. Spindle position in meiosis II was assessed visually 7 h after polar body extrusion on live oocytes incubated with SiR-tub (100 nM).

Cortical thickness (including subcortical F-actin) was measured on live oocytes expressing GFP-UtrCH at NEBD+7 h. The cortical thickness value is the mean of four measurements taken manually and randomly per oocyte on the oocyte equatorial plane (Chaigne et al., 2013; Bennabi et al., 2020) using Metamorph software.

Chromosome alignment was assessed on live oocytes expressing H2B-RFP by manually framing the chromosomes in a bounding box (Bennabi et al., 2020). The height and width of the bounding boxes were measured 30 min before anaphase using Metamorph software only on spindles parallel to the observation plane.

### Statistical analysis

Statistical analysis was carried out using GraphPad Prism software version 7.0a. For two-group comparison, the normality of each group distribution was tested with a D'Agostino and Pearson normality test. The group means were subsequently compared either with a parametric two-tailed unpaired *t*-test (with Welch's correction in the case of not equal variances for MYO10 cytoplasmic integrated intensity) or with a non-parametric two-tailed Mann-Whitney test. For the rate of polar body extrusion, the repartition of each condition was tested for statistical significance with a two-sided Fisher's exact test. Each test was carried out with a confidence interval of 95%. Error bars represent either standard deviation or standard error of mean for relative *Myo10* mRNA quantity. n.s., non-significant ( $P>0.05$ ; \*\*\*\* $P<0.0001$ ).

### Ethical statement

All experimental procedures used for the project have been approved by the ministry of agriculture to be conducted in our CIRB animal facility (authorization number 75-1170). The use of all the genetically modified organisms described in this project has been granted by the DGRI (Direction Générale de la Recherche et de l'Innovation: Agrément OGM; DUO-5291).

### Acknowledgements

We thank all past and present members of the Verhac-Terret laboratory for discussions and Dr Nicolas Plachta, (University of Pennsylvania, Philadelphia, PA, USA) for the pCS2-GFP-Myosin10 construct.

### Competing interests

The authors declare no competing or financial interests.

### Author contributions

Conceptualization: F.C., M.-H.V., M.-E.T.; Methodology: F.C., C.D.S., M.-E.T.; Formal analysis: F.C., C.D.S., M.-E.T.; Investigation: F.C., C.D.S.; Writing - original draft: F.C.; Writing - review & editing: F.C., M.-H.V., M.-E.T.; Supervision: M.-E.T.; Funding acquisition: F.C., M.-H.V., M.-E.T.

### Funding

This work was supported by the Fondation pour la Recherche Médicale (FRM Label EQU201903007796 to M.-H.V.), by the Agence Nationale de la Recherche [ANR-18-

CE13 to M.-H.V. and Auguste Genovesio (IBENS/ENS), and ANR-16-CE13 to M.-E.T.] and by the France Canada Research Fund [FCRF 2017 to M.-E.T. and Hugh J. Clarke (McGill University, Montreal, Canada)]. F.C. obtained a grant from the Fondation pour la Recherche Médicale for her 4th PhD year (FDT202001010906). This work has also received support from the Fondation Bettencourt Schueller, under the program Investissements d'Avenir launched by the French Government and implemented by the Agence Nationale de la Recherche (ANR-10-LABX-54 MEMO LIFE, and ANR-11-IDEX-0001-02 PSL\* Research University). Deposited in PMC for immediate release.

### Supplementary information

Supplementary information available online at <https://dev.biologists.org/lookup/doi/10.1242/dev.199364.supplemental>

### Peer review history

The peer review history is available online at <https://journals.biologists.com/dev/article-lookup/148/7/dev199364/>

### References

- Azoury, J., Lee, K. W., Georget, V., Rassinier, P., Leader, B. and Verlhac, M.-H.** (2008). Spindle positioning in mouse oocytes relies on a dynamic meshwork of actin filaments. *Curr. Biol.* **18**, 1514-1519. doi:10.1016/j.cub.2008.08.044
- Bennabi, I., Terret, M.-E. and Verlhac, M.-H.** (2016). Meiotic spindle assembly and chromosome segregation in oocytes. *J. Cell Biol.* **215**, 611-619. doi:10.1083/jcb.201607062
- Bennabi, I., Crozet, F., Nikalayevich, E., Chaigne, A., Letort, G., Manil-Ségalen, M., Campillo, C., Cadart, C., Othmani, A., Attia, R. et al.** (2020). Artificially decreasing cortical tension generates aneuploidy in mouse oocytes. *Nat. Commun.* **11**, 1649. doi:10.1038/s41467-020-15470-y
- Berg, J. S., Derfler, B. H., Pennisi, C. M., Corey, D. P. and Cheney, R. E.** (2000). Myosin-X, a novel myosin with pleckstrin homology domains, associates with dynamic actin. *J. Cell Sci.* **113**, 3439-3451.
- Briño-Enríquez, M. A., Moak, S. L., Holloway, J. K. and Cohen, P. E.** (2017). NIMA-related kinase 1 (NEK1) regulates meiosis I spindle assembly by altering the balance between  $\alpha$ -Adducin and Myosin X. *PLoS ONE* **12**, e0185780. doi:10.1371/journal.pone.0185780
- Chaigne, A., Campillo, C., Gov, N. S., Voituriez, R., Azoury, J., Umaña-Díaz, C., Almonacid, M., Queguiner, I., Nassoy, P., Sykes, C. et al.** (2013). A soft cortex is essential for asymmetric spindle positioning in mouse oocytes. *Nat. Cell Biol.* **15**, 958-966. doi:10.1038/ncb2799
- Chaigne, A., Campillo, C., Gov, N. S., Voituriez, R., Sykes, C., Verlhac, M. H. and Terret, M. E.** (2015). A narrow window of cortical tension guides asymmetric spindle positioning in the mouse oocyte. *Nat. Commun.* **6**, 6027. doi:10.1038/ncomms7027
- Di Pietro, F., Echard, A. and Morin, X.** (2016). Regulation of mitotic spindle orientation: an integrated view. *EMBO Rep.* **17**, 1106-1130. doi:10.15252/embr.201642292
- Dogterom, M. and Koenderink, G. H.** (2019). Actin-microtubule crosstalk in cell biology. *Nat. Rev. Mol. Cell Biol.* **20**, 38-54. doi:10.1038/s41580-018-0067-1
- Duan, X., Li, Y., Yi, K., Guo, F., Wang, H. Y., Wu, P.-H., Yang, J., Mair, D. B., Morales, E. A., Kalab, P. et al.** (2020). Dynamic organelle distribution initiates actin-based spindle migration in mouse oocytes. *Nat. Commun.* **11**, 277. doi:10.1038/s41467-019-14068-3
- Dumont, J., Million, K., Sunderland, K., Rassinier, P., Lim, H., Leader, B. and Verlhac, M.-H.** (2007a). Formin-2 is required for spindle migration and for the late steps of cytokinesis in mouse oocytes. *Dev. Biol.* **301**, 254-265. doi:10.1016/j.ydbio.2006.08.044
- Dumont, J., Petri, S., Pellegrin, F., Terret, M.-E., Bohnsack, M. T., Rassinier, P., Georget, V., Kalab, P., Gruss, O. J. and Verlhac, M.-H.** (2007b). A centriole and RanGTP-independent spindle assembly pathway in meiosis I of vertebrate oocytes. *J. Cell Biol.* **176**, 295-305. doi:10.1083/jcb.200605199
- Fink, J., Carpi, N., Betz, T., Bétard, A., Chebah, M., Azioune, A., Bornens, M., Sykes, C., Fetler, L., Cuvelier, D. et al.** (2011). External forces control mitotic spindle positioning. *Nat. Cell Biol.* **13**, 771-778. doi:10.1038/ncb2269
- Gruhn, J. R., Zielinska, A. P., Shukla, V., Blanshard, R., Capalbo, A., Cimadomo, D., Nikiforov, D., Chan, A. C.-H., Newnham, L. J., Vogel, I. et al.** (2019). Chromosome errors in human eggs shape natural fertility over reproductive life span. *Science* **365**, 1466-1469. doi:10.1126/science.aav7321
- Hirano, Y., Hatano, T., Takahashi, A., Toriyama, M., Inagaki, N. and Hakoshima, T.** (2011). Structural basis of cargo recognition by the myosin-X MyTH4-FERM domain. *EMBO J.* **30**, 2734-2747. doi:10.1038/emboj.2011.177
- Homma, K., Saito, J., Ikebe, R. and Ikebe, M.** (2001). Motor function and regulation of myosin X. *J. Biol. Chem.* **276**, 34348-34354. doi:10.1074/jbc.M104785200
- Kitajima, T. S., Ohsugi, M. and Ellenberg, J.** (2011). Complete kinetochore tracking reveals error-prone homologous chromosome biorientation in mammalian oocytes. *Cell* **146**, 568-581. doi:10.1016/j.cell.2011.07.031
- Kwon, M., Bagonis, M., Danuser, G. and Pellman, D.** (2015). Direct microtubule-binding by Myosin-10 orients centrosomes toward retraction fibers and subcortical actin clouds. *Dev. Cell* **34**, 323-337. doi:10.1016/j.devcel.2015.06.013
- Kyogoku, H. and Kitajima, T. S.** (2017). Large cytoplasm is linked to the error-prone nature of oocytes. *Dev. Cell* **41**, 287-298.e4. doi:10.1016/j.devcel.2017.04.009
- Larson, S. M., Lee, H. J., Hung, P.-H., Matthews, L. M., Robinson, D. N. and Evans, J. P.** (2010). Cortical mechanics and meiosis II completion in mammalian oocytes are mediated by myosin-II and Ezrin-Radixin-Moesin (ERM) proteins. *Mol. Biol. Cell* **21**, 3182-3192. doi:10.1091/mbc.e10-01-0066
- Leader, B., Lim, H., Carabatsos, M. J., Harrington, A., Ecsedy, J., Pellman, D., Maas, R. and Leder, P.** (2002). Formin-2, polyploidy, hypofertility and positioning of the meiotic spindle in mouse oocytes. *Nat. Cell Biol.* **4**, 921-928. doi:10.1038/ncb880
- Li, H., Guo, F., Rubinstein, B. and Li, R.** (2008). Actin-driven chromosomal motility leads to symmetry breaking in mammalian meiotic oocytes. *Nat. Cell Biol.* **10**, 1301-1308. doi:10.1038/ncb1788
- Liu, K. C., Jacobs, D. T., Dunn, B. D., Fanning, A. S. and Cheney, R. E.** (2012). Myosin-X functions in polarized epithelial cells. *Mol. Biol. Cell* **23**, 1675-1687. doi:10.1091/mbc.e11-04-0358
- Longo, F. J. and Chen, D.-Y.** (1985). Development of cortical polarity in mouse eggs: Involvement of the meiotic apparatus. *Dev. Biol.* **107**, 382-394. doi:10.1016/0012-1606(85)90320-3
- Mitsushima, M., Aoki, K., Ebisuya, M., Matsumura, S., Yamamoto, T., Matsuda, M., Toyoshima, F. and Nishida, E.** (2010). Revolving movement of a dynamic cluster of actin filaments during mitosis. *J. Cell Biol.* **191**, 453-462. doi:10.1083/jcb.201007136
- Mogessie, B. and Schuh, M.** (2017). Actin protects mammalian eggs against chromosome segregation errors. *Science* **357**, eaal1647. doi:10.1126/science.aal1647
- Morin, X. and Bellaïche, Y.** (2011). Mitotic spindle orientation in asymmetric and symmetric cell divisions during animal development. *Dev. Cell* **21**, 102-119. doi:10.1016/j.devcel.2011.06.012
- Pfender, S., Kuznetsov, V., Pleiser, S., Kerkhoff, E. and Schuh, M.** (2011). Spire-type actin nucleators cooperate with Formin-2 to drive asymmetric oocyte division. *Curr. Biol.* **21**, 955-960. doi:10.1016/j.cub.2011.04.029
- Reis, A., Chang, H. Y., Levasseur, M. and Jones, K. T.** (2006). APCcdh1 activity in mouse oocytes prevents entry into the first meiotic division. *Nat. Cell Biol.* **8**, 539-540. doi:10.1038/ncb1406
- Reymann, A.-C., Boujemaa-Paterski, R., Martiel, J.-L., Guérin, C., Cao, W., Chin, H. F., De La Cruz, E. M., Théry, M. and Blanchoin, L.** (2012). Actin network architecture can determine myosin motor activity. *Science* **336**, 1310-1314. doi:10.1126/science.1221708
- Samwer, M., Dehne, H.-J., Spira, F., Kollmar, M., Gerlich, D. W., Urlaub, H. and Görllich, D.** (2013). The nuclear F-actin interactome of *Xenopus* oocytes reveals an actin-bundling kinesin that is essential for meiotic cytokinesis. *EMBO J.* **32**, 1886-1902. doi:10.1038/emboj.2013.108
- Sandquist, J. C., Larson, M. E. and Hine, K. J.** (2016). Myosin-10 independently influences mitotic spindle structure and mitotic progression. *Cytoskeleton* **73**, 351-364. doi:10.1002/cm.21311
- Sandquist, J. C., Larson, M. E., Woolner, S., Ding, Z. and Bement, W. M.** (2018). An interaction between myosin-10 and the cell cycle regulator Wee1 links spindle dynamics to mitotic progression in epithelia. *J. Cell Biol.* **217**, 849-859. doi:10.1083/jcb.201708072
- Schuh, M. and Ellenberg, J.** (2007). Self-organization of MTOCs replaces centrosome function during acentrosomal spindle assembly in live mouse oocytes. *Cell* **130**, 484-498. doi:10.1016/j.cell.2007.06.025
- Schuh, M. and Ellenberg, J.** (2008). A new model for asymmetric spindle positioning in mouse oocytes. *Curr. Biol.* **18**, 1986-1992. doi:10.1016/j.cub.2008.11.022
- So, C., Seres, K. B., Steyer, A. M., Mönlich, E., Clift, D., Pejkovska, A., Möbius, W. and Schuh, M.** (2019). A liquid-like spindle domain promotes acentrosomal spindle assembly in mammalian oocytes. *Science* **364**, eaat9557. doi:10.1126/science.aat9557
- Sousa, A. D., Berg, J. S., Robertson, B. W., Meeker, R. B. and Cheney, R. E.** (2006). Myo10 in brain: developmental regulation, identification of a headless isoform and dynamics in neurons. *J. Cell Sci.* **119**, 184-194. doi:10.1242/jcs.02726
- Szollósi, D., Calarco, P. and Donahue, R. P.** (1972). Absence of centrioles in the first and second meiotic spindles of mouse oocytes. *J. Cell Sci.* **11**, 521-541.
- Théry, M., Racine, V., Pépin, A., Piel, M., Chen, Y., Sibarita, J.-B. and Bornens, M.** (2005). The extracellular matrix guides the orientation of the cell division axis. *Nat. Cell Biol.* **7**, 947-953. doi:10.1038/ncb1307
- Toyoshima, F. and Nishida, E.** (2007). Integrin-mediated adhesion orients the spindle parallel to the substratum in an EB1- and myosin X-dependent manner. *EMBO J.* **26**, 1487-1498. doi:10.1038/sj.emboj.7601599
- Tsurumi, C., Hoffmann, S., Geley, S., Graeser, R. and Polanski, Z.** (2004). The spindle assembly checkpoint is not essential for CSF arrest of mouse oocytes. *J. Cell Biol.* **167**, 1037-1050. doi:10.1083/jcb.200405165
- Verlhac, M. H., Kubiak, J. Z., Clarke, H. J. and Maro, B.** (1994). Microtubule and chromatin behavior follow MAP kinase activity but not MPF activity during meiosis in mouse oocytes. *Development* **120**, 1017-1025.
- Verlhac, M.-H., Lefebvre, C., Guillaud, P., Rassinier, P. and Maro, B.** (2000). Asymmetric division in mouse oocytes: with or without Mos. *Curr. Biol.* **10**, 1303-1306. doi:10.1016/S0960-9822(00)00753-3

- Weber, K. L., Sokac, A. M., Berg, J. S., Cheney, R. E. and Bement, W. M. (2004).** A microtubule-binding myosin required for nuclear anchoring and spindle assembly. *Nature* **431**, 325-329. doi:10.1038/nature02834
- Weck, M. L., Grega-Larson, N. E. and Tyska, M. J. (2017).** MyTH4-FERM myosins in the assembly and maintenance of actin-based protrusions. *Curr. Opin. Cell Biol.* **44**, 68-78. doi:10.1016/j.ceb.2016.10.002
- Woolner, S. and Papalopulu, N. (2012).** Spindle position in symmetric cell divisions during epiboly is controlled by opposing and dynamic apicobasal forces. *Dev. Cell* **22**, 775-787. doi:10.1016/j.devcel.2012.01.002
- Woolner, S., O'Brien, L. L., Wiese, C. and Bement, W. M. (2008).** Myosin-10 and actin filaments are essential for mitotic spindle function. *J. Cell Biol.* **182**, 77-88. doi:10.1083/jcb.200804062
- Yanez, L. Z., Han, J., Behr, B. B., Pera, R. A. R. and Camarillo, D. B. (2016).** Human oocyte developmental potential is predicted by mechanical properties within hours after fertilization. *Nat. Commun.* **7**, 10809. doi:10.1038/ncomms10809
- Yi, K., Rubinstein, B., Unruh, J. R., Guo, F., Slaughter, B. D. and Li, R. (2013).** Sequential actin-based pushing forces drive meiosis I chromosome migration and symmetry breaking in oocytes. *J. Cell Biol* **200**, 567-576. doi:10.1083/jcb.201211068

## **Article #2:**

**Granulosa cells enhance the oocyte  
developmental potential through  
transzonal projections**

*This project has a particular value for me because I saw it emerge and gradually gathered data to lead to the following manuscript. The launch of this project was totally unexpected, but nevertheless went smoothly, thanks to the benevolence of Marie-Hélène and Marie-Emilie who managed to create a motivating and confident climate to embark on the unknown.*

*After realizing that we owned a total Myosin-X knockout, and that our first observations of Myo10<sup>-/-</sup> full oocytes showed a reduction in the density of transzonal projections, we were curious to study the importance of these structures for oocyte quality. Taking advantage of the above study indicating that oocyte MYO10 does not play an essential role in mouse oocyte development and female fertility, we suggest that granulosa cells contribute to oocyte quality through MYO10-dependent TZPs. In particular, we propose that cumulus cells negatively regulate a subset of oocyte transcripts to enhance the completion of meiotic maturation.*

*Note that in this article, granulosa cells are referred to as follicular cells. They are, however, the same cells*

# Cellular protrusions of the surrounding somatic cells shape the developmental potential of the oocyte

Flora Crozet<sup>1</sup>, Gaëlle Letort<sup>1</sup>, Christelle Da Silva<sup>1</sup>, Morgane Belle<sup>2</sup>, Adrien Eichmuller<sup>1</sup>, Dumont Julien<sup>1</sup>, Tristan Piolot<sup>1</sup>, Aurélien Dauphin<sup>3</sup>, Fanny Couplier<sup>4</sup>, Alain Chédotal<sup>2</sup>, Marie-Hélène Verlhac<sup>1</sup>, Hugh.J Clarke<sup>5</sup>, Marie-Emilie Terret<sup>1\*</sup>.

<sup>1</sup> Center for Interdisciplinary Research in Biology (CIRB), Collège de France, CNRS, INSERM, Université PSL, Paris, France.

<sup>2</sup> Institut de la Vision, CNRS, INSERM, Sorbonne Université, Paris, France.

<sup>3</sup> Institut Curie, CNRS, INSERM, Paris, France.

<sup>4</sup> Genomics core facility, Institut de Biologie de l'ENS (IBENS), Département de biologie, Ecole normale supérieure, CNRS, INSERM, Université PSL, Paris, France.

<sup>5</sup> Department of Obstetrics and Gynecology, McGill University, Montreal, Canada.

\* Correspondence should be addressed to M.E.T ([marie-emilie.terret@college-de-france.fr](mailto:marie-emilie.terret@college-de-france.fr)).

## Abstract

The oocyte must grow and mature prior to fertilization. The surrounding somatic cells support its growth by directing filopodia-like protrusions, termed transzonal projections (TZPs), to the oocyte membrane. To further investigate the contribution of these somatic protrusions to oocyte quality, we generated a full knockout mouse of the TZP structural component Myosin-X (MYO10). By spinning disk and super-resolution microscopies, we show that the lack of *Myo10* causes a significant decrease in TZP density prior to meiosis resumption. Using a machine learning approach to characterize oocyte morphology, we evidence that oocytes lacking somatic contacts manage to grow to canonical size but display subtle differences in oocyte-matrix interplay, arguing for a possible structural role of TZP within the germ-somatic

complex. Importantly, we reveal by transcriptomic analysis that TZP-deprived oocytes up-regulate a subset of transcripts at the end of growth. This correlates with a tendency for oocytes to arrest development in metaphase of first meiotic division. We herein propose that cellular protrusions of somatic cells modulate the expression of a subset of oocyte transcripts involved in oocyte maturation, thereby enhancing the developmental potential of the oocyte.

## Introduction

Female mammals are born with a non-renewable reserve of oocytes produced during embryogenesis. Postnatal oocytes are initially quiescent in the ovarian reserve and become competent for fertilization after undergoing a process of differentiation that lasts several months in women and about two to three weeks in mice (for review see El-Hayek and Clarke 2016). Oocyte differentiation begins with the exit from quiescence and entry into a growth phase characterized by significant morphological changes. The oocyte increases drastically in size and remodels its cytoplasm, storing a large supply of macromolecules necessary to complete its development and early embryogenesis (Fig.1 A). During growth, the oocyte remains arrested in prophase and gradually acquires the competence to resume meiosis (Sorensen and Wassarman 1976). Once fully grown, it further differentiates by undergoing meiotic maturation, a process consisting of two successive meiotic divisions (meiosis I and II) at the end of which the oocyte is haploid.

Fundamental for the production of a good quality embryo, the oocyte progressively acquires meiotic and developmental competence with the support of surrounding somatic cells, primarily follicular cells (for reviews see Kidder and Vanderhyden 2010, El-Hayek and Clarke 2016, Clarke 2018 and Alam and Miyano 2019). Together with the oocyte, the follicular cells form a germ-somatic complex termed ovarian follicle. The follicle also undergoes morphological changes during oocyte growth. It is classified as preantral or antral depending on growth progression and the appearance of the antrum, a fluid-filled chamber (Fig1. A). In antral follicles, the population of follicular cells that closely surround the oocyte forms an interactive subcomplex with the oocyte called the cumulus-oocyte complex (Fig1. A).

Important in shaping oocyte quality, bidirectional communication between the oocyte and follicular cells provides the oocyte with the right balance of inputs for optimal development (Kidder and Vanderhyden 2010, Clarke 2018, Alam and Miyano, 2019). While the oocyte communicates with its surroundings via secreted factors (Kidder and Vanderhyden 2010, Clarke 2018, Alam and Miyano 2019), somatic communication occurs mostly through cell-cell contacts mediated by cytoplasmic protrusions of follicular cells termed transzonal projections (TZPs) (Anderson and Albertini 1976, Baena and Terasaki 2019, for reviews see Albertini 2001 and Clarke

2018, Fig1. B). TZPs are filopodia-like actin-rich protrusions (El-Hayek 2018) that cross the *zona pellucida*, the extracellular matrix surrounding the oocyte, and make contact with the oocyte membrane at their tips. TZPs are characterized by intercellular signaling properties and their mediated communication allows follicular cells to metabolically support the oocyte and prevent early meiotic resumption (El-Hayek and Clarke 2016 and Clarke 2018). Notably, gap junctions located at the tips of TZPs (Anderson and Albertini 1976, Simon 1997, Fig.1 B) allow the exchange of small nutrients and signaling molecules with the oocyte. In addition, TZPs may provide structural support in the follicle by maintaining cohesion between the oocyte and follicular cells. This may be achieved through adherens junctions located at the interface between the TZP and the oocyte membrane (Mora 2012, Baena and Terasaki 2019, Fig.1 B).

While the involvement of TZPs in oocyte development as mediators of intercellular dialogue is increasingly well-understood, further studies on the exogenous regulation of oocyte quality by cell-cell contact are required for fundamental and applied purposes. In particular, this may provide further insight into the acquisition of oocyte developmental competence and increase the efficiency of assisted reproductive technologies. In this study, we sought to holistically characterize TZP contribution to oocyte development by impairing the entire TZP structure. As a candidate gene, we selected Myosin-X (MYO10), a structural component of TZPs (El-Hayek 2018, Fig.1 B) known to promote filopodia formation (Berg 2002, Bohil 2006, Heimsath 2017). We generated a complete knockout of *Myo10* in all cell types to completely deplete it from the ovarian follicle (*Myo10*<sup>-/-</sup> full). In addition, we took advantage of our previously generated mouse strain that is conditionally deleted for *Myo10* in oocytes (Crozet 2021, *Myo10*<sup>-/-</sup> oo) to distinguish phenotypes caused by loss of somatic MYO10 from those caused by loss of oocyte MYO10. We show that loss of somatic but not of oocyte MYO10 decreases the density of TZPs in fully grown cumulus-oocyte complexes. Surprisingly, oocytes deprived of TZPs develop to normal size at the end of growth. However, they display morphological differences compared to control oocytes, such as a more circular shape and a *zona pellucida* more uniformly detached from the oocyte. Importantly, they differentially express a subset of transcripts and this deregulation of gene expression correlates with a tendency of TZP-deprived oocytes to stop development in metaphase of the first meiotic division with a properly assembled spindle and correctly aligned chromosomes.

By reducing the density of TZPs through deletion of the gene encoding one of their structural components, we show that follicular cells, via their cytoplasmic protrusions, modulate the oocyte transcriptome at the end of growth. This transcriptomic remodeling prior to meiosis resumption may promote the completion of the meiotic divisions and consequently enhance oocyte ability to produce a viable embryo.

## Results

### Global deletion of *Myo10* decreases the density of transzonal projections in fully grown cumulus-oocyte complexes

To alter the integrity of TZPs, we generated mutant mice lacking the TZP component MYO10 in all cell types (Fig.S1 A-D). Complete loss of MYO10 in mice was previously characterized as semi-lethal, some animals dying during embryogenesis following exencephaly and some able to develop until adulthood (Heimsath 2017). Similar to this study, we obtained adult *Myo10*<sup>-/-</sup> mice (named *Myo10*<sup>-/-</sup> full thereafter) and most showed phenotypes characteristic of the earlier described *Myo10* full knockout, such as a white spot on the abdomen and webbed fingers (Heimsath 2017, Fig.S1 B). In addition to this strain, we used our previously generated mouse strain conditionally deleted of *Myo10* in oocytes (named *Myo10*<sup>-/-</sup> oo thereafter) as a control for oocyte-autonomous phenotypes (Crozet 2021, Fig.S1 A, D).

In follicles, MYO10 signal is diffuse in the cytoplasm of the oocyte and follicular cells (Crozet 2021, Fig.2 A) and accumulates in foci in the *zona pellucida* where TZPs are located (El-Hayek 2018, Fig.2 A, B). These foci were entirely lost in the *zona pellucida* of fully grown cumulus-oocyte complexes of *Myo10*<sup>-/-</sup> full mice (Fig.2 A, B, upper panels). Conversely, the density of these foci remained comparable to controls in *Myo10*<sup>-/-</sup> oo complexes lacking MYO10 only in the oocyte (Fig.2 A, B, lower panels). This suggests that the vast majority of MYO10 foci in the *zona pellucida* of control complexes originate from follicular cells.

Importantly, the loss of MYO10 foci in the *zona pellucida* of *Myo10*<sup>-/-</sup> full complexes correlated with a significant decrease in the density of phalloidin-labeled TZPs (Fig.2 A, B, upper panels). This decrease in cell-cell contacts was most apparent when imaging TZPs by super-resolution microscopy in *Myo10*<sup>-/-</sup> full oocytes cleared of follicular cells (Movie.S1 OMX; Fig.2 C STED). This reduction was not observed in *Myo10*<sup>-/-</sup> oo complexes (Fig.2 A, B, lower panels), implying that TZP density is related to the presence of MYO10 foci in the *zona pellucida*. Consistent with these observations in fixed cumulus-oocyte complexes, we also detected a significant decrease in TZP density in live, fully grown *Myo10*<sup>-/-</sup> full oocytes stained with SiR-actin (SiR-act) to label F-actin (Fig.2 D, E). To assess global TZP density, we measured the signal intensity of all SiR-act labeled TZPs in fully grown oocytes. This signal intensity

was fivefold lower in *Myo10*<sup>-/-</sup> full oocytes than in control oocytes (Fig.2 E, control =  $0.63 \pm 0.25$  and *Myo10*<sup>-/-</sup> full =  $0.13 \pm 0.06$ ). As a few TZPs are microtubule-rich in the ovarian follicle (Albertini 2001, El-Hayek 2018), we confirmed that loss of MYO10 not only decreases actin-rich TZPs but total TZP density by staining oocytes with the membrane probe FM 1-43 (Fig.S2). Conversely, TZP density remained similar to controls in live *Myo10*<sup>-/-</sup> oo oocytes labeled with SiR-actin (Fig.2 D, E, control =  $0.35 \pm 0.23$  and *Myo10*<sup>-/-</sup> oo =  $0.37 \pm 0.23$ ).

As previously reported, we confirmed that MYO10 is a structural component of TZPs (El-Hayek 2018), and show that it is essential for TZP formation and/or maintenance. By removing MYO10 from all cell types, and especially in follicular cells, we significantly reduced the density of TZPs in fully grown cumulus-oocyte complexes, i.e. the amount of somatic contacts between the oocyte and surrounding follicular cells. Importantly, *Myo10* deletion only in the oocyte does not alter TZP density, indicating that *Myo10*<sup>-/-</sup> oo oocytes retain a canonical amount of follicular cell contacts.

### **Decreased TZP-mediated contacts between the oocyte and follicular cells do not alter ovarian follicular organization**

Impaired intercellular communication between the oocyte and follicular cells in mice deficient in the gap junction subunit connexin 37 (Simon 1997) or deficient in the oocyte-secreted factor GDF9 (Dong 1996, Carabatsos 1998) led to ovaries with abnormal morphology, lacking fully grown follicles. We therefore tested whether decreasing TZP density altered the integrity of *Myo10*<sup>-/-</sup> full ovaries. To gain access to intra-ovarian organization, whole ovaries from adult mice were cleared as described in (Belle 2017). Like control ovaries, *Myo10*<sup>-/-</sup> full ovaries contained late antral follicles (Fig.3 A). However, *Myo10*<sup>-/-</sup> full mice showed a variation in the volume of their ovaries, which were either smaller or similar than controls (Movie.S2 A, B). Because of this variation, we assessed global ovarian integrity by measuring the follicular density of the ovary (counts of follicles normalized by ovarian area) rather than the absolute number of follicles per ovary. Interestingly, follicular density was not significantly different between control and *Myo10*<sup>-/-</sup> full ovaries (Fig.3 A, B control =  $4.86 \pm 0.68$  and *Myo10*<sup>-/-</sup> full =  $4.07 \pm 2.13$ ), indicating that the complete loss of MYO10 and subsequent reduction in TZP density do not alter global follicular organization in the ovary.

## Oocytes deprived of TZPs reach normal size at the end of growth but show morphological differences

To determine the TZP-mediated contribution of follicular cells to oocyte development, we assessed whether *Myo10*<sup>-/-</sup> full oocytes deprived of TZPs develop properly. As previously stated, we used *Myo10*<sup>-/-</sup> oo oocytes as controls for oocyte-autonomous phenotypes, as they lack MYO10 while retaining a canonical degree of somatic contacts. We first characterized the morphology of competent *Myo10*<sup>-/-</sup> full oocytes arrested in prophase of the first meiotic division (prophase I). Meiotic competence, defined as the ability of oocytes to resume meiosis at the end of growth, was based on the central position of the nucleus, a *zona pellucida* with a regular outer border and at least one point of detachment between the oocyte and the *zona pellucida*, i.e. a visible perivitelline space. Surprisingly, competent *Myo10*<sup>-/-</sup> full oocytes grew to normal size with a similar equatorial plane area as control oocytes (Fig.4 A, B control = 4254 ± 298.9 and *Myo10*<sup>-/-</sup> full = 4217 ± 289.3; Control = 4284 ± 317.2 and *Myo10*<sup>-/-</sup> oo = 4250 ± 269.4). Hence, reducing TZP density did not prevent oocytes from growing to a canonical size. This result contrasts with previous studies where the impairment of intercellular communication between the oocyte and follicular cells following deletion of connexin 37 or GDF9 (Simon 1997, Dong 1996, Carabatsos 1998) led to oocytes respectively smaller or larger than control oocytes. However, we found that the *zona pellucida* of competent *Myo10*<sup>-/-</sup> full oocytes was slightly thicker than that of controls (Fig.4 A, C control = 9.48 ± 0.41 and *Myo10*<sup>-/-</sup> full = 9.76 ± 0.37). This difference was not due to a role of oocyte-expressed MYO10 in the integrity of the *zona pellucida* as *Myo10*<sup>-/-</sup> oo oocytes displayed a *zona pellucida* of similar thickness to controls (Fig.4 A, C control = 9.43 ± 0.59 and *Myo10*<sup>-/-</sup> oo = 9.35 ± 0.49). Finally, we observed at a low frequency some follicular-like cells located ectopically in the perivitelline space of *Myo10*<sup>-/-</sup> full oocytes, a phenotype not observed in controls (Fig.S3 A).

To extend the morphological characterization of competent *Myo10*<sup>-/-</sup> full oocytes deprived of TZPs, we used our previously developed machine learning algorithm (Letort *in preparation*, Fig.4 D-G; S3 B-E). This approach allowed us to detect in an unbiased manner the morphological features that differed the most between control and *Myo10*<sup>-/-</sup> full oocytes. One of the most important features used by our algorithm to distinguish controls from *Myo10*<sup>-/-</sup> full oocytes was the presence of vertical TZP-like structures in the *zona pellucida* (Fig.4 D, E, F; S3 B, E). Intriguingly, these structures

were detected significantly more frequently in *Myo10*<sup>-/-</sup> full oocytes than in controls (Fig.4 F control =  $1.01 \pm 0.52$  and *Myo10*<sup>-/-</sup> full =  $1.60 \pm 0.67$ ; control =  $1.11 \pm 0.65$  and *Myo10*<sup>-/-</sup> oo =  $1.12 \pm 0.55$ ). As we have shown that total TZP density is decreased in *Myo10*<sup>-/-</sup> full oocytes, it is likely that this feature reflects an alteration in the structure of the remaining TZPs. It may also reveal a difference in the transparency of the *Myo10*<sup>-/-</sup> full *zona pellucida* which would make the remaining protrusions crossing it more apparent.

The distribution of the perivitelline space around the oocyte was a second important feature used by our algorithm and was detected to be more uniform in *Myo10*<sup>-/-</sup> full oocytes than in controls (Fig.4 D, G; S3 B, E). This was evidenced by a lower coefficient of variation of the perivitelline space thickness in *Myo10*<sup>-/-</sup> full oocytes compared to controls (Fig.4 G control =  $0.57 \pm 0.17$  and *Myo10*<sup>-/-</sup> full =  $0.41 \pm 0.15$ ). The coefficient of variation of the perivitelline space thickness was also lower in *Myo10*<sup>-/-</sup> oo oocytes than in controls, but to a lesser extent than in *Myo10*<sup>-/-</sup> full oocytes compared to their relative controls (Fig.4 G control =  $0.58 \pm 0.21$  and *Myo10*<sup>-/-</sup> oo =  $0.50 \pm 0.16$ ). Furthermore, our machine learning algorithm identified *Myo10*<sup>-/-</sup> full oocytes as more circular than control oocytes (Fig.4 D; S3 B, C, E), as indicated by a significantly lower aspect ratio in TZP-deprived oocytes (Fig.S3 C control =  $1.06 \pm 0.06$  and *Myo10*<sup>-/-</sup> full =  $1.04 \pm 0.03$ ; control =  $1.05 \pm 0.05$  and *Myo10*<sup>-/-</sup> oo =  $1.05 \pm 0.05$ ). In accordance with this feature, the perimeter of *Myo10*<sup>-/-</sup> full oocytes was slightly smaller than control oocytes for a similar area (Fig.S3 D control =  $234 \pm 8.44$  and *Myo10*<sup>-/-</sup> full =  $232 \pm 7.99$ ; control =  $233 \pm 8.98$  and *Myo10*<sup>-/-</sup> oo =  $233 \pm 9.27$ ).

Using manual and automatic approaches, we thus show that competent *Myo10*<sup>-/-</sup> full oocytes can reach normal size but display small morphological differences from control oocytes, such as a more circular shape and a larger *zona pellucida* more homogeneously detached from the oocyte. These differences may reflect a change in *zona pellucida* assembly or integrity following TZP depletion, which may account for easier detection of remaining TZPs and the possible looser adhesion between the oocyte and *zona pellucida* in *Myo10*<sup>-/-</sup> full oocytes.

### **Oocytes deprived of TZPs differentially express a subset of transcripts at the end of growth**

We next asked whether differences in the density of communicating structures between the oocyte and its follicular cells and in the morphology of the oocyte resulted

in an alteration of the developmental potential of the oocyte. During growth, the oocyte accumulates a substantial amount of transcripts. It becomes transcriptionally silent towards the end of growth (De La Fuente and Eppig 2001) and is transcriptionally inactive throughout the meiotic maturation process. Consequently, protein synthesis during the meiotic divisions relies predominantly on the translational regulation of transcripts accumulated during growth, making this storage critical for oocyte quality (for reviews see Clarke 2012, Conti and Franciosi 2018). Interestingly, follicular cells have been shown to modulate the chromatin configuration and thus global transcriptional activity of the oocyte during growth (De La Fuente and Eppig 2001, Luciano 2011). In addition, it was shown in bovine oocytes at least that some transcripts, such as mRNA and long non-coding RNA, are transferred from follicular cells to the oocyte via TZPs, potentially through extracellular vesicles (Macaulay 2014, Macaulay 2016, Fig.1 B). Since *Myo10*<sup>-/-</sup> full oocytes lack follicular cell contacts and potentially benefit less from exogenous transcriptional regulation, we tested whether their transcriptome differed from that of control oocytes.

By performing differential transcriptomic analysis by RNA-Seq between competent *Myo10*<sup>+/-</sup> and *Myo10*<sup>-/-</sup> full oocytes arrested in prophase I as done in (Almonacid 2019), we found that *Myo10*<sup>-/-</sup> full oocytes differentially expressed a subset of transcripts at the end of growth (Fig.5 A; S4 A; Table.1). Interestingly, the vast majority of these transcripts were up-regulated (605 of 685 or 88.3% of deregulated transcripts), implying that the reduction in TZP density led to either a higher transcription rate or increased stability of this subset of transcripts. Interestingly, the deregulated transcripts in TZP-depleted oocytes were primarily associated with Gene Ontology terms related to the metabolism of polyamine, RNA processing and RNA translation (Fig.5 B; S4. B, C; Table.1), with a nontrivial amount encoding for ribosomal proteins (Fig.5 C; Table.1). RT-qPCR analysis performed on competent *Myo10*<sup>+/-</sup> and *Myo10*<sup>-/-</sup> full oocytes arrested in prophase I validated the differential expression of some of the transcripts deregulated in the RNA-Seq analysis (Fig.5 C). Among them, *Myo10* mRNA was confirmed to be down-regulated in *Myo10*<sup>-/-</sup> full oocytes, validating both our RNA-Seq analysis and our genetic deletion tool. Other transcripts related to RNA translation (*Eif4e*, *Rps4x* and *Rpl19*) were also confirmed as differentially expressed by RT-qPCR in *Myo10*<sup>-/-</sup> full oocytes (Fig.5 C).

Since modulation of oocyte transcriptional activity by follicular cells has been associated with remodeling of chromatin configuration (De La Fuente and Eppig 2001,

Luciano 2011), we assessed whether deregulation of gene expression in *Myo10*<sup>-/-</sup> full oocytes correlated with a change in chromatin compaction. Incompetent and competent oocytes arrested in prophase I from antral follicles were stained with DAPI to label DNA (Fig.5 D). Interestingly, we observed no difference in chromatin compaction in incompetent and competent *Myo10*<sup>-/-</sup> full oocytes compared to control oocytes. Chromatin was correctly predominantly decondensed in the nucleoplasm of incompetent *Myo10*<sup>-/-</sup> full oocytes (Fig.5 D, left panels) and properly condensed around the nucleolus in competent oocytes (Fig.5 D, right panels), as in control oocytes at the same stage of development.

In addition, given that most of the deregulated transcripts in *Myo10*<sup>-/-</sup> full oocytes were up-regulated in our RNA-Seq analysis, we next tested whether this deregulation reflected a change in the global transcriptional rate of TZP-deprived oocytes. Incompetent and competent *Myo10*<sup>-/-</sup> full oocytes arrested in prophase I from antral follicles were incubated with the uridine analog 5-ethynyl uridine (EU) to label global RNA synthesis (Fig.5 D, E). Oocytes were also incubated without EU as a negative control. To measure global RNA synthesis, the signal intensity of EU was normalized to the DAPI signal intensity. Interestingly, global RNA synthesis was not different in incompetent and competent *Myo10*<sup>-/-</sup> full oocytes compared to control oocytes (Fig.5 E, for incompetent oocytes with EU control =  $0.39 \pm 0.21$  and *Myo10*<sup>-/-</sup> full =  $0.40 \pm 0.20$ ; for competent oocytes with EU control =  $0.05 \pm 0.03$  and *Myo10*<sup>-/-</sup> full =  $0.05 \pm 0.03$ ). In summary, we demonstrate here that the lack of somatic contacts caused by decreased TZP density does not affect oocyte chromatin configuration but leads to a non-global deregulation of oocyte gene expression at the end of growth.

### **TZP-deprived oocytes are prone to stop development in meiosis I**

We showed above that reduction of somatic contacts does not prevent oocytes from properly growing but modulates their transcriptome. Since oocytes depend on transcripts synthesized during growth to develop until fertilization (Clarke 2012 and Conti and Franciosi 2018), we tested whether TZP-deprived oocytes successfully undergo the developmental step following growth, namely the meiotic divisions. After nuclear envelope breakdown (NEBD), the oocyte experiences an asymmetric division in size and leads to a large cell, the oocyte, and a tiny cell, the polar body. This size difference is essential to keep the nutrients stored during growth in the prospective fertilized oocyte for embryogenesis (Kyogoku 2017). Importantly, we observed that

*Myo10*<sup>-/-</sup> full oocytes deprived of TZPs showed an increased frequency of developmental arrest at meiosis I, without extruding a polar body (Movie.S3; Fig.6 A, B, percentage of polar body extruding oocytes: control = 85.45% and *Myo10*<sup>-/-</sup> full = 61.70%). We previously showed that oocyte-expressed MYO10 is dispensable for oocyte meiotic divisions and female fertility (Crozet 2021), indicating that the meiotic arrest observed in a subset of *Myo10*<sup>-/-</sup> full oocytes is non-cell autonomous, but likely a consequence of decreased follicular cell contacts prior to meiosis resumption. By monitoring the progression of meiosis I by live spinning disk microscopy, we observed that the subpopulation of *Myo10*<sup>-/-</sup> full oocytes that extruded a polar body did so with a timing similar to controls (Movie.S3; Fig.6 A, C, timing of polar body extrusion after NEBD: control =  $8.91 \pm 0.95$  and *Myo10*<sup>-/-</sup> full =  $9.14 \pm 0.97$ ), indicating that complete loss of MYO10 and subsequent TZP depletion did not delay polar body extrusion in oocytes who did it. Therefore, oocytes deprived of TZPs have a lower developmental potential than oocytes that retain a canonical amount of follicular cell contacts, reinforcing the concept that surrounding somatic cells participate in the acquisition of oocyte developmental competence.

### **Oocytes deprived of TZP have well-formed and correctly positioned meiosis I spindles**

To gain insight into the origin of the meiotic arrest observed in some TZP-deprived oocytes, we first investigated whether the division spindles were correctly formed in *Myo10*<sup>-/-</sup> full oocytes. After NEBD, microtubules organize into a ball near the chromosomes that gradually bipolarizes to form a barrel-shape spindle (for review see Bennabi 2016). To assess spindle morphogenesis, oocytes were stained with SiR-tubulin (SiR-tub) to label microtubules and followed throughout meiotic maturation using spinning disk microscopy. We observed that in both *Myo10*<sup>-/-</sup> full oocytes that extruded a polar body and those that did not, meiosis I spindles bipolarized properly and within similar times as in control oocytes (Movie.S4; Fig.7 A-D). We assessed the timing of spindle bipolarization by the percentage of oocytes with a bipolarized spindle as a function of time after NEBD. For each meiosis I time point, the percentage of *Myo10*<sup>-/-</sup> full oocytes with a bipolarized spindle was not different from control oocytes (Fig.7 C). To further evaluate spindle morphogenesis in *Myo10*<sup>-/-</sup> full oocytes, we measured spindle interpolar length and central width 7 hours after NEBD once spindle morphogenesis is complete. *Myo10*<sup>-/-</sup> full spindles were slightly shorter and wider than

control spindles, but not significantly different (Fig.7 B, D, interpolar length control =  $34.05 \pm 4.48$  and *Myo10*<sup>-/-</sup> full =  $31.86 \pm 3.24$ , central width control =  $14.79 \pm 0.67$  and *Myo10*<sup>-/-</sup> full =  $15.34 \pm 1.07$ ). Importantly, by monitoring meiotic maturation using live spinning disk microscopy, we observed that *Myo10*<sup>-/-</sup> full oocytes that did not extrude a polar body arrested development in metaphase I, without experiencing anaphase (Movie.S4; Fig.7 A).

In addition to assessing spindle formation, we also examined meiosis I spindle positioning in *Myo10*<sup>-/-</sup> full oocytes. During meiosis I, the spindle first assembles in the center of the oocyte and then migrates to the cell cortex by a process involving F-actin, resulting in extreme oocyte asymmetric division in size (for review see Chaigne 2017). By live spinning disk microscopy, we monitored the positioning of SiR-tub labeled spindles throughout meiosis I and specifically examined their cell localization 30 minutes before anaphase for oocytes that extruded a polar body or up to 12 hours after NEBD for those that did not. We chose 12 hours after NEBD as a decisive time point to assess spindle positioning as some oocytes extrude a polar body up to this time in controls, and to avoid improper scoring of spindles that initially migrated to the cortex but relocated to the oocyte center, as can occur after abnormally long meiosis I without extrusion.

The percentage of *Myo10*<sup>-/-</sup> full oocytes with an off-centered spindle was not different from control oocytes (Movie.S4; Fig.7 A, E, percentage of oocytes with an off-centered spindle control = 90.00% and *Myo10*<sup>-/-</sup> full = 96.67%). In agreement with unaltered spindle positioning, we did not observe a defect in the organization of the F-actin cytoplasmic network mediating spindle migration in fixed *Myo10*<sup>-/-</sup> full oocytes labeled with phalloidin (Fig.S5 A-C). In mouse oocytes, F-actin is organized in a mesh in the cytoplasm, including an actin-cage that encloses the microtubule spindle (Azoury 2008, Schuh 2008, Bennabi 2020). The cytoplasmic F-actin mesh was correctly organized and the actin-cage properly shaped around the spindles in *Myo10*<sup>-/-</sup> full oocytes 6 hours after NEBD (Fig.S5 A, C). However, the signal intensity of cytoplasmic F-actin was slightly higher in *Myo10*<sup>-/-</sup> full oocytes compared to control oocytes (Fig.S5 A, B, control =  $0.76 \pm 0.08$  and *Myo10*<sup>-/-</sup> full =  $0.82 \pm 0.08$ ). This difference did not prevent spindles from migrating to the oocyte cortex. These results refine our understanding of the meiotic arrest of some *Myo10*<sup>-/-</sup> full oocytes by showing that they arrest in metaphase I with a normally assembled and positioned spindle.

### **Oocytes deprived of TZP have correctly aligned metaphase I chromosomes**

Since severe chromosome misalignment could prevent anaphase onset by sustaining the spindle assembly checkpoint in mouse oocytes (for review see Mihajlović and FitzHarris 2018), we assessed chromosome alignment in *Myo10*<sup>-/-</sup> full oocytes deprived of TZPs. Oocytes were injected with H2B-GFP to label chromosomes and chromosome alignment was monitored during meiosis I by spinning disk microscopy (Movie.S5; Fig.7 F, G). Interestingly, metaphase I chromosomes were aligned on the metaphase plate similarly to controls in *Myo10*<sup>-/-</sup> full oocytes, as evidenced by a metaphase plate height not significantly different from controls 30 minutes before anaphase for oocytes that extruded a polar body or 12 hours after NEBD for those that did not (Fig.7 G left, metaphase plate height control =  $11.03 \pm 1.61$  and *Myo10*<sup>-/-</sup> full =  $11.41 \pm 1.71$ ). The width of the metaphase plate was wider in *Myo10*<sup>-/-</sup> full oocytes than in controls, in agreement with the fact that spindles are slightly wider in TZP-deprived oocytes, as indicated above (Fig.7 G right, metaphase plate width control =  $16.28 \pm 0.79$  and *Myo10*<sup>-/-</sup> full =  $16.87 \pm 0.71$ ). Therefore, the metaphase I arrest of some *Myo10*<sup>-/-</sup> full oocytes is not caused by severe chromosome misalignment. Its origin remains to be further investigated.

## Discussion

In this study, we aimed to gain more insight into the contribution of cellular protrusions established by surrounding somatic cells to postnatal oocyte development. By genetically deleting the transzonal projection component MYO10 in all murine cell types, including follicular cells, we drastically reduced the density of oocyte-follicular cell contacts in the cumulus-oocyte complex and assessed resulting oocyte development.

Interestingly, although complete loss of MYO10 decreased by fivefold TZP density in fully grown oocytes, a small fraction of TZPs remained. This implies that a subpopulation of TZPs may be MYO10-independent or that the remaining TZPs found alternative means to form or be maintained in a MYO10-free context. The remaining TZPs in *Myo10*<sup>-/-</sup> full follicles may explain how oocytes surprisingly managed to grow to canonical size despite likely reduced intercellular communication, and maintain the meiotic arrest in prophase I. It is noteworthy that the lack of gap junctional communication between the oocyte and follicular cells in mice deficient in Connexin 37, the major connexin located at the oocyte-somatic interface (Simon 1997, Veitch 2004), led to smaller oocytes that did not achieve meiotic competence (Simon 1997). We can therefore assume that functional gap junctions are located at the tip of the remaining TZPs in *Myo10*<sup>-/-</sup> full oocytes, with a sufficient threshold amount to maintain the supply of nutrients and signaling molecules required for oocyte growth and maintain the oocytes arrested in prophase I.

It is also possible that the nutrients and other molecules delivered via the remaining gap junctions alone are not sufficient for ensuring the growth of the TZP-deprived oocyte and that the oocyte initiates increased nutrient uptake from the follicular cells by modulating its factor secretion. Indeed, the oocyte influences follicular cell differentiation via the secretion of paracrine factors, such as GDF9, for timely and optimal exogenous inputs (Kidder and Vanderhyden 2010, Clarke 2018, Alam and Miyano 2019). Mice deficient in GDF9 produce larger oocytes than controls despite reduced TZP density (Dong 1996, Carabatsos 1998), possibly because GDF9 negatively regulates expression of the paracrine factor Kit ligand by follicular cells which promotes oocyte growth (Elvin 1999). We can therefore speculate that TZP-deprived oocytes secrete factors at different rates than control oocytes to compensate for the reduction in cell-cell contacts, thereby modulating nutrient uptake, secretion of

paracrine factors, or potentially extracellular vesicle release from the follicular cells to the oocyte (Macaulay 2014, Macaulay 2016).

In favor of increased nutrient uptake by the oocyte, it is possible that the remaining TZPs in *Myo10*<sup>-/-</sup> full oocytes display a higher content of organelles than in controls, potentially providing increased energy supply for the oocyte. Of note, the remaining TZPs in mice deficient in GDF9 were large and organelle-rich (Carabatsos 1998, Albertini 2001). In our case, this assumption is supported by the fact that our machine learning algorithm more readily detected TZPs in *Myo10*<sup>-/-</sup> full oocytes than in controls, potentially indicating a difference in TZP structure and, speculatively, in TZP organelle content. Hence, TZP-deprived oocytes may have developed to normal size by the remaining TZPs, with or without increased nutrient uptake by the oocyte. It is also possible that paracrine factors or extracellular vesicles not mediated by TZPs, but directly released from follicular cell bodies and traversing the *zona pellucida*, ensured proper oocyte growth in a context of reduced oocyte-follicular cell contacts.

Even though TZP-deprived oocytes grew to normal size, we identified small morphological differences, mostly related to the integrity of the *zona pellucida*. The *zona pellucida*, which is the extracellular matrix surrounding the oocyte, is composed of proteins secreted by the oocyte throughout growth and assembled in cross-linked filaments (for review see Wassarman and Litscher 2018). We found that oocytes lacking TZPs had a thicker *zona pellucida* than oocytes that retained a canonical number of somatic contacts. This is reminiscent of the Embryonic poly(A)-binding protein EPAB-deficient mice that display oocytes with fewer TZPs and a thicker *zona pellucida* than controls (Lowther 2017). Although these oocytes had other developmental defects not linked to TZP depletion, it is interesting to observe a similar difference in *zona pellucida* thickness in a context of reduced oocyte-follicular cell contacts.

Using our machine learning algorithm to morphologically characterize *Myo10*<sup>-/-</sup> full oocytes, we identified additional *zona pellucida* features that differ from control oocytes. Notably, detachment of the *zona pellucida* from the oocyte was detected as more homogeneous in TZP-deprived oocytes than in controls. It is likely that reduction in TZP density, and consequently the decrease in adherens junctions between the oocyte and follicular cells (Mora 2012, Baena and Terasaki 2019), led to this apparent looser oocyte-matrix adhesion. As previously mentioned, our machine learning algorithm detected TZP-like structures more readily in *Myo10*<sup>-/-</sup> full oocytes than in

controls, despite their decrease in TZP density. In addition to a difference in the remaining TZP structure, this may also indicate a more transparent *zona pellucida*. All these features taken together may reflect impaired assembly or maintenance of the *zona pellucida* in oocytes with reduced cell-cell contacts. In support of this, we occasionally observed some follicular-like cells in the perivitelline space of TZP-deprived oocytes. The same ectopic localization was observed in GDF9-deficient mice, which also displayed oocytes with reduced TZP density, and such abnormal localization of follicular cells was correlated with low oocyte viability (Carabatsos 1998). Interestingly, the presence of follicular-like cells in the perivitelline space has been observed in mice lacking ZP1 (Rankin 1999), the secreted *zona pellucida* protein that mediates the cross-linking of the matrix filaments (Wassarman and Litscher 2018). It is therefore worth considering that TZPs may be involved in *zona pellucida* integrity by modulating matrix filament cross-linking. TZPs may also indirectly affect *zona pellucida* integrity by enhancing oocyte quality through TZP-mediated communication, thereby coordinating the secretion of *zona pellucida* proteins by the oocyte.

Importantly, in addition to these discrete morphological differences, TZP-deprived oocytes have lower developmental competence than control oocytes, as they more frequently arrest at metaphase of the first meiotic division. Consistent with our results, a decrease in oocyte developmental potential correlated with reduced TZP density was also observed in oocytes lacking the focal adhesion kinase Proline-rich tyrosine kinase 2 (McGinnis and Kinsey 2015). In that case, reduced oocyte-follicular cell contacts were associated with impaired early embryogenesis and lower female fertility. In *Myo10*<sup>-/-</sup> full oocytes, the basis of the meiotic arrest observed in a subpopulation of oocytes remains to be deciphered. This developmental arrest may be the readout of the altered oocyte transcriptome since we revealed by RNA-Seq analysis that TZP-depleted oocytes differentially express a subset of transcripts prior to meiosis resumption. As oocytes undergo meiotic divisions relying on transcripts synthesized and stored during growth (Clarke 2012, Conti and Franciosi 2018), an impairment in this storage could lead to an altered proteome and compromise oocyte quality.

In addition to this unbalanced representation of a transcript subset, the proteome of *Myo10*<sup>-/-</sup> full oocytes could have been further altered as some of the deregulated transcripts in TZP-deprived oocytes encode proteins associated with RNA translation, such as ribosomal proteins and proteins involved in polyamine metabolism.

Polyamines are small polycationic molecules involved in protein synthesis (for review see Dever and Ivanov 2018). Deregulated expression of proteins critical for polyamine metabolism could in principle lead to variation in RNA translation. Additionally, in favor of an altered proteome driving the meiotic arrest observed in some TZP-deprived oocyte, follicular cells have been shown to regulate the translation of a subset of oocyte mRNAs important for developmental competence through activation of the PI(3)K-AKT-mTOR pathway in the oocyte (Chen 2013). It is therefore possible that reduction in TZP density prior to meiosis resumption led to an alteration in both synthesis/stability and translation of mRNAs coding for key proteins involved in the progression of meiotic divisions. Cyclin B1 is a candidate protein worthy of consideration, because we confirmed its mRNA to be up-regulated by RNA-Seq and RT-qPCR analysis in oocytes deprived of TZPs. It is possible that this transcriptomic deregulation led to a higher level of Cyclin B1 protein throughout meiosis I, which potentially sustained the activity of the maturation-promoting factor and inhibited the onset of anaphase in some TZP-deprived oocytes (Ledan 2001, Herbert 2003, for review see Li 2019).

In addition to an altered proteome, an aberrant level of reactive oxygen species (ROS) in the oocyte could have led to the meiotic arrest observed in some TZP-deprived oocytes. Indeed, among the deregulated transcripts, some encode proteins involved in the cellular response to ROS, in particular in response to hydrogen peroxide. Notably, aldo-keto reductase family 1, member B3 (*Akr1b3*) and oxidative stress responsive serine rich 1 (*Oser1*) are the most deregulated transcripts in our RNA-Seq analysis based on P adj. The deregulation of these transcripts may reflect an abnormal ROS amount in TZP-deprived oocytes, which could impair oocyte quality (for review see Lin and Wang 2020). As follicular cells are known to modulate the oocyte content of ROS, notably through the supply of antioxidants (Lin and Wang 2020), it is possible that decreased TZP density led to oxidative stress in the oocyte, impairing oocyte development.

In conclusion, we have shown that cytoplasmic protrusions of surrounding somatic cells enhance the developmental potential of the oocyte. Consistent with others studies, we suggest that TZP contribute to oocyte-matrix adhesion, playing a structural role in the ovarian follicle. In addition, we propose a novel role for TZPs as modulators, mostly repressors, of the synthesis/stability of specific transcripts at the end of growth that are required for successful meiotic divisions. Interestingly, as the density of TZPs decreases with maternal age (El-Hayek 2018), investigating their

contribution to oocyte quality could be of great benefit to further unraveling female fertility, which decreases with maternal age. This may be of particular interest to increase the efficiency of assisted reproductive technologies. More broadly, our results may be valuable for the comprehension of other cellular models relying on cell-cell contact communication to function (for review see Yamashita 2018). It may notably provide clues as to how cellular development is modulated by exogenous regulation of gene expression through direct intercellular dialogue.

## Material and methods

### Mouse strain generation and genotyping

To generate *Myo10<sup>wt/flox</sup>* mice, two *loxP* sites flanking *Myo10* exons 23-25 and an FRT-flanked neomycin selection cassette located between *Myo10* exons 22 and 23 were inserted in the genome of C57BL/6 mice by genOway. Mice were then mated with *Zp3-Cre* mice already housed in the laboratory.

To obtain *Myo10* full knockout mice (*Myo10<sup>-/-</sup>* full), the neomycin selection cassette was retained to allow its promoter to interfere with *Myo10* expression independently of Cre expression (Pham 1996, Fig.S1 A). We used the following primers to detect the presence of the neomycin selection cassette at the *Myo10* locus: 5'-ACA GCC CAT ATC ACT GTC TAG AGA CCC ATT-3', 5'-ATC GCC TTC TAT CGC CTT GAC G-3' and 5'-GAG GAT CCA GAC TTG GAC CCG GTC-3'.

Mice conditionally deleted for *Myo10* in oocytes (*Myo10<sup>-/-</sup>* oo mice) were previously generated from the above strain by removing the neomycin selection cassette after mating with *FLPo* mice (Crozet 2021, Fig.S1A). To detect Cre-mediated excision at the *Myo10* locus after removing of the neomycin selection cassette, the following PCR primers were used: for the *Cre*, 5'-GCG GTC TGG CAG TAA AAA CTA TC-3' and 5'-GTG AAA CAG CAT TGC TGT CAC TT-3'; and for the *Myo10*, 5'-ACC CCA GTA CTT GTT CAT ACA TCC TAT ATC CTA CA-3', 5'-GAC TAC ACC ATT CTG AAT GTG CCT GAT CTC-3' and 5'-GAG TAT CTG CCA TCT TGT CCC TAA AGG TGG-3'.

For the *Myo10* full knockout strain, we used *Myo10<sup>wt/wt</sup>; Cre<sup>+</sup>*, *Myo10<sup>wt/flox</sup>; Cre<sup>+</sup>*, *Myo10<sup>wt/Δ</sup>; Cre<sup>+</sup>*, *Myo10<sup>wt/flox</sup>; Cre<sup>-</sup>* as control mice and *Myo10<sup>flox/flox</sup>; Cre<sup>+</sup>*, *Myo10<sup>flox/Δ</sup>; Cre<sup>+</sup>*, *Myo10<sup>flox/flox</sup>; Cre<sup>-</sup>* as *Myo10<sup>-/-</sup>* full mice. For the *Myo10* oocyte knockout strain, we used *Myo10<sup>wt/flox</sup>; Cre<sup>+</sup>*, *Myo10<sup>wt/flox</sup>; Cre<sup>-</sup>*, *Myo10<sup>flox/flox</sup>; Cre<sup>-</sup>* as control mice and *Myo10<sup>flox/flox</sup>; Cre<sup>+</sup>* as *Myo10<sup>-/-</sup>* oo mice.

### Immunoblotting

Immunoblotting was performed as in Heimsath 2017 on extracts from *Myo10<sup>wt/flox</sup>; Cre<sup>+</sup>*, *Myo10<sup>flox/flox</sup>; Cre<sup>+</sup>* and *Myo10<sup>flox/flox</sup>; Cre<sup>-</sup>* mice from the *Myo10* full knockout strain. Whole liver, whole spleen and one kidney per mouse were extracted, weighed and immediately added to 1X Laemmli sample buffer (50 mM Tris, pH 7.4, 2% SDS, 6% glycerol, 0.1 M DTT and 0.25% bromophenol blue) at 1 mL/20 mg wet tissue weight

and boiled for 15 min. Samples were crushed with a glass potter to dissociate the tissue and the lysates were centrifuged at 20,000 rpm for 30 min at room temperature. The pellets were discarded and the supernatants were stored at -80°C. Final loading volumes were adjusted for immunoblot based on quantification of the actin band from preliminary tests, so that the same protein amount is deposited in all the wells. Samples were boiled 1 min and subjected to SDS-PAGE using a 4-15% Mini-PROTEAN TGX Stain-Free Protein Gel (Bio-Rad Ref. 4568085). After SDS-PAGE, lysates were transferred to Immobilon-P PVDF Membrane (Sigma-Aldrich Ref. IPVH00010) at room temperature in transfer buffer (25 mM Tris, 192 mM Glycine, 0.3% SDS and 20% methanol) using a Trans-Blot SD Semi-Dry Transfer Cell (Bio-Rad) set at 100 mA constant power with a volt limit of 25 V for 45 min. Prior to transfer, the PVDF membrane was wetted in methanol, rinsed in distilled water and equilibrated 10 min in transfer buffer. After the transfer, the membrane was washed in 50 mM Tris, 150 mM NaCl, 0.05% Tween 20 (TBST thereafter) and blocked for 1h in TBST containing 5% dried milk powder. The membrane was washed in TBST and incubated for 1h in TBST containing 4% dried milk and rabbit anti-MYO10 (1:300, Sigma-Aldrich Ref. HPA024223) as primary antibodies. The membrane was washed in TBST, blocked for 1h in TBST containing 5% dried milk powder, rinsed in TBST and incubated for 45 min in TBST containing 4% dried milk and donkey anti-rabbit IgG HRP-linked (1:10000, Amersham Ref. NA934) as secondary antibodies. The membrane was washed in TBST and incubated 5 min in SuperSignal West Femto Maximum Sensitivity Substrate (Thermo Fisher Scientific Ref. 34095). Protein expression was revealed using a chemiluminescence Image Analyzer (FUSION FX; Vilber, 20 sec illumination). The membrane was then rinsed in TBST and stripped 10 min in Restore Western Blot Stripping Buffer (Life Technology Ref. 21059). The membrane was washed in TBST and incubated for 45 min in TBST containing 4% dried milk and HRP mouse anti-beta Actin AC-15 (1:25000, abcam Ref. ab49900). The membrane was washed in TBST and incubated 1 min in ECL Western Blotting Substrate (Thermo Fisher Scientific Ref. 32109). Protein expression was revealed using a chemiluminescence Image Analyzer (FUSION FX; Vilber, 20 sec illumination).

### **Whole ovary immunostaining and clearing**

Ovaries collected from two control mice (*Myo10*<sup>wt/flox</sup>; *Cre*<sup>+</sup>, 9 and 12 weeks old) and two *Myo10*<sup>-/-</sup> full mice (*Myo10*<sup>flox/flox</sup>; *Cre*<sup>+</sup>, 9 and 12 weeks old) were fixed in 1X PBS,

4% paraformaldehyde for 4h with agitation at room temperature and subsequently washed in 1X PBS where they were stored at 4°C. Bleaching, immunostaining and clearing were performed as in Belle 2017. Ovaries were first dehydrated in increasing concentrations of methanol (1X PBS, methanol 50%, 80% and 100% methanol twice) for 1h each time with agitation at room temperature. Ovaries were then bleached in 100% methanol + 6% hydrogen peroxide overnight at 4°C and rehydrated in decreasing concentrations of methanol (100% twice, 1X PBS, methanol 80% and 50%) for 1h each time with agitation at room temperature. Ovaries were blocked and permeabilized in 1X PBS, 0.2% gelatin, 0.5% Triton X-100 (PBSGT thereafter) for 4 days with rotation at room temperature. Antibody incubations were performed in PBSGT + 10X saponin (10 mg/mL) at 37°C with rotation at 70 rpm for one week for primary antibodies and overnight for secondary antibodies. Washes between antibody incubations and after secondary antibody incubation were done in PBSGT for 1day with rotation at room temperature. We used rabbit anti-MYO10 (1:1000, Sigma-Aldrich Ref. HPA024223) and rat anti-MECA-32 (1:500, BD Pharmingen Ref. 550563, data not shown) as primary antibodies and Cy3-conjugated donkey anti-rabbit IgG (1:500, Jackson Immuno research Ref. 711-165-152) and Alexa Fluor 790-conjugated donkey anti-rat IgG (1:250, Jackson Immuno research Ref. 712-655-153) as secondary antibodies (data not shown). Incubation with TO-PRO-3 (1: 100, ThermoFisher Scientific Ref. T3605) was performed along with secondary antibody incubation to stain nucleic acid. Ovaries were embedded in 1X TAE, 1.5 % agarose and cleared using an adapted 3DISCO clearing protocol with rotation at 12 rpm and protected from light at room temperature. Ovaries were dehydrated in H<sub>2</sub>O, 50% tetrahydrofuran (THF anhydrous with 250 ppm butylated hydroxytoluene inhibitor, Sigma-Aldrich Ref.186562) overnight and in H<sub>2</sub>O, 80% THF and 100% THF twice for 1 h 30 each time. Ovaries were then incubated in dichloromethane (DCM - Sigma-Aldrich Ref.270997) for 30 min for delipidation and cleared overnight in benzyl ether (DBE - Sigma-Aldrich Ref.108014).

### **Follicle/oocyte collection and culture**

Preantral follicles, cumulus-oocyte complexes and oocytes isolated from antral follicles were collected from 2- to 5-month-old mice in M2 + BSA medium supplemented with 1µM milrinone (Reis 2006) to maintain oocytes arrested in prophase I. Oocytes from late antral follicles were manually released from follicular cells by repeated pipette

aspirations. Meiosis resumption was induced by transferring oocytes to M2 + BSA medium free of milrinone. Culture and live imaging were performed at 37°C under oil. To assess the rate of polar body extrusion, oocytes were cultured overnight in M2 + BSA medium in a Heracell 150i CO<sub>2</sub> Incubator (Thermo Fisher Scientific) and analyzed the next day for polar body extrusion.

### **Fluorescent probes for live imaging**

Oocytes were incubated for 1 h in M2 + BSA, milrinone medium supplemented with 100 nM SiR-actin (Spirochrome Ref. SC006) to label F-actin, 5 µg/mL FM 1-43 (Thermo Fisher Scientific Ref. T35356) to label membranes or 100 nM SiR-DNA (Spirochrome Ref. SC007) to label DNA. Oocytes were incubated in M2 + BSA medium supplemented with 100 nM SiR-tubulin (Spirochrome Ref. SC006) at least 1 h before the start of spinning disk movies and throughout movie acquisitions to label microtubules.

### ***In vitro* cRNA synthesis and oocyte microinjection**

The pRN3-Histone(H2B)-GFP plasmid (Manil-Ségalen 2018) was linearized with SfiI restriction enzyme and *in vitro* transcribed using the mMACHINE T3 Transcription Kit (Ambion Ref. AM1348). cRNAs were purified using the RNeasy Mini Kit (QIAGEN Ref. 74104), centrifuged at 4°C and microinjected into prophase I arrested oocytes with a FemtoJet microinjector (Eppendorf). Oocytes were maintained in prophase I for 2 h to express cRNAs before meiosis resumption.

### **Immunostaining and global transcription detection**

Preantral follicles, cumulus-oocyte complexes and oocytes isolated from antral follicles were immunostained as in Crozet 2021. Incorporation and detection of 5-ethynyl uridine (EU) into nascent oocyte RNAs were performed similarly to Almonacid 2019. For all protocols, follicles, complexes and oocytes were washed in M2 + PVP medium and adhered to gelatin and polylysine-coated coverslips before fixation.

#### **- Phalloidin labeling of transzonal projections**

Preantral follicles and cumulus-oocyte complexes were fixed and permeabilized in 1X PBS, HEPES (100 mM, pH 7), EGTA (50 mM, pH 7), MgSO<sub>4</sub> (10 mM) buffer with 2% Triton X-100 and 0.3% formaldehyde for 30 min at 37°C. Follicles and complexes were then washed in 1X PBS where they were stored overnight or 2 days at 4°C. Follicles

and complexes were further permeabilized in 1X PBS, 0.5% Triton X-100 for 10 min and washed in 1X PBS and 1X PBS, 0.1% TWEEN 20 (PBSTw thereafter). Blocking and antibody incubations were performed in PBSTw, 3% BSA at room temperature for 30 min for blocking, 1 h 30 for primary antibody incubation and 1h for secondary antibody incubation. Washes between antibody incubations and after secondary antibody incubation were done in PBSTw at room temperature and an additional wash in 1X PBS was performed before mounting. For spinning disk and OMX microscopies, follicles and complexes were mounted on slide wells filled with VECTASHIELD Antifade Mounting Medium with DAPI (for *Myo10* oocyte knockout strain, data not shown) or without DAPI (for *Myo10* full knockout mice) (Vector Laboratories Ref. H-1200 and H-1000). We used rabbit anti-MYO10 (1:200, Sigma-Aldrich Ref. HPA024223) as primary antibodies and Cy3-conjugated donkey anti-rabbit IgG (1:150, Jackson ImmunoResearch Ref. 711-165-152) as secondary antibodies. Incubation with Alexa Fluor 488-conjugated Phalloidin (10 U/mL, Thermo Fisher Scientific Ref. A12379) was performed concurrently with secondary antibody incubation to stain F-actin. For STED microscopy, follicles and complexes were mounted on slide wells filled with Abberior liquid antifade mounting medium (Ref. MM-2009). We used rabbit anti-MYO10 (1:200, Sigma-Aldrich Ref. HPA024223) as primary antibodies and Abberior STAR 580-conjugated anti-rabbit (1:200, Ref. ST580-1002) as secondary antibodies. Incubation of Abberior STAR RED-conjugated Phalloidin (1:200, Ref. STRED-0100) was performed with secondary antibody incubation to stain F-actin.

- Phalloidin labeling of oocyte cytoplasmic F-actin

Oocytes isolated from antral follicles were cleared of the *zona pellucida* in acid Tyrode 1 h – 1 h 30 before fixation. Immunostaining was performed using a modified protocol from Schuh 2008. Oocytes were fixed and permeabilized 6 h after NEBD in 1X PBS, HEPES (100 mM, pH 7), EGTA (50 mM, pH 7), MgSO<sub>4</sub> (10 mM) buffer with 0.2% Triton X-100 and 2% formaldehyde for 30 min at 37°C. Oocytes were then washed in 1X PBS, 0.1% Triton X-100 (PBSTr thereafter) where they were stored overnight at 4°C. The remaining immunostaining protocol is similar to that for phalloidin TZP labeling for spinning disk and OMX microscopies, except that oocytes were directly blocked the day after fixation and blocking and antibody incubations were performed in PBSTr, 3% BSA. Oocytes were mounted on slide wells filled with VECTASHIELD Antifade Mounting Medium with DAPI (Vector Laboratories Ref. H-1200, data not shown). We used mouse anti- $\alpha$ -Tubulin (1:200, Sigma-Aldrich Ref. T8203) as primary antibodies

and Cy3-conjugated donkey anti-mouse IgG (1:150, Jackson ImmunoResearch Ref. 715-165-151) as secondary antibodies. Incubation with Alexa Fluor 488-conjugated Phalloidin (10 U/mL, Thermo Fisher Scientific Ref. A12379) was performed along with secondary antibody incubation.

- EU labeling of nascent oocyte RNAs

As in Almonacid 2019, oocytes arrested in prophase I isolated from antral follicles were cleared of the *zona pellucida* in M2 + BSA, milrinone medium with 0.4% pronase. EU incorporation and detection were performed using the Click-iT RNA Alexa Fluor 488 Imaging Kit (Thermo Fisher Scientific Ref. C10329). Oocytes were incubated in M2 + BSA, milrinone medium with or without 0.5 mM EU for 3 h at 37°C and fixed in 1X PBS, 4% paraformaldehyde for 30 min at 37°C. Oocytes were subsequently washed in 1X PBS where they were stored overnight at 4°C. Oocyte permeabilization and washes were done at room temperature in 1X PBS, 0.5% Triton X-100 for 10 min and in 1X PBS, respectively. EU detection was performed as indicated by the manufacturer and oocytes were then washed twice in Click-iT reaction rinse buffer and mounted on slide wells filled with VECTASHIELD Antifade Mounting Medium with DAPI (Vector Laboratories Ref. H-1200).

## **Imaging**

- *Spinning disk microscopy*: Images were acquired with a Plan-APO 40x/1.25 NA objective on a Leica DMI6000B microscope enclosed in a thermostatic chamber (Life Imaging Service) equipped with a Retiga 3 CCD camera (QImaging) coupled to a Sutter filter wheel (Roper Scientific) and a Yokogawa CSU-X1-M1 spinning disk. Data were collected with Metamorph software (Universal Imaging).

- *STED microscopy*: STED imaging was performed with a STEDYCON add-on module mounted on a Zeiss AxioObserver 7 inverted-Videomicroscope coupled to a sCMOS camera (Hamamatsu Flash 4) and a PlanAPO 100x oil-immersion objective (NA = 1.46) for an effective pixel size of 50 nm (Zeiss).

- *OMX microscopy*: For super resolution imaging, structured illumination (3D-SIM) was performed using a DeltaVision OMX Blaze microscope (GE Healthcare) coupled to a Photometrics Evolve 512 EMMCD camera (Photometrics, Tucson, AZ) and a PlanAPO 60x oil-immersion objective (NA = 1.4) for an effective pixel size of 80 nm and 40 nm after reconstruction (Olympus, Melville, NY).

- *Light-sheet fluorescence microscopy*: The cleared samples are acquired with the ultramicroscope I (LaVision BioTec-Miltenyi) assisted by the InspectorPro software (LaVision BioTec-Miltenyi). The light sheet is created by two cylindrical lenses using laser with 3 specific wavelengths: 561nm, 640nm and 785nm (Coherent Sapphire Laser, LaVision BioTec-Miltenyi). For all the acquisitions we used a binocular stereomicroscope (MXV10, Olympus) with a 2x objective (MVPLAPO, Olympus) adding a protective dipping cap with corrective lens. For detection we used a Zyla SCMOS camera (2,048 × 2,048 pixel) from Andor Oxford Instrument. The images were in 16-bit. We used for zoom magnification 3.2X (pixel sizes x,y=1.02um). Samples were dived in a quartz tank (LaVision BioTec-Miltenyi) filled with DBE to maintain the clearing. The z step size between each image was 1µm with 150ms time exposure.

### **Oocyte RNA extraction**

Total RNA extraction was performed as in Crozet 2021 from competent oocytes with *zona pellucida*. For the RNA-Seq analysis, three biological replicates were performed each containing 10 oocytes from two *Myo10<sup>flox/flox</sup>; Cre<sup>+</sup>* mice (*Myo10<sup>-/-</sup>* full oocytes) and two *Myo10<sup>wt/flox</sup>; Cre<sup>+</sup>* (*Myo10<sup>+/-</sup>* oocytes). For the RT-qPCR analysis, two biological replicates were made containing 30 and 24 oocytes from two *Myo10<sup>flox/flox</sup>; Cre<sup>-</sup>* mice (*Myo10<sup>-/-</sup>* full oocytes) and two *Myo10<sup>wt/flox</sup>; Cre<sup>+</sup>* (*Myo10<sup>+/-</sup>* oocytes). Total RNA extraction was performed using the RNAqueous-Micro Total RNA Isolation Kit (Thermo Fisher Scientific Ref. AM1931). Briefly, oocytes were washed three times in 1X PBS, transferred to lysis buffer (supplemented with 1 µL β-mercaptoethanol for the RNA-Seq analysis) and freezed in liquid nitrogen where they were stored at -80°C for 1 h. After thawing, RNA extraction was performed as described by the manufacturer. RNAs were eluted twice in 10 µL elution buffer and treated with DNaseI.

### **RNA-Seq and data analysis**

- *cDNA libraries and RNA-Seq*: Library preparation and Illumina sequencing were performed at the Ecole normale superieure genomic core facility (Paris, France). 5 ng of total RNA was amplified and converted to cDNA using the SMART-Seq v4 Ultra Low Input RNA kit (Clontech Ref. 634889). Afterwards, an average of 500 pg of amplified cDNA was used to prepare the libraries following Nextera XT DNA kit (Illumina Ref. FC-131-1096). Libraries were multiplexed by 6 on a high-output flow cells. A 75 bp

read sequencing was performed on a NextSeq 500 device (Illumina). A mean of  $26 \pm 4$  million passing Illumina quality filter reads was obtained for each of the 6 samples.

- *Bioinformatics analysis*: The analysis was performed using the Galaxy server of ARTbio bioinformatics platform. All galaxy workflows are available at [https://github.com/ARTbio/tools-artbio/tree/master/scripts/Crozet\\_et\\_al\\_2021/galaxy-workflows](https://github.com/ARTbio/tools-artbio/tree/master/scripts/Crozet_et_al_2021/galaxy-workflows). Sequencing quality control was carried out with FastQC (Babraham Bioinformatics) (Galaxy Version v0.72+galaxy1) and MultiQC tools (v1.6). Alignment of reads to the genome of *Mus musculus* mm10 reference genome was done with Bowtie 2 (v2.3.4.2) (Langmead 2012) with fast local option for soft clipping of the Nextera transposase adapter sequence. We used mm10 GTF file (Ensembl GTF *Mus\_musculus.GRCm38.94.chr*) as annotation files. Counting of reads per gene and differential gene expression analysis were performed with featureCounts (v1.6.3+galaxy2) and DESeq2 (v2.11.40.4), respectively. Transcripts were determined as differentially expressed based on a P adj (adjusted P value with false discovery rate correction) of less than 0.05. Of note, 222 deregulated transcripts were annotated as predicted (32.4% of the deregulated transcripts, Table.1) and were predominantly pseudogenes (84.2% of deregulated predicted transcripts).

- *Gene Ontology (GO) enrichment analysis*: The analysis was performed with the PANTHER Classification System using a Fisher's exact test with a P value with false discovery rate correction (FDR) threshold of 0.05. For each annotation set (GO biological process complete, cellular component complete and molecular function complete), the deregulated transcripts list from the RNA-Seq analysis was used as the input list and the *Mus musculus* genome as the reference list.

## RT-qPCR

Reverse transcription of the extracted RNAs was performed using iScript Reverse Transcription Supermix (Bio-Rad Ref. 1708840). We used SsoAdvanced Universal SYBR Green Supermix (Bio-Rad Ref. 1725270) and CFX-96 (Bio-Rad) for quantitative PCR of cDNAs using the primers shown below. Two technical replicates were made for each condition. mRNA quantity was normalized to *Gapdh* and relative levels of mRNA expression were calculated with the  $2^{-\Delta\Delta C}$ . The mean and standard error of mean were normalized to *Myo10*<sup>+/-</sup>.

	Forward primer	Reverse primer
--	----------------	----------------

<i>Gapdh</i>	TGGAGAAACCTGCCAAGTATG	GGTCCTCAGTGTAGCCCAAG
<i>Akr1b3</i>	AGAGCATGGTGAAAGGAGCC	CCATAGCCGTCCAAGTGTCC
<i>Ccnb1</i>	GAGAGGTTGACGTCGAGCAG	GAGTTGGTGTCCATTACCG
<i>Eif4e</i>	GAGGTTGCTAACCCAGAGCA	CATAGGCTCAATCCCGTCCTT
<i>Hsp90aa1</i>	CGTCTCGTGCGTGTTTCATTC	CCAGAGCGTCCGATGAATTG
<i>Myo10</i>	GGCACGAAAGCAATATAGAAAGG	CTTCTGGAACACGATGGCTG
<i>Oaz1</i>	CAGCAGCGAGAGTTCTAGGG	CTCGTCGGAGTACAGGATGC
<i>Oser1</i>	CCAGCTGCGAGGAGTATTAAC	GGGCCTTCTCCAACAGACAG
<i>Paox</i>	GGTCCAGCCTTCTTTTGAGTCT	GTAGGAACCTCGGGTGTACG
<i>Psm5</i>	CAGGTGCTATGTCTCGTCCC	ATGAGCGAGGACTTGATGGC
<i>Rpl19</i>	CGCTGCGGGAAAAAGAAGGT	CCTCTTCCCTATGCCCATATGC
<i>Rps4x</i>	GGCGAGTCTCTTTCCGTTCC	GGATGGACGAGGAGCAAACAC
<i>Stxbp5l</i>	GATTTGCAAGACAGTTCGGC	TGGCAGTAACAGTCAACAC

### Machine learning approach for oocyte morphological characterization

We used our machine learning approach presented in Letort *in preparation* to automatically compare the morphology of *Myo10*<sup>-/-</sup> and control oocytes from brightfield images. Oocyte and *zona pellucida* contours were automatically determined with 2 neural networks trained specifically for these tasks. This segmentation allowed us to extract the value of 89 features for each oocyte-*zona pellucida* complex. These features characterize the size, shape, global intensity repartition, local texture and spatial organization of the oocyte, perivitelline space and *zona pellucida*. The complete list and description of the defined features are given in Letort *in preparation*. Note that we did not use features based on oocyte dynamics as images were acquired with a low temporal resolution. As the features are not independent between themselves, we then automatically selected a subset of uncorrelated features (with a threshold of 0.75) as described in Letort *in preparation*. We next trained a Random Forest classifier (Breiman 2001) with these features to distinguish between competent *Myo10*<sup>-/-</sup> and control oocytes arrested in prophase I and cleared of follicular cells. Oocytes were considered competent if they showed a visible perivitelline space, a centrally located nucleus and a regular outer border of the *zona pellucida*. We evaluated the performance of the trained algorithm by 15-fold cross validation on our dataset. We obtained a classification accuracy of 82% (with a precision of 80.9% and a recall of 83%). More importantly for our study, the Random Forest algorithm scored each feature according to its importance for classification, based on the Gini index. The most important features for classification concerned the presence of vertical linear structures

in the *zona pellucida* (TZP-like structure), the texture of the cytoplasm, the heterogeneity in the thickness of the perivitelline space and the circularity of both the oocyte and the internal limit of the *zona pellucida*. Manual inspection of these features suggested that the difference in the texture of the cytoplasm was mainly due to differences in nucleolus focus rather than actual morphological differences, and this feature was not statistically different between *Myo10*<sup>-/-</sup> full and control oocytes during meiotic maturation. We therefore decided not to explore this characteristic further.

Description of the features showed in this study:

- *Vertical linear structure in the zona pellucida*: To quantify the presence of vertical linear structures resembling TZPs, the area in the segmented *zona pellucida* was first flattened with the « Flatten » option in Fiji (NIH) to obtain a horizontal rectangle. Linear structures were then detected by measuring and thresholding the « tubeness » of each pixel in the image (with « Tubeness » plugin in Fiji which is based on the eigenvalues of the Hessian matrix of the image). Finally, only fairly vertical structures were kept by applying Sobel filters on the thresholded images.
- *Perivitelline space thickness*: Thickness was calculated as the distance between the oocyte shape and the internal limit of the *zona pellucida* at each angle around the oocyte center. The mean, minimum, maximum, standard deviation (data not shown) and coefficient of variation were then calculated from the distribution of distances.
- *Oocyte aspect ratio*: Ratio between the maximum Feret diameter (longest distance) of the oocyte shape and the minimum Feret diameter (distance in the perpendicular direction to the maximum Feret diameter). A circle has an aspect ratio of 1, while an elongated shape has a higher aspect ratio.

### **Image analysis**

For all signal intensity measurements, the image background was subtracted using Metamorph software.

- *Signal intensity of SiR-actin labeled TZPs*: Measurements were performed on competent oocytes arrested in prophase I, cleared of follicular cells and labeled with SiR-actin. For each oocyte, the 5th image among 8 Z acquisitions spaced 4  $\mu\text{m}$  apart was selected for measurement, which broadly corresponded to the oocyte equatorial plane. After background subtraction, we manually drew an ellipsoidal ROI band along the *zona pellucida* pericenter of 3 pixels (0.34  $\mu\text{m}$ ) width using Fiji. The mean gray value of SiR-actin signal in the ROI was measured as a readout of TZP density.

For each oocyte, the mean gray value was normalized to that of the control oocyte with the highest mean gray value.

- *Signal intensity of EU labeled RNAs*: Measurements were performed using Metamorph similarly to Almonacid 2019 on incompetent and competent oocytes arrested in prophase I from antral follicles. After background subtraction and Sum Z projection of the DAPI and EU signal images (images were spaced 1  $\mu\text{m}$  apart and selected for Z projection based on DAPI signal), the integrated intensity of the DAPI and EU signals was measured in a ROI of 77,577 pixels (999  $\mu\text{m}^2$ ). The same ROI was used for all measurements and was drawn to encompass the DAPI signal of each oocyte. The integrated intensity of the EU signal was then normalized to that of the DAPI signal. For each oocyte, the relative EU intensity value was normalized to that of the control oocyte with the highest relative EU intensity value.

- *Signal intensity of phalloidin labeled cytoplasmic F-actin*: Measurements were done on oocytes fixed 6 hours after NEBD using Metamorph as in Crozet 2021. After background subtraction, the integrated intensity of the phalloidin signal was measured in a ROI containing the cytoplasm of the oocyte equatorial plane. For each oocyte, we used the same ROI of 216,290 pixels (2,786  $\mu\text{m}^2$ ) and the integrated intensity of the phalloidin signal was normalized to that of the control oocyte with the highest value of phalloidin signal intensity.

- *Ovarian follicular density*: Cleared ovaries were imaged by light-sheet fluorescence microscopy and ovarian slices, one every 50 slices, were selected for measurement (slices were spaced 1  $\mu\text{m}$  apart). For each image, the area of the ovarian slice was measured by thresholding the TO-PRO-3 signal using Fiji. Briefly, images were preprocessed with a gamma and a median filter and thresholded with the Otsu dark method. When image thresholding led to more than one ovarian area due to discontinuous signal, only the largest thresholded area was selected. For each image, we manually counted the number of follicles in the thresholded ovarian slice. Follicles were empirically determined as such based on a defined outline, with an apparent oocyte surrounded by visible follicular cell layers (this includes preantral and antral follicles). We opted for a stringent follicle count to avoid counting follicle-like ovarian holes. Note that this may have led to several uncounted follicles. The number of follicles in the thresholded ovarian slice was then normalized to the slice area. The

follicular density of the ovary corresponds to the mean of the follicular density of the slices analyzed.

- *Oocyte size and zona pellucida width*: Measurements were made manually on brightfield images of competent oocytes arrested in prophase I. Oocyte size was assessed by measuring the area of the oocyte equatorial plane using Fiji. The width of the *zona pellucida* was measured 6 times where the *zona pellucida* was in focus and with a regular outer border using Metamorph. The *zona pellucida* width used for statistical analysis is the mean of these 6 measurements.

- *Timing of polar body extrusion*: The timing of the first polar body extrusion was empirically determined in oocytes monitored by live spinning disk microscopy (this includes oocytes incubated with SiR-tubulin or injected with H2B-GFP). Only movies with control oocytes extruding a polar body before 12 hours after NEBD were selected.

- *Spindle bipolarization and positioning*: Spindle morphogenesis and positioning were assessed in SiR-tubulin labeled oocytes monitored during meiotic maturation by live spinning disk microscopy. The timing of spindle bipolarization was empirically assessed by scoring the percentage of oocytes with a bipolarized spindle every hour from 1 to 6 h after NEBD. Spindle interpolar length and central width were measured manually 7 h after NEBD using Metamorph. Only spindles parallel to the acquisition plane were measured. Spindle cell localization was assessed by empirically scoring the percentage of oocytes with a central or off-centered spindle 30 min before anaphase for oocytes that extruded a polar body or up to 12 h after NEBD for those that did not.

- *Chromosome alignment*: Metaphase plate height and width were measured manually as in Crozet 2021 using Metamorph in H2B-GFP expressing oocytes monitored during meiotic maturation by live spinning disk microscopy. We measured the height and width of a ROI rectangle enclosing chromosomes 30 min before anaphase for oocytes that extruded a polar body or 12 h after NEBD for those that did not. Only metaphase plates oriented parallel to the acquisition plane were measured.

### **Statistical analysis**

We used GraphPad Prism 7.0a software for statistical analysis of RT-qPCR, oocyte polar body extrusion rate and image data. The Gaussian distribution of values was tested using a D'Agostino & Pearson normality test. Comparison of means was performed by a two-tailed unpaired t test (with Welch's correction for unequal

variances) or by a two-tailed Mann Whitney test (for a non-Gaussian distribution of values). We used a two-sided Fisher's exact test for contingency table analysis. All tests were performed with a confidence interval of 95%. n.s (not significant) P value  $\geq$  0.05, \* P value  $<$  0.05, \*\* P value  $<$  0.01, \*\*\* P value  $<$  0.001 and \*\*\*\* P value  $<$  0.0001. For each graph, the error bars indicate the standard deviation or standard error of mean.

### **Ethical statement**

All experimental procedures used for the project have been approved by the ministry of agriculture to be conducted in our CIRB animal facility (authorization N°75-1170). The use of all the genetically modified organisms described in this project has been granted by the DGRI (Direction Générale de la Recherche et de l'Innovation: Agrément OGM; DUO-5291).

### **Acknowledgments**

We thank XXX for comments on the manuscript and discussions; C. Antoniewski and N. Naouar from the IBPS ARTbio bioinformatics platform for their services and discussion. The STED microscopy was performed at the Orion Platform (member of France–Bioimaging ANR-10-INBS-XX) of the Center for Interdisciplinary Research in Biology (UMR7241/U1050) of Collège de France. The OMX microscopy was performed at the Cell and Tissue Imaging Platform -PICT-IBiSA (member of France–Bioimaging ANR-10-INBS-04) of the Genetics and Developmental Biology Department (UMR3215/U934) of Institut Curie, supported by the European Research Council (ERC EPIGENETIX N°250367). The work at IBENS Genomic Platform was supported by the France Génomique national infrastructure, funded as part of the "Investissements d'Avenir" program managed by the Agence Nationale de la Recherche (reference: ANR-10-INBS-09). This work was supported by the Fondation pour la Recherche Médicale (FRM Label EQU201903007796 to MHV), from the Agence Nationale de la Recherche (ANR-18-CE13 to MHV and Auguste Genovesio, IBENS/ENS, ANR-16-CE13 to MET) and from the France Canada Research Fund (FCRF 2017 to MET and HC, McGill University). FCr obtained a grant from the Fondation pour la Recherche Médicale for her 4<sup>th</sup> PhD year (FDT202001010906). This work has received support from the Fondation Bettencourt Schueller, support under the program « Investissements d'Avenir » launched by the French Government and implemented

by the Agence Nationale de la Recherche, with the references: ANR-10-LABX-54 MEMO LIFE, ANR-11-IDEX-0001-02 PSL\* Research University.

### **Author contributions**

FCr, MHV, HC and MET conceptualized the project. MET supervised the project. FCr wrote the manuscript, which was read and corrected by all authors. FCr and MET did most of the experiments. FCr, GL and MET did most of the data analysis. GL performed the machine learning approach. CDS carried out the RT-qPCR experiment and analysis. MB and AC performed whole ovary immunostaining, clearing and imaging. AE participated in the EU labeling experiment and collection of oocytes for RT-qPCR analysis. JD imaged oocytes by STED microscopy. TP and AD imaged oocytes by OMX microscopy. FCo performed the cDNA libraries and RNA-Seq.

### **Competing interests**

The authors declare that they have no competing interests.

## References

- Alam MH, Miyano T. Interaction between growing oocytes and granulosa cells in vitro. *Reprod Med Biol*. 2019 Aug 22;19(1):13-23.
- Almonacid M, Al Jord A, El-Hayek S, Othmani A, Couplier F, Lemoine S, Miyamoto K, Grosse R, Klein C, Piolot T, Mailly P, Voituriez R, Genovesio A, Verlhac MH. Active Fluctuations of the Nuclear Envelope Shape the Transcriptional Dynamics in Oocytes. *Dev Cell*. 2019 Oct 21;51(2):145-157.e10.
- Albertini DF, Combelles CM, Benecchi E, Carabatsos MJ. Cellular basis for paracrine regulation of ovarian follicle development. *Reproduction*. 2001 May;121(5):647-53.
- Anderson E, Albertini DF. Gap junctions between the oocyte and companion follicle cells in the mammalian ovary. *J Cell Biol*. 1976 Nov;71(2):680-6.
- Azoury J, Lee KW, Georget V, Rassinier P, Leader B, Verlhac MH. Spindle positioning in mouse oocytes relies on a dynamic meshwork of actin filaments. *Curr Biol*. 2008 Oct 14;18(19):1514-9.
- Baena V, Terasaki M. Three-dimensional organization of transzonal projections and other cytoplasmic extensions in the mouse ovarian follicle. *Sci Rep*. 2019 Feb 4;9(1):1262.
- Belle M, Godefroy D, Couly G, Malone SA, Collier F, Giacobini P, Chédotal A. Tridimensional Visualization and Analysis of Early Human Development. *Cell*. 2017 Mar 23;169(1):161-173.e12.
- Bennabi I, Terret ME, Verlhac MH. Meiotic spindle assembly and chromosome segregation in oocytes. *J Cell Biol*. 2016 Dec 5;215(5):611-619.
- Bennabi I, Crozet F, Nikalayevich E, Chaigne A, Letort G, Manil-Ségalen M, Campillo C, Cadart C, Othmani A, Attia R, Genovesio A, Verlhac MH, Terret ME. Artificially decreasing cortical tension generates aneuploidy in mouse oocytes. *Nat Commun*. 2020 Apr 3;11(1):1649.
- Berg JS, Cheney RE. Myosin-X is an unconventional myosin that undergoes intrafilopodial motility. *Nat Cell Biol*. 2002 Mar;4(3):246-50.
- Bohil AB, Robertson BW, Cheney RE. Myosin-X is a molecular motor that functions in filopodia formation. *Proc Natl Acad Sci U S A*. 2006 Aug 15;103(33):12411-6.
- Breiman L. Random Forests. *Machine Learning*. 2001;45:5–32.
- Carabatsos MJ, Elvin J, Matzuk MM, Albertini DF. Characterization of oocyte and follicle development in growth differentiation factor-9-deficient mice. *Dev Biol*. 1998 Dec 15;204(2):373-84.
- Chaigne A, Terret ME, Verlhac MH. Asymmetries and Symmetries in the Mouse Oocyte and Zygote. *Results Probl Cell Differ*. 2017;61:285-299.

Chen J, Torcia S, Xie F, Lin CJ, Cakmak H, Franciosi F, Horner K, Onodera C, Song JS, Cedars MI, Ramalho-Santos M, Conti M. Somatic cells regulate maternal mRNA translation and developmental competence of mouse oocytes. *Nat Cell Biol.* 2013 Dec;15(12):1415-23.

Clarke HJ. Post-transcriptional control of gene expression during mouse oogenesis. *Results Probl Cell Differ.* 2012;55:1-21.

Clarke HJ. Regulation of germ cell development by intercellular signaling in the mammalian ovarian follicle. *Wiley Interdiscip Rev Dev Biol.* 2018 Jan;7(1):10.1002/wdev.294.

Conti M, Franciosi F. Acquisition of oocyte competence to develop as an embryo: integrated nuclear and cytoplasmic events. *Hum Reprod Update.* 2018 May 1;24(3):245-266.

Crozet F, Da Silva C, Verlhac MH, Terret ME. Myosin-X is dispensable for spindle morphogenesis and positioning in the mouse oocyte. *Development.* 2021 Mar 15;dev.199364.

De La Fuente R, Eppig JJ. Transcriptional activity of the mouse oocyte genome: companion granulosa cells modulate transcription and chromatin remodeling. *Dev Biol.* 2001 Jan 1;229(1):224-36.

Dever TE, Ivanov IP. Roles of polyamines in translation. *J Biol Chem.* 2018 Nov 30;293(48):18719-18729.

Dong J, Albertini DF, Nishimori K, Kumar TR, Lu N, Matzuk MM. Growth differentiation factor-9 is required during early ovarian folliculogenesis. *Nature.* 1996 Oct 10;383(6600):531-5.

El-Hayek S, Clarke HJ. Control of Oocyte Growth and Development by Intercellular Communication Within the Follicular Niche. *Results Probl Cell Differ.* 2016;58:191-224.

El-Hayek S, Yang Q, Abbassi L, FitzHarris G, Clarke HJ. Mammalian Oocytes Locally Remodel Follicular Architecture to Provide the Foundation for Germline-Soma Communication. *Curr Biol.* 2018 Apr 2;28(7):1124-1131.e3.

Elvin JA, Yan C, Wang P, Nishimori K, Matzuk MM. Molecular characterization of the follicle defects in the growth differentiation factor 9-deficient ovary. *Mol Endocrinol.* 1999 Jun;13(6):1018-34.

Heimsath EG Jr, Yim YI, Mustapha M, Hammer JA, Cheney RE. Myosin-X knockout is semi-lethal and demonstrates that myosin-X functions in neural tube closure, pigmentation, hyaloid vasculature regression, and filopodia formation. *Sci Rep.* 2017 Dec 11;7(1):17354.

Herbert M, Levasseur M, Homer H, Yallop K, Murdoch A, McDougall A. Homologue disjunction in mouse oocytes requires proteolysis of securin and cyclin B1. *Nat Cell Biol.* 2003 Nov;5(11):1023-5.

Kidder GM, Vanderhyden BC. Bidirectional communication between oocytes and follicle cells: ensuring oocyte developmental competence. *Can J Physiol Pharmacol*. 2010 Apr;88(4):399-413.

Kyogoku H, Kitajima TS. Large Cytoplasm Is Linked to the Error-Prone Nature of Oocytes. *Dev Cell*. 2017 May 8;41(3):287-298.e4.

Langmead B, Salzberg SL. Fast gapped-read alignment with Bowtie 2. *Nat Methods*. 2012 Mar 4;9(4):357-9.

Ledan E, Polanski Z, Terret ME, Maro B. Meiotic maturation of the mouse oocyte requires an equilibrium between cyclin B synthesis and degradation. *Dev Biol*. 2001 Apr 15;232(2):400-13.

Li J, Qian WP, Sun QY. Cyclins regulating oocyte meiotic cell cycle progression. *Biol Reprod*. 2019 Nov 21;101(5):878-881.

Lin J, Wang L. Oxidative Stress in Oocytes and Embryo Development: Implications for *In Vitro* Systems. *Antioxid Redox Signal*. 2020 Dec 8.

Lowther KM, Favero F, Yang CR, Taylor HS, Seli E. Embryonic poly(A)-binding protein is required at the preantral stage of mouse folliculogenesis for oocyte-somatic communication. *Biol Reprod*. 2017 Feb 1;96(2):341-351.

Luciano AM, Franciosi F, Modina SC, Lodde V. Gap junction-mediated communications regulate chromatin remodeling during bovine oocyte growth and differentiation through cAMP-dependent mechanism(s). *Biol Reprod*. 2011 Dec;85(6):1252-9.

Macaulay AD, Gilbert I, Caballero J, Barreto R, Fournier E, Tossou P, Sirard MA, Clarke HJ, Khandjian ÉW, Richard FJ, Hyttel P, Robert C. The gametic synapse: RNA transfer to the bovine oocyte. *Biol Reprod*. 2014 Oct;91(4):90.

Macaulay AD, Gilbert I, Scantland S, Fournier E, Ashkar F, Bastien A, Saadi HA, Gagné D, Sirard MA, Khandjian ÉW, Richard FJ, Hyttel P, Robert C. Cumulus Cell Transcripts Transit to the Bovine Oocyte in Preparation for Maturation. *Biol Reprod*. 2016 Jan;94(1):16.

Manil-Ségalen M, Łuksza M, Kanaan J, Marthiens V, Lane SIR, Jones KT, Terret ME, Basto R, Verlhac MH. Chromosome structural anomalies due to aberrant spindle forces exerted at gene editing sites in meiosis. *J. Cell Biol*. 2018 Oct 1; 217(10): 3416–3430.

McGinnis LK, Kinsey WH. Role of focal adhesion kinase in oocyte-follicle communication. *Mol Reprod Dev*. 2015 Feb;82(2):90-102.

Mihajlović AI, FitzHarris G. Segregating Chromosomes in the Mammalian Oocyte. *Curr Biol*. 2018 Aug 20;28(16):R895-R907.

Mora JM, Fenwick MA, Castle L, Baithun M, Ryder TA, Mobberley M, Carzaniga R, Franks S, Hardy K. Characterization and significance of adhesion and junction-related proteins in mouse ovarian follicles. *Biol Reprod*. 2012 May 17;86(5):153, 1-14.

Pham CT, MacIvor DM, Hug BA, Heusel JW, Ley TJ. Long-range disruption of gene expression by a selectable marker cassette. *Proc Natl Acad Sci U S A*. 1996 Nov 12;93(23):13090-5.

Rankin T, Talbot P, Lee E, Dean J. Abnormal zonae pellucidae in mice lacking ZP1 result in early embryonic loss. *Development*. 1999 Sep;126(17):3847-55.

Reis A, Chang HY, Levasseur M, Jones KT. APC<sup>cdh1</sup> activity in mouse oocytes prevents entry into the first meiotic division. *Nat Cell Biol*. 2006 May;8(5):539-40.

Schuh M, Ellenberg J. A new model for asymmetric spindle positioning in mouse oocytes. *Curr Biol*. 2008 Dec 23;18(24):1986-92.

Simon AM, Goodenough DA, Li E, Paul DL. Female infertility in mice lacking connexin 37. *Nature*. 1997 Feb 6;385(6616):525-9.

Sorensen RA, Wassarman PM. Relationship between growth and meiotic maturation of the mouse oocyte. *Dev Biol*. 1976 Jun;50(2):531-6.

Veitch GI, Gittens JE, Shao Q, Laird DW, Kidder GM. Selective assembly of connexin37 into heterocellular gap junctions at the oocyte/granulosa cell interface. *J Cell Sci*. 2004 Jun 1;117(Pt 13):2699-707.

Wassarman PM, Litscher ES. The Mouse Egg's Zona Pellucida. *Curr Top Dev Biol*. 2018;130:331-356.

Yamashita YM, Inaba M, Buszczak M. Specialized Intercellular Communications via Cytonemes and Nanotubes. *Annu Rev Cell Dev Biol*. 2018 Oct 6;34:59-84.

## FIGURE LEGENDS

### **Figure 1: Surrounding somatic cells support oocyte growth**

**A)** Summary scheme of oocyte growth. Growth begins with the exit from quiescence and consists of an increase in oocyte size and storage of macromolecules. The oocyte develops surrounded by somatic cells, forming a complex termed the ovarian follicle. The emergence of the antrum, the fluid-filled chamber of the follicle, marks the transition from preantral to antral follicle. In antral follicles, a subpopulation of follicular cells tightly surrounds the oocyte and constitutes the cumulus-oocyte complex (COC) with the oocyte. Fully grown oocytes are competent to resume meiosis and undergo meiotic maturation.

**B)** Scheme of intercellular contacts between the oocyte and the follicular cells. Transzonal projections (TZPs), follicular cell protrusions, contact the oocyte by crossing the *zona pellucida* extracellular matrix. TZPs are mainly actin-rich and contain Myosin-X (MYO10). TZPs mediate junctional communication (GAP j) between the oocyte and follicular cells, providing metabolites and signaling molecules. Transcripts (RNA) are transferred from follicular cells to the oocyte potentially through extracellular vesicles. Adherens junctions at the interface between the TZP and the oocyte membrane are thought to maintain follicular cell-oocyte adhesion.

### **Figure 2: Global deletion of *Myo10* decreases the density of transzonal projections in fully grown cumulus-oocyte complexes.**

**A)** Fully grown cumulus-oocyte complexes stained for Myosin-X (MYO10, left images) and stained with phalloidin to label F-actin (right images). The upper panel shows complexes from the *Myo10* full knockout strain (full) and the lower panel complexes from the *Myo10* oocyte knockout strain (oo). For each panel, control complexes are at the top and *Myo10*<sup>-/-</sup> complexes are at the bottom. For MYO10 staining, contrast adjustment is similar between complexes of the same strain. Scale bar 10 μm.

**B)** Cropped images of the red dotted rectangles shown in A) focusing on the *zona pellucida*. MYO10 staining is on the left and phalloidin staining is on the right. Scale bar 5 μm.

**C)** STED microscopy images of phalloidin labeled oocytes arrested in prophase I freed of follicular cells, focusing on the *zona pellucida* of a control oocyte (left) and a *Myo10*<sup>-/-</sup> full oocyte (right). Scale bar 2  $\mu$ m.

**D)** Live fully grown oocytes arrested in prophase I stained with SiR-actin (SiR-act) to label F-actin. The upper images are oocytes from the MYO10 full invalidation strain and the lower images are oocytes from the MYO10 oocyte invalidation strain. Controls are on the left and *Myo10*<sup>-/-</sup> oocytes are on the right. Scale bar 10  $\mu$ m.

**E)** Scatter plot of the intensity of all SiR-act labeled TZPs of fully grown oocytes arrested in prophase I. Control and *Myo10*<sup>-/-</sup> full oocytes are in dark gray and green, respectively. Control and *Myo10*<sup>-/-</sup> oo oocytes are in light gray and blue, respectively. (n) is the number of oocytes analyzed. Data are mean $\pm$ s.d. with individual data points plotted. Data are from five independent experiments for control and *Myo10*<sup>-/-</sup> full oocytes and from three independent experiments for control and *Myo10*<sup>-/-</sup> oo oocytes. Statistical significance of differences was assessed by a two-tailed unpaired t test with Welch's correction, P value < 0.0001 (*Myo10*<sup>-/-</sup> full oocytes compared to control oocytes) and by a two-tailed unpaired t test, P value = 0.7271 (*Myo10*<sup>-/-</sup> oo oocytes compared to control oocytes). n.s not significant.

### **Figure 3: Follicular density is not impaired in *Myo10*<sup>-/-</sup> full ovaries**

**A)** Light-sheet fluorescence microscopy images of cleared ovaries stained with TO-PRO-3 (blue) to label nucleic acid. The control ovary is on the left and the *Myo10*<sup>-/-</sup> full ovary is on the right. Scale bar 0.25 mm. The images inserted at the top right show antral follicles from the magnification of the yellow dotted rectangles. Scale bar 0.1 mm.

**B)** Scatter plot of the relative number of follicles per ovary. Control ovaries are in dark gray and *Myo10*<sup>-/-</sup> full ovaries are in green. For each condition, data are from two different mice. (N) is the number of ovaries analyzed. Data are mean $\pm$ s.d. with individual data points plotted. Statistical significance of differences was assessed by a two-tailed Mann Whitney test, P value = 0.4857. n.s not significant.

### **Figure 4: Morphological characterization of competent *Myo10*<sup>-/-</sup> full oocytes arrested in prophase I**

**A)** Brightfield images of competent oocytes arrested in prophase I from the *Myo10* full knockout strain (left panel) and from the *Myo10* oocyte knockout strain (right panel).

For each panel, controls are on the left and *Myo10*<sup>-/-</sup> oocytes are on the right. Scale bar 10 μm.

**B)** Scatter plot of the equatorial plane area of competent oocytes arrested in prophase I. Control and *Myo10*<sup>-/-</sup> full oocytes are in dark gray and green, respectively. Control and *Myo10*<sup>-/-</sup> oo oocytes are in light gray and blue, respectively. (n) is the number of oocytes analyzed. Data are mean±s.d. with individual data points plotted. Data are from ten independent experiments for control and *Myo10*<sup>-/-</sup> full oocytes and from three independent experiments for control and *Myo10*<sup>-/-</sup> oo oocytes. Statistical significance of differences was assessed by a two-tailed unpaired t test, P value = 0.4672 (*Myo10*<sup>-/-</sup> full oocytes compared to control oocytes) and by a two-tailed Mann Whitney test, P value = 0.4304 (*Myo10*<sup>-/-</sup> oo oocytes compared to control oocytes). n.s not significant.

**C)** Scatter plot of the *zona pellucida* (ZP) width of competent oocytes arrested in prophase I. Control and *Myo10*<sup>-/-</sup> full oocytes are in dark gray and green, respectively. Control and *Myo10*<sup>-/-</sup> oo oocytes are in light gray and blue, respectively. (n) is the number of oocytes analyzed. Data are mean±s.d. with individual data points plotted. Data are from three independent experiments for both control and *Myo10*<sup>-/-</sup> full oocytes and control and *Myo10*<sup>-/-</sup> oo oocytes. Statistical significance of differences was assessed by two-tailed unpaired t tests, P value = 0.0342 (*Myo10*<sup>-/-</sup> full oocytes compared to control oocytes) and P value = 0.5342 (*Myo10*<sup>-/-</sup> oo oocytes compared to control oocytes). n.s not significant.

**D)** Brightfield images of a competent control oocyte (left panel) and a competent *Myo10*<sup>-/-</sup> full oocyte (right panel) arrested in prophase I. For each panel, the bottom image displays the automatic segmentation of the oocyte perivitelline space (Aut. perivitelline space, green). Scale bar = 10 μm.

**E)** Images of flattened *zona pellucida* obtained from segmentation of the oocytes shown in D). The top panel shows a control *zona pellucida* and the lower panel a *Myo10*<sup>-/-</sup> full *zona pellucida*. For each panel, the brightfield image of the *zona pellucida* is at the top and the representation of automatic detection of vertical linear “TZP-like” structures at the bottom (black). Scale bar 10 μm.

**F)** Scatter plot of the presence of vertical TZP-like structures in the *zona pellucida* (ZP) of competent oocytes arrested in prophase I, as represented by the schemes on the left. The detection of these structures was performed automatically and represents one of the most important features used by our machine learning algorithm to discriminate

controls from *Myo10*<sup>-/-</sup> full oocytes. Control and *Myo10*<sup>-/-</sup> full oocytes are in dark gray and green, respectively. Control and *Myo10*<sup>-/-</sup> oo oocytes are in light gray and blue, respectively. (n) is the number of oocytes analyzed. Data are mean±s.d. with individual data points plotted. Data are from thirteen independent experiments for control and *Myo10*<sup>-/-</sup> full oocytes and from four independent experiments for control and *Myo10*<sup>-/-</sup> oo oocytes. Statistical significance of differences was assessed by a two-tailed unpaired t test with Welch's correction, P value < 0.0001 (*Myo10*<sup>-/-</sup> full oocytes compared to control oocytes) and by a two-tailed unpaired t test, P value = 0.9474 (*Myo10*<sup>-/-</sup> oo oocytes compared to control oocytes). n.s not significant.

**G)** Scatter plot of the coefficient of variation of the perivitelline space thickness of competent oocytes arrested in prophase I, as represented by the schemes on the left. The heterogeneity of the perivitelline space thickness was measured automatically and represents one of the most important features used by our machine learning algorithm to discriminate controls from *Myo10*<sup>-/-</sup> full oocytes. Control and *Myo10*<sup>-/-</sup> full oocytes are in dark gray and green, respectively. Control and *Myo10*<sup>-/-</sup> oo oocytes are in light gray and blue, respectively. (n) is the number of oocytes analyzed. Data are mean±s.d. with individual data points plotted. Data are from thirteen independent experiments for control and *Myo10*<sup>-/-</sup> full oocytes and from four independent experiments for control and *Myo10*<sup>-/-</sup> oo oocytes. Statistical significance of differences was assessed by a two-tailed Mann Whitney test, P value < 0.0001 (*Myo10*<sup>-/-</sup> full oocytes compared to control oocytes) and by a two-tailed unpaired t test, P value = 0.0308 (*Myo10*<sup>-/-</sup> oo oocytes compared to control oocytes).

**Figure 5: Non-global differential gene expression between competent *Myo10*<sup>+/-</sup> and *Myo10*<sup>-/-</sup> full oocytes arrested in prophase I**

**A)** Volcano plot of differential gene expression between competent *Myo10*<sup>+/-</sup> and *Myo10*<sup>-/-</sup> full oocytes arrested in prophase I. Differential transcriptomic analysis was performed by RNA-Seq. Up-regulated transcripts are shown in red (up, 605 transcripts), down-regulated transcripts are shown in blue (down, 80 transcripts, including *Myo 10*), and non-deregulated transcripts are shown in gray (not significant, 15,702 transcripts). Significance was set at P adj < 0.05. *Myo10*<sup>-/-</sup> full oocytes were collected from two *Myo10*<sup>flox/flox</sup>; *Cre*<sup>+</sup> mice and *Myo10*<sup>+/-</sup> oocytes from two *Myo10*<sup>wt/flox</sup>; *Cre*<sup>+</sup> mice. For each condition, three biological replicates (each containing 10 oocytes) and three technical replicates were performed.

**B)** Bar graph of significantly over-represented GO biological process terms in the deregulated gene list from the RNA-Seq analysis shown in A). Statistical significance of differences was assessed by a Fisher's exact test with false discovery rate correction. Note that the list of terms is not exhaustive.

**C)** Bar graph of the relative mRNA quantity in competent prophase I arrested *Myo10*<sup>-/-</sup> full oocytes (colored bars) normalized to competent prophase I arrested *Myo10*<sup>+/-</sup> oocytes (gray bars) performed by RT-qPCR. The selected mRNAs were chosen based on their biological relevance and their deregulatory strength (log<sub>2</sub>(FC) and P adj) in the RNA-Seq analysis described in A). mRNAs indicated as up- or down-regulated by RNA-Seq analysis are shown in red and blue, respectively. *Myo10*<sup>-/-</sup> full oocytes were collected from *Myo10*<sup>flox/flox</sup>; *Cre*<sup>-</sup> mice and *Myo10*<sup>+/-</sup> oocytes from *Myo10*<sup>wt/flox</sup>; *Cre*<sup>+</sup> mice. For each condition, two biological replicates were performed (one containing 30 oocytes and the other 24 oocytes) from two different mice each time and two technical replicates were performed. Standard error of mean (SEM) is shown. For each mRNA, the mean of *Myo10*<sup>+/-</sup> oocytes was normalized to *Myo10*<sup>+/-</sup> oocytes. The mean and SEM for *Myo10*<sup>-/-</sup> full oocytes = 0.08 ± 0.004 (*Myo10*); 0.59 ± 0.171 (*Stxbp5l*); 0.99 ± 0.079 (*Akr1b3*); 1.19 ± 0.059 (*Oser1*); 1.48 ± 0.222 (*Hsp90aa1*); 1.48 ± 0.034 (*Oaz1*); 1.49 ± 0.333 (*Eif4e*); 1.27 ± 0.037 (*Ccnb1*); 1.44 ± 0.034 (*Rps4x*); 1.53 ± 0.179 (*Rpl19*). Statistical significance of differences was assessed by two-tailed unpaired t tests. P value < 0.0001 (*Myo10*); P value = 0.1394 (*Stxbp5l*); 0.9001 (*Akr1b3*); 0.0864 (*Oser1*); 0.1612 (*Hsp90aa1*); 0.0050 (*Oaz1*); 0.2765 (*Eif4e*); 0.0180 (*Ccnb1*); 0.0060 (*Rps4x*); 0.0987 (*Rpl19*).

**D)** Sum of Z Projection images of oocytes stained with DAPI to label DNA (blue, top images of each panel) and incubated or not with 5-ethynyl uridine to label global RNA transcription (EU, bottom images of each panel). For each panel, control oocytes are on the left and *Myo10*<sup>-/-</sup> full oocytes are on the right. Incompetent and competent oocytes arrested in prophase I are on the left and right panels, respectively. Oocytes incubated with or without EU are in the upper and lower panels, respectively. For EU staining, contrast adjustment is similar between all conditions except for incompetent oocytes incubated with EU for which the signal intensity is too high to be shown with the same adjustment as the others. Scale bar 10 μm.

**E)** Scatter plot of the relative EU signal intensity normalized to the DAPI signal intensity in control (dark gray) and *Myo10*<sup>-/-</sup> full (green) incompetent or competent prophase I arrested oocytes incubated or not with EU. (n) is the number of oocytes analyzed. Data

are mean±s.d. with individual data points plotted. Data are from three independent experiments (for incompetent control oocytes with EU, competent control oocytes with EU and incompetent control oocytes without EU), four independent experiments (for competent control oocytes without EU, incompetent *Myo10*<sup>-/-</sup> full oocytes with EU, competent *Myo10*<sup>-/-</sup> full oocytes with EU and competent *Myo10*<sup>-/-</sup> full oocytes without EU), and five independent experiments (for incompetent *Myo10*<sup>-/-</sup> full oocytes without EU). Statistical significance of differences was assessed by two-tailed Mann Whitney tests, P value = 0.7688 (incompetent *Myo10*<sup>-/-</sup> full oocytes with EU compared to incompetent control oocytes with EU), P value = 0.7564 (competent *Myo10*<sup>-/-</sup> full oocytes with EU compared to competent control oocytes with EU), P value = 0.0326 (incompetent *Myo10*<sup>-/-</sup> full oocytes without EU to incompetent control oocytes without EU), P value < 0.0001 (incompetent control oocytes with EU compared to incompetent control oocytes without EU), P value < 0.0001 (incompetent *Myo10*<sup>-/-</sup> full oocytes with EU compared to incompetent *Myo10*<sup>-/-</sup> full oocytes without EU), P value < 0.0001 (competent control oocytes with EU compared to competent control oocytes without EU) and P value < 0.0001 (competent *Myo10*<sup>-/-</sup> full oocytes with EU compared to competent *Myo10*<sup>-/-</sup> full oocytes without EU). Statistical significance of differences was assessed by a two-tailed unpaired t test to compare competent *Myo10*<sup>-/-</sup> full oocytes without EU to competent control oocytes without EU, P value = 0.2647. n.s not significant.

### **Figure 6: *Myo10*<sup>-/-</sup> full oocytes tend to arrest development in meiosis I**

**A)** Brightfield images from spinning disk movies from 3 h to 18 h after NEBD. The top images show a control oocyte, the middle images a *Myo10*<sup>-/-</sup> full oocyte that extruded a polar body (PB) and the bottom images show a *Myo10*<sup>-/-</sup> full oocyte that did not extrude a polar body (no PB). The blue asterisk indicates a lysed polar body. Scale bar 10 μm.

**B)** Stacked bars of first polar body extrusion rate as a percentage of control and *Myo10*<sup>-/-</sup> full oocytes. The gray bars represent the percentage of oocytes that extruded a polar body (PB) and the white bars the percentage of oocytes that did not extrude a polar body (no PB). (n) is the number of oocytes analyzed. Data are from three independent experiments. Statistical significance of differences was assessed by a two-sided Fisher's exact test, P value = 0.0113.

**C)** Scatter plot of the timing after NEBD of first polar body extrusion of control (dark gray) and *Myo10*<sup>-/-</sup> (green) full oocytes. (n) is the number of oocytes analyzed. Data are mean±s.d. with individual data points plotted. Data are from six independent experiments. Statistical significance of differences was assessed by a two-tailed Mann Whitney test, P value = 0.3194. n.s not significant.

**Figure 7: *Myo10*<sup>-/-</sup> full oocytes have correctly formed and positioned spindles and normally aligned chromosomes**

**A)** Max Intensity Z Projection images of oocytes stained with SiR-tubulin to label microtubules (SiR-tub, yellow) merged with corresponding brightfield images. Images are extracted from spinning disk movies from 30 min to 14 h 30 after NEBD. The top images show a control oocyte, the middle images a *Myo10*<sup>-/-</sup> full oocyte that extruded a polar body (PB) and the bottom images a *Myo10*<sup>-/-</sup> full oocyte that did not extrude a polar body (no PB). Scale bar 10 μm.

**B)** Max Intensity Z Projection images of oocytes stained with SiR-tub (yellow) 7h after NEBD. The top image shows the spindle of a control oocyte, the middle image the spindle of a *Myo10*<sup>-/-</sup> full oocyte that extruded a polar body (PB) and the bottom image shows the spindle of a *Myo10*<sup>-/-</sup> full oocyte that did not extrude a polar body (no PB). Scale bar 5 μm.

**C)** Graph of the percentage of control (dark gray) and *Myo10*<sup>-/-</sup> (green) full oocytes with a bipolarized spindle as a function of time after NEBD. Data are from four independent experiments. For each time point, statistical significance of differences was assessed by a two-sided Fisher's exact test. P value > 0.9999 for 1 h after NEBD; P value = 0.3433 for 2 h after NEBD; P value = 0.7765 for 3 h after NEBD; P value > 0.9999 for 4 h after NEBD; P value = 0.6937 for 5h after NEBD; P value > 0.9999 for 6h after NEBD.

**D)** Scatter plots of spindle interpolar length (left) and central width (right) 7 h after NEBD in control (dark gray) and *Myo10*<sup>-/-</sup> (green) full oocytes. (n) is the number of oocytes analyzed. Data are mean±s.d. with individual data points plotted. Data are from four independent experiments. Statistical significance of differences was assessed by a two-tailed unpaired t test, P value = 0.0989 for the length and by a two-tailed unpaired t test with Welch's correction, P value = 0.0753 for the width. n.s not significant.

**E)** Stacked bars of spindle cell localization 30 min before anaphase for oocytes that extruded a polar body or 12 h after NEBD for those that did not, as a percentage of control and *Myo10*<sup>-/-</sup> full oocytes. Gray bars represent the percentage of oocytes with an off-centered spindle and orange bars the percentage of oocytes with a central spindle. (n) is the number of oocytes analyzed. Data are from four independent experiments. Statistical significance of differences was assessed by a two-sided Fisher's exact test, P value = 0.3832. n.s not significant.

**F)** Max Intensity Z Projection images from spinning disk movies of oocytes injected with H2B-GFP to label chromosomes (H2B, cyan) in a control oocyte (top images), in a *Myo10*<sup>-/-</sup> full oocyte that extruded a polar body (PB, middle images) and in a *Myo10*<sup>-/-</sup> full oocyte that did not extrude a polar body (no PB, bottom image). Left images show chromosomes 30 min before anaphase for polar body extruding oocytes or 12h after NEBD for the *Myo10*<sup>-/-</sup> full oocyte that did not extrude a polar body. Right images show chromosomes after anaphase. Scale bar 5  $\mu$ m.

**G)** Scatter plots of metaphase plate height (left) and width (right), as shown in the lower schemes, 30 min before anaphase for oocytes that extruded a polar body or 12 h after NEBD for those that did not. Control and *Myo10*<sup>-/-</sup> full oocytes are in dark gray and green, respectively. (n) is the number of oocytes analyzed. Data are mean $\pm$ s.d. with individual data points plotted. Data are from three independent experiments. Statistical significance of differences was assessed by two-tailed unpaired t tests. P value = 0.5331 for the height and P value = 0.0395 for the width. n.s not significant.

### **Figure S1: *Myo10* full knockout, generation and validation**

**A)** Scheme of the *Myo10* gene with introns in light blue rectangles and exons in black vertical lines according to Ensembl database. The red dotted rectangle indicates the region targeted to invalidate MYO10. 1) For *Myo10* full knockout: the neomycin selection cassette (neo, green rectangle) inserted between exons 22 and 23 was retained, allowing its promoter to interfere with MYO10 expression in all cell types. 2) For *Myo10* conditional knockout in oocytes: the neo cassette was removed following Flp-mediated excision at the FRT sites (dark blue rectangles). ZP3 Cre-mediated excision at the *loxP* sites (yellow rectangles and triangles) flanking exons 23-25 results in a premature stop codon and absence of MYO10 in oocytes.

**B)** Control (left panel) and *Myo10*<sup>-/-</sup> full (right panel) mice of the *Myo10* full knockout strain. Scale bar 10 mm. For each panel, the image on the right shows the mouse front

paw. Some phenotypes characteristic of previously described *Myo10* full knockout were observed in our *Myo10*<sup>-/-</sup> full mice, such as a white belly spot and webbed digits. Scale bar 5 mm.

**C)** Immunoblotting performed on liver, kidney and spleen extracts from mice from the *Myo10* full knockout strain. Control (Ctrl) extracts are from a *Myo10*<sup>wt/flox</sup>; *Cre*<sup>+</sup> genotyped mouse, *Cre*<sup>+</sup> extracts are from a *Myo10*<sup>flox/flox</sup>; *Cre*<sup>+</sup> genotyped mouse and *Cre*<sup>-</sup> extracts are from a *Myo10*<sup>flox/flox</sup>; *Cre*<sup>-</sup> genotyped mouse. The membrane was stained for MYO10 (upper image) and for Actin (lower image) as a loading control. Indicated ladders: 37, 50 and 250 kDa.

**D)** Preantral follicles from the *Myo10* full knockout strain (upper images) and the *Myo10* oocyte knockout strain (lower images). Follicles were stained for MYO10 (left panel) and stained with phalloidin (right panel). For each panel, control follicles are on the left and *Myo10*<sup>-/-</sup> follicles are on the right. For MYO10 staining, contrast adjustment is similar between follicles of the same strain. Scale bar 10 μm.

### **Figure S2: Reduction of total TZP density in fully grown *Myo10*<sup>-/-</sup> full oocytes**

Images of a fully grown control oocyte (upper panel) and a fully grown *Myo10*<sup>-/-</sup> full oocyte (lower panel) stained with FM 1-43 (green, middle images) to label membranes and with SiR-actin (SiR-act, orange, right images) to label F-actin. The left images show oocyte brightfield images. Scale bar 10 μm.

### **Figure S3: Morphological characterization of competent *Myo10*<sup>-/-</sup> full oocytes arrested in prophase I**

**A)** Competent control (left panel) and *Myo10*<sup>-/-</sup> full (right panel) oocytes arrested in prophase I stained with SiR-DNA (blue). For each panel, the brightfield image of the oocyte is at the top and the corresponding SiR-DNA labeling at the bottom. Some follicular-like cells are ectopically located in the perivitelline space of the *Myo10*<sup>-/-</sup> full oocyte. Scale bar 10 μm.

**B)** Bar graph of morphological features of competent prophase I arrested oocytes used by our machine learning algorithm to discriminate control oocytes from *Myo10*<sup>-/-</sup> full oocytes. Features are ranked according to their importance for oocyte classification.

**C)** Scatter plot of the aspect ratio (circularity) of competent oocytes arrested in prophase I, as represented by the schemes on the left. The oocyte aspect ratio was measured automatically and represents a relevant feature used by our machine

learning algorithm to discriminate control oocytes from *Myo10*<sup>-/-</sup> full oocytes. Control and *Myo10*<sup>-/-</sup> full oocytes are in dark gray and green, respectively. Control and *Myo10*<sup>-/-</sup> oo oocytes are in light gray and blue, respectively. (n) is the number of oocytes analyzed. Data are mean±s.d. with individual data points plotted. Data are from thirteen independent experiments for control and *Myo10*<sup>-/-</sup> full oocytes and from four independent experiments for control and *Myo10*<sup>-/-</sup> oo oocytes. Statistical significance of differences was assessed by two-tailed Mann Whitney tests, P value = 0.0004 (*Myo10*<sup>-/-</sup> full oocytes compared to control oocytes) and P value = 0.8235 (*Myo10*<sup>-/-</sup> oo oocytes compared to control oocytes). n.s not significant.

**D)** Scatter plot of the perimeter of competent oocytes arrested in prophase I. Control and *Myo10*<sup>-/-</sup> full oocytes are in dark gray and green, respectively. Control and *Myo10*<sup>-/-</sup> oo oocytes are in light gray and blue, respectively. (n) is the number of oocytes analyzed. Data are mean±s.d. with individual data points plotted. Data are from thirteen independent experiments for control and *Myo10*<sup>-/-</sup> full oocytes and from four independent experiments for control and *Myo10*<sup>-/-</sup> oo oocytes. Statistical significance of differences between *Myo10*<sup>-/-</sup> full oocytes and control oocytes was assessed by a two-tailed unpaired t test, P value = 0.0409. Statistical significance of differences between *Myo10*<sup>-/-</sup> oo oocytes and control oocytes was assessed by a two-tailed Mann Whitney test, P value = 0.7405. n.s not significant.

**E)** Schemes summarizing the most important morphological features used by our machine learning algorithm to discriminate a control oocyte (left image) from a *Myo10*<sup>-/-</sup> full oocyte (right image). Features include detection of vertical TZP-like structures in the *zona pellucida* (Fig.4 D-F), heterogeneity in perivitelline space thickness (Fig.4 D, G) and oocyte circularity C).

**Figure S4: Biotype of deregulated transcripts and enriched GO terms from *Myo10*<sup>+/-</sup> and *Myo10*<sup>-/-</sup> full oocytes RNA-Seq analysis**

**A)** Pie chart of deregulated transcript biotypes from the RNAseq analysis described in Fig.3A. lincRNA: long intergenic non-coding RNAs, miRNA: microRNA precursors, Mt-tRNA: transfer RNA located in the mitochondrial genome and TEC: To be Experimentally Confirmed.

**B)** Bar graph of significantly over-represented GO cellular component terms in the RNA-Seq deregulated gene list. Statistical significance of differences was assessed

by a Fisher's exact test with false discovery rate correction. Note that the list of terms is not exhaustive.

**C)** Bar graph of significantly over-represented GO molecular function terms in the RNA-Seq deregulated gene list. Statistical significance of differences was assessed by a Fisher's exact test with false discovery rate correction. Note that the list of terms is not exhaustive.

**Figure S5: The cytoplasmic F-actin network is normally organized in *Myo10*<sup>-/-</sup> full oocytes**

**A)** Equatorial planes of control (left) and *Myo10*<sup>-/-</sup> full (right) oocytes stained with phalloidin 6h after NEBD. Scale bar 10 μm.

**B)** Scatter plot of cytoplasmic F-actin intensity 6h after NEBD in control (dark gray) and *Myo10*<sup>-/-</sup> (green) full oocytes. (n) is the number of oocytes analyzed. Data are mean±s.d. with individual data points plotted. Data are from three independent experiments. Statistical significance of differences was assessed by a two-tailed Mann Whitney test, P value = 0.0111.

**C)** Images of spindles and F-actin cages from control (left panel) and *Myo10*<sup>-/-</sup> full (right panel) oocytes 6h after NEBD. Oocytes are stained for Tubulin (TUB, yellow, left panel images) and stained with phalloidin (black, right panel images). Scale bar 10 μm.

**Table 1: Differential gene expression between competent *Myo10*<sup>+/-</sup> and *Myo10*<sup>-/-</sup> full oocytes arrested in prophase I performed by RNA-Seq**

**Sheet 1)** Raw data from the RNA-Seq analysis shown in Fig.3A. **Sheet 2)** The 685 deregulated transcripts selected with a P adj < 0.05. The transcripts highlighted in green are those selected to be validated by the RT-qPCR analysis presented in Fig.3B. **Sheet 3)** The exhaustive list of significantly over-represented GO biological process terms in the list of deregulated transcripts. Significance was set at FDR P < 0.05. Terms highlighted in green are those shown in the bar graph in Fig.3C. **Sheet 4)** The exhaustive list of significantly over-represented GO cellular component terms in the list of deregulated genes. Significance was set at FDR P < 0.05. Terms highlighted in green are those shown in the bar graph in Fig.S3B. **Sheet 5)** The exhaustive list of significantly over-represented GO molecular function terms in the list of deregulated genes. Significance was set at FDR P < 0.05. Terms highlighted in green are those shown in the bar graph in Fig.S3C.

**Movie S1: Decreased TZP density in *Myo10*<sup>-/-</sup> full oocytes highlighted by OMX super-resolution microscopy**

OMX microscopy movies showing TZPs of oocytes arrested in prophase I, freed of follicular cells and stained with phalloidin. The control oocyte is on the left and the *Myo10*<sup>-/-</sup> full oocyte is on the right. Movies are 3D projection images reconstructed from the 125 nm spaced Z acquisition from the outer layer of the *zona pellucida* (ZP) to the oocyte cortex. Movies start with the top view of the ZP outer layer, rotate to a ZP cross-sectional view and come back to the ZP outer layer. Scale bar 5  $\mu\text{m}$ .

**Movie S2: Intra-ovarian organization of *Myo10*<sup>-/-</sup> full mice**

Light-sheet fluorescence microscopy movies of cleared ovaries stained with TO-PRO-3 to label nucleic acid. Movies are cross-sectional images of the ovaries spaced 1  $\mu\text{m}$  apart. **A)** Movies of four ovaries from two adult control mice. **B)** Movies of four ovaries from two adult *Myo10*<sup>-/-</sup> full mice. Scale bars 200  $\mu\text{m}$ .

**Movie S3: A subpopulation of *Myo10*<sup>-/-</sup> full oocyte arrest development in meiosis**

!

Spinning disk movies showing brightfield images of a control oocyte (top movie), a *Myo10*<sup>-/-</sup> full oocyte that extruded a polar body (middle movie) and a *Myo10*<sup>-/-</sup> full oocyte that did not extrude a polar body (bottom movie). The oocytes are those shown in Fig.6 A. Movies start 2 h 30 after NEBD and end 18 h after NEBD. Images are acquired every 30 min. Scale bar 10  $\mu\text{m}$ .

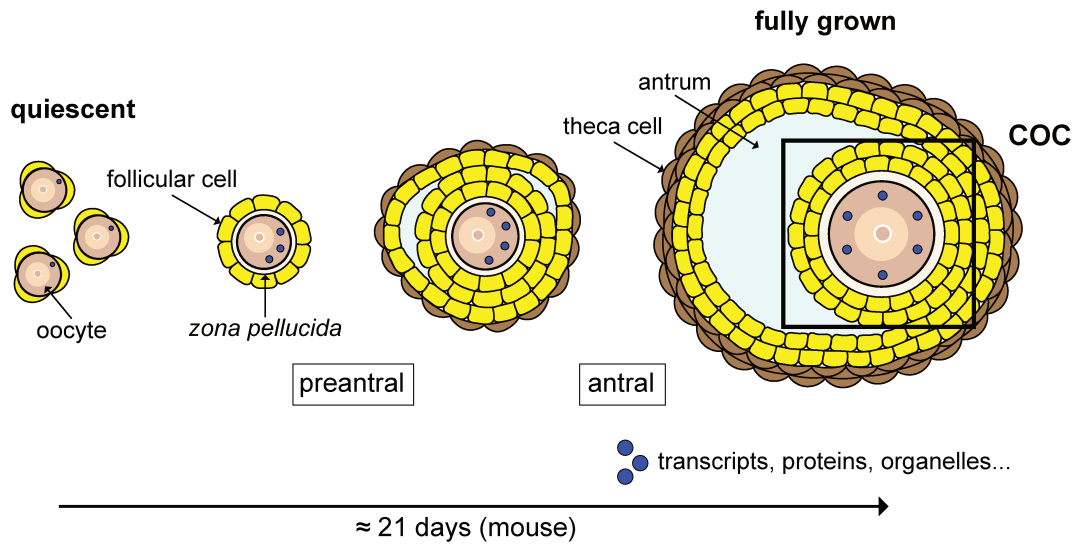
**Movie S4: *Myo10*<sup>-/-</sup> full oocytes correctly form and position meiosis I spindles**

Spinning disk movies of oocytes stained with SiR-tubulin (SiR-tub) to label microtubules (yellow) from 30 min to 14 h 30 after NEBD. The top movies show a control oocyte, the middle movies a *Myo10*<sup>-/-</sup> full oocyte that extruded a polar body and the bottom movies a *Myo10*<sup>-/-</sup> full oocyte that did not extrude a polar body. For each oocyte, the left movie shows Max intensity Z Projection of SiR-tub labeling and the right movie the same SiR-tub labeling merged with the corresponding brightfield images. The oocytes are those shown in Fig.7 A. Images are acquired every 30 min. Scale bar 10  $\mu\text{m}$ .

**Movie S5: *Myo10*<sup>-/-</sup> full oocytes properly align meiosis I chromosomes**

Spinning disk movies of oocytes injected with H2B-GFP to label chromosomes from 2 h 30 to 18 h after NEBD. Images are Max Intensity Z Projection of H2B labeling. The top movie shows chromosomes of a control oocyte, the middle movie chromosomes of a *Myo10*<sup>-/-</sup> full oocyte that extruded a polar body, and the bottom movie chromosomes of a *Myo10*<sup>-/-</sup> full oocyte that did not extrude a polar body. The oocytes are those shown in Fig.7 F. Images are acquired every 30 min. Scale bar 10 μm.

A



B

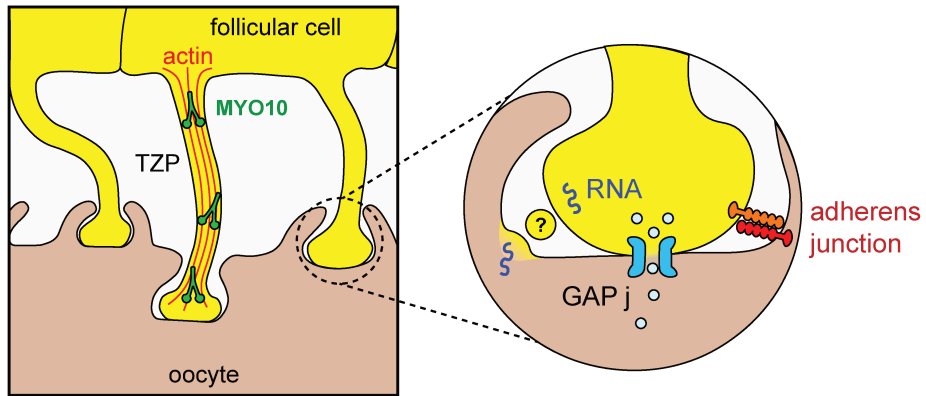
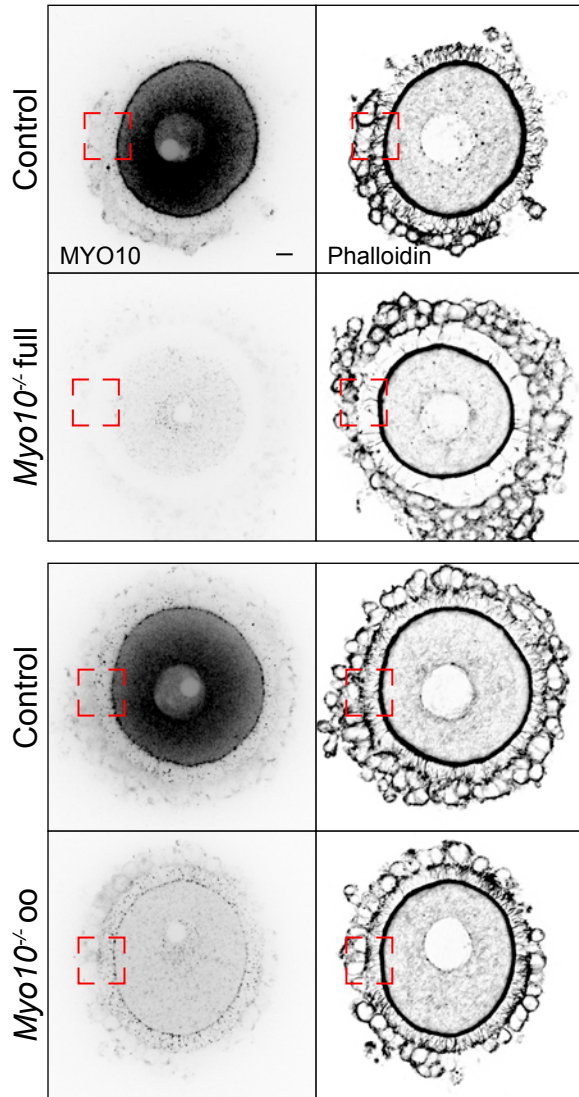
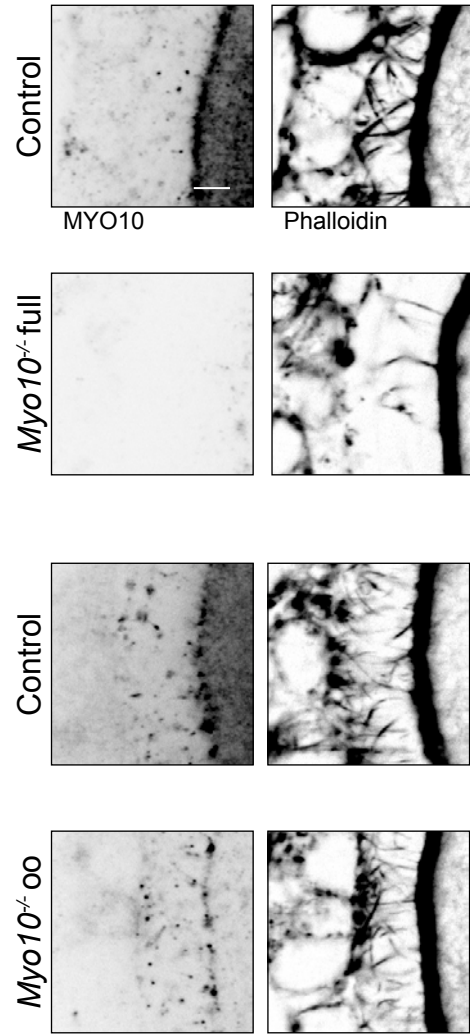
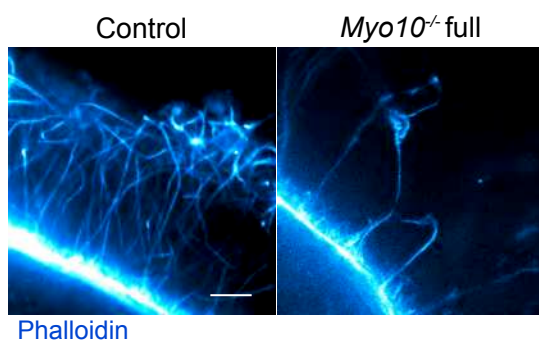
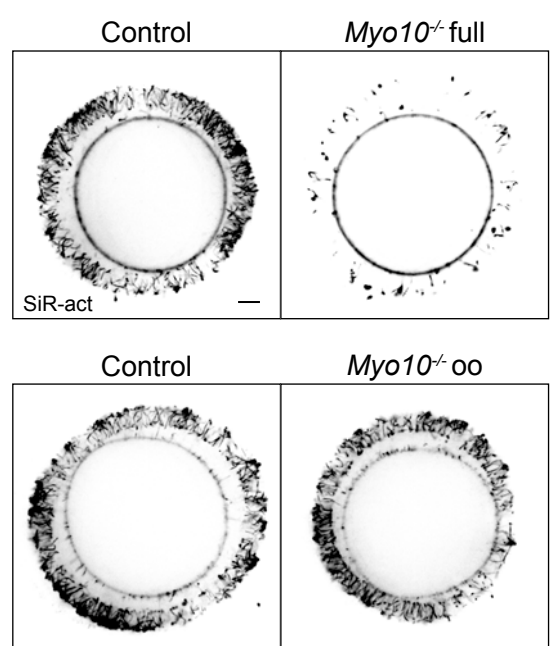
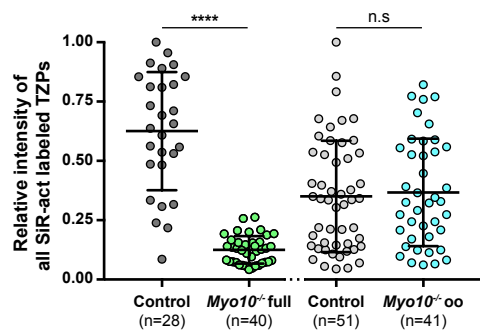
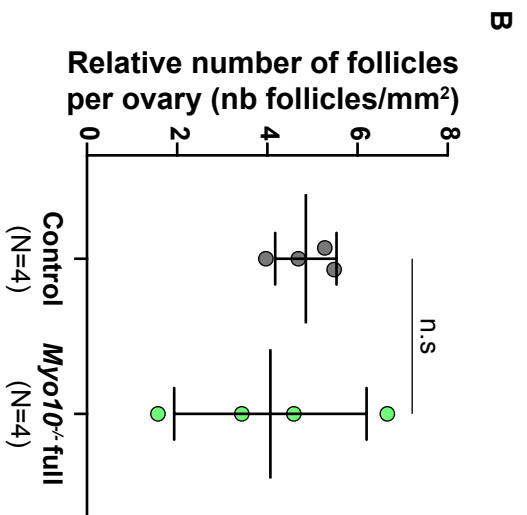
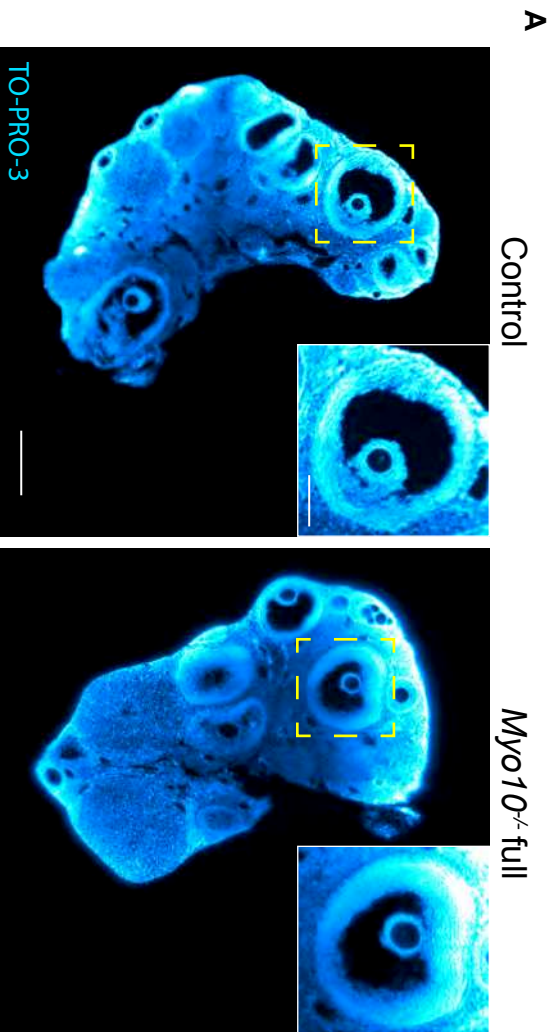
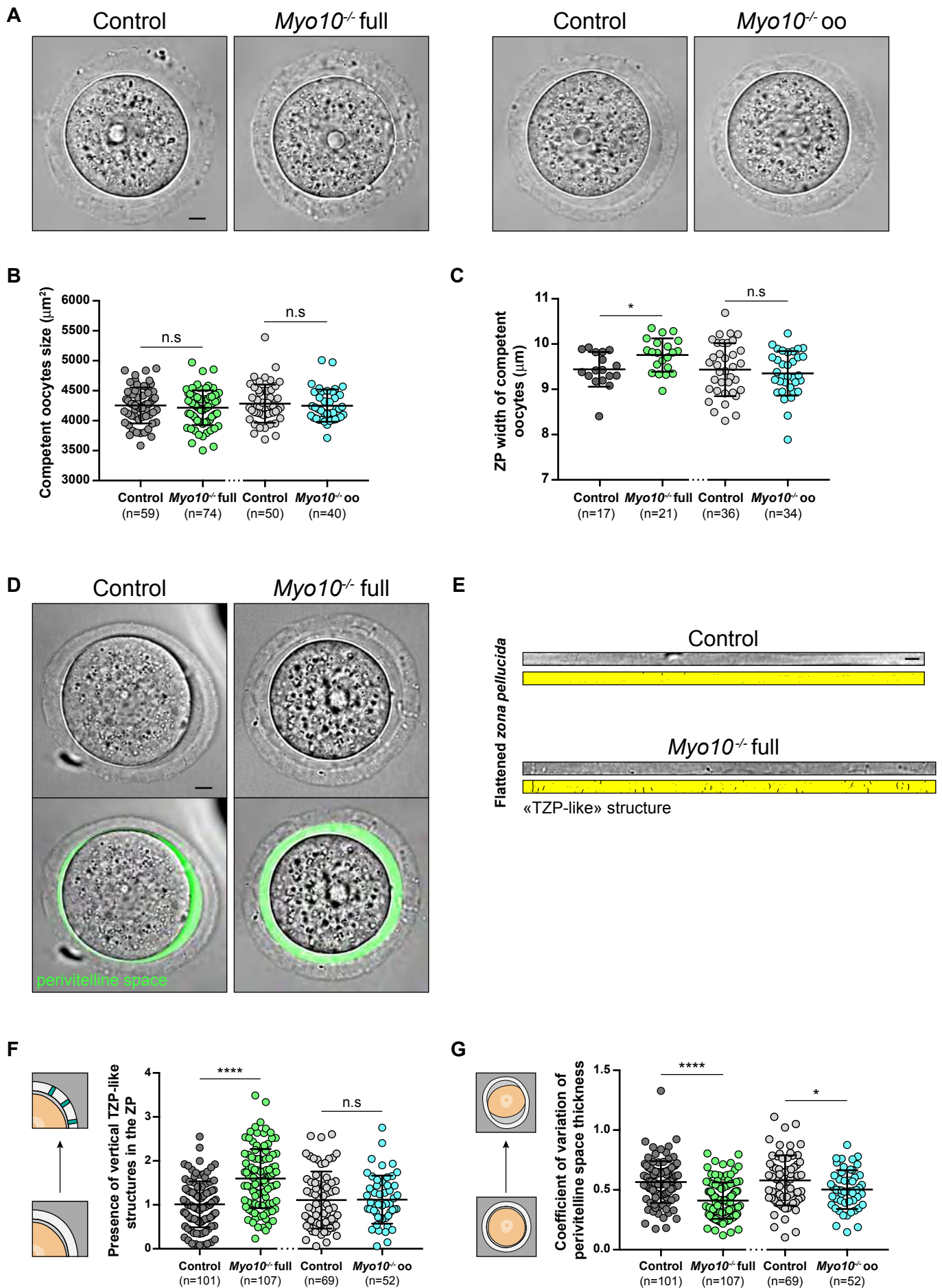


Figure 1

**A****B****C****D****E****Figure 2**



**Figure 3**



**Figure 4**

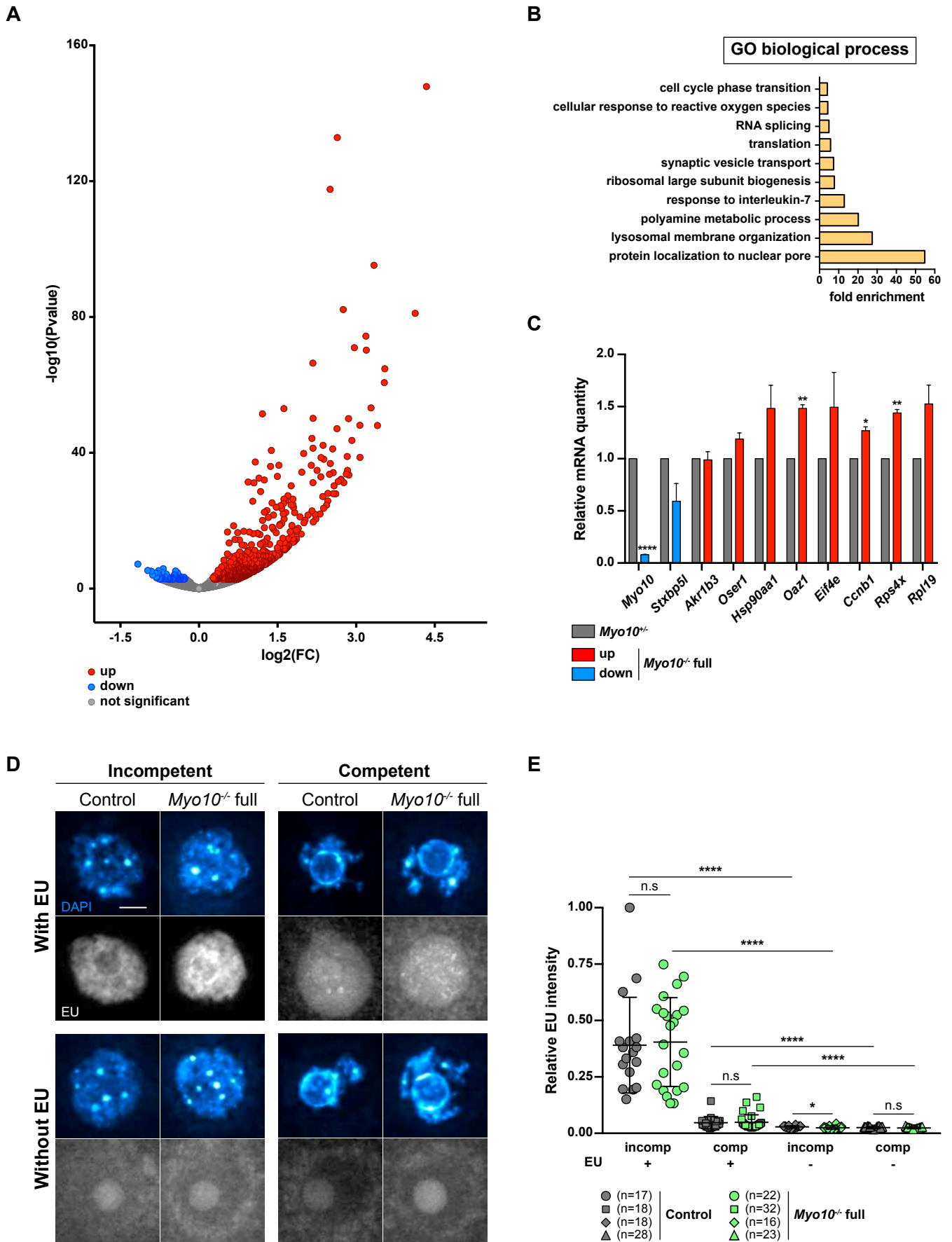
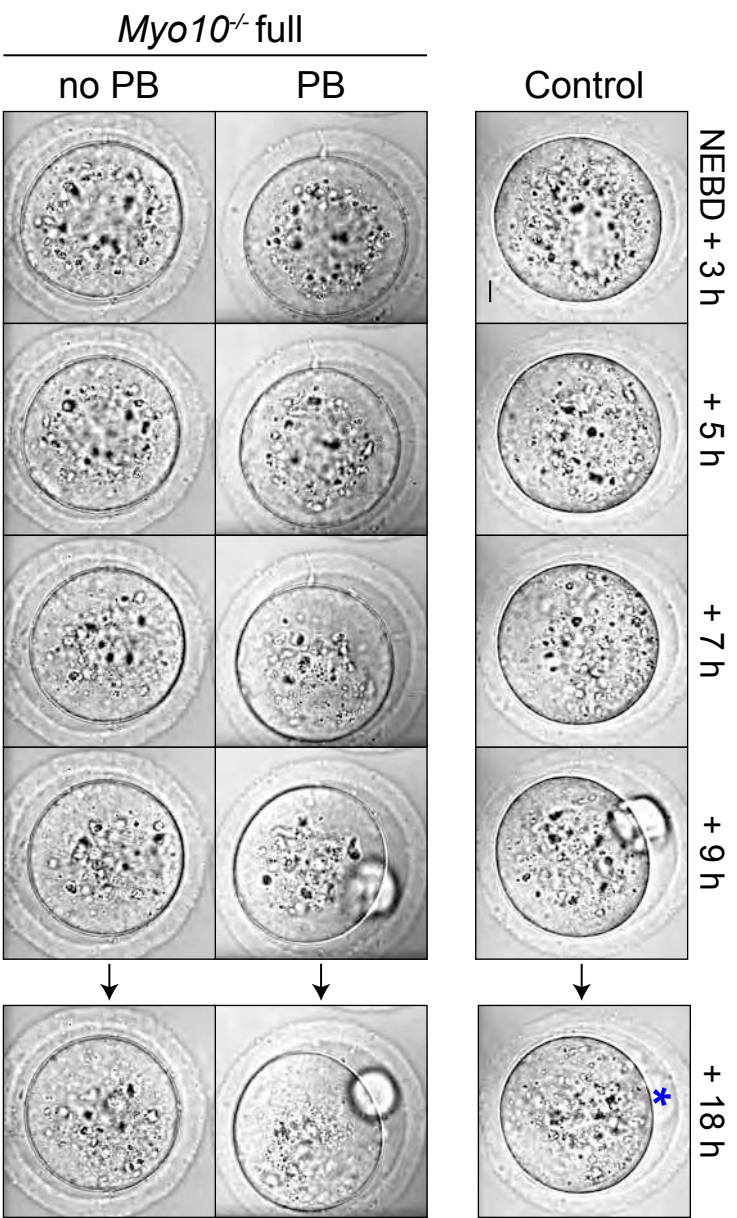
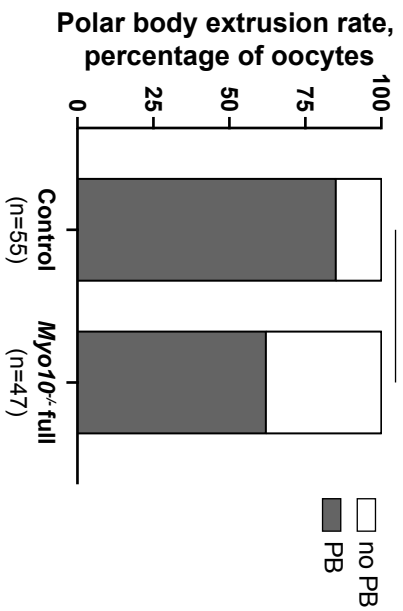
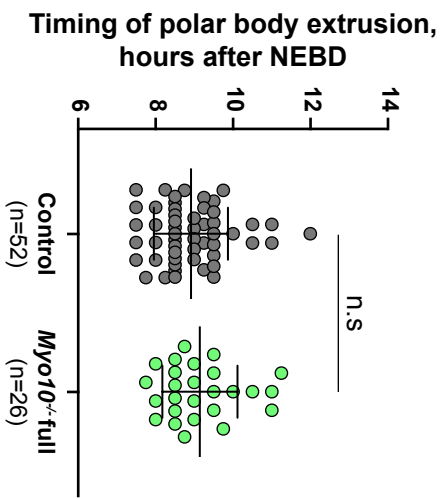
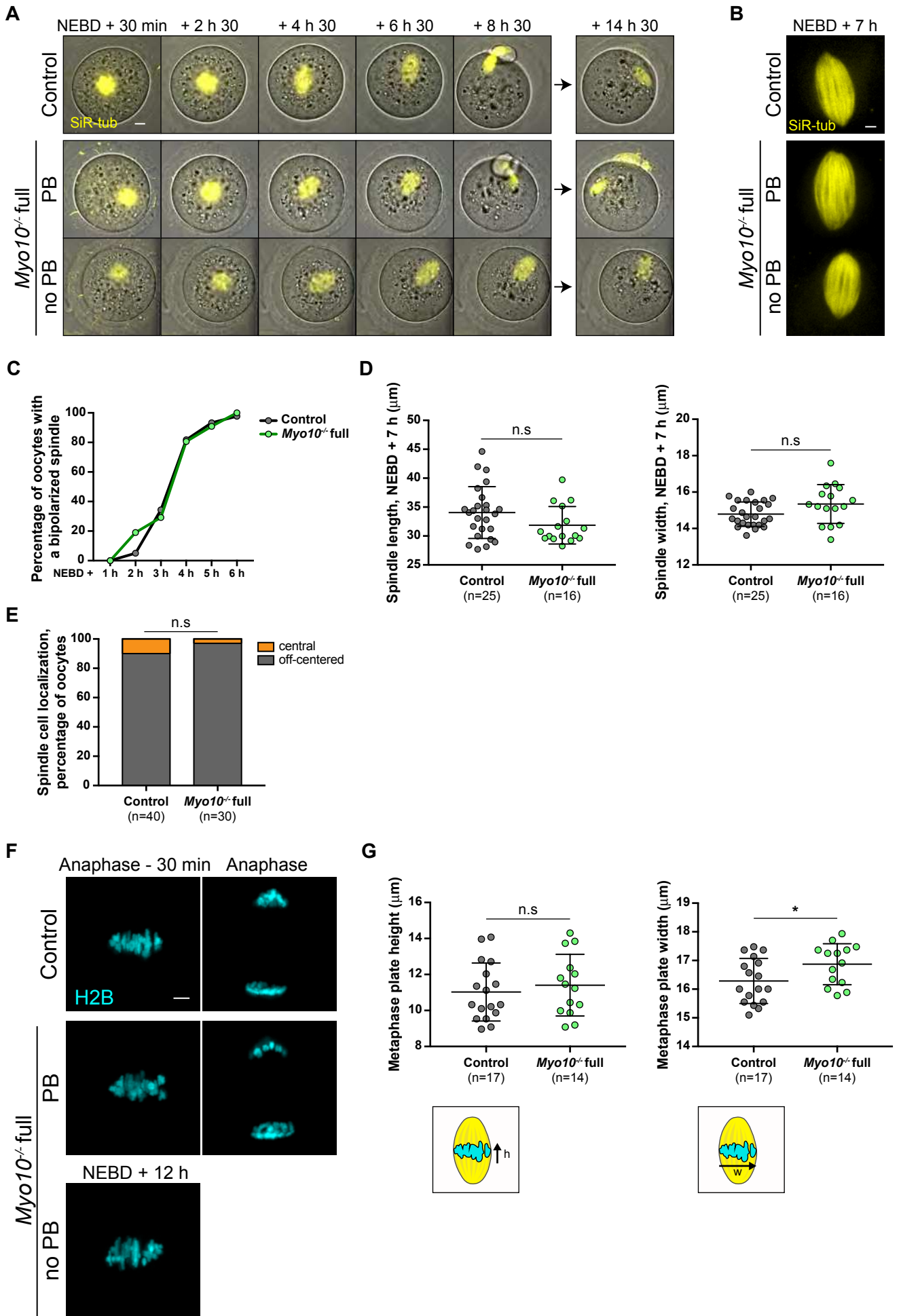
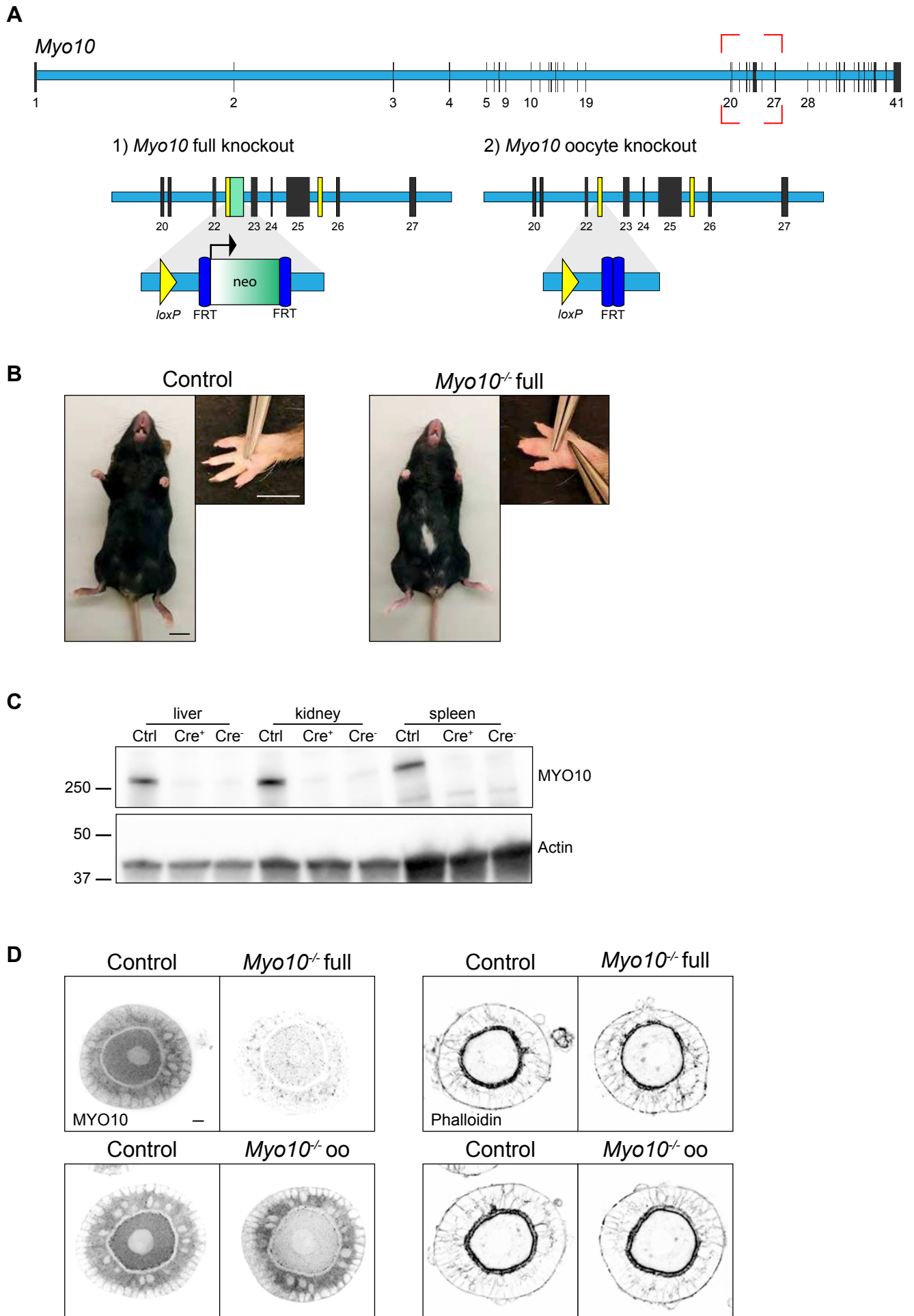


Figure 5

**A****B****C****Figure 6**



**Figure 7**



**Figure S1**

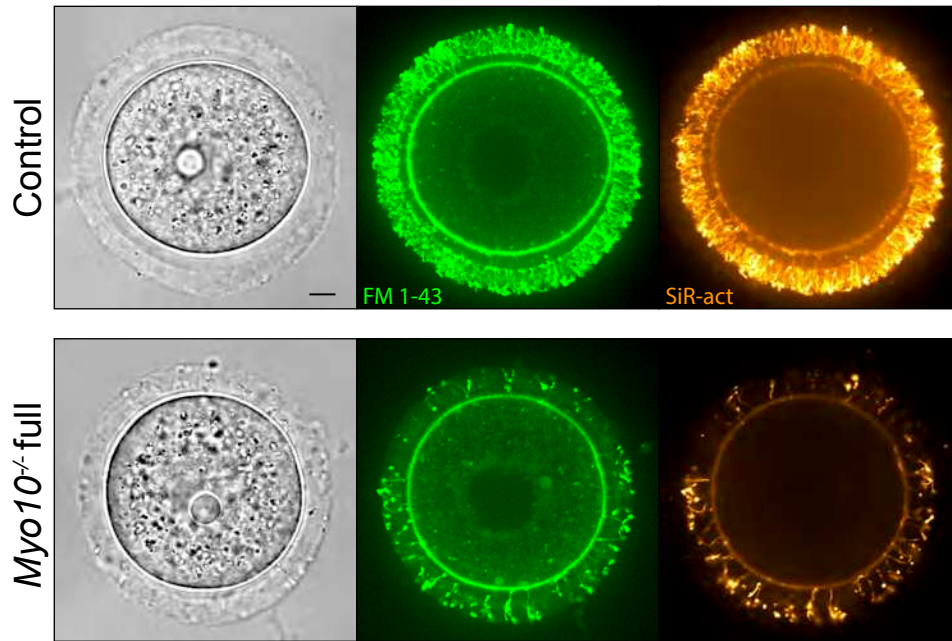


**Figure S2**

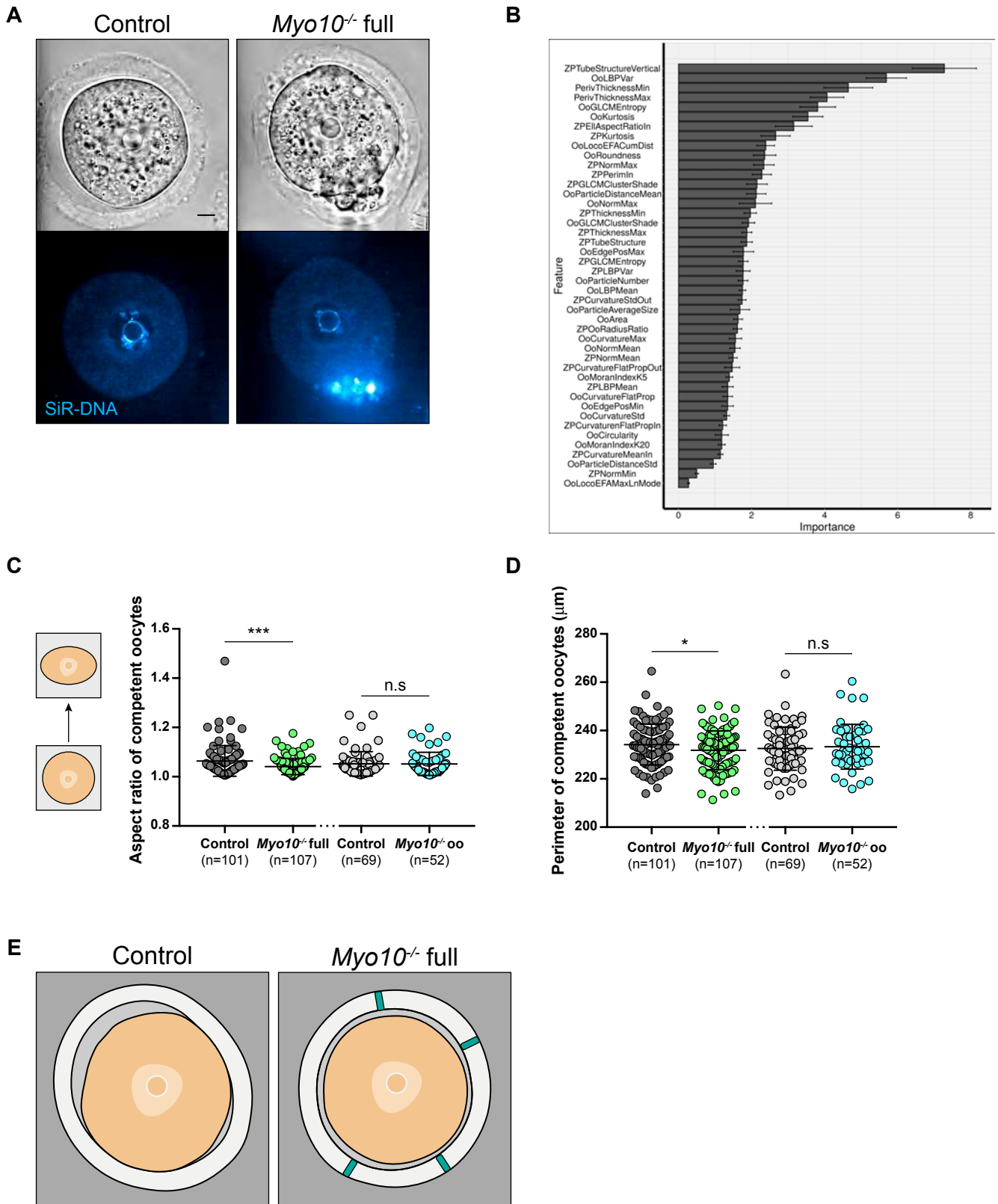
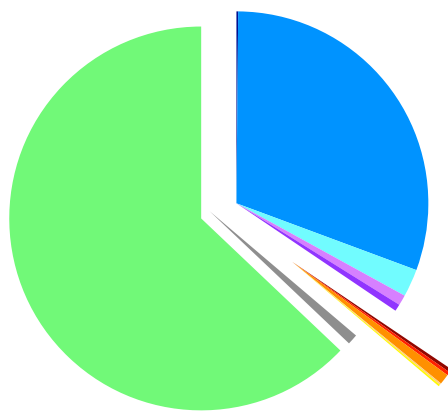
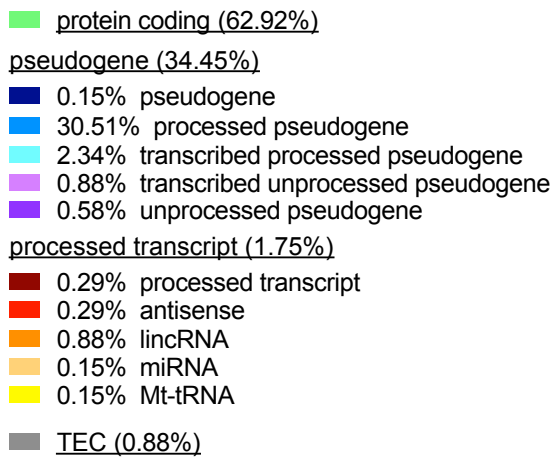


**Figure S3**

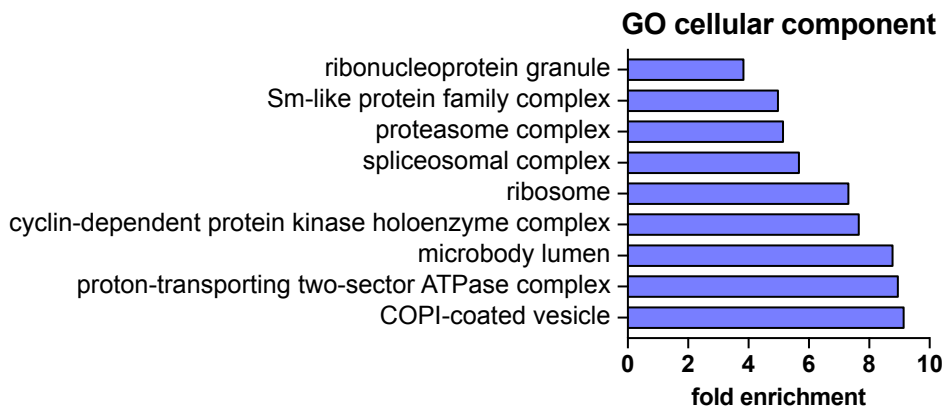
**A**



**Biotype of deregulated transcripts**



**B**



**C**

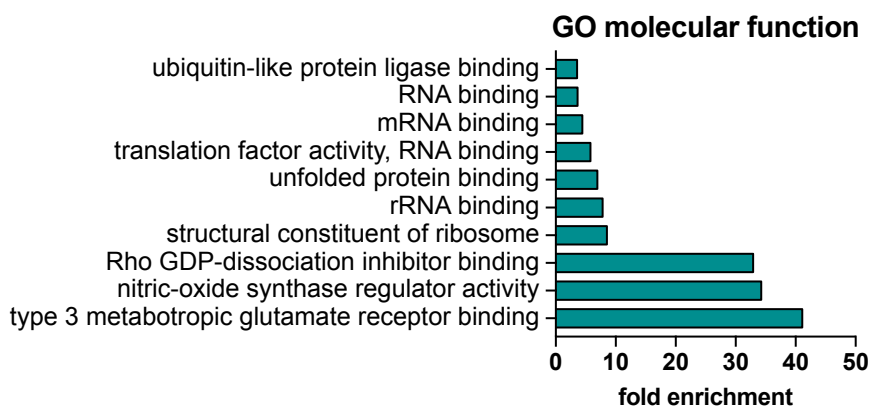


**Figure S4**

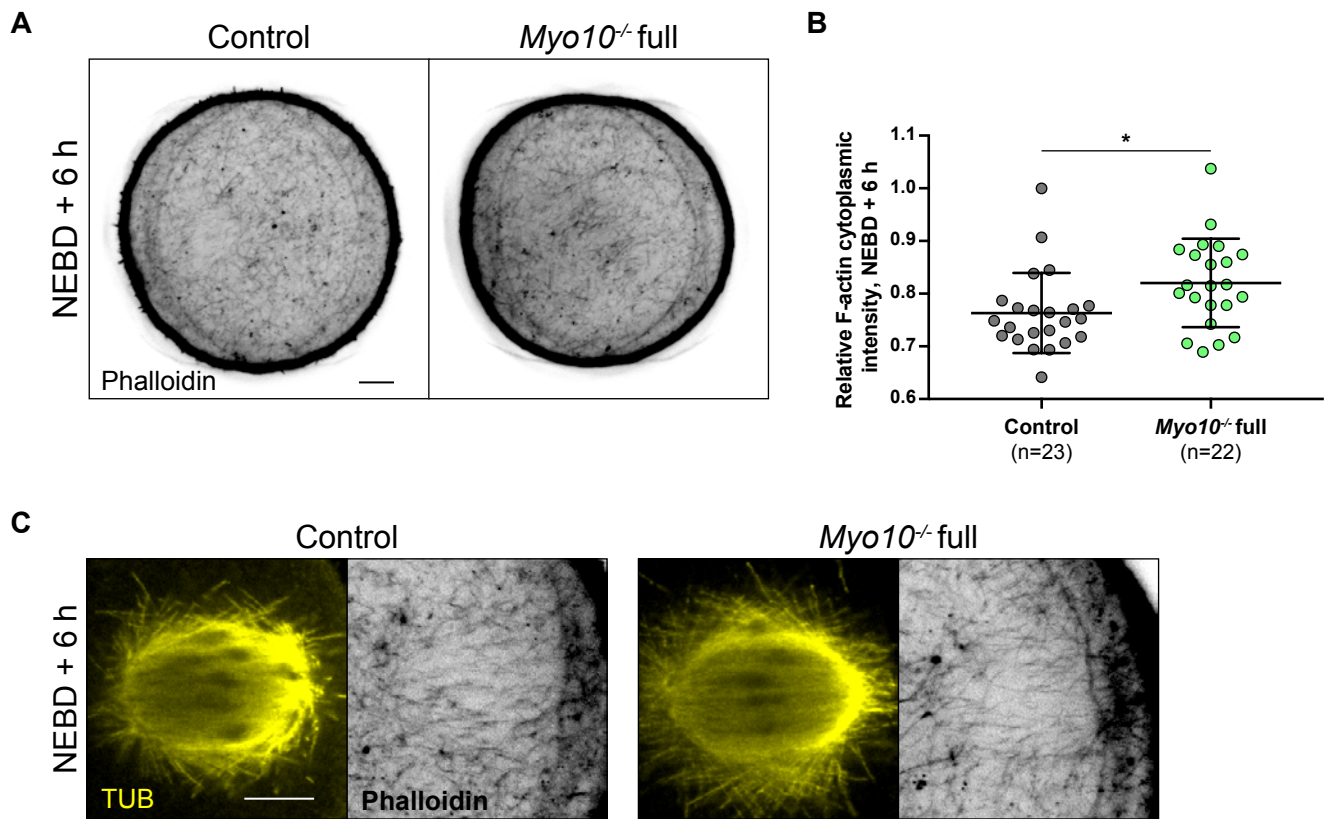


**Figure S5**

# **DISCUSSION**

*This section expands on the discussion initiated in the main article of this study, i.e. the involvement of transzonal projections in oocyte developmental competence. In this regard, I develop here the three axes discussed earlier in the article: the unexpected canonical size attained by TZP-deprived oocytes at the end of growth, the likely impact of TZPs on zona pellucida integrity, and the possible origins of the meiosis I arrest observed in some TZP-deprived oocytes.*

By generating mice totally depleted of Myosin-X, the molecular motor identified as a likely component of transzonal projections, we severely reduced the density of somatic contacts received by the oocyte before the resumption of meiosis. We studied the impact of this reduction on oocyte quality, focusing on the morphology of competent oocytes at the end of growth and their ability to complete meiotic maturation. Taken together, our results support the consensus that TZPs are required for oocyte quality. Interestingly, they also tend to revise downward the extent of TZP support for oocyte development, as pointed out by our collaborator Hugh Clarke early in this study. Here, I will discuss the possible origins of oocyte phenotypes caused by reduced TZP density. I will also provide my interpretation of how some aspects of oocyte development, particularly oocyte growth, were not affected to the extent expected by decreased TZP density.

## **I) TZP-deprived oocytes reach canonical size**

### **1) TZP density reduction and oocyte size in the literature**

Several studies in mice have reported TZP disruption or decreased TZP density following targeted gene deletion (Carabatsos 1998, McGinnis and Kinsey 2015, Lowther 2017, Zhang 2021) or in aged females (El-Hayek 2018). In these situations, oocyte size has been measured. Although the role of decreased TZP density on oocyte size in these studies should be taken with caution, as additional follicular defects caused by the various gene deletions may have affected oocyte growth, it is interesting to note the correlation between decreased TZP density and oocyte size.

Among these studies, the following reported a decrease in oocyte size or delay in oocyte growth when TZP density was reduced (Lowther and Mehlmann 2015, Lowther 2017, McGinnis and Kinsey 2015, Zhang 2021). In Lowther 2017, TZP disruption was observed as early as the late preantral stage in mice deficient in EPAB, an oocyte poly(A)-binding protein. The decrease in size of these oocytes compared to controls was reported as discrete in Lowther and Mehlmann 2015. However, it should be considered that EPAB depletion may have impacted the expression of oocyte transcripts accumulated during growth, thereby potentially affecting oocyte size independently of TZP number. McGinnis and Kinsey reported a reduction in TZP

number following depletion in the oocyte of Proline-rich tyrosine kinase 2, a focal adhesion kinase involved in the formation and maintenance of adhesion junctions. In their study, oocyte diameter was measured at metaphase II, after extrusion of the first polar body. A measurement of oocyte size in prophase I would have been of interest to exclude a possible defect in spindle migration in these oocytes that could have led to a change in division geometry and contributed to the decrease in oocyte size compared to controls. The reduction in TZP density in Zhang 2021 was observed following deletion in the oocyte of radixin, a gene involved in microvilli formation, which led to a loss of oocyte microvilli. The authors proposed that the reduction in TZP density may have been caused by altered release of oocyte factors, such as GDF-9, following the loss of oocyte microvilli. In this study, although interesting to consider, the role of TZPs in oocyte growth cannot be separated from that of oocyte microvilli.

Reversely, in El-Hayek 2018 and Carabatsos 1998, an increase in oocyte diameter was reported to correlate with decreased TZP numbers. El-Hayek and colleagues observed this correlation in aged mice. In this context, other oocyte defects triggered by aging could also have contributed to the increase in oocyte size. Carabatsos and colleagues noted the reduction in TZP density in mice deficient in GDF-9. As discussed earlier in the Results section, the increase in the diameter of these oocytes could have resulted from the lack of GDF-9 regulation of Kit ligand expression in granulosa cells (Elvin 1999), which may have impacted oocyte growth.

In mice lacking MYO10, we did not measure a difference in size between competent TZP-deprived oocytes and controls. In our case, we did not measure TZP density during the growth of *Myo10*<sup>-/-</sup> follicles, as we only assessed TZP density at the antral stage. Indeed, we lack robust data on TZP density at the preantral stage, as our fixation protocols used for immunostaining did not preserve the integrity of preantral follicles from control and *Myo10*<sup>-/-</sup> mice. In addition, it is possible that the preantral follicles collected were undergoing atresia. Therefore, we cannot exclude that oocytes from *Myo10*<sup>-/-</sup> full follicles received a canonical number of somatic contacts (or a sufficient TZP density to grow properly) during the preantral stage. This could have led to oocytes having a similar size to controls at the end of growth despite the reduction in TZP density later in the antral stage.

Therefore, there are two possibilities to explain the lack of growth defects in *Myo10*<sup>-/-</sup> full oocytes. First, it is possible that MYO10 depletion led to a reduction in TZP density too late in follicular growth to affect oocyte size. Second, it is possible that

the decrease in TZP density occurred early in growth, but that TZPs play a minor role in shaping oocyte size, or do not need to be in large numbers for the latter, or that compensatory factors have been implemented to compensate the decrease in TZP density. The same hypotheses of sufficient remaining intercellular communication, or compensatory mechanism, were proposed by Lowther 2017 to explain how follicles from EPAB-deficient mice could develop beyond the preantral stage despite TZP disruption.

To determine the latter, it would be worthwhile to measure the density of live-labeled-TZPs (as done in the article) of all the antral stage oocytes we have already collected. This would encompass both incompetent oocytes (including those that have not completed growth) and competent oocytes (fully grown). We will then plot the density of TZPs as a function of oocyte size. This will allow us to determine, first, whether TZP density is different between control and *Myo10*<sup>-/-</sup> full oocytes of similar size, especially the smaller ones. Second, this will allow us to compare TZP density between *Myo10*<sup>-/-</sup> full oocytes of different sizes, and therefore determine the extent of TZP density decrease throughout the completion of the growth phase. If we do not measure a decrease in TZP density between small control and *Myo10*<sup>-/-</sup> full oocytes, this will indicate that MYO10 is involved in the maintenance of TZPs, rather than their formation. However, if we measure a significant decrease in TZP density between the two conditions in small antral stage oocytes, then we will need to determine TZP density further upstream in oocyte growth, in preantral stage oocytes, to conclude on the latter.

To access TZP density at the preantral stage, it would be important to follow TZPs dynamics in live during oocyte growth. Crossing mice of the *Myo10*<sup>-/-</sup> full knockout strain with mice expressing a membrane-targeted fluorescent protein (as used in El-Hayek 2018 and Zhang 2021) would allow live labeling and monitoring of TZPs throughout growth in *in vitro* follicular assays (with a microscope enabling live acquisition of whole follicles) and measure the correlation between TZP density and the growth rate of *Myo10*<sup>-/-</sup> full and control oocytes.

## 2) Oocyte-directed compensation for increased nutrient uptake?

Although we do not know if *Myo10*<sup>-/-</sup> full oocytes were provided with fewer somatic contacts than controls early in their growth, I will assume for the rest of the discussion that they received a reduced density of TZPs for a substantial period of growth. This will allow me to discuss whether the remaining TZPs were in sufficient numbers to allow the growth of *Myo10*<sup>-/-</sup> full oocytes, or whether compensatory mechanisms occurred to offset the reduction in somatic contacts.

As discussed earlier in the article, the presence of functional gap junctions located at the interface between the remaining TZPs and the oocyte is a reasonable assumption to explain how the competent *Myo10*<sup>-/-</sup> full oocytes achieved a canonical size. In this way, the junctional coupling between the granulosa cells and the oocyte, required for proper oocyte development (Simon 1997), would have been preserved to allow oocyte growth. In this regard, it is possible that the number of TZP-oocyte gap junctions was sufficient to permit the growth of *Myo10*<sup>-/-</sup> full oocytes without oocyte-ordered compensation. However, we can also assume that *Myo10*<sup>-/-</sup> full oocytes requested the granulosa cells to enhance metabolic coupling to compensate for the decrease in TZP density.

In this respect, it is possible that *Myo10*<sup>-/-</sup> full oocytes modulated the expression level of connexins (or proteins promoting gap junction formation and function) in granulosa cells to increase oocyte-somatic cells coupling. This hypothesis is supported by the fact that Bone morphogenetic protein 15, a factor secreted by the oocyte, down-regulated the expression of Connexin 43 in immortalized human granulosa cells, a connexin that composes gap junctions at the interface between granulosa cells (Chang 2014). The latter was correlated with a decrease in the activity of gap junction communication between granulosa cells. Similarly, but in reverse, it is possible that *Myo10*<sup>-/-</sup> full oocytes increase the expression in granulosa cells of connexins located at the TZP-oocyte interface, or of genes involved in promoting gap junction formation or function, to enhance oocyte-somatic cell coupling.

In addition, the *Myo10*<sup>-/-</sup> full oocyte may also have instructed the granulosa cells to increase their accumulation of metabolites for subsequent uptake by the oocyte. Interestingly, it has been shown in mice that the oocyte regulates the expression in granulosa cells of genes encoding glycolytic enzymes (Sugiura 2005) and the amino acid transporter Solute carrier family 38, member 3 (Eppig 2005). These modulations

would notably allow an adequate level of metabolites in the granulosa cells for subsequent transfer to the oocyte. Therefore, *Myo10*<sup>-/-</sup> full oocytes could increase the metabolic activity of the granulosa cells to obtain sufficient metabolite content. This would account for the correct growth of *Myo10*<sup>-/-</sup> full oocytes despite the decrease in somatic contacts.

## II) Possible effects of TZPs on *zona pellucida* integrity

### 1) Impaired *zona pellucida* due to altered expression/secretion of its component proteins?

We described several phenotypes in *Myo10*<sup>-/-</sup> full oocytes that suggest that they display an altered *zona pellucida*. Notably, their matrix is discreetly thicker than that of controls and occasionally allows granulosa-like cells to be present in an ectopic manner in the perivitelline space.

Given that the proteins composing the *zona pellucida* are exclusively expressed by the oocyte in mice (Wassarman and Litscher 2018), TZPs may participate indirectly in this process by modulating their expression or secretion by the oocyte through the mediation of intercellular communication. In this regard, decreased TZP density in *Myo10*<sup>-/-</sup> full follicles may have led to impaired communication between granulosa cells and the oocyte. This potential impairment, while not preventing the oocyte from reaching canonical size (see paragraph above), may have affected the ability of the oocyte to properly mediate *zona pellucida* assembly. It should be noted that transcripts encoding ZP1, 2 and 3, the three proteins that compose the *zona pellucida* in mice, are not significantly deregulated in *Myo10*<sup>-/-</sup> full oocytes compared to control oocytes, as revealed by our RNA-Seq analysis. However, it is possible that the protein level of ZP1, 2 or 3 is altered, or that *Myo10*<sup>-/-</sup> full oocytes secreted these proteins in an impaired or unregulated manner, leading to the phenotypes described above.

### 2) Impaired *zona pellucida* due to lack of matrix degradation by TZPs?

In addition to a possible indirect role of TZPs in regulating expression/secretion of *zona pellucida* proteins by the oocyte, it is possible that TZPs modulate the

extracellular matrix by secreting proteases locally. In fact, it remains to be understood how TZPs penetrate and develop in the matrix. One possibility is that TZPs degrade the *zona pellucida* to create a path through which they can grow.

This latter process would be reminiscent of that used by invadopodia, cellular protrusions established by cancer cells that are suggested to promote cell invasion into the stroma by degrading basement membranes (Schoumacher 2010, Paterson and Courtneidge 2018). Interestingly, MYO10 is involved in the formation of invadopodia (Schoumacher 2010). MYO10 depletion in cancer cell lines by siRNA not only resulted in a decrease in the proportion of long invadopodia in the cells, but also reduced the number of cells capable of matrix degradation and the extent of that degradation. Schoumacher and colleagues notably hypothesized that MYO10 would transport matrix metalloproteinases, proteases involved in basement membrane degradation, along the invadopodia. It is interesting to consider that TZPs, also MYO10-rich protrusions, could make their way into the *zona pellucida* in a similar manner. In this regard, the decrease in TZP density in *Myo10*<sup>-/-</sup> full follicles would lead to a decrease in extracellular matrix digestion. This could account for the discreet increase in *zona pellucida* thickness measured in *Myo10*<sup>-/-</sup> full oocytes compared to controls.

Since the *zona pellucida* is involved in fertilization and early embryo development, alteration of its integrity could lead to fertility defects. It would be interesting to *in vitro* fertilize *Myo10*<sup>-/-</sup> full oocytes with control spermatozoa to assess whether oocytes can be fertilized and sustain early embryonic development with a presumed altered *zona pellucida*.

### **III) Origins of metaphase I arrest in some TZP-deprived oocytes**

As discussed in the first part of this section, functional gap junctions between the oocyte and granulosa cells are the most likely hypothesis to explain the fact that competent *Myo10*<sup>-/-</sup> full oocytes were able to reach a canonical size. Nevertheless, we cannot exclude that gap junctions were not sufficient in number or efficient enough to mediate other biological processes in the follicle than oocyte size increase. In addition, other intercellular communications (e.g., potential exchange of extracellular vesicles) may have been impaired as a result of the decrease in TZP density. Such an alteration in oocyte-somatic cell interaction may have lowered the quality of *Myo10*<sup>-/-</sup> full oocytes

prior to meiosis resumption. This may explain the slightly reduced ability of these oocytes to complete meiosis I. However, it should be considered that oocyte defects caused by possible impaired communication with granulosa cells are probably moderate, as more than half of the *Myo10*<sup>-/-</sup> full oocytes successfully reached meiosis II. However, we still do not know if these meiosis II oocytes give rise to good quality embryos after fertilization, since these experiments are still ongoing.

### 1) Alteration of oocyte lipid content?

Interestingly, it has been shown in cows that Fatty acid-binding protein 3 (FABP3), a protein involved in fatty acid transport, is contained in TZPs (Del Collado 2017). The authors proposed that TZPs may mediate the transport of FABP3, and by extension fatty acids, from cumulus cells to the oocyte during *in vitro* maturation, and thereby be involved in lipid accumulation in the oocyte. This hypothesis is supported by the fact that oocyte lipid content decreased when TZPs were disrupted by cytochalasin B during *in vitro* maturation, compared to untreated controls. Therefore, granulosa cells may act as modulators of oocyte lipid content through potential TNP-mediated transport of protein-associated fatty acids.

In our case, *Myo10*<sup>-/-</sup> full oocytes underwent meiotic maturation devoid of cumulus cells. Hence, assuming that TZPs regulate oocyte lipid content, this regulation could only have occurred earlier during oocyte growth. It is conceivable that the decrease in TNP density led to a decline in intercellular fatty acid transport, causing a decrease in oocyte lipid content before and during meiotic maturation.

Importantly, while a relative increase in oocyte lipid content has been associated with impaired meiotic maturation in mice (Yang 2012, as cited in Del Collado 2017), the effect of decreased oocyte lipid content on maturation has not been addressed to my knowledge. Indeed, mouse oocytes from COCs undergoing *in vitro* maturation in human follicular fluid considered lipid-rich had higher lipid content and decreased ability to reach metaphase II than oocytes from COCs cultured in follicular fluid considered lipid-poor (Yang 2012). It should be noted that in this study, the lipid content of oocytes from COCs matured in lipid-poor follicular fluid was not different from that of oocytes matured *in vivo*. Therefore, although outside the scope of this article, Yang's 2012 study cannot provide information on the effect of low oocyte lipid content on

meiotic maturation. However, considering that fatty acids are involved in different biological processes, including regulating the physical properties of cellular membranes and supplying cells with energy (de Carvalho and Caramujo 2018), it is conceivable that a possible decrease in oocyte lipid content prior to meiosis resumption could have participated in the metaphase I arrest occurring in some *Myo10*<sup>-/-</sup> full oocytes. An easy experiment to determine this, which we have begun to perform, would be to incubate oocytes with a lipid dye (e.g., Nile red) in prophase I and compare the total cell intensity signal of the dye in *Myo10*<sup>-/-</sup> full oocytes with that in control oocytes. At present, we have not observed any alteration in the cellular localization and organization of Nile red in *Myo10*<sup>-/-</sup> full oocytes compared to controls, but the signal intensity of the dye remains to be quantified. If a decrease in lipid content is confirmed in TZP-deprived oocytes, then it would be interesting to test whether there is a correlation between the intensity or pattern of the Nile red signal and whether or not the *Myo10*<sup>-/-</sup> full oocyte has succeeded in extruding a polar body.

## 2) Unregulated oocyte pH<sub>i</sub> during growth?

Oocytes have a poor ability to regulate their intracellular pH (pH<sub>i</sub>) during growth. They rely on granulosa cells to perform this process until they become progressively autonomous to do so as they increase in size. It is proposed that through oocyte-somatic cell gap junctions, oocytes benefit from the pH-regulatory mechanisms of the granulosa cells (e.g., HCO<sub>3</sub><sup>-</sup>/Cl<sup>-</sup> or Na<sup>+</sup>/H<sup>+</sup> exchangers) to regulate oocyte pH<sub>i</sub> (FitzHarris and Baltz 2006 and 2009).

During follicular growth, as discussed above, the number or efficiency of gap junctions between granulosa cells and the oocyte may have been altered following total depletion of MYO10. Therefore, it is possible that the granulosa cells had a decreased ability to regulate pH<sub>i</sub> of *Myo10*<sup>-/-</sup> full oocytes before or during the period when oocytes begin to achieve this ability. Interestingly, growing oocytes devoid of granulosa cells display reduced pH<sub>i</sub> compared to same size follicle-enclosed oocytes (FitzHarris and Baltz 2006). In this regard, the quality of *Myo10*<sup>-/-</sup> full oocytes may have been impaired prior to meiosis resumption due to uncorrected low pH<sub>i</sub> during growth. This may have reduced their ability to successfully complete meiotic maturation. To assess this, a pH<sub>i</sub> measurement of preantral stage oocytes, as performed by FitzHarris and Baltz, would be of interest to determine whether *Myo10*<sup>-/-</sup> full oocytes had

uncorrected low  $pH_i$  during their growth. However, this latter experiment first requires that we improve our collection of preantral follicles and confirm that TZP density is decreased at a stage when oocytes are still dependent on granulosa cells for  $pH_i$  regulation.

### 3) Indirect cause of an altered transcriptome?

By performing RNA-Seq analysis on competent oocytes arrested in prophase I, we were able to reveal that several transcripts are deregulated (mostly up-regulated) in *Myo10*<sup>-/-</sup> full oocytes compared to controls. These deregulations may have occurred in response to abnormalities in the oocyte (e.g., excessive amount of reactive oxygen species, as proposed in the Results section). It is also possible that these deregulations reflect the fact that the synthesis or stability of certain oocyte transcripts is under the control of granulosa cells. The lack of a statistically significant change in the global transcriptional activity between *Myo10*<sup>-/-</sup> full oocytes and control oocytes suggests that the modulation of the oocyte transcriptome by granulosa cells would involve only a subset of transcripts. Therefore, it is attractive to consider that granulosa cells, via TZPs, may selectively regulate the expression or stability of oocyte target genes that may be involved in the achievement of meiotic maturation, and possibly early embryogenesis.

#### *3.1- Somatic regulation of the oocyte transcriptome through TZP-mediated transfer of RNA?*

To explain the high proportion of up-regulated transcripts in *Myo10*<sup>-/-</sup> full oocytes compared to controls, granulosa cells may act as repressors of expression of a subset of oocyte genes. First, it is possible that somatic paracrine factors that are released by TZPs down-regulate the expression of specific genes in the oocyte. Second, it is conceivable that granulosa cells use their own transcripts to selectively modulate the oocyte transcriptome. This hypothesis is supported by the fact that TZPs have been shown to enable the transfer of mRNAs and long noncoding RNAs from cumulus cells to the oocyte in cows (Macaulay 2014, Macaulay 2016).

Interestingly, tunneling nanotubes, although a different type of cellular protrusion than TZPs, have also been proposed to mediate the transfer of RNA (such as mRNA, microRNA or viral RNA) from one cell to another (Haimovich 2021). As pointed out by the authors of this review, the biological relevance of the TNT-mediated transfer of RNA remains to be better deciphered. It may coordinate a myriad of biological processes in the acceptor cell, which could serve as inspiration for future studies aimed at elucidating the role of the TZP-mediated transfer of RNA in the oocyte, if it occurs.

Similar to what has been suggested for TNTs connecting donor and acceptor cells (Haimovich 2021), TZPs could mediate the transfer of microRNAs from granulosa cells to the oocyte, which could be critical for degradation or prevention of translation of specific mRNAs in the oocyte. As a second possibility, again similar to what has been proposed for TNTs connecting donor and acceptor cells (Haimovich 2021), TZP-mediated transfer of mRNAs encoding transcription factors may regulate the expression of target genes in the oocyte. In *Myo10*<sup>-/-</sup> full follicles, the decrease in TZP density may have reduced the transfer to the oocyte of somatic microRNAs or mRNAs encoding transcriptional repressors. This could explain the high proportion of up-regulated transcripts in *Myo10*<sup>-/-</sup> full oocytes compared to controls, as revealed by our RNA-Seq analysis. Therefore, it is interesting to consider that a subset of oocyte genes, if not down-regulated by granulosa cells to some extent, may interfere directly or indirectly with the process of meiotic maturation and potentially further embryo development.

### *3.2- Impaired MPF regulation in Myo10<sup>-/-</sup> full oocytes?*

As discussed in the Results section, cyclin B1 is a possible gene down-regulated by granulosa cells for optimal completion of meiotic maturation. We confirmed that its mRNA is up-regulated in *Myo10*<sup>-/-</sup> full oocytes arrested in prophase I by RNA-Seq and RT-qPCR analysis. It remains to be determined (by immunostaining or immunoblotting) whether this up-regulation led to an increase in Cyclin B1 protein synthesis in prophase I and throughout meiotic maturation in *Myo10*<sup>-/-</sup> full oocytes. If the latter hypothesis is confirmed, it is conceivable that this resulted in sustained MPF activity that possibly may have prevented anaphase onset in some TZP-deprived

oocytes. Indeed, overexpression of cyclin B1 has been associated with metaphase I block in mouse oocytes (Ledan 2001). To determine whether impaired regulation of MPF activity plays a role in meiotic arrest of *Myo10*<sup>-/-</sup> full oocytes, we began incubating oocytes with Roscovitine, a drug inhibiting cyclin-dependent kinases. If drug treatment rescues the onset of anaphase I in *Myo10*<sup>-/-</sup> full oocytes, this would be consistent with a role for impaired MPF regulation in metaphase I arrest in these oocytes. It should be noted that *Myo10*<sup>-/-</sup> full oocytes do not seem to spontaneously resume meiosis when cultured *in vitro* in a medium maintaining a high level of oocyte cAMP. This indicates that the possible overexpression of Cyclin B1 is modest in these oocytes, at least in prophase I.

## Concluding remarks

By generating mice fully depleted of MYO10, we have shown that a decrease in TZP density does not prevent the oocyte from growing, plausibly alters the integrity of the *zona pellucida*, and slightly reduces the ability of oocytes to complete meiosis I. To further determine the role of TZPs in oocyte developmental potential, it would be worthwhile to test whether *Myo10*<sup>-/-</sup> full oocytes that have extruded a polar body are capable of undertaking early embryogenesis to the same extent as control oocytes. To this end, monitoring of the first embryonic divisions after *in vitro* fertilization with control spermatozoa or mating with a control male is required, as well as fertility tests, all of which are ongoing.

Taken together, our results confirm that TZPs enhance the developmental potential of the oocyte. We suggest an interesting role for granulosa cells as repressors of specific genes in the oocyte involved directly or indirectly in the completion of meiotic maturation and potentially early embryo development. Our results also tend to moderate the extent of TZP contribution to oocyte development. To confirm this, it is crucial that we determine at what stage of follicular growth the decrease in TZP density is initiated in mice totally lacking MYO10.

# REFERENCES

- Abbassi L, El-Hayek S, Carvalho KF, Wang W, Yang Q, Granados-Aparici S, Mondadori R, Bordignon V, Clarke HJ. Epidermal growth factor receptor signaling uncouples germ cells from the somatic follicular compartment at ovulation. *Nat Commun.* 2021 Mar 4;12(1):1438. doi: 10.1038/s41467-021-21644-z.
- Alam MH, Miyano T. Interaction between growing oocytes and granulosa cells in vitro. *Reprod Med Biol.* 2019 Aug 22;19(1):13-23. doi: 10.1002/rmb2.12292.
- Albertini DF, Rider V. Patterns of intercellular connectivity in the mammalian cumulus-oocyte complex. *Microsc Res Tech.* 1994 Feb 1;27(2):125-33. doi: 10.1002/jemt.1070270206.
- Albertini DF, Combelles CM, Benecchi E, Carabatsos MJ. Cellular basis for paracrine regulation of ovarian follicle development. *Reproduction.* 2001 May;121(5):647-53. doi: 10.1530/rep.0.1210647.
- Albertini DF, Sanfins A, Combelles CM. Origins and manifestations of oocyte maturation competencies. *Reprod Biomed Online.* 2003 Jun;6(4):410-5. doi: 10.1016/s1472-6483(10)62159-1.
- Almonacid M, Ahmed WW, Bussonnier M, Mailly P, Betz T, Voituriez R, Gov NS, Verlhac MH. Active diffusion positions the nucleus in mouse oocytes. *Nat Cell Biol.* 2015 Apr;17(4):470-9. doi: 10.1038/ncb3131.
- Almonacid M, Al Jord A, El-Hayek S, Othmani A, Couplier F, Lemoine S, Miyamoto K, Grosse R, Klein C, Piolot T, Mailly P, Voituriez R, Genovesio A, Verlhac MH. Active Fluctuations of the Nuclear Envelope Shape the Transcriptional Dynamics in Oocytes. *Dev Cell.* 2019 Oct 21;51(2):145-157.e10. doi: 10.1016/j.devcel.2019.09.010.
- Anderson E, Albertini DF. Gap junctions between the oocyte and companion follicle cells in the mammalian ovary. *J Cell Biol.* 1976 Nov;71(2):680-6. doi: 10.1083/jcb.71.2.680.
- Azoury J, Lee KW, Georget V, Rassinier P, Leader B, Verlhac MH. Spindle positioning in mouse oocytes relies on a dynamic meshwork of actin filaments. *Curr Biol.* 2008 Oct 14;18(19):1514-9. doi: 10.1016/j.cub.2008.08.044.
- Baena V, Terasaki M. Three-dimensional organization of transzonal projections and other cytoplasmic extensions in the mouse ovarian follicle. *Sci Rep.* 2019 Feb 4;9(1):1262. doi: 10.1038/s41598-018-37766-2.
- Belle M, Godefroy D, Couly G, Malone SA, Collier F, Giacobini P, Chédotal A. Tridimensional Visualization and Analysis of Early Human Development. *Cell.* 2017 Mar 23;169(1):161-173.e12. doi: 10.1016/j.cell.2017.03.008.
- Bennabi I, Terret ME, Verlhac MH. Meiotic spindle assembly and chromosome segregation in oocytes. *J Cell Biol.* 2016 Dec 5;215(5):611-619. doi: 10.1083/jcb.201607062.

- Bennabi I, Crozet F, Nikalayevich E, Chaigne A, Letort G, Manil-Ségalen M, Campillo C, Cadart C, Othmani A, Attia R, Genovesio A, Verlhac MH, Terret ME. Artificially decreasing cortical tension generates aneuploidy in mouse oocytes. *Nat Commun.* 2020 Apr 3;11(1):1649. doi: 10.1038/s41467-020-15470-y.
- Berg JS, Derfler BH, Pennisi CM, Corey DP, Cheney RE. Myosin-X, a novel myosin with pleckstrin homology domains, associates with regions of dynamic actin. *J Cell Sci.* 2000 Oct;113 Pt 19:3439-51.
- Berg JS, Cheney RE. Myosin-X is an unconventional myosin that undergoes intrafilopodial motility. *Nat Cell Biol.* 2002 Mar;4(3):246-50. doi: 10.1038/ncb762.
- Biggers JD, Whittingham DG, Donahue RP. The pattern of energy metabolism in the mouse oöcyte and zygote. *Proc Natl Acad Sci U S A.* 1967 Aug;58(2):560-7. doi: 10.1073/pnas.58.2.560.
- Bohil AB, Robertson BW, Cheney RE. Myosin-X is a molecular motor that functions in filopodia formation. *Proc Natl Acad Sci U S A.* 2006 Aug 15;103(33):12411-6. doi: 10.1073/pnas.0602443103.
- Breiman L. Random Forests. *Machine Learning.* 2001;45:5–32.
- Briño-Enríquez MA, Moak SL, Holloway JK, Cohen PE. NIMA-related kinase 1 (NEK1) regulates meiosis I spindle assembly by altering the balance between  $\alpha$ -Adducin and Myosin X. *PLoS One.* 2017 Oct 5;12(10):e0185780. doi: 10.1371/journal.pone.0185780.
- Byskov, AG., & Nielsen, M. (2003). *Ontogeny of the mammalian ovary.* In A. Trounson, & R. Gosden (Eds.), *Biology and pathology of the oocyte: its role in fertility and reproductive medicine.* (pp.13-28). Cambridge University Press.
- Carabatsos MJ, Elvin J, Matzuk MM, Albertini DF. Characterization of oocyte and follicle development in growth differentiation factor-9-deficient mice. *Dev Biol.* 1998 Dec 15;204(2):373-84. doi: 10.1006/dbio.1998.9087.
- Chaigne A, Campillo C, Gov NS, Voituriez R, Azoury J, Umaña-Díaz C, Almonacid M, Queguiner I, Nassoy P, Sykes C, Verlhac MH, Terret ME. A soft cortex is essential for asymmetric spindle positioning in mouse oocytes. *Nat Cell Biol.* 2013 Aug;15(8):958-66. doi: 10.1038/ncb2799.
- Chaigne A, Campillo C, Gov NS, Voituriez R, Sykes C, Verlhac MH, Terret ME. A narrow window of cortical tension guides asymmetric spindle positioning in the mouse oocyte. *Nat Commun.* 2015 Jan 19;6:6027. doi: 10.1038/ncomms7027.
- Chaigne A, Terret ME, Verlhac MH. Asymmetries and Symmetries in the Mouse Oocyte and Zygote. *Results Probl Cell Differ.* 2017;61:285-299. doi: 10.1007/978-3-319-53150-2\_13.
- Chang HM, Cheng JC, Taylor E, Leung PC. Oocyte-derived BMP15 but not GDF9 down-regulates connexin43 expression and decreases gap junction intercellular

communication activity in immortalized human granulosa cells. *Mol Hum Reprod*. 2014 May;20(5):373-83. doi: 10.1093/molehr/gau001.

- Chen J, Torcia S, Xie F, Lin CJ, Cakmak H, Franciosi F, Horner K, Onodera C, Song JS, Cedars MI, Ramalho-Santos M, Conti M. Somatic cells regulate maternal mRNA translation and developmental competence of mouse oocytes. *Nat Cell Biol*. 2013 Dec;15(12):1415-23. doi: 10.1038/ncb2873.

- Clarke HJ. Post-transcriptional control of gene expression during mouse oogenesis. *Results Probl Cell Differ*. 2012;55:1-21. doi: 10.1007/978-3-642-30406-4\_1.

- Clarke HJ. Regulation of germ cell development by intercellular signaling in the mammalian ovarian follicle. *Wiley Interdiscip Rev Dev Biol*. 2018 Jan;7(1):10.1002/wdev.294. doi: 10.1002/wdev.294.

- Combelles CM, Carabatsos MJ, Kumar TR, Matzuk MM, Albertini DF. Hormonal control of somatic cell oocyte interactions during ovarian follicle development. *Mol Reprod Dev*. 2004 Nov;69(3):347-55. doi: 10.1002/mrd.20128.

- Combes, A., Spiller, C., & Koopman, P. (2010). *Sex determination and gonadal development*. In M-H. Verlhac, & A. Villeneuve (Eds.), *Oogenesis: the universal process*. (pp. 27-79). John Wiley & Sons, Ltd.

- Conti M, Franciosi F. Acquisition of oocyte competence to develop as an embryo: integrated nuclear and cytoplasmic events. *Hum Reprod Update*. 2018 May 1;24(3):245-266. doi: 10.1093/humupd/dmx040.

- Coticchio G, Dal Canto M, Mignini Renzini M, Guglielmo MC, Brambillasca F, Turchi D, Novara PV, Fadini R. Oocyte maturation: gamete-somatic cells interactions, meiotic resumption, cytoskeletal dynamics and cytoplasmic reorganization. *Hum Reprod Update*. 2015 Jul-Aug;21(4):427-54. doi: 10.1093/humupd/dmv011.

- Crozet F, Da Silva C, Verlhac MH, Terret ME. Myosin-X is dispensable for spindle morphogenesis and positioning in the mouse oocyte. *Development*. 2021 Apr 1;148(7):dev199364. doi: 10.1242/dev.199364.

- Da Broi MG, Giorgi VSI, Wang F, Keefe DL, Albertini D, Navarro PA. Influence of follicular fluid and cumulus cells on oocyte quality: clinical implications. *J Assist Reprod Genet*. 2018 May;35(5):735-751. doi: 10.1007/s10815-018-1143-3.

- de Carvalho CCCR, Caramujo MJ. The Various Roles of Fatty Acids. *Molecules*. 2018 Oct 9;23(10):2583. doi: 10.3390/molecules23102583.

- De La Fuente R, Eppig JJ. Transcriptional activity of the mouse oocyte genome: companion granulosa cells modulate transcription and chromatin remodeling. *Dev Biol*. 2001 Jan 1;229(1):224-36. doi: 10.1006/dbio.2000.9947.

- Del Collado M, da Silveira JC, Sangalli JR, Andrade GM, Sousa LRDS, Silva LA, Meirelles FV, Perecin F. Fatty Acid Binding Protein 3 And Transzonal Projections Are

Involved In Lipid Accumulation During In Vitro Maturation Of Bovine Oocytes. *Sci Rep*. 2017 Jun 1;7(1):2645. doi: 10.1038/s41598-017-02467-9.

- Dever TE, Ivanov IP. Roles of polyamines in translation. *J Biol Chem*. 2018 Nov 30;293(48):18719-18729. doi: 10.1074/jbc.TM118.003338.

- di Pietro F, Echard A, Morin X. Regulation of mitotic spindle orientation: an integrated view. *EMBO Rep*. 2016 Aug;17(8):1106-30. doi: 10.15252/embr.201642292.

- Dogterom M, Koenderink GH. Actin-microtubule crosstalk in cell biology. *Nat Rev Mol Cell Biol*. 2019 Jan;20(1):38-54. doi: 10.1038/s41580-018-0067-1.

- Donahue RP, Stern S. Follicular cell support of oocyte maturation: production of pyruvate in vitro. *J Reprod Fertil*. 1968 Nov;17(2):395-8. doi: 10.1530/jrf.0.0170395.

- Dong J, Albertini DF, Nishimori K, Kumar TR, Lu N, Matzuk MM. Growth differentiation factor-9 is required during early ovarian folliculogenesis. *Nature*. 1996 Oct 10;383(6600):531-5. doi: 10.1038/383531a0.

- Duan X, Li Y, Yi K, Guo F, Wang H, Wu PH, Yang J, Mair DB, Morales EA, Kalab P, Wirtz D, Sun SX, Li R. Dynamic organelle distribution initiates actin-based spindle migration in mouse oocytes. *Nat Commun*. 2020 Jan 14;11(1):277. doi: 10.1038/s41467-019-14068-3.

- Dumont J, Million K, Sunderland K, Rassinier P, Lim H, Leader B, Verlhac MH. Formin-2 is required for spindle migration and for the late steps of cytokinesis in mouse oocytes. *Dev Biol*. 2007a Jan 1;301(1):254-65. doi: 10.1016/j.ydbio.2006.08.044.

- Dumont J, Petri S, Pellegrin F, Terret ME, Bohnsack MT, Rassinier P, Georget V, Kalab P, Gruss OJ, Verlhac MH. A centriole- and RanGTP-independent spindle assembly pathway in meiosis I of vertebrate oocytes. *J Cell Biol*. 2007b Jan 29;176(3):295-305. doi: 10.1083/jcb.200605199.

- El-Hayek S, Clarke HJ. Control of Oocyte Growth and Development by Intercellular Communication Within the Follicular Niche. *Results Probl Cell Differ*. 2016;58:191-224. doi: 10.1007/978-3-319-31973-5\_8.

- El-Hayek S, Yang Q, Abbassi L, FitzHarris G, Clarke HJ. Mammalian Oocytes Locally Remodel Follicular Architecture to Provide the Foundation for Germline-Soma Communication. *Curr Biol*. 2018 Apr 2;28(7):1124-1131.e3. doi: 10.1016/j.cub.2018.02.039.

- Elvin JA, Yan C, Wang P, Nishimori K, Matzuk MM. Molecular characterization of the follicle defects in the growth differentiation factor 9-deficient ovary. *Mol Endocrinol*. 1999 Jun;13(6):1018-34. doi: 10.1210/mend.13.6.0309.

- Eppig JJ. A comparison between oocyte growth in coculture with granulosa cells and oocytes with granulosa cell-oocyte junctional contact maintained in vitro. *J Exp Zool*. 1979 Aug;209(2):345-53. doi: 10.1002/jez.1402090216.

- Eppig JJ, Wigglesworth K, Pendola FL. The mammalian oocyte orchestrates the rate of ovarian follicular development. *Proc Natl Acad Sci U S A*. 2002 Mar 5;99(5):2890-4. doi: 10.1073/pnas.052658699.
- Eppig JJ, Pendola FL, Wigglesworth K, Pendola JK. Mouse oocytes regulate metabolic cooperativity between granulosa cells and oocytes: amino acid transport. *Biol Reprod*. 2005 Aug;73(2):351-7. doi: 10.1095/biolreprod.105.041798.
- Faddy, M., & Gosden, R. (2003). *Modelling the dynamics of ovarian follicle utilization throughout life*. In A. Trounson, & R. Gosden (Eds.), *Biology and pathology of the oocyte: its role in fertility and reproductive medicine*. (pp.44-52). Cambridge University Press.
- Fink J, Carpi N, Betz T, Bétard A, Chebah M, Azioune A, Bornens M, Sykes C, Fetler L, Cuvelier D, Piel M. External forces control mitotic spindle positioning. *Nat Cell Biol*. 2011 Jun 12;13(7):771-8. doi: 10.1038/ncb2269.
- Fitzharris G, Baltz JM. Granulosa cells regulate intracellular pH of the murine growing oocyte via gap junctions: development of independent homeostasis during oocyte growth. *Development*. 2006 Feb;133(4):591-9. doi: 10.1242/dev.02246.
- FitzHarris G, Baltz JM. Regulation of intracellular pH during oocyte growth and maturation in mammals. *Reproduction*. 2009 Oct;138(4):619-27. doi: 10.1530/REP-09-0112.
- Gallop JL. Filopodia and their links with membrane traffic and cell adhesion. *Semin Cell Dev Biol*. 2020 Jun;102:81-89. doi: 10.1016/j.semcdb.2019.11.017.
- Ge L, Sui HS, Lan GC, Liu N, Wang JZ, Tan JH. Coculture with cumulus cells improves maturation of mouse oocytes denuded of the cumulus oophorus: observations of nuclear and cytoplasmic events. *Fertil Steril*. 2008 Dec;90(6):2376-88. doi: 10.1016/j.fertnstert.2007.10.054.
- Gousset K, Marzo L, Commere PH, Zurzolo C. Myo10 is a key regulator of TNT formation in neuronal cells. *J Cell Sci*. 2013 Oct 1;126(Pt 19):4424-35. doi: 10.1242/jcs.129239.
- Gruhn JR, Zielinska AP, Shukla V, Blanshard R, Capalbo A, Cimadomo D, Nikiforov D, Chan AC, Newnham LJ, Vogel I, Scarica C, Krapchev M, Taylor D, Kristensen SG, Cheng J, Ernst E, Bjørn AB, Colmorn LB, Blayney M, Elder K, Liss J, Hartshorne G, Grøndahl ML, Rienzi L, Ubaldi F, McCoy R, Lukaszuk K, Andersen CY, Schuh M, Hoffmann ER. Chromosome errors in human eggs shape natural fertility over reproductive life span. *Science*. 2019 Sep 27;365(6460):1466-1469. doi: 10.1126/science.aav7321.
- Haghighat N, Van Winkle LJ. Developmental change in follicular cell-enhanced amino acid uptake into mouse oocytes that depends on intact gap junctions and transport system Gly. *J Exp Zool*. 1990 Jan;253(1):71-82. doi: 10.1002/jez.1402530110.

- Haimovich G, Dasgupta S, Gerst JE. RNA transfer through tunneling nanotubes. *Biochem Soc Trans.* 2021 Feb 26;49(1):145-160. doi: 10.1042/BST20200113.
- Heimsath EG Jr, Yim YI, Mustapha M, Hammer JA, Cheney RE. Myosin-X knockout is semi-lethal and demonstrates that myosin-X functions in neural tube closure, pigmentation, hyaloid vasculature regression, and filopodia formation. *Sci Rep.* 2017 Dec 11;7(1):17354. doi: 10.1038/s41598-017-17638-x.
- Herbert M, Lévasseur M, Homer H, Yallop K, Murdoch A, McDougall A. Homologue disjunction in mouse oocytes requires proteolysis of securin and cyclin B1. *Nat Cell Biol.* 2003 Nov;5(11):1023-5. doi: 10.1038/ncb1062.
- Hirano Y, Hatano T, Takahashi A, Toriyama M, Inagaki N, Hakoshima T. Structural basis of cargo recognition by the myosin-X MyTH4-FERM domain. *EMBO J.* 2011 Jun 3;30(13):2734-47. doi: 10.1038/emboj.2011.177.
- Homma K, Saito J, Ikebe R, Ikebe M. Motor function and regulation of myosin X. *J Biol Chem.* 2001 Sep 7;276(36):34348-54. doi: 10.1074/jbc.M104785200.
- Huelgas-Morales G, Greenstein D. Control of oocyte meiotic maturation in *C. elegans*. *Semin Cell Dev Biol.* 2018 Dec;84:90-99. doi: 10.1016/j.semcdb.2017.12.005.
- Jacquemet G, Hamidi H, Ivaska J. Filopodia in cell adhesion, 3D migration and cancer cell invasion. *Curr Opin Cell Biol.* 2015 Oct;36:23-31. doi: 10.1016/j.ceb.2015.06.007. Erratum in: *Curr Opin Cell Biol.* 2015 Dec;37:119.
- Kerber ML, Cheney RE. Myosin-X: a MyTH-FERM myosin at the tips of filopodia. *J Cell Sci.* 2011 Nov 15;124(Pt 22):3733-41. doi: 10.1242/jcs.023549.
- Kidder GM, Vanderhyden BC. Bidirectional communication between oocytes and follicle cells: ensuring oocyte developmental competence. *Can J Physiol Pharmacol.* 2010 Apr;88(4):399-413. doi: 10.1139/y10-009.
- Kim S, Spike C, Greenstein D. Control of oocyte growth and meiotic maturation in *Caenorhabditis elegans*. *Adv Exp Med Biol.* 2013;757:277-320. doi: 10.1007/978-1-4614-4015-4\_10.
- Kitajima TS, Ohsugi M, Ellenberg J. Complete kinetochore tracking reveals error-prone homologous chromosome biorientation in mammalian oocytes. *Cell.* 2011 Aug 19;146(4):568-81. doi: 10.1016/j.cell.2011.07.031. Erratum in: *Cell.* 2011 Sep 16;146(6):1042.
- Kwon M, Bagonis M, Danuser G, Pellman D. Direct Microtubule-Binding by Myosin-10 Orients Centrosomes toward Retraction Fibers and Subcortical Actin Clouds. *Dev Cell.* 2015 Aug 10;34(3):323-37. doi: 10.1016/j.devcel.2015.06.013.
- Kyogoku H, Kitajima TS. Large Cytoplasm Is Linked to the Error-Prone Nature of Oocytes. *Dev Cell.* 2017 May 8;41(3):287-298.e4. doi: 10.1016/j.devcel.2017.04.009.

- Langmead B, Salzberg SL. Fast gapped-read alignment with Bowtie 2. *Nat Methods*. 2012 Mar 4;9(4):357-9. doi: 10.1038/nmeth.1923.
- Larson SM, Lee HJ, Hung PH, Matthews LM, Robinson DN, Evans JP. Cortical mechanics and meiosis II completion in mammalian oocytes are mediated by myosin-II and Ezrin-Radixin-Moesin (ERM) proteins. *Mol Biol Cell*. 2010 Sep 15;21(18):3182-92. doi: 10.1091/mbc.E10-01-0066.
- Leader B, Lim H, Carabatsos MJ, Harrington A, Ecsedy J, Pellman D, Maas R, Leder P. Formin-2, polyploidy, hypofertility and positioning of the meiotic spindle in mouse oocytes. *Nat Cell Biol*. 2002 Dec;4(12):921-8. doi: 10.1038/ncb880.
- Ledan E, Polanski Z, Terret ME, Maro B. Meiotic maturation of the mouse oocyte requires an equilibrium between cyclin B synthesis and degradation. *Dev Biol*. 2001 Apr 15;232(2):400-13. doi: 10.1006/dbio.2001.0188.
- Li H, Guo F, Rubinstein B, Li R. Actin-driven chromosomal motility leads to symmetry breaking in mammalian meiotic oocytes. *Nat Cell Biol*. 2008 Nov;10(11):1301-8. doi: 10.1038/ncb1788.
- Li J, Qian WP, Sun QY. Cyclins regulating oocyte meiotic cell cycle progression†. *Biol Reprod*. 2019 Nov 21;101(5):878-881. doi: 10.1093/biolre/ioz143.
- Lin J, Wang L. Oxidative Stress in Oocytes and Embryo Development: Implications for *In Vitro* Systems. *Antioxid Redox Signal*. 2020 Dec 8. doi: 10.1089/ars.2020.8209.
- Litscher ES, Wassarman PM. Zona Pellucida Proteins, Fibrils, and Matrix. *Annu Rev Biochem*. 2020 Jun 20;89:695-715. doi: 10.1146/annurev-biochem-011520-105310.
- Liu C, Litscher ES, Mortillo S, Sakai Y, Kinloch RA, Stewart CL, Wassarman PM. Targeted disruption of the mZP3 gene results in production of eggs lacking a zona pellucida and infertility in female mice. *Proc Natl Acad Sci U S A*. 1996 May 28;93(11):5431-6. doi: 10.1073/pnas.93.11.5431.
- Liu KC, Jacobs DT, Dunn BD, Fanning AS, Cheney RE. Myosin-X functions in polarized epithelial cells. *Mol Biol Cell*. 2012 May;23(9):1675-87. doi: 10.1091/mbc.E11-04-0358.
- Longo FJ, Chen DY. Development of cortical polarity in mouse eggs: involvement of the meiotic apparatus. *Dev Biol*. 1985 Feb;107(2):382-94. doi: 10.1016/0012-1606(85)90320-3.
- Lowther KM, Mehlmann LM. Embryonic Poly(A)-Binding Protein Is Required During Early Stages of Mouse Oocyte Development for Chromatin Organization, Transcriptional Silencing, and Meiotic Competence. *Biol Reprod*. 2015 Aug;93(2):43. doi: 10.1095/biolreprod.115.131359.
- Lowther KM, Favero F, Yang CR, Taylor HS, Seli E. Embryonic poly(A)-binding protein is required at the preantral stage of mouse folliculogenesis for oocyte-somatic

communication. Biol Reprod. 2017 Feb 1;96(2):341-351. doi: 10.1095/biolreprod.116.141234.

- Luciano AM, Franciosi F, Modena SC, Lodde V. Gap junction-mediated communications regulate chromatin remodeling during bovine oocyte growth and differentiation through cAMP-dependent mechanism(s). Biol Reprod. 2011 Dec;85(6):1252-9. doi: 10.1095/biolreprod.111.092858.

- Luciano AM, Lodde V, Franciosi F, Tessaro I, Corbani D, Modena S. Large-scale chromatin morpho-functional changes during mammalian oocyte growth and differentiation. Eur J Histochem. 2012 Aug 10;56(3):e37. doi: 10.4081/ejh.2012.e37.

- Macaulay AD, Gilbert I, Caballero J, Barreto R, Fournier E, Tossou P, Sirard MA, Clarke HJ, Khandjian ÉW, Richard FJ, Hyttel P, Robert C. The gametic synapse: RNA transfer to the bovine oocyte. Biol Reprod. 2014 Oct;91(4):90. doi: 10.1095/biolreprod.114.119867.

- Macaulay AD, Gilbert I, Scantland S, Fournier E, Ashkar F, Bastien A, Saadi HA, Gagné D, Sirard MA, Khandjian ÉW, Richard FJ, Hyttel P, Robert C. Cumulus Cell Transcripts Transit to the Bovine Oocyte in Preparation for Maturation. Biol Reprod. 2016 Jan;94(1):16. doi: 10.1095/biolreprod.114.127571.

- Makabe S, Naguro T, Stallone T. Oocyte-follicle cell interactions during ovarian follicle development, as seen by high resolution scanning and transmission electron microscopy in humans. Microsc Res Tech. 2006 Jun;69(6):436-49. doi: 10.1002/jemt.20303.

- Manil-Ségalen M, Łuksza M, Kanaan J, Marthiens V, Lane SIR, Jones KT, Terret ME, Basto R, Verlhac MH. Chromosome structural anomalies due to aberrant spindle forces exerted at gene editing sites in meiosis. J Cell Biol. 2018 Oct 1;217(10):3416-3430. doi: 10.1083/jcb.201806072.

- Mattila PK, Lappalainen P. Filopodia: molecular architecture and cellular functions. Nat Rev Mol Cell Biol. 2008 Jun;9(6):446-54. doi: 10.1038/nrm2406.

- McGinnis LK, Kinsey WH. Role of focal adhesion kinase in oocyte-follicle communication. Mol Reprod Dev. 2015 Feb;82(2):90-102. doi: 10.1002/mrd.22446.

- Mihajlović AI, FitzHarris G. Segregating Chromosomes in the Mammalian Oocyte. Curr Biol. 2018 Aug 20;28(16):R895-R907. doi: 10.1016/j.cub.2018.06.057.

- Mitsushima M, Aoki K, Ebisuya M, Matsumura S, Yamamoto T, Matsuda M, Toyoshima F, Nishida E. Revolving movement of a dynamic cluster of actin filaments during mitosis. J Cell Biol. 2010 Nov 1;191(3):453-62. doi: 10.1083/jcb.201007136.

- Mogessie B, Schuh M. Actin protects mammalian eggs against chromosome segregation errors. Science. 2017 Aug 25;357(6353):eaal1647. doi: 10.1126/science.aal1647.

- Mora JM, Fenwick MA, Castle L, Baithun M, Ryder TA, Mobberley M, Carzaniga R, Franks S, Hardy K. Characterization and significance of adhesion and junction-related proteins in mouse ovarian follicles. *Biol Reprod.* 2012 May 17;86(5):153, 1-14. doi: 10.1095/biolreprod.111.096156.
- Morin X, Bellaïche Y. Mitotic spindle orientation in asymmetric and symmetric cell divisions during animal development. *Dev Cell.* 2011 Jul 19;21(1):102-19. doi: 10.1016/j.devcel.2011.06.012.
- Moros-Nicolás C, Chevret P, Jiménez-Movilla M, Algarra B, Cots-Rodríguez P, González-Brusi L, Avilés M, Izquierdo-Rico MJ. New Insights into the Mammalian Egg Zona Pellucida. *Int J Mol Sci.* 2021 Mar 23;22(6):3276. doi: 10.3390/ijms22063276.
- Motta PM, Makabe S, Naguro T, Correr S. Oocyte follicle cells association during development of human ovarian follicle. A study by high resolution scanning and transmission electron microscopy. *Arch Histol Cytol.* 1994 Oct;57(4):369-94. doi: 10.1679/aohc.57.369.
- Norris RP, Ratzan WJ, Freudzon M, Mehlmann LM, Krall J, Movsesian MA, Wang H, Ke H, Nikolaev VO, Jaffe LA. Cyclic GMP from the surrounding somatic cells regulates cyclic AMP and meiosis in the mouse oocyte. *Development.* 2009 Jun;136(11):1869-78. doi: 10.1242/dev.035238.
- O'Connell JM, Pepling ME. Primordial Follicle Formation - Some Assembly Required. *Curr Opin Endocr Metab Res.* 2021 Jun;18:118-127. doi: 10.1016/j.coemr.2021.03.005.
- Oktem O, Urman B. Understanding follicle growth in vivo. *Hum Reprod.* 2010 Dec;25(12):2944-54. doi: 10.1093/humrep/deq275.
- Paterson EK, Courtneidge SA. Invadosomes are coming: new insights into function and disease relevance. *FEBS J.* 2018 Jan;285(1):8-27. doi: 10.1111/febs.14123.
- Pfender S, Kuznetsov V, Pleiser S, Kerkhoff E, Schuh M. Spire-type actin nucleators cooperate with Formin-2 to drive asymmetric oocyte division. *Curr Biol.* 2011 Jun 7;21(11):955-60. doi: 10.1016/j.cub.2011.04.029.
- Pham CT, MacIvor DM, Hug BA, Heusel JW, Ley TJ. Long-range disruption of gene expression by a selectable marker cassette. *Proc Natl Acad Sci U S A.* 1996 Nov 12;93(23):13090-5. doi: 10.1073/pnas.93.23.13090.
- Rankin T, Familiarì M, Lee E, Ginsberg A, Dwyer N, Blanchette-Mackie J, Drago J, Westphal H, Dean J. Mice homozygous for an insertional mutation in the Zp3 gene lack a zona pellucida and are infertile. *Development.* 1996 Sep;122(9):2903-10.
- Rankin T, Talbot P, Lee E, Dean J. Abnormal zonae pellucidae in mice lacking ZP1 result in early embryonic loss. *Development.* 1999 Sep;126(17):3847-55.

- Rankin TL, O'Brien M, Lee E, Wigglesworth K, Eppig J, Dean J. Defective zonae pellucidae in Zp2-null mice disrupt folliculogenesis, fertility and development. *Development*. 2001 Apr;128(7):1119-26.
- Ratchford AM, Esguerra CR, Moley KH. Decreased oocyte-granulosa cell gap junction communication and connexin expression in a type 1 diabetic mouse model. *Mol Endocrinol*. 2008 Dec;22(12):2643-54. doi: 10.1210/me.2007-0495.
- Reis A, Chang HY, Levasseur M, Jones KT. APC<sup>c</sup>dh1 activity in mouse oocytes prevents entry into the first meiotic division. *Nat Cell Biol*. 2006 May;8(5):539-40. doi: 10.1038/ncb1406.
- Reymann AC, Boujemaa-Paterski R, Martiel JL, Guérin C, Cao W, Chin HF, De La Cruz EM, Théry M, Blanchoin L. Actin network architecture can determine myosin motor activity. *Science*. 2012 Jun 8;336(6086):1310-4. doi: 10.1126/science.1221708.
- Ropars V, Yang Z, Isabet T, Blanc F, Zhou K, Lin T, Liu X, Hissier P, Samazan F, Amigues B, Yang ED, Park H, Pylypenko O, Cecchini M, Sindelar CV, Sweeney HL, Houdusse A. The myosin X motor is optimized for movement on actin bundles. *Nat Commun*. 2016 Sep 1;7:12456. doi: 10.1038/ncomms12456.
- Samwer M, Dehne HJ, Spira F, Kollmar M, Gerlich DW, Urlaub H, Görlich D. The nuclear F-actin interactome of *Xenopus* oocytes reveals an actin-bundling kinesin that is essential for meiotic cytokinesis. *EMBO J*. 2013 Jul 3;32(13):1886-902. doi: 10.1038/emboj.2013.108.
- Sandquist JC, Larson ME, Hine KJ. Myosin-10 independently influences mitotic spindle structure and mitotic progression. *Cytoskeleton (Hoboken)*. 2016 Jun;73(7):351-64. doi: 10.1002/cm.21311.
- Sandquist JC, Larson ME, Woolner S, Ding Z, Bement WM. An interaction between myosin-10 and the cell cycle regulator Wee1 links spindle dynamics to mitotic progression in epithelia. *J Cell Biol*. 2018 Mar 5;217(3):849-859. doi: 10.1083/jcb.201708072.
- Schoumacher M, Goldman RD, Louvard D, Vignjevic DM. Actin, microtubules, and vimentin intermediate filaments cooperate for elongation of invadopodia. *J Cell Biol*. 2010 May 3;189(3):541-56. doi: 10.1083/jcb.200909113.
- Schuh M, Ellenberg J. Self-organization of MTOCs replaces centrosome function during acentrosomal spindle assembly in live mouse oocytes. *Cell*. 2007 Aug 10;130(3):484-98. doi: 10.1016/j.cell.2007.06.025.
- Schuh M, Ellenberg J. A new model for asymmetric spindle positioning in mouse oocytes. *Curr Biol*. 2008 Dec 23;18(24):1986-92. doi: 10.1016/j.cub.2008.11.022.
- Simon AM, Goodenough DA, Li E, Paul DL. Female infertility in mice lacking connexin 37. *Nature*. 1997 Feb 6;385(6616):525-9. doi: 10.1038/385525a0.

- Skinner MK. Regulation of primordial follicle assembly and development. *Hum Reprod Update*. 2005 Sep-Oct;11(5):461-71. doi: 10.1093/humupd/dmi020.
- So C, Seres KB, Steyer AM, Mönnich E, Clift D, Pejkovska A, Möbius W, Schuh M. A liquid-like spindle domain promotes acentrosomal spindle assembly in mammalian oocytes. *Science*. 2019 Jun 28;364(6447):eaat9557. doi: 10.1126/science.aat9557.
- Sorensen RA, Wassarman PM. Relationship between growth and meiotic maturation of the mouse oocyte. *Dev Biol*. 1976 Jun;50(2):531-6. doi: 10.1016/0012-1606(76)90172-x.
- Sousa AD, Berg JS, Robertson BW, Meeker RB, Cheney RE. Myo10 in brain: developmental regulation, identification of a headless isoform and dynamics in neurons. *J Cell Sci*. 2006 Jan 1;119(Pt 1):184-94. doi: 10.1242/jcs.02726.
- Sugiura K, Pendola FL, Eppig JJ. Oocyte control of metabolic cooperativity between oocytes and companion granulosa cells: energy metabolism. *Dev Biol*. 2005 Mar 1;279(1):20-30. doi: 10.1016/j.ydbio.2004.11.027.
- Szollosi D, Calarco P, Donahue RP. Absence of centrioles in the first and second meiotic spindles of mouse oocytes. *J Cell Sci*. 1972 Sep;11(2):521-41.
- Théry M, Racine V, Pépin A, Piel M, Chen Y, Sibarita JB, Bornens M. The extracellular matrix guides the orientation of the cell division axis. *Nat Cell Biol*. 2005 Oct;7(10):947-53. doi: 10.1038/ncb1307.
- Toyoshima F, Nishida E. Integrin-mediated adhesion orients the spindle parallel to the substratum in an EB1- and myosin X-dependent manner. *EMBO J*. 2007 Mar 21;26(6):1487-98. doi: 10.1038/sj.emboj.7601599.
- Tsurumi C, Hoffmann S, Geley S, Graeser R, Polanski Z. The spindle assembly checkpoint is not essential for CSF arrest of mouse oocytes. *J Cell Biol*. 2004 Dec 20;167(6):1037-50. doi: 10.1083/jcb.200405165.
- Van Blerkom J, Bell H. Regulation of development in the fully grown mouse oocyte: chromosome-mediated temporal and spatial differentiation of the cytoplasm and plasma membrane. *J Embryol Exp Morphol*. 1986 Apr;93:213-38.
- Veitch GI, Gittens JE, Shao Q, Laird DW, Kidder GM. Selective assembly of connexin37 into heterocellular gap junctions at the oocyte/granulosa cell interface. *J Cell Sci*. 2004 Jun 1;117(Pt 13):2699-707. doi: 10.1242/jcs.01124.
- Verlhac MH, Kubiak JZ, Clarke HJ, Maro B. Microtubule and chromatin behavior follow MAP kinase activity but not MPF activity during meiosis in mouse oocytes. *Development*. 1994 Apr;120(4):1017-25.
- Verlhac MH, Lefebvre C, Guillaud P, Rassinier P, Maro B. Asymmetric division in mouse oocytes: with or without Mos. *Curr Biol*. 2000 Oct 19;10(20):1303-6. doi: 10.1016/s0960-9822(00)00753-3.

- Verlhac MH, Terret ME. Oocyte Maturation and Development. *F1000Res*. 2016 Mar 9;5:F1000 Faculty Rev-309. doi: 10.12688/f1000research.7892.1.
- Wang Q, Moley KH. Maternal diabetes and oocyte quality. *Mitochondrion*. 2010 Aug;10(5):403-10. doi: 10.1016/j.mito.2010.03.002.
- Wassarman PM, Josefowicz WJ. Oocyte development in the mouse: an ultrastructural comparison of oocytes isolated at various stages of growth and meiotic competence. *J Morphol*. 1978 May;156(2):209-35. doi: 10.1002/jmor.1051560206.
- Wassarman PM, Litscher ES. The Mouse Egg's Zona Pellucida. *Curr Top Dev Biol*. 2018;130:331-356. doi: 10.1016/bs.ctdb.2018.01.003.
- Weber KL, Sokac AM, Berg JS, Cheney RE, Bement WM. A microtubule-binding myosin required for nuclear anchoring and spindle assembly. *Nature*. 2004 Sep 16;431(7006):325-9. doi: 10.1038/nature02834.
- Weck ML, Grega-Larson NE, Tyska MJ. MyTH4-FERM myosins in the assembly and maintenance of actin-based protrusions. *Curr Opin Cell Biol*. 2017 Feb;44:68-78. doi: 10.1016/j.ceb.2016.10.002.
- Woolner S, O'Brien LL, Wiese C, Bement WM. Myosin-10 and actin filaments are essential for mitotic spindle function. *J Cell Biol*. 2008 Jul 14;182(1):77-88. doi: 10.1083/jcb.200804062.
- Woolner S, Papalopulu N. Spindle position in symmetric cell divisions during epiboly is controlled by opposing and dynamic apicobasal forces. *Dev Cell*. 2012 Apr 17;22(4):775-87. doi: 10.1016/j.devcel.2012.01.002.
- Yamashita YM, Inaba M, Buszczak M. Specialized Intercellular Communications via Cytosomes and Nanotubes. *Annu Rev Cell Dev Biol*. 2018 Oct 6;34:59-84. doi: 10.1146/annurev-cellbio-100617-062932.
- Yanez LZ, Han J, Behr BB, Pera RAR, Camarillo DB. Human oocyte developmental potential is predicted by mechanical properties within hours after fertilization. *Nat Commun*. 2016 Feb 24;7:10809. doi: 10.1038/ncomms10809.
- Yang X, Wu LL, Chura LR, Liang X, Lane M, Norman RJ, Robker RL. Exposure to lipid-rich follicular fluid is associated with endoplasmic reticulum stress and impaired oocyte maturation in cumulus-oocyte complexes. *Fertil Steril*. 2012 Jun;97(6):1438-43. doi: 10.1016/j.fertnstert.2012.02.034.
- Yi K, Rubinstein B, Unruh JR, Guo F, Slaughter BD, Li R. Sequential actin-based pushing forces drive meiosis I chromosome migration and symmetry breaking in oocytes. *J Cell Biol*. 2013 Mar 4;200(5):567-76. doi: 10.1083/jcb.201211068.
- Young JM, McNeilly AS. Theca: the forgotten cell of the ovarian follicle. *Reproduction*. 2010 Oct;140(4):489-504. doi: 10.1530/REP-10-0094.

- Zhang Y, Wang Y, Feng X, Zhang S, Xu X, Li L, Niu S, Bo Y, Wang C, Li Z, Xia G, Zhang H. Oocyte-derived microvilli control female fertility by optimizing ovarian follicle selection in mice. *Nat Commun.* 2021 May 5;12(1):2523. doi: 10.1038/s41467-021-22829-2.
- Zurzolo C. Tunneling nanotubes: Reshaping connectivity. *Curr Opin Cell Biol.* 2021 Apr 15;71:139-147. doi: 10.1016/j.ceb.2021.03.003.
- *Biology and pathology of the oocyte: its role in fertility and reproductive medicine.* 2003 Cambridge University Press. Editors Alan Trounson and Roger Gosden.
- *Oogenesis: the universal process.* 2010 John Wiley & Sons, Ltd. Editors Marie-Hélène Verlhac and Anne Villeneuve.

# **ANNEXES**

*Attached is the manuscript published in Nature Communications in April 2020 with Isma Bennabi, a former PhD student in the lab, as first author. The article further investigates the molecular and cellular repercussions in the mouse oocyte of excessive decrease in oocyte cortical tension following exogenous nucleation of subcortical branched F-actin. Importantly, the article demonstrates that an aberrantly soft cortex enhances chromosome misalignment before anaphase of the first meiotic division. This reinforces the concept that a defined range of oocyte cortical tension is not only critical for spindle off-centering, but also for oocyte quality, as chromosome misalignment before anaphase is at the possible origin of aneuploidy. I participated in this project by helping to confirm that an excessively low cortical tension mediated by another means than exogenous nucleation of subcortical F-actin, i.e., following an exogenous nucleation of straight F-actin at the cortex, would also impair spindle off-centering and chromosome alignment in the mouse oocyte.*

# Artificially decreasing cortical tension generates aneuploidy in mouse oocytes

Isma Bennabi <sup>1</sup>, Flora Crozet<sup>1,7</sup>, Elvira Nikalayevich<sup>1,7</sup>, Agathe Chaigne <sup>2</sup>, Gaëlle Letort <sup>1</sup>, Marion Manil-Ségalen<sup>1</sup>, Clément Campillo <sup>3</sup>, Clotilde Cadart <sup>4,5</sup>, Alice Othmani<sup>6</sup>, Rafaele Attia<sup>4,5</sup>, Auguste Genovesio <sup>6</sup>, Marie-Hélène Verlhac <sup>1</sup>✉ & Marie-Emilie Terret <sup>1</sup>✉

Human and mouse oocytes' developmental potential can be predicted by their mechanical properties. Their development into blastocysts requires a specific stiffness window. In this study, we combine live-cell and computational imaging, laser ablation, and biophysical measurements to investigate how deregulation of cortex tension in the oocyte contributes to early developmental failure. We focus on extra-soft cells, the most common defect in a natural population. Using two independent tools to artificially decrease cortical tension, we show that chromosome alignment is impaired in extra-soft mouse oocytes, despite normal spindle morphogenesis and dynamics, inducing aneuploidy. The main cause is a cytoplasmic increase in myosin-II activity that could sterically hinder chromosome capture. We describe here an original mode of generation of aneuploidies that could be very common in oocytes and could contribute to the high aneuploidy rate observed during female meiosis, a leading cause of infertility and congenital disorders.

<sup>1</sup>CIRB, Collège de France, UMR7241/U1050, 75005 Paris, France. <sup>2</sup>MRC Laboratory for Molecular Cell Biology, UCL, London WC1E 6BT, UK. <sup>3</sup>LAMBE, Université d'Evry val d'Essonne, UMR 8587 Evry, France. <sup>4</sup>Institut Curie, PSL Research University, CNRS, UMR 144, F-75005 Paris, France. <sup>5</sup>Institut Pierre-Gilles de Gennes, PSL Research University, F-75005 Paris, France. <sup>6</sup>IBENS, Ecole Normale Supérieure, UMR8197/U1024, 75005 Paris, France. <sup>7</sup>These authors contributed equally: Flora Crozet, Elvira Nikalayevich. ✉email: [marie-helene.verlhac@college-de-france.fr](mailto:marie-helene.verlhac@college-de-france.fr); [marie-emilie.terret@college-de-france.fr](mailto:marie-emilie.terret@college-de-france.fr)

**M**eiosis in human females is error prone, resulting in aneuploidy, and as such is the leading cause of miscarriage and developmental disabilities such as trisomies<sup>1</sup>. It was recently shown that human and mouse oocytes developmental potential is accurately predicted by mechanical properties within hours after fertilization<sup>2,3</sup>. In previous studies, we have deciphered how cortex tension is regulated in mouse oocytes and embryos<sup>4–6</sup>. Using multidisciplinary approaches, we showed that the nucleation of a cortical F-actin thickening by the Arp2/3 complex in meiosis I excludes myosin-II from the cortex, decreasing cortical tension<sup>4,5</sup>. This change in cortex mechanics amplifies an initial imbalance of potential pulling forces exerted by myosin-II at the actin cage surrounding the microtubule (MT) spindle<sup>5,7–9</sup>, the forces being probably stronger at the pole closest to the cortex because of the initial slight asymmetry of spindle position<sup>10</sup>. Spindle motion is slow<sup>8,10</sup> but is amplified by the progressive deformation of the cortex, made possible by lowering of cortical tension. This reduced cortex tension allows the recruitment of filaments between the cortex and the spindle, and therefore potential amplification of initial forces. The change in cortex mechanics is required for spindle migration from the oocyte center to its cortex, generating an asymmetric division in size after anaphase. The asymmetry in size of the meiotic division allows the preservation of maternal stores accumulated during oocyte growth and required for embryo development. Although the drop in cortex tension is required for spindle migration in oocytes<sup>4</sup>, spindle migration is also prevented by a too low tension<sup>5</sup>. Thus, the geometry of the division depends on a narrow window of cortical tension, regulated by myosin-II cortical localization, itself fine-tuned by actin nucleation. Defects in cortical tension affect the geometry of oocyte divisions, potentially impacting on their developmental potential<sup>11</sup>. In this study, we address the origin of early developmental failure due to cortical tension defects in the oocyte other than perturbation in the geometry of the division. We focused on extra-soft oocytes, which represent the most common case in a natural population of human and mouse oocytes<sup>2</sup>. To specifically enrich in this subpopulation to be able to analyze a large number of cells, we generated extra-soft oocytes by using two constructs promoting a decrease in cortical tension when expressed in mouse oocytes. First, we used the cortical verprolin-homology cofilin-homology acidic (cVCA) construct<sup>5</sup> that forces Arp2/3-dependent actin nucleation at the cortex of oocytes, chasing myosin-II from the cortex, leading to cortical tension decrease and apparent softening<sup>4,5</sup>. Second, we designed a construct that induces ectopic actin assembly by the FH1FH2 nucleating domain of formin 2 at the cortex of oocytes. We show that expression of this construct also induces myosin-II cortical displacement and reduces cortical tension.

Using these two approaches, we observe impaired chromosome alignment and aneuploidy in extra-soft oocytes, despite normal spindle assembly and dynamics as assessed by MT density and growth measurements. By performing laser ablation experiments, we show the presence of forces applied by F-actin on the spindle and transmitted to the chromosomes. Even though the intensity of these forces appears reduced in extra-soft oocytes, they do not seem to contribute to chromosome misalignment. Rather, a cytoplasmic increase in myosin-II activity appears as the main cause of chromosome misalignment, potentially sterically hindering chromosome capture, as decreasing myosin-II activity in extra-soft oocytes rescues alignment. In this work, we describe a possible mode of generation of aneuploidies that could be very common in female gametes. Indeed, 36% of oocytes are measured as too soft in a natural population<sup>2</sup>. A fraction of these naturally soft oocytes might present chromosome alignment defects impeding on their future development after fertilization,

contributing to the high aneuploidy rate measured in female meiosis, a leading cause of infertility<sup>1</sup>.

## Results

**Too soft oocytes are aneuploid.** Extra-soft oocytes are the most represented case in a natural population of mouse and human oocytes<sup>2</sup>. To specifically enrich in this subpopulation and be able to analyze a large number of cells, we developed tools able to decrease cortical tension.

The first one is the cVCA (Fig. 1a), a construct that forces branched Arp2/3-dependent nucleation of F-actin at the cortex, chasing cortical myosin-II and leading to a decrease in cortical tension<sup>5</sup>. As a consequence, cVCA-expressing oocytes (named cVCA oocytes hereafter) are extra soft. We followed chromosome alignment and segregation by live spinning-disk microscopy during meiosis I in cVCA oocytes. Whereas chromosomes are aligned on the metaphase I plate in controls, cVCA oocytes display chromosome alignment defects before anaphase I (Fig. 1b). We defined oocytes with misaligned chromosomes before anaphase I as having one or several chromosomes away from the metaphase plate. Using this criterion, 48% of cVCA oocytes present chromosomes that are not aligned before anaphase I (Fig. 1c right gray bar) compared with 15 % in controls (Fig. 1c left gray bar). cVCA oocytes still undergo anaphase on time, despite having misaligned chromosomes<sup>5</sup>. This leads to aberrant chromosome segregation at anaphase I (Fig. 1b red asterisk) and aneuploidy (Supplementary Fig. 1 80% of oocytes are euploid in controls vs. 37.5% in cVCA oocytes and Supplementary Movie 1), as measured on intact oocytes using Monastrol spreads<sup>12</sup> (see Methods). To further characterize the phenotype of cVCA oocytes, we developed an automated and blind approach to discriminate statistically significant features different between control and extra-soft oocytes. This was achieved using an unbiased computational imaging approach to automatically threshold the stacks of images (control and cVCA oocytes 30 min before anaphase I) and extract the features differing the most between controls and extra-soft oocytes (as in ref. 13). The aspect ratio was the most significantly different feature between the two conditions (Fig. 1d). This feature is defined by the ratio of the minor axis length to the major axis length. When this ratio is 1, both axes are equal and the shape is close to a circle (Fig. 1d red circle on the right). On the opposite, when the ratio is close to 0, the minor axis is much smaller than the major axis and the shape is flat (Fig. 1d red ellipse on the left). For controls, the aspect ratio was close to 0 (Fig. 1d black curve bars), showing that the chromosomes were aligned. In cVCA oocytes, aspect ratios formed a bimodal distribution between 0 and 1, arguing that some of the oocytes displayed chromosomes that were aligned as in the controls but others displayed chromosomes that were misaligned (Fig. 1d blue curve bars). This computational approach allowed us to quantify and validate the chromosome alignment defect we observed in cVCA oocytes, and allowed us to find an easy criterion to measure it in an unbiased manner (Fig. 1d). This criterion was then applied manually in the rest of the study by drawing the bounding boxes around the chromosomes and measuring their width as a readout for chromosome alignment (Fig. 1h).

To exclude the possibility that impaired chromosome alignment was specific to cVCA-expressing oocytes, we designed another tool able to decrease cortical tension, the cFH1FH2. This construct was obtained by fusing the FH1FH2 domain of formin 2 to ezrin (Fig. 1e), forcing linear actin nucleation at the cortex of mouse oocytes. Similar to the cVCA, the cFH1FH2 localizes specifically to the oocyte cortex (Supplementary Fig. 2A bottom left panel). Unlike the cVCA and probably due to the difference

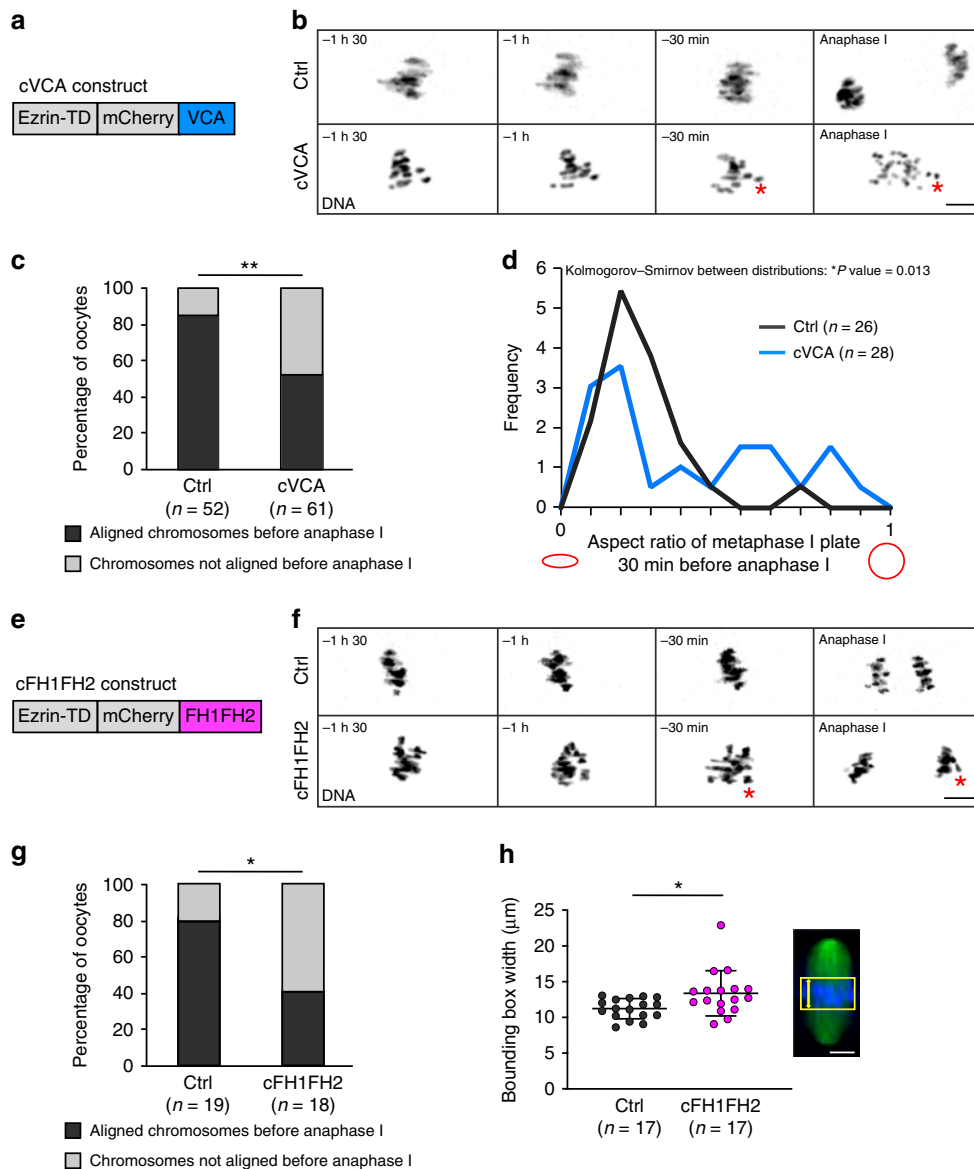


**Fig. 1 Extra-soft oocytes have chromosome alignment defects in metaphase I.** **a** Scheme of the cVCA construct. **b** Representative time-lapse movies of chromosomes (black, (H2B)-GFP) in control and cVCA oocytes starting 1 h 30 min before anaphase I (10 independent experiments). Scale bar: 10 μm. The red asterisk points at a misaligned chromosome segregated in the oocyte. **c** Bar graph representing the percentage of oocytes with aligned (black) or not (gray) chromosomes 30 min before anaphase I for controls and cVCA oocytes. *n* is the number of oocytes analyzed. Data are from ten independent experiments. Statistical significance of differences is assessed with a two-sided  $\chi^2$ -test: \*\**P*-value = 0.0003. **d** Graph representing the aspect ratio (close to 1 is a circle, close to 0 an ellipse as shown in red) for controls and cVCA oocytes. Quantifications 30 min before anaphase I. *n* is the numbers of oocytes analyzed. Data are from seven independent experiments. Statistical significance of differences between distributions is assessed with a two-sided Kolmogorov–Smirnov test: \**P*-value = 0.013. **e** Scheme of the cFH1FH2 construct. **f** Representative time-lapse movies of chromosomes (black, (H2B)-GFP) in control and cFH1FH2 oocytes starting 1 h 30 min before anaphase I (three independent experiments). Scale bar: 10 μm. The red asterisk points at a misaligned chromosome segregated in the oocyte. **g** Bar graph representing the percentage of oocytes with aligned (black) or not (gray) chromosomes 30 min before anaphase I for controls and cFH1FH2 oocytes. *n* is the number of oocytes analyzed. Data are from three independent experiments. Statistical significance of differences is assessed with a two-sided Fisher’s test: \**P*-value = 0.0201. **h** Dot plot showing the width of the bounding box containing the chromosomes 30 min before anaphase I in controls and cFH1FH2 oocytes. *n* is the number of oocytes analyzed. Data obtained from three independent experiments. Black bars and whiskers represent mean and SD. Statistical significance of differences is tested with a two-sided Mann–Whitney test: \**P*-value = 0.0134. The bounding box corresponds to the yellow square in the image of spindle (green) with chromosomes (blue), its width to the yellow dashed line. Scale bar: 5 μm.

in the nature of the network nucleated (branched for cVCA vs. linear for cFH1FH2), oocytes expressing the cFH1FH2 (named cFH1FH2 oocytes hereafter) do not nucleate a cortical actin thickening (Supplementary Fig. 2A bottom right panel and quantification in 2B). Surprisingly, expression of the cFH1FH2 construct is associated with a reduction in cortical myosin-II

levels (Supplementary Fig. 2C and quantification in 2D). These data show that overnucleation of linear actin by FH1FH2 at the cortex of oocytes is sufficient to chase myosin-II. It suggests that myosin-II can be chased by steric hindrance and not by preferential binding to one type of actin network (linear vs. branched) at the cortex of mouse oocytes. Finally, cFH1FH2

expression induces an eight-fold decrease in cortical tension measured by micropipette aspiration (Supplementary Fig. 2E,  $3.58 \pm 1.1$  nN per  $\mu\text{m}$  for controls and  $0.41 \pm 0.2$  nN per  $\mu\text{m}$  for cFH1FH2 oocytes). Thus, cortical myosin-II removal in cFH1FH2 oocytes leads to cortex softening as for cVCA oocytes. Similar to what was observed with the cVCA construct, meiosis I spindle length is comparable to controls in cFH1FH2 oocytes (Supplementary Fig. 2F), but its migration is impaired (Supplementary Fig. 2G and quantification in 2H), consistent with the fact that cortical tension impacts meiosis I spindle migration in mouse oocytes<sup>4,5</sup>. Very interestingly, cFH1FH2-expressing oocytes also display chromosome alignment defects (Fig. 1f). In controls, chromosomes are aligned on the metaphase plate at the end of meiosis I (Fig. 1f upper panels), whereas chromosomes in cFH1FH2 oocytes do not form a proper plate (Fig. 1f bottom panels). In particular, 61% of cFH1FH2 oocytes have misaligned chromosome before anaphase against 21% of controls (Fig. 1g). To further quantify chromosome alignment, we measured the width of the bounding box encompassing the metaphase I plate (Fig. 1h yellow square and yellow dash line). If chromosomes are misaligned, the bounding box width should be larger than when chromosomes are tightly aligned. Indeed, the bounding box width is increased before anaphase in cFH1FH2 oocytes ( $13.37 \pm 3.1$   $\mu\text{m}$ ; Fig. 1h magenta dots) compared with controls ( $11.23 \pm 1.4$   $\mu\text{m}$ ; Fig. 1h black dots). cFH1FH2 oocytes still undergo anaphase and first polar body extrusion (Fig. 1f and Supplementary Fig. 2I), despite having misaligned chromosomes, leading to aberrant chromosome segregation at anaphase I (Fig. 1f red asterisk).

In conclusion, actin accumulation at the oocyte cortex, regardless of its organization, sterically excludes myosin-II, decreasing cortical tension. Remarkably, chromosome alignment errors could be a hallmark of oocytes with a too low cortical tension.

**Too soft oocytes, smaller, have normal cytoplasmic activity.** As observed before<sup>5</sup>, cVCA oocytes display strong shape deformations inherent to their decrease in cortical tension (Supplementary Fig. 3A). The same is true for cFH1FH2 oocytes (Supplementary Fig. 2A, C). These deformations are stable at long time scales (Supplementary Fig. 3B spanning 1 h 30 min) and at short time scales, as observed by high-frequency video microscopy (Supplementary Movie 2). The presence of deformations in cVCA oocytes prompted us to precisely measure their volume. For this, we took advantage of the fluorescence exclusion measurement (FXm) method initially described in ref. <sup>14</sup>, to measure the volume of control and cVCA oocytes (Supplementary Fig. 3C). The mean volume of cVCA oocytes is reduced by 9.45% compared with controls (Supplementary Fig. 3D).

We then wondered what could be the consequences of this volume reduction of about 10%, and in particular if it could impact cytoplasmic activity. Cytoplasmic activity represents the movement of the cytoplasm within a cell. The cytoplasmic motion translates into the movement of all intracellular organelles, as has been observed in Prophase I mouse oocytes<sup>15</sup>. One could imagine that extra-soft oocytes with a reduced volume would have a more viscous cytoplasm, reflected by a lower cytoplasmic activity, impairing chromosome movement and resulting in chromosome misalignment. To test this hypothesis, we assessed oocyte cytoplasmic activity by tracking the movement of vesicles using high-frequency spinning-disk microscopy (Supplementary Movie 3), as previously described in ref. <sup>15</sup>. We measured the mean square displacement (MSD) of the vesicles, representing the space they explore, obtained by averaging the square of the distance traveled per unit of time. The MSD plots describing vesicle movement in the cytoplasm are similar,

suggesting that the cytoplasmic activity is not impaired in cVCA oocytes (Supplementary Fig. 3E). In conclusion, chromosome misalignment in cVCA oocytes is not due to a difference in cytoplasmic activity.

### Too soft oocytes transmit weaker forces to chromosomes.

Defects in chromosome alignment could be due to altered forces transmitted from the cortex to the chromosomes. We first directly tested whether forces are mechanically transmitted to chromosomes in control oocytes and then whether a decrease in cortical tension results in aberrant forces, potentially impairing chromosome alignment in extra-soft oocytes.

In control oocytes, chromosomes migrate from the oocyte center to its cortex. This migration depends only on F-actin<sup>7,8,10,16,17</sup> and not on the presence of astral MTs as in mitotic cells<sup>18–20</sup>, as oocytes are devoid of centrioles and astral MTs<sup>21,22</sup>. Actin is organized in a cytoplasmic network including an actin cage around the MT spindle, which is connected to the subcortical actin network<sup>5,7–9</sup> (Supplementary Fig. 4A). The force generator element for spindle migration is likely myosin-II, which seems to exert pulling forces on the actin cage surrounding the MT spindle as shown using inhibitors<sup>5,8</sup>. However, there is no direct evidence that forces are applied on the spindle by actomyosin networks in oocytes. We assessed qualitatively these forces by performing laser ablation. The F-actin cytoplasmic network was cut between the spindle pole and the closest cortex at the end of meiosis I, 6 h 30 min after nuclear envelope breakdown (BD + 6 h 30 min) on several Z stacks spanning the entire thickness of the metaphase plate (Supplementary Fig. 4A yellow dotted line, Supplementary Fig. 4B, C, and Supplementary Movies 4 and 5). Laser ablation did not damage oocytes, as they all extruded a polar body and arrested in metaphase II normally following ablation. After laser ablation, the response of Histone (H2B)-GFP labeled chromosomes was monitored by live microscopy during 1 min. MTs were visualized using very low doses of EB3-GFP to follow the spindle and make sure that the ablation was not performed within the spindle but away from spindle poles (Supplementary Fig. 4B, C and Supplementary Movies 4 and 5). Before laser ablation, the chromosomes are clustered and aligned on the metaphase plate in control oocytes at BD + 6 h 30 min (Supplementary Fig. 4B upper left panel  $t = 0$  min). One minute after laser cutting, the metaphase plate shrinks (Supplementary Fig. 4B upper middle panel). To quantify this effect, we measured the width of the bounding box encompassing the metaphase plate before and after laser ablation (Supplementary Fig. 4B in plain and dotted yellow lines, respectively). The width of the bounding box decreases progressively after ablation (Supplementary Fig. 4B upper panels and Supplementary Fig. 4D black curve) arguing that the actomyosin networks exerts forces on the chromosomes. In contrast, when we performed laser ablation at BD + 3 h before spindle-cortex attachment<sup>7,23</sup>, we did not see an impact on chromosome behavior (Supplementary Fig. 4E and Supplementary Movie 6). In addition, we never observed progressive decrease in the width of the bounding box without laser ablation in oocytes at BD + 6 h 30 min (Supplementary Fig. 4F and Supplementary Movie 7). Our results demonstrate that the actomyosin network exerts forces on the chromosomes, which are indeed responsible for the motion of the spindle to the cortex in mouse oocyte.

Previous work showed that spindle migration is impaired in extra-soft oocytes, suggesting that the forces applied on the spindle are altered<sup>5</sup>. This was also predicted by a theoretical model, but never directly tested experimentally<sup>5</sup>. In cVCA oocytes, chromosomes are scattered on the metaphase plate before ablation at BD + 6 h 30 min (Supplementary Fig. 4B

bottom left panel  $t = 0$  min). After cutting of the spindle-cortex connection, the chromosomes remain scattered on the metaphase plate, which stays stable in width (Supplementary Fig. 4B bottom panels, Supplementary Fig. 4D blue curve, and Supplementary Movie 4). This suggests that, at that stage, the intensity of the forces applied on the chromosomes is reduced in cVCA oocytes compared with controls. Our results validate the mathematical modeling of spindle migration predicting that the intensity of forces transmitted to the spindle are diminished in extra-soft oocytes<sup>5</sup>. We then wondered whether the decrease in forces applied to the meiotic spindle could have consequences on chromosome alignment.

To test this, we turned to another type of oocytes, the *Fmn2*<sup>-/-</sup> oocytes, which have reduced forces applied on their spindle. Indeed, *Fmn2*<sup>-/-</sup> oocytes are invalidated for the cytoplasmic actin nucleator formin 2 and lack the cytoplasmic network and the actin cage<sup>7,8</sup>. As a consequence, the spindle is not attached to the cortex and does not migrate<sup>16,24</sup>. Thus, in *Fmn2*<sup>-/-</sup> oocytes, the actomyosin networks do not apply forces on the spindle or chromosomes. However, *Fmn2*<sup>-/-</sup> oocytes do not have chromosome alignment defects in metaphase I<sup>9</sup> (Supplementary Fig. 4G). In conclusion, it is unlikely that the reduction in the intensity of the forces applied to chromosomes in cVCA oocytes is the main mechanism involved in the generation of misaligned chromosomes.

**Spindle morphogenesis is normal in extra-soft oocytes.** To gain insight into the origin of the chromosome alignment defects, we observed how spindle morphogenesis proceeded in extra-soft oocytes. Indeed, in mitotic cells, aberrant cortical tension impairs spindle formation, leading to chromosome segregation errors<sup>25</sup>. We monitored spindle morphogenesis by live spinning-disk microscopy during meiosis I in mouse oocytes incubated with SiR-Tubulin to label MTs (Fig. 2a and Supplementary Movie 8). Although they have misaligned chromosomes (Fig. 2a bottom panels), the spindle appears to form properly in cVCA oocytes as in controls (Fig. 2a top panels).

We then measured relative MT densities and MT growth early on during spindle morphogenesis, since defects at this stage are known to induce chromosome misalignment later on<sup>26–28</sup>. Control and cVCA oocytes expressing EB3-GFP, a MT plus-end tracker, were imaged at BD + 2 h after Monastrol treatment to inhibit spindle bipolarization (as in ref. 29, Supplementary Movie 9). MT densities and monoaster sizes are comparable in control (gray dots) and extra-soft (blue dots) oocytes (Fig. 2b dot plots and yellow dashed circles). Tracking of individual MT plus ends (Fig. 2c red tracks) shows that MT growth rates are also comparable in control (gray dots) and extra-soft oocytes (blue dots in Fig. 2c). Consistent with these observations, the spindle length of cVCA oocytes is comparable to controls at BD + 7 h ( $29.93 \pm 1.64 \mu\text{m}$  in cVCA oocytes compared with  $29.27 \pm 1.80 \mu\text{m}$  in controls; Fig. 2d).

All these data indicate that spindle morphogenesis and dynamics are comparable to controls in extra-soft cVCA oocytes. Moreover, it was shown previously that cVCA expression does not alter the architecture nor the dynamics of the cytoplasmic actin network<sup>5</sup>, two features that could potentially affect spindle formation when they are modified<sup>23</sup>.

**Chromosome capture is less efficient in extra-soft oocytes.** As we did not observe gross spindle defects, to further explore the reason for chromosome alignment defects in extra-soft oocytes, we performed a more thorough analysis of chromosome movements. For this, we tracked individual chromosomes on the metaphase I plate during 20 min at BD + 6 h 30 min. Individual

chromosome tracks suggest that chromosomes explore more space in metaphase I cVCA oocytes than in controls (Fig. 3a for representative examples and Supplementary Movie 10), which is confirmed by their MSD analysis (Fig. 3b). Fitting of the MSD slopes to a simple linear model and statistical comparison of the slopes revealed different diffusion coefficient in control vs. cVCA oocytes (Fig. 3b) demonstrating that chromosomes in cVCA oocytes explore more space than in controls. This could reflect a problem in chromosome capture.

To test this hypothesis, we analyzed chromosome distribution throughout meiosis I in control and cVCA oocytes from NEBD to BD + 7 h 30 min. To do so, we fitted an ellipse around the chromosomes (Supplementary Movie 11), measured the length of its major axis and compared its variation over a window of 2 h (Fig. 3c). This variation is a measure of chromosome alignment efficiency: if it is negative, it means that the ellipse shortens reflecting chromosome gathering. In control and cVCA oocytes, the variation is positive between NEBD and BD + 2 h, indicating that the ellipse elongates, corresponding to chromosome condensation and individualization (as described in ref. 30). Starting between BD + 2 h and 2 h 30 min, the variation becomes negative in the controls (black curve), showing that the ellipse shortens, suggesting that chromosomes are converging/aligning. In cVCA oocytes, the variation is close to 0 and significantly different from the controls at BD + 3 h and BD + 3 h 30 min (blue curve), showing that the ellipse does not vary, suggesting that chromosome alignment is less efficient or slower. The phase between BD + 2 h 30 min and 4 h corresponds to chromosome capture and the first chromosome biorientation attempts<sup>30</sup>, suggesting that chromosomes are less efficiently captured in cVCA oocytes despite normal MT density and growth (Fig. 2b, c).

If it is the case, chromosomes should experience less tension across opposite kinetochores of bivalents in cVCA oocytes. To test that, we measured the distance between major satellite repeats in each bivalent at BD + 6 h 30 min (Fig. 3d and Supplementary Movie 12), an indirect measure of tension across bivalents<sup>31</sup>. We represent a distribution graph showing the percentage of bivalents falling in a certain range of major satellite repeats distances (Fig. 3e). For cVCA oocytes, the curve (Fig. 3e blue) is shifted towards smaller distances, showing that cVCA bivalents experience less tension, consistent with the fact that chromosomes are less efficiently captured in cVCA oocytes.

**Accumulation of myosin-II generates chromosome misalignment.** It was shown recently in starfish oocytes that actin structures can sterically hinder kinetochore-MT attachments, a physiological process important to coordinate chromosome capture by MTs<sup>32</sup>. We thus wondered whether such a mechanism could be at play in extra-soft oocytes, leading to less efficient chromosome capture. It was shown previously that the expression of the cVCA does not alter the architecture nor the dynamics of the cytoplasmic actin network<sup>5</sup>. However, we analyzed in more detail actin organization in extra-soft oocytes at later stages and tested whether depolymerizing actin could rescue chromosome alignment. We visualized F-actin at BD + 6 h 30 min by staining oocytes with fluorescent phalloidin (Fig. 4a gray). F-actin forms a cytoplasmic network and an actin cage in controls, as previously described<sup>7,8</sup> (Fig. 4a left panels). The same organization can be observed in cVCA oocytes (Fig. 4a right panels). We quantified F-actin fluorescent intensity levels on the spindle and in the cytoplasm in control and cVCA oocytes (Fig. 4b, c). We could not detect any significant difference between control and cVCA oocytes, suggesting that chromosome capture in cVCA oocytes is not hindered by an accumulation of F-actin. Accordingly,

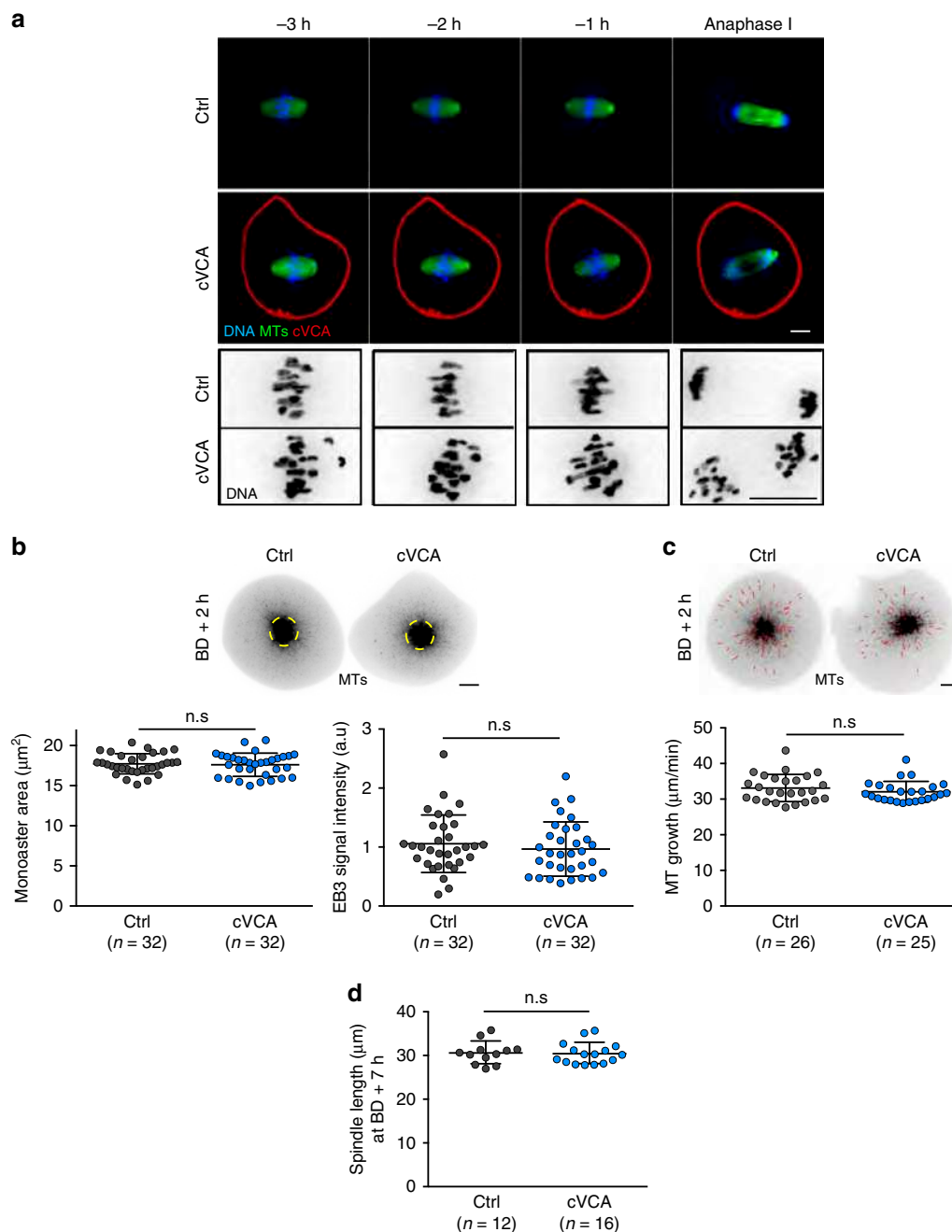


**Fig. 2 Spindle morphogenesis is normal in extra-soft oocytes. a** Representative time-lapse movies of control and cVCA (red) oocytes expressing Histone (H2B)-GFP (blue). Microtubules (MTs, green) are visualized with SiR-Tubulin. Movies start 3 h before anaphase I. The bottom rows show magnification of the chromosomes (black) from the upper panels. Scale bars: 10  $\mu\text{m}$ . Four independent experiments. **b** Top panel: control and cVCA oocytes observed at BD + 2 h expressing EB3-GFP (black) and treated with Monastrol. Scale bar: 10  $\mu\text{m}$ . Bottom panels: dot plots showing the area (left panel) and fluorescence intensity (right panel) of the EB3-GFP monoasters (yellow dashed circles highlighted on the top panels) in controls and cVCA oocytes. Data are from three independent experiments. Statistical significance is determined with an unpaired *t*-test for monoaster size n.s. *P*-value = 0.7336 and a two-sided Mann-Whitney test for monoaster fluorescence intensity n.s. *P*-value = 0.3871. **c** Top panel: control and cVCA oocytes observed at BD + 2 h expressing EB3-GFP (black) treated with Monastrol. Scale bar: 10  $\mu\text{m}$ . EB3-GFP comets were tracked on a single plane and average comet speed per oocyte is displayed on the dot plot (bottom panel), reflecting MT growth. Example of tracks in control and cVCA oocytes are highlighted in red (top panel). Data are from three independent experiments. Statistical significance is determined with a two-sided Mann-Whitney test: n.s. *P*-value = 0.3739. **d** Spindle length quantifications for controls and cVCA oocytes 7 h after nuclear envelope breakdown (BD + 7 h). *n* is the number of oocytes analyzed. Data are from four independent experiments. Statistical significance is determined with a two-sided Mann-Whitney test: n.s. *P*-value = 0.432. For **b**, **c**, **d**, black bars and whiskers represent mean and SD.

depolymerizing F-actin in extra-soft oocytes does not rescue chromosome alignment defects (Fig. 4d, e), suggesting also that F-actin is not the cause of chromosome misalignment in extra-soft oocytes.

We thus wondered what could hinder chromosome capture in extra-soft oocytes and hypothesized that it could be an excess of myosin-II in the cytoplasm. Indeed, oocytes expressing the cVCA or the cFH1FH2 constructs share chromosome alignment defects

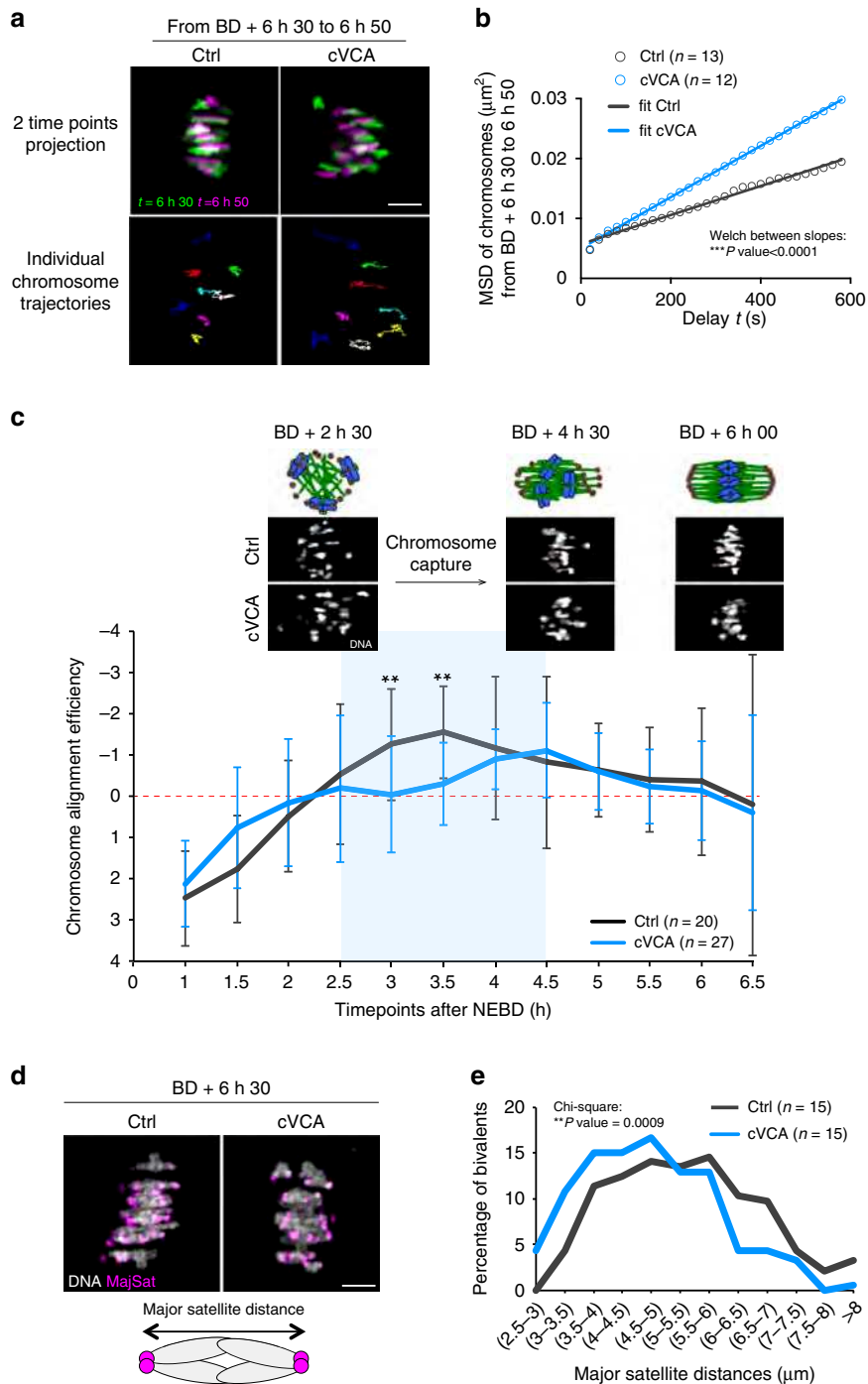


**Fig. 3 Chromosome capture is less efficient in extra-soft oocytes.** **a** Representative temporal color-coded projections from time-lapse movies of a control and cVCA oocyte (upper panels). Scale bar: 5  $\mu\text{m}$ . Bottom panels show individual chromosome trajectories corresponding to the upper panels. Each color represents one chromosome track. Four independent experiments. **b** Graph representing the mean square displacement (MSD) of individual chromosome between BD + 6 h 30 min and 6 h 50 min. Fifty-nine chromosomes among 13 controls and 60 chromosomes among 12 cVCA oocytes were analyzed. Data are from four independent experiments. MSD data are fitted to a simple linear regression model ( $R^2 > 0.97$ ). Statistical significance of differences of slopes between Ctrl and cVCA is assessed with a two-sided Welch's test: \*\*\* $P$ -value < 0.0001. **c** Graph representing the variation of elongation of the ellipse fitting the chromosomes between nuclear envelope BD (NEBD) and BD + 7 h 30 min for controls and cVCA oocytes.  $n$  is the number of oocytes analyzed. Data are from five independent experiments. The mean and SD are shown. Statistical significance of differences is assessed with a two-sided Wilcoxon's test: \*\* $P$ -value = 0.005. The blue part of the graph corresponds to the chromosome capture phase. Images (chromosomes in white) and corresponding schemes (microtubules in green, DNA in blue, microtubule organizing centers in brown) are shown for BD + 2 h 30 min, 4 h 30 min, and 6 h. **d** Representative projections from time-lapse movies of control and cVCA oocytes at BD + 6 h 30 min expressing Histone(H2B)-GFP (gray) and MajSat-mClover (magenta). Scale bar: 5  $\mu\text{m}$ . The scheme represents a bivalent (major satellite repeats in magenta). Five independent experiments. **e** Distribution graph representing the distance between major satellite repeats in live oocytes at BD + 6 h 30 min for controls and cVCA oocytes. One hundred and eighty-five chromosomes among 15 controls and 186 chromosomes among 15 cVCA oocytes were analyzed. Data are from five independent experiments. Statistical significance of differences is assessed with a two-sided  $\chi^2$ -test. \*\* $P$  = 0.0009.

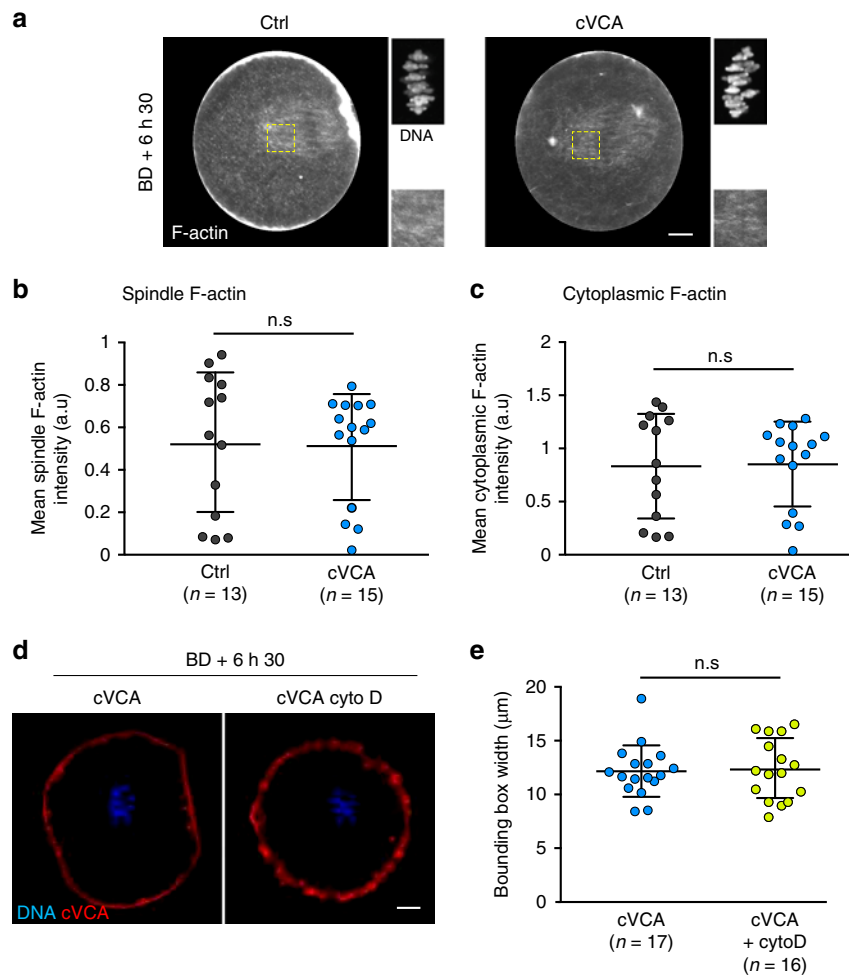


**Fig. 4 Actin organization and density in extra-soft oocytes is similar to controls and its depolymerization does not rescue chromosome alignment.**

**a** Cropped images of representative immunofluorescence of control and cVCA oocytes stained for F-actin (gray) at BD + 6 h 30 min. Insets are magnification of the chromosomes (gray) and of regions marked by yellow dashed line boxes. Scale bar: 10  $\mu\text{m}$ . Three independent experiments. **b** Dot plot representing the F-actin spindle intensity at BD + 6 h 30 min in controls and cVCA oocytes.  $n$  is the number of oocytes analyzed. Data are from three independent experiments. Statistical significance of differences is assessed with a two-sided Mann-Whitney test: n.s.  $P$ -value = 0.6832. **c** Dot plot representing the F-actin cytoplasm intensity at BD + 6 h 30 min in controls and cVCA oocytes.  $n$  is the number of oocytes analyzed. Data are from three independent experiments. Statistical significance of differences is assessed with a two-sided Mann-Whitney test: n.s.  $P$ -value = 0.8207. **d** Oocytes at BD + 6 h 30 min expressing Histone(H2B)-GFP (blue) and cVCA (red). The oocyte on the right panel were treated with 1  $\mu\text{g}/\text{ml}$  cytochalasin D. Scale bar: 10  $\mu\text{m}$ . Five independent experiments. **e** Dot plot representing the metaphase I plate width at BD + 6 h 30 min in cVCA oocytes treated or not with 1  $\mu\text{g}/\text{ml}$  cytochalasin D.  $n$  is the number of oocytes analyzed. Data are from five independent experiments. Statistical significance of differences is assessed with a two-sided Mann-Whitney test: n.s.  $P$ -value = 0.810. For **b**, **c**, **e**, black bars and whiskers represent mean and SD.

(Fig. 1b, f) and chase precociously myosin-II from the cortex (Supplementary Figs. 2C, D and 5) leading to a softened cortex<sup>5</sup> (Supplementary Figure 2E). First, we quantified myosin-II accumulation over time in the cytoplasm in control and extra-soft oocytes (Supplementary Fig. 5). We followed endogenous myosin-II using a specific GFP-coupled intrabody directed against myosin-II<sup>4,33</sup> (Supplementary Fig. 5A) and measured the fluorescence signal intensity in the cytoplasm 2 h and 9 h after cRNA injection in control and extra-soft oocytes (Supplementary Fig. 5B). Levels of cytoplasmic myosin-II are comparable 2 h after cRNA injection in all conditions (control, cVCA, cFH1FH2, Supplementary Fig. 5B). Nine hours after cRNA injection, extra-soft oocytes have 1.9 (for cFH1FH2) and 2.5 (for cVCA oocytes) times more myosin-II in their cytoplasm compared with control oocytes at the same stage (Supplementary Fig. 5B). In addition, extra-soft oocytes accumulate more myosin-II in their cytoplasm over time compared with controls (1.5 times accumulation of myosin-II for controls, 2.1 for cFH1FH2, and 2.7 for cVCA

oocytes; Supplementary Fig. 5B). We hypothesized that this could lead to higher levels of cytoplasmic myosin-II during meiosis I, sterically affecting chromosome capture. We thus visualized active myosin-II at BD + 6 h 30 min, by staining against its phosphorylated light chain pMLC2 (Fig. 5a). Active myosin-II localizes in the cytoplasm and is enriched on the spindle and at the cortex facing the spindle at BD + 6 h 30 min in control oocytes<sup>4,8,16</sup> (Fig. 5a left panels). This staining is specific, as it disappears in oocytes treated with the ML-7 inhibitor, a drug that inhibits myosin-II activation by MLCK phosphorylation<sup>4,8</sup> (Fig. 5a right panels). Active myosin-II is also localized in the cytoplasm and enriched on the spindle at BD + 6 h 30 min in cVCA oocytes (Fig. 5a middle panels). By quantifying active myosin-II fluorescent intensity, we show that the levels of active myosin-II in the cytoplasm and spindle are higher in cVCA oocytes compared with controls (Fig. 5b, c, 1.6 times more active myosin-II in the cytoplasm and 1.4 more in the spindle in cVCA oocytes), reinforcing our hypothesis. Next, we inhibited the

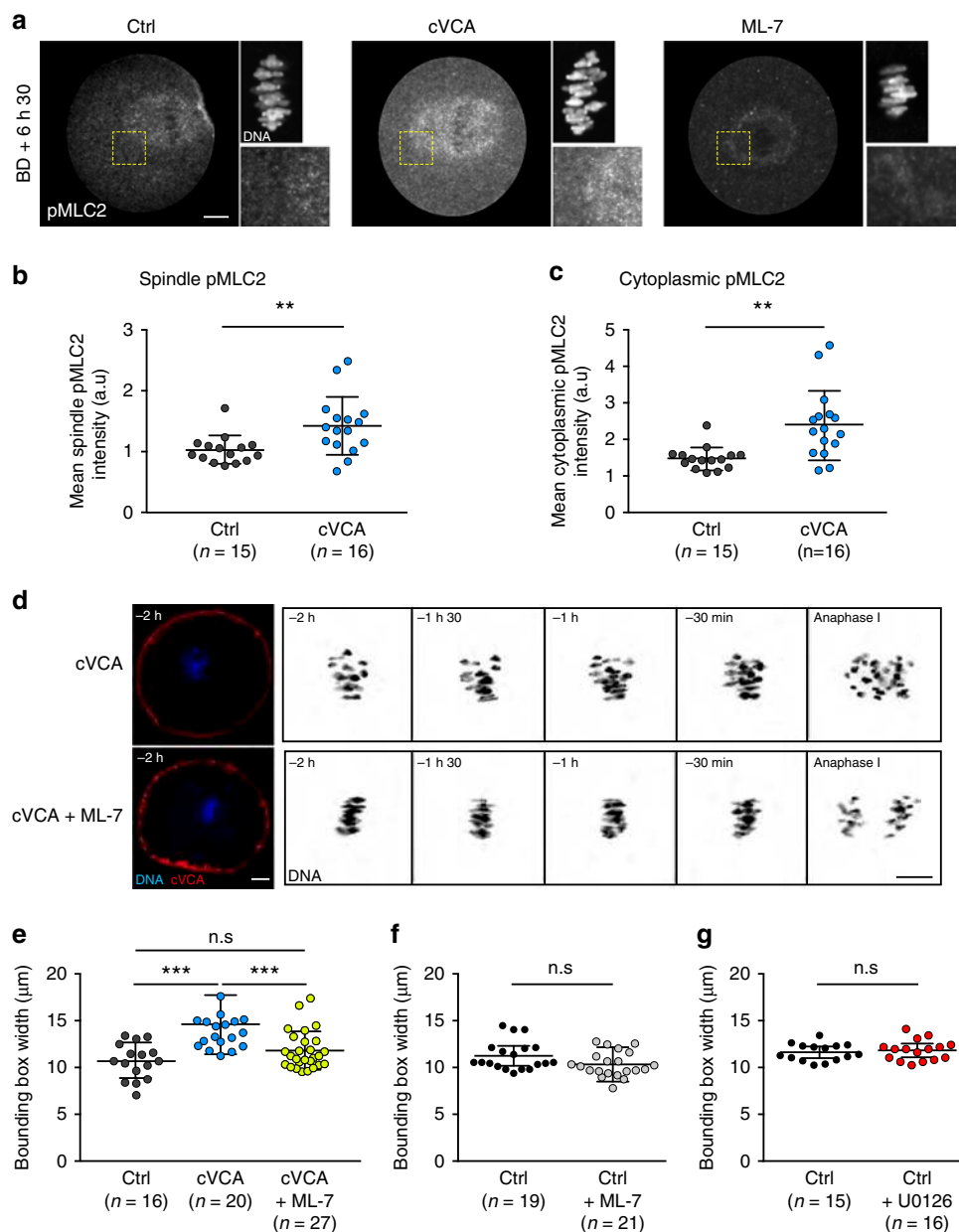


**Fig. 5 Active myosin-II accumulates in extra-soft oocytes and decreasing its activity rescues chromosome misalignment.** **a** Cropped images of representative control, cVCA, and ML-7-treated oocytes stained for active phosphorylated myosin-II (pMLC2, gray) at BD + 6 h 30 min. Insets are magnification of the chromosomes (gray) and of regions marked by yellow dashed line boxes. Same oocytes as in Fig. 4a. Scale bar: 10  $\mu$ m. Three independent experiments. **b** Dot plot representing pMLC2 spindle intensity at BD + 6 h 30 min in control and cVCA oocytes. *n* is the number of oocytes analyzed. Data are from three independent experiments. Statistical significance of differences is assessed with a two-sided Mann-Whitney test: \*\**P*-value = 0.0042. **c** Dot plot representing pMLC2 cytoplasm intensity at BD + 6 h 30 min in controls and cVCA oocytes. *n* is the number of oocytes analyzed. Data are from three independent experiments. Statistical significance of differences is assessed with a two-sided Mann-Whitney test: \*\**P*-value = 0.0004. **d** Representative time-lapse movies of cVCA oocytes treated or not with ML-7, expressing Histone(H2B)-GFP (blue or black) and cVCA (red). Acquisitions were taken every 30 min starting 2 h before anaphase I. Scale bar: 10  $\mu$ m. Six independent experiments. **e** Dot plot representing the metaphase I plate width 30 min before anaphase I in control and cVCA oocytes treated or not with ML-7. *n* is the number of oocytes analyzed. Data are from six independent experiments. Statistical significance of differences is assessed with a two-sided Mann-Whitney test: n.s. *P*-value = 0.1708 and \*\*\**P*-value < 0.0001. **f** Same as **e** for control oocytes treated or not with ML-7. *n* is the number of oocytes analyzed. Data are from four independent experiments. Statistical significance of differences is assessed with a two-sided *t*-test: n.s. *P*-value = 0.0547. **g** Same as **e** for control oocytes treated or not with U0126. *n* is the number of oocytes analyzed. Data are from three independent experiments. Statistical significance of differences is assessed with a two-sided *t*-test: n.s. *P*-value = 0.5756. For **b**, **c**, **e-g**, black bars and whiskers represent mean and SD.

activation of myosin-II in extra-soft cVCA oocytes and tested whether it was sufficient to rescue chromosome alignment. cVCA oocytes present chromosome misalignment in metaphase I (Fig. 1b bottom panels, Fig. 2a bottom panels, and Fig. 5d top

panels). However, these chromosome defects are no longer observed when they are treated with ML-7: chromosomes are well-aligned on the metaphase I plate until anaphase (Fig. 5d bottom panels). We quantified it by measuring the bounding box

surrounding the metaphase I plate width. The bounding box width is larger in cVCA oocytes (Figs. 5e,  $14.61 \pm 3.25 \mu\text{m}$  for cVCA oocytes compared with  $10.67 \pm 1.90 \mu\text{m}$  for controls). Remarkably, the bounding box width is significantly rescued in ML-7-treated cVCA oocytes and is comparable to controls (Fig. 5e,  $11.81 \pm 2.04 \mu\text{m}$  for cVCA oocytes treated with ML-7). These results argue that an excess of active myosin-II in the cytoplasm impairs chromosome alignment in extra-soft oocytes.

In addition, we tested whether reducing myosin-II activity in control oocytes could improve chromosome alignment, as basal rates of chromosome misalignment (Fig. 1c, g) and aneuploidy (Supplementary Fig. 1) are observed in control populations of mouse oocytes<sup>1</sup>. The bounding box width is reduced in control oocytes treated with ML-7 (Fig. 5f,  $11.41 \pm 1.58 \mu\text{m}$  for controls compared with  $10.48 \pm 1.37 \mu\text{m}$  for controls treated with ML-7). This trend reinforces the hypothesis that too much active myosin-II in the cytoplasm/spindle hampers chromosome alignment in oocytes.

At last, we quantified chromosome alignment in stiff oocytes. For that, we treated control oocytes with U0126, an inhibitor of the MEK1/2 kinases that mimics a *mos*<sup>-/-</sup> phenotype by inhibiting the nucleation of the Arp2/3-dependent subcortex, leading to retention of myosin-II at the cortex and high cortical tension, as we show in a previous study<sup>4</sup>. The bounding box width in U0126-treated oocytes is comparable to controls (Fig. 5g,  $11.58 \pm 0.92 \mu\text{m}$  for controls compared with  $11.79 \pm 1.09 \mu\text{m}$  for controls treated with U0126), showing that cortical tension per se does not impact chromosome alignment.

## Discussion

In this study, we show that chromosome alignment is impaired by artificial reduction of cortex tension in mouse oocytes (Fig. 1), leading to errors in chromosome segregation and aneuploidy (Supplementary Fig. 1). It is usually thought that changes in cortical tension are transmitted mechanically to the MT spindle. In particular, F-actin is known to impact MT architecture and dynamics, potentially acting on chromosome behavior in oocytes and other systems<sup>9,34–38</sup>. There is also evidence showing that myosin-II is involved in MT functions and thus potentially in chromosome behavior. Myosin-II localizes to the spindle and is implicated in kinetochore-MT flux in metaphase I carpe fly spermatocytes<sup>39,40</sup>. It is also localized to chromosome arms and to the spindle in PtK1 cells<sup>41</sup>. In addition, myosin-II is required for proper spindle assembly and positioning in mitotic cells<sup>42</sup> and mouse cardiac myocytes<sup>43</sup>. Another interesting example is the mechanosensitive role of cortical myosin-II on MT growth in endothelial cells, where inhibition of myosin-II activity prevents mitotic centromere-associated kinesin (MCAK)-mediated MT growth<sup>44</sup>. Finally, myosin-II was shown to interact directly with kinesins in astrocytes, which is essential for their migration<sup>45</sup>. Here we show using laser ablation experiments that changes in cortical tension are transmitted mechanically to the MT spindle, but that they do not impact chromosome alignment (Supplementary Fig. 4). We propose that the signal transduction between a strong decrease in cortical tension and chromosome alignment may rather be biochemical. With decreased cortical tension, myosin-II dissociates precociously from the cortex and thus its global concentration increases in the cytoplasm (Fig. 5). This could sterically hinder chromosome capture (Fig. 3), leading to chromosome misalignment and segregation defects. This is reminiscent of starfish oocytes where an actin structure can sterically block kinetochore-MT attachments<sup>32</sup>. Other examples of biochemical signaling between the cortex and the chromosomes are emerging, such as the coordination by Cdk1 of cortical tension maintenance and SAC inactivation at anaphase onset in

mitotic cells<sup>46</sup>. We lack proper tools to investigate precisely how excess of myosin-II presence and/or activity in the cytoplasm could sterically hinder chromosome capture in our model. However, phosphorylation of the regulatory light chain of myosin-II not only increases its ATPase activity but also promotes assembly of myosin-II bipolar thick filaments (for review, see ref. 47), which could sterically perturb the local capture of kinetochores by MTs. In the future, it would be interesting to address it by computational modeling or using in-vitro models as described in refs. 48,49.

Our results potentially describe an original mode of generation of aneuploidies that could be very common in female gametes. Indeed, 36% of mouse and human oocytes are measured as too soft in a natural population<sup>2</sup> and lower levels of cortical active myosin-II and lower cortical tension are associated with post-ovulatory aging<sup>50</sup>. Thus, some of these naturally soft oocytes could also present chromosome misalignment impeding their future development after fertilization, contributing to the high aneuploidy rate measured in female meiosis<sup>1,51,52</sup>. Measures of cortical mechanical properties could serve as a minimally invasive technique to assess oocyte developmental potential for assisted reproductive technology, as already explored for tumors (for reviews, see refs. 53,54).

Finally, aberrant cortical tension, and especially cortex softening, are found in a variety of cancer cells<sup>55–58</sup>. Deregulation of myosin-II activity levels has also been described in several human disorders impacting neurons and vessels<sup>59</sup>. Interestingly, overexpression of myosin-II is implicated in cancer progression and metastasis, and myosin-II regulatory pathway genes are increasingly found in disease-associated copy-number variants, particularly in neuronal disorders such as autism and schizophrenia<sup>59</sup>, stressing the importance of its regulation. A recent study identified genes involved in mitotic cell rounding, most of which affect cortical myosin-II<sup>60</sup>. The mechanisms described in our study could therefore be relevant for somatic cells in normal and pathological contexts.

## Methods

**Oocyte collection, culture, and microinjection.** Ovaries were collected from 11-week-old OF1 (wt) or *Fmn2*<sup>+/-</sup> or *Fmn2*<sup>-/-24</sup> female mice. Fully grown oocytes were extracted by shredding the ovaries<sup>61</sup> in M2 + bovine serum albumin (BSA) medium supplemented with 1  $\mu\text{M}$  milrinone to block and synchronize them in Prophase I<sup>62</sup>. Transferring oocytes into milrinone-free M2 + BSA medium triggers meiosis resumption. All live culture and imaging were carried out under oil at 37 °C.

**Constructs.** We used the following constructs: pRN3-Histone(H2B)-GFP<sup>63</sup>, pRN3-hEB3-GFP<sup>29</sup>, pspc3-GFP-UtrCH7, pRN3-SF9-GFP<sup>4,33</sup>, pRN3-EzTD-mCherry-VCA<sup>5</sup>, pRN3-EzTD-mCherry<sup>5,64</sup>, and pTALYM3-TALE-mClover-MajSat<sup>31</sup> (gift from Keith T. Jones, University of Adelaide, Australia).

The pRN3-EzTD-mCherry-FH1FH2 was constructed by cloning a linker GSGGGGSG connected to the FH1FH2 domain of formin 2 (amino acids 734–1578) amplified from a pCS2-FH1FH2-eGFP<sup>13</sup> into pRN3-EzTD-mCherry<sup>5,64</sup>.

**In-vitro transcription of cRNAs and microinjection.** Plasmids were linearized using appropriate restriction enzymes. cRNAs were synthesized with the mMessage mMachine kit (Ambion) and subsequently purified using the RNeasy kit (Qiagen). Their concentration was measured using NanoDrop 2000 from Thermo-Scientific. cRNAs were centrifuged at 4 °C during 45 min prior to microinjection into the cytoplasm of oocytes blocked in Prophase I in M2 + BSA medium supplemented with 1  $\mu\text{M}$  milrinone at 37 °C. cRNAs were microinjected using an Eppendorf Femtojet microinjector<sup>10</sup>. After microinjection, cRNA translation was allowed for 1 or 2 h and oocytes were then transferred into milrinone-free M2 + BSA medium to allow meiosis resumption and meiotic divisions.

**Drug treatments.** ML-7 (Calbiochem, Ref 475880) was diluted at 30 mM in dimethyl sulfoxide (DMSO) and stored at 4 °C. After dilution in M2 medium, it was used on oocytes at 60  $\mu\text{M}$  and added 5 h after NEBD, because at that stage the spindle is bipolar but did not yet migrate to the closest cortex<sup>10</sup>. Control

experiments were conducted in M2 + BSA medium with equivalent concentrations of DMSO.

Nile red stain (Sigma, Ref. N3013) was used to label the total pool of vesicles. It was diluted at 5 mg/ml in DMSO and stored at room temperature. It was used on oocytes at 10 µg/ml.

Cytochalasin D (Life Technologies, Ref. PHZ1063) was diluted at 10 mg/ml in DMSO and stored at -20 °C. It was used on oocytes at 1 µg/ml and added 5 h after NEBD.

Monastrol (Sigma, Ref. M8515) was diluted at 30 mM in DMSO and stored at -20 °C. It was used at 100 µM on oocytes in meiosis I for half an hour starting 1 h 30 min after NEBD and at 200 µM for 2 h on oocytes arrested in meiosis II.

U0126 (Sigma, Ref. 662005) was diluted at 10 mM in DMSO and stored at -20 °C. It was used at 40 µM on oocytes in meiosis I starting 3 h after NEBD<sup>4</sup>.

**Immunofluorescence.** After in-vitro culture of oocytes, their zona pellucida was removed by incubation in acid Tyrode's medium (pH 2.3). Oocytes were fixed for 30 min at 37 °C in 4% Formaldehyde (Methanol free) on coverslips treated with gelatin and polylysine. After 20 min of blocking in 0.5% Triton X-100, 3% BSA, antibody staining was performed in phosphate-buffered saline, 0.5% Triton X-100, 3% BSA. As primary antibody, we used rabbit anti-Phospho-MLC2 (Ser19) (Cell Signaling; 1 : 200), at 4 °C overnight. As a secondary antibody, we used Alexa-594-labeled anti-rabbit antibody (Invitrogen; 1 : 400) for 1 h at room temperature. Oocytes were incubated 1 h at room temperature with phalloidin 488 (Invitrogen; 10 U/ml). DNA was stained with Prolong-DAPI (10 µg/ml final 4',6-diamidino-2-phenylindole (DAPI)).

**Live imaging.** Spinning Disk movies were acquired using (1) a Plan-APO ×40/1.25 NA objective on a Leica DMI6000B microscope enclosed in a thermostatic chamber (Life Imaging Service) equipped with a CoolSnap HQ2/CCD camera coupled to a Sutter filter wheel (Roper Scientific) and a Yokogawa CSU-X1-M1 spinning disk or 2) a Plan-APO ×60/1.4 NA objective on a Ti Nikon microscope enclosed in a thermostatic chamber (Life Imaging Service) equipped with a cMOS camera coupled to a Yokogawa CSU-X1 spinning disk. Metamorph Software (Universal Imaging) was used to collect data.

**Chromosome movement analysis at high temporal resolution.** Oocytes were microinjected in Prophase I with cRNAs encoding Histone(H2B)-GFP with or without cRNAs encoding EzTD-mCherry-VCA to label the chromosomes and decrease or not cortical tension. After microinjection, cRNAs translation was allowed for 1 h. Oocytes were then imaged under a spinning disk at BD + 6 h 30 min. Oocytes were positioned so that their spindle was parallel to the plane of observation and illuminated with an excitation wavelength of 561 nm during 300 ms (first timepoint only) and 491 nm during 300 ms (all timepoints). Acquisitions were taken every 20 s for 20 min, on 3 planes (z-step of 2 µm) focused on the chromosomes. The manual tracking plugin on Fiji (NIH) was used to track chromosome movement and velocity. Only the chromosomes individualized and visible on the three planes for the whole duration of the movie were tracked. For each tracked cluster representing either a chromosome or a group of chromosomes in a given spindle, the squared distances for all possible time steps (dt) were computed and averaged per time step producing an individual MSD value per dt, thus an MSD curve per cluster. All curves corresponding to all clusters of chromosomes were averaged to obtain one MSD curve per spindle. Following this, all curves corresponding to a spindle were averaged per condition to produce one MSD curve per condition.

**Chromosome alignment analysis throughout meiosis I.** Oocytes were microinjected in Prophase I with cRNAs encoding Histone(H2B)-GFP with or without cRNAs encoding EzTD-mCherry-VCA to label the chromosomes and decrease or not cortical tension. After microinjection, cRNAs translation was allowed for 1 h. Oocytes were imaged under the spinning between NEBD and BD + 7 h 30 min. Acquisitions were taken every 30 min on ten z-planes (z-step of 4 µm). Chromosome distribution throughout meiosis I was analyzed in controls and cVCA oocytes. To quantify the repartition of chromosomes, we thresholded the chromosome signal and fitted an ellipse around the binarized images based on image moments within ImageJ. The length of the major axis was given by the eigenvalues of the image moments. We compared the variation of the ellipse lengths during time. For this, we measured the slope of the linear regression of the length over time for a window of 2 h around each timepoint (thus, the slope given at a timepoint  $t$  is taken from the values of the ellipsoid length between  $t - 1$  h and  $t + 1$  h). For each timepoint, we tested for differences of the slope between control and cVCA oocytes spindles with a Wilcoxon's rank test in R.

**Inter major satellites repeats distance.** Oocytes were microinjected in prophase I with cRNAs encoding Histone(H2B)-GFP and MajSat-mClover<sup>65,66</sup> to label the chromosomes and the Major satellite repeats, with or without cRNAs encoding EzTD-mCherry-VCA to decrease or not cortical tension. After microinjection, cRNAs translation was allowed for 1 h. Oocytes were imaged under the spinning disk at BD + 6 h 30 min. Acquisitions were taken on 100 z-planes (z-step of 0.5 µm). For accurate measurements, oocytes were positioned so that their spindle was

parallel to the plane of observation. The distance between major satellites on each bivalent was measured using Metamorph software and used as a proxy to qualitatively assess tension across homologous chromosomes<sup>31</sup>.

**Chromosome counting in intact oocytes: monastrol spreads.** Oocytes were microinjected in Prophase I with cRNAs encoding Histone(H2B)-RFP and MajSat-mClover<sup>65,66</sup> to label the chromosomes and the major satellite repeats, with or without cRNAs encoding EzTD-mCherry-VCA to decrease or not cortical tension. Oocytes underwent meiotic maturation in the incubator and arrested in metaphase of meiosis II. At that stage, oocytes were incubated 2 h in 200 µM monastrol, a kinesin-5 inhibitor that causes the bipolar meiosis II spindle to collapse into a monopolar spindle and results in chromosome dispersion<sup>12</sup>. Oocytes were imaged under the spinning disk, with acquisitions spanning the region covering all the chromosomes (z-step of 0.5 µm). The number of chromosomes (MajSat-Clover spots) was counted using the TrackMate plugin in Fiji (<http://fiji.sc/TrackMate>).

**Oocyte volume measurement using FXm.** The FXm method was initially described in ref. <sup>14</sup> and a detailed protocol is available in ref. <sup>67</sup>. Measurements were made in PDMS chambers that consisted in a simple straight 113 µm high channel. A 2 mm diameter inlet and a 0.5 mm diameter outlet were punched on either side of the channel. The chambers were irreversibly bound to glass-bottomed Petri dishes (Fluorodishes) by plasma treatment. To prevent cell adhesion of the cell and allow reusing the chamber for successive measurements on different cells, chambers were coated with PLL-g-PEG (1%). Before starting the experiment, the chamber was rinsed with M2 + BSA medium containing 0.5 mg/ml of 70 kDa FITC-Dextran (Sigma, Ref FD70S). Oocytes were measured one by one. Each time, the cell was deposited with a mouth-pipette in the inlet. To aspirate the oocyte into the middle of the chamber in a controlled manner, a 250 µl glass syringe was plugged to the outlet via an ~30 cm-long polytetrafluoroethylene (PTFE) tube previously filled with 100 µl of the M2 + BSA dextran solution. The oocyte was then positioned in the center of the chamber and far from the borders of the channel. The chamber was then transferred to a Leica DMIRBE inverted microscope. Bright-field and fluorescence images (excitation wavelength of 491 nm) were acquired using a ×10 NA0.3 objective. For the image analysis, a home-made Matlab software described in ref. <sup>67</sup> was used. Briefly, fluorescent signal was calibrated for every image using the fluorescence intensity ( $I_{min}$ ) under the borders of the chamber ( $h_{min} = 0$ ) and the intensity ( $I_{max}$ ) of the background around the cell ( $h_{max} =$  chamber height = 113 µm). The calibration factor  $\alpha$  was then calculated as follows:  $\alpha = (I_{max} - I_{min})/h_{max}$ . The volume of the cell ( $V_{cell}$ ) was obtained by integrating the fluorescence intensity collected under the cell.

$$V_{cell} = \iint_{x,y} \frac{I_{max}(x,y) - I(x,y)}{\alpha} dx dy$$

**Cytoplasmic activity measurements.** The total vesicles stained with Nile red contained in oocytes at BD + 6 h 30 min were imaged every 500 ms with the stream acquisition mode of Metamorph on excitation at 491 nm. Nile Red-labeled vesicle tracking and MSD quantification was performed as described in ref. <sup>15</sup> as follows. After subtracting the background, time-lapse videos were realigned using the rigidbody algorithm of the stackreg plugin in Fiji and then denoised on Metamorph using the Saffir denoising program (Roper Scientific). Stacks were then corrected for bleaching using the Histogram Matching algorithm in Fiji and thresholded on Metamorph to generate a binary stack of vesicles. Tracking was then performed on these binary vesicle videos with the TrackMate plugin in Fiji (<http://fiji.sc/TrackMate>) using DoG detector with a detected object diameter adjusted according to the pattern of vesicles, a thresholding of 1 and sub-pixel localization, and the following settings for gap closing in the simple LAP tracker: linking maximum distance of 1 µm, gap closing maximum distance of 1 µm, and a maximum gap of two frames allowed. Tracks were filtered according to their duration, considering only tracks lasting for more than 25 s. The results of the tracking, including the diameter and the velocities of the vesicles, were provided as Excel and xml files. The velocities values correspond to the mean velocity of a vesicle within a track. For MSD analysis of vesicles trajectories, we used the @msdanalyzer MATLAB class described in: <http://bradleymonk.com/matlab/msd/MSDTuto.html>. Trajectories were provided in the xml files from Fiji TrackMate analysis.

**Cortical tension measurements.** Cortical tension was measured by micropipette aspiration as described in ref. <sup>4</sup>. Briefly, the zona pellucida of prophase I arrested oocytes was removed by incubating oocytes into M2 + BSA medium supplemented with 0.4% pronase. Oocytes were loaded onto a chamber equilibrated with M2 + BSA medium. A glass micropipette of a diameter five times smaller than the oocyte diameter was connected to a water reservoir of adjustable height to apply a defined aspiration pressure. Zero aspiration pressure was set before each experiment by checking the absence of visible flow inside the pipette. Observations were made through an inverted microscope (Axiovert 200, Zeiss) equipped with a ×40 immersion oil objective (Neofluar 1.3 NA) and connected to a CCD camera (XC-ST70CE, Sony). For every applied pressure, we monitored the length  $L$  of the oocyte portion aspirated in the pipette after 30 s and measure at which pressure  $L/R = 1$ ,  $R$  being the internal radius of the micropipette. This critical aspiration

pressure  $\Delta P_c$  allows calculating the cortical tension  $T_c$  of the aspired cell using a viscous drop model<sup>68</sup>,

$$T_c = \frac{R\Delta P_c}{2(1 - \frac{R}{R_c})}$$

where  $R_c$  is the cell radius.

**Microtubule growth speed and density.** Oocytes were microinjected with crNAs encoding EB3-GFP, with or without crNAs encoding EzTD-mCherry-VCA. Oocytes were allowed to proceed into prometaphase. At BD + 1 h 30 min, oocytes were incubated in M2 medium supplemented with 100  $\mu$ M Monastrol for 30 min. MT growth speed was assessed through imaging a single Z plane for 5 s every 250 ms. EB3-GFP comets were tracked with Mosaic plugin for ImageJ<sup>69</sup>. Only the unidirectional tracks with comets visible for ten frames or more were selected and the oocytes included in the analysis had five or more of such tracks.

The monoaster size and brightness were assessed on a maximum brightness projection image from stacks covering the whole volume of the monoaster. The monoaster size was measured by manually fitting an oval around the brightest part of the aster. The fluorescence intensity of EB3-GFP was measured within the central part of the monoaster and normalized by the background fluorescence in the oocyte cytoplasm.

**Laser ablation.** Laser ablation was performed as described in<sup>70</sup>. We used a 355 laser and i-LAS<sup>2</sup> module (Roper Scientific) coupled to a Leica DMI6000B microscope enclosed in a thermostatic chamber (Life Imaging Service) equipped with a Retiga 3 CCD camera (QImaging) coupled to a Sutter filter wheel (Roper Scientific) and a Yokogawa CSU-X1-M1 spinning disc using a Plan-APO  $\times 40/1.25$  NA objective. Metamorph (Universal Imaging) was used to process the data. After calibrating the system, the ablation zone (region of interest, ROI) was determined. It consisted of a line of  $15 \pm 1 \mu$ m in length positioned after the spindle pole in the cytoplasm of the oocyte. To perform the laser ablation, the spindle must be oriented with its long axis parallel to the observation plane. The laser ablation parameters used were as follows: 350 nm laser Z thickness 10  $\mu$ m, dZ 1  $\mu$ m. Oocytes were then imaged after ablation with the following parameters: 491 nm laser power during 500 ms, acquisitions every 20 s for 2 min, on one plane. Metaphase plate width was measured by performing bounding boxes containing all the chromosomes with the Fiji (NIH) software. The Microsoft Excel software was used to normalize the data.

**Quantitative image analysis.** Computation of chromosome shapes 30 min before anaphase I: detections were obtained from manually cropped region of interest around the chromosomes using the Phansalkar thresholding method with radius 130 available in Fiji. All pixels of the detection were subsequently used to compute a covariance matrix. Eigenvalues  $L_{\min}$  and  $L_{\max}$  were obtained after diagonalization of this matrix and the aspect ratio ( $L_{\min}/L_{\max}$ ), that is the ratio of the minor axis length to the major axis length, was reported for each cell.

**Quantifications.** - Metaphase plate width was measured on oocytes expressing Histone(H2B)-GFP by performing bounding boxes with the Fiji (NIH) software. Measurements were done 30 minutes before anaphase only on spindles parallel to the imaging plane.

- Myosin-II cortical enrichment was quantified by measuring the ratio of the cortical and cytoplasmic SF9-GFP<sup>33</sup> fluorescence intensities. Oocytes expressed SF9-GFP alone (controls) and together with the cFH1FH2 construct for five hours in Prophase I. The background was removed from all images analyzed using Metamorph software. Cytoplasmic and cortical integrated fluorescence intensities were measured randomly six times in each compartment (cortex and cytoplasm) per oocyte using the same square ROI of 0.12  $\mu$ m<sup>2</sup> (region smaller than the cortex width). Measurements were taken on one focal plane (corresponding to the oocyte longest diameter). The cortical fluorescence intensity per square pixels was then divided by the cytoplasmic one.

- For myosin-II cytoplasmic accumulation over time, oocytes expressed SF9-GFP alone (controls) and together with the cFH1FH2 or cVCA constructs for nine hours in Prophase I. The background was removed from all analyzed images using Metamorph software. Integrated fluorescence intensities 2 h and 9 h after crNA injection were measured randomly six times in the cytoplasm per oocyte using the same square ROI of 80  $\mu$ m<sup>2</sup>. Measurements were taken on one focal plane (corresponding to the oocyte longest diameter).

- Cortical thickness measurements were performed as described in<sup>4</sup>. Briefly, cortical thickness, consisting of the cortical outer layer (stable throughout meiosis I) and the cortical inner layer (absent in Prophase I and progressively nucleated after NEBD in controls) was measured manually using Fiji software. Oocytes expressed GFP-UtrCH alone (controls) and together with the cFH1FH2 construct for three hours in Prophase I. Four measures per oocyte were randomly taken along the cortex on one focal plane (corresponding to the oocyte longest diameter). The difference between the cytoplasmic and cortical GFP-UtrCH signals was strong enough to discriminate between the two actin networks and to detect the cortical actin network boundary.

- Spindle migration was quantified by measuring distances between the centroid of the oocyte and the centroid of the spindle (oocytes were incubated in SiR-Tubulin at 0.1  $\mu$ M) using the Fiji (NIH) software. Measuring the distance traveled between the centroid of the spindle relative to the centroid of the oocyte allows discriminating between oocyte movement and spindle movement. Measurements were performed at two timepoints: 4 h before anaphase I when the spindle has not yet started to migrate to the cortex and 30 min before anaphase I when the spindle has almost reached the cortex in the controls. Analyses were done on a Z-projection of 8 stacks of 4  $\mu$ m, allowing to get the entire spindle. Only spindle parallels to the plane of observation were quantified.

- The spindle length measurements were performed using Metamorph software. Spindle length was measured as the distance between poles in spindles parallel to the imaging plane only.

- The pMLC2 (active phosphorylated myosin-II) and F-actin levels were measured using Metamorph software. Three measures per oocyte were randomly taken within the spindle, and six measures per oocytes were taken within the cytoplasm on a projection of 20 focal planes.

**Statistical analysis.** Experiments were repeated as indicated in the figure legends and a sample of sufficient size was used. The statistical analysis was performed using GraphPad Prism version 8.00 for MacOS, GraphPad Software, La Jolla, CA, USA, [www.graphpad.com](http://www.graphpad.com). For comparisons between two groups, the normality of the variables was checked (D'agostino-Pearson's normality test) and parametric Student's *t*-tests (with Welch's correction when indicated) or non-parametric comparison tests were performed with a confidence interval of 95%. For chromosome alignment experiments, repartitions were analyzed for statistical significance using Fisher's test with a confidence interval of 95%. For volume measurements, a Wilcoxon rank sum test was performed to compare the mean of the two conditions. For the time evolution of SF9-GFP cytoplasmic intensity, a One-way analysis of variance test was performed with a family-wise significance and confidence level of 0.05 (95% confidence interval).

To compare the regression slope values for MSDs, we did a Welch's test of the regression models, as presented in ref. <sup>71</sup> (as the residual variances of the models were not equal).

All error bars are expressed as SD. Values of  $P < 0.05$  were considered significant. In all figures, \* $P$ -value  $< 0.05$ , \*\* $P$ -value  $< 0.005$ , \*\*\* $P$ -value  $< 0.0001$ ; n.s., not statistically significant.

**Ethical statement.** All experimental procedures used for the project have been approved by the ministry of agriculture to be conducted in our animal facility (authorization N°75-1170). The use of all the genetically modified organisms described in this project has been granted by the DGRI (Direction Générale de la Recherche et de l'Innovation: Agrément OGM; DUO-1783).

**Reporting summary.** Further information on research design is available in the Nature Research Reporting Summary linked to this article.

## Data availability

All relevant data supporting the finding of this study are available from the corresponding author upon request.

Received: 25 June 2019; Accepted: 10 March 2020;

Published online: 03 April 2020

## References

- Nagaoka, S. I., Hassold, T. J. & Hunt, P. A. Human aneuploidy: mechanisms and new insights into an age-old problem. *Nat. Rev. Genet.* **13**, 493–504 (2012).
- Yanez, L. Z., Han, J., Behr, B. B., Reijo Pera, R. A. & Camarillo, D. B. Human oocyte developmental potential is predicted by mechanical properties within hours after fertilization. *Nat. Commun.* **7**, 10809 (2016).
- Larson, S. M. et al. Cortical mechanics and meiosis II completion in mammalian oocytes are mediated by myosin-II and Ezrin-Radixin-Moesin (ERM) proteins. *Mol. Biol. Cell.* **21**, 3182–3192 (2010).
- Chaigne, A. et al. A soft cortex is essential for asymmetric spindle positioning in mouse oocytes. *Nat. Cell Biol.* **15**, 958–966 (2013).
- Chaigne, A. et al. A narrow window of cortical tension guides asymmetric spindle positioning in the mouse oocyte. *Nat. Commun.* **6**, 6027 (2015).
- Chaigne, A. et al. F-actin mechanics control spindle centring in the mouse zygote. *Nat. Commun.* **7**, 10253 (2016).
- Azoury, J. et al. Spindle positioning in mouse oocytes relies on a dynamic meshwork of actin filaments. *Curr. Biol.* **18**, 1514–1519 (2008).
- Schuh, M. & Ellenberg, J. A new model for asymmetric spindle positioning in mouse oocytes. *Curr. Biol.* **18**, 1986–1992 (2008).
- Mogessie, B. & Schuh, M. Actin protects mammalian eggs against chromosome segregation errors. *Science* **357**, eaal1647 (2017).

10. Verlhac, M. H., Lefebvre, C., Guillaud, P., Rassnier, P. & Maro, B. Asymmetric division in mouse oocytes: with or without Mos. *Curr. Biol.* **10**, 1303–1306 (2000).
11. Kyogoku, H. & Kitajima, T. S. Large cytoplasm is linked to the error-prone nature of oocytes. *Dev. Cell.* **41**, 287–298.e4 (2017).
12. Duncan, F. E., Chiang, T., Schultz, R. M. & Lampson, M. A. Evidence that a defective spindle assembly checkpoint is not the primary cause of maternal age-associated aneuploidy in mouse eggs. *Biol. Reprod.* **81**, 768–776 (2009).
13. Almonacid, M. et al. Active fluctuations of the nuclear envelope shape the transcriptional dynamics in oocytes. *Dev. Cell.* **51**, 145–157 (2019).
14. Zlotek-Zlotkiewicz, E., Monnier, S., Cappello, G., Le Berre, M. & Piel, M. Optical volume and mass measurements show that mammalian cells swell during mitosis. *J. Cell Biol.* **211**, 765–774 (2015).
15. Almonacid, M. et al. Active diffusion positions the nucleus in mouse oocytes. *Nat. Cell Biol.* **17**, 470–479 (2015).
16. Dumont, J. et al. Formin-2 is required for spindle migration and for the late steps of cytokinesis in mouse oocytes. *Dev. Biol.* **301**, 254–265 (2007).
17. Li, H., Guo, F., Rubinstein, B. & Li, R. Actin-driven chromosomal motility leads to symmetry breaking in mammalian meiotic oocytes. *Nat. Cell Biol.* **10**, 1301–1308 (2008).
18. Théry, M., Jiménez-Dalmaroni, A., Racine, V., Bornens, M. & Jülicher, F. Experimental and theoretical study of mitotic spindle orientation. *Nature* **447**, 493–496 (2007).
19. Fink, J. et al. External forces control mitotic spindle positioning. *Nat. Cell Biol.* **13**, 771–778 (2011).
20. Kwon, M., Bagonis, M., Danuser, G. & Pellman, D. Direct microtubule-binding by myosin-10 orients centrosomes toward retraction fibers and subcortical actin clouds. *Dev. Cell.* **34**, 323–337 (2015).
21. Sathananthan, A. H. Mitosis in the human embryo: the vital role of the sperm centrosome (centriole). *Histol. Histopathol.* **12**, 827–856 (1997).
22. Szollosi, D., Calarco, P. & Donahue, R. P. Absence of centrioles in the first and second meiotic spindles of mouse oocytes. *J. Cell Sci.* **11**, 521–541 (1972).
23. Azoury, J., Lee, K. W., Georget, V., Hikal, P. & Verlhac, M. H. Symmetry breaking in mouse oocytes requires transient F-actin meshwork destabilization. *Development* **138**, 2903–2908 (2011).
24. Leader, B. et al. Formin-2, polyploidy, hypofertility and positioning of the meiotic spindle in mouse oocytes. *Nat. Cell Biol.* **4**, 921–928 (2002).
25. Lancaster, O. M. et al. Mitotic rounding alters cell geometry to ensure efficient bipolar spindle formation. *Dev. Cell.* **25**, 270–283 (2013).
26. Bennabi, I., Terret, M. E. & Verlhac, M. H. Meiotic spindle assembly and chromosome segregation in oocytes. *J. Cell Biol.* **215**, 611–619 (2016).
27. Bennabi, I. et al. Shifting meiotic to mitotic spindle assembly in oocytes disrupts chromosome alignment. *EMBO Rep.* **19**, 368–381 (2018a).
28. Letort, G. et al. A computational model of the early stages of acentriolar meiotic spindle assembly. *Mol. Biol. Cell* **30**, 863–875 (2019).
29. Breuer, M. et al. HURP permits MTOC sorting for robust meiotic spindle bipolarity, similar to extra centrosome clustering in cancer cells. *J. Cell Biol.* **191**, 1251–1260 (2010).
30. Kitajima, T. S., Ohsugi, M. & Ellenberg, J. Complete kinetochore tracking reveals error-prone homologous chromosome biorientation in mammalian oocytes. *Cell* **146**, 568–581 (2011).
31. Wu, T., Lane, S. I. R., Morgan, S. L. & Jones, K. T. Spindle tubulin and MTOC asymmetries may explain meiotic drive in oocytes. *Nat. Commun.* **9**, 2952 (2018).
32. Burdyniuk, M., Callegari, A., Mori, M., Nédélec, F. & Lénárt, P. F-Actin nucleated on chromosomes coordinates their capture by microtubules in oocyte meiosis. *J. Cell Biol.* **217**, 2661–2674 (2018).
33. Nizak, C. et al. Recombinant antibodies against subcellular fractions used to track endogenous Golgi protein dynamics in vivo. *Traffic J.* **739–753** (2003).
34. Colin, A., Singaravelu, P., Théry, M., Blanchoin, L. & Gueroui, Z. Actin-network architecture regulates microtubule dynamics. *Curr. Biol.* **28**, 2647–2656 (2018).
35. Inoue, D. et al. Actin filaments regulate microtubule growth at the centrosome. *EMBO J.* **38**, e99630 (2019).
36. Farina, F. et al. Local actin nucleation tunes centrosomal microtubule nucleation during passage through mitosis. *EMBO J.* **38**, e99843 (2019).
37. Kita, A. M. et al. Spindle-F-actin interactions in mitotic spindles in an intact vertebrate epithelium. *Mol. Biol. Cell* **30**, 1645–1654 (2019).
38. Plessner, M., Knerr, J. & Grosse, R. Centrosomal actin assembly is required for pmitotic spindle formation and chromosome congression. *iScience* **15**, 274–281 (2019).
39. Silverman-Gavrila, R. V. & Forer, A. Myosin localization during meiosis I of crane-fly spermatocytes gives indications about its role in division. *Cell Motil. Cytoskeleton.* **55**, 97–113 (2003).
40. Forer, A., Spurck, T. & Pickett-Heaps, J. D. Actin and myosin inhibitors block elongation of kinetochore fibre stubs in metaphase crane-fly spermatocytes. *Protoplasma* **232**, 79–85 (2007).
41. Robinson, R. W. & Snyder, J. A. Localization of myosin II to chromosome arms and spindle fibers in PtK1 cells: a possible role for an actomyosin system in mitosis. *Protoplasma* **225**, 113–122 (2005).
42. Rosenblatt, J., Cramer, L. P., Baum, B. & McGee, K. M. Myosin II-dependent cortical movement is required for centrosome separation and positioning during mitotic spindle assembly. *Cell* **117**, 361–372 (2004).
43. Ma, X. et al. Ablation of nonmuscle myosin II-B and II-C reveals a role for nonmuscle myosin II in cardiac myocyte karyokinesis. *Mol. Biol. Cell* **21**, 3952–3962 (2010).
44. D’Angelo, L., Myer, N. M. & Myers, K. A. MCAK-mediated regulation of endothelial cell microtubule dynamics is mechanosensitive to myosin-II contractility. *Mol. Biol. Cell* **28**, 1223–1237 (2017).
45. Feng, J. et al. Depletion of kinesin-12, a myosin-IIB-interacting protein, promotes migration of cortical astrocytes. *J. Cell Sci.* **129**, 2438–2447 (2016).
46. Nishimura, K. et al. Cdk1-mediated DIAPH1 phosphorylation maintains metaphase cortical tension and inactivates the spindle assembly checkpoint at anaphase. *Nat. Commun.* **10**, 981 (2019).
47. Shutova, M. S. & Svitkina, T. M. Mammalian nonmuscle myosin II comes in three flavors. *Biochem. Biophys. Res. Commun.* **506**, 394–402 (2018).
48. Reymann, A. C. et al. Actin network architecture can determine myosin motor activity. *Science* **336**, 1310–1314 (2012).
49. Ennomani, H. et al. Architecture and connectivity govern actin network contractility. *Curr. Biol.* **26**, 616–626 (2016).
50. Mackenzie, A. C. L. et al. Cortical mechanics and myosin-II abnormalities associated with post-ovulatory aging: implications for functional defects in aged eggs. *Mol. Hum. Reprod.* **22**, 397–409 (2016).
51. Hassold, T. & Hunt, P. To err (meiotically) is human: the genesis of human aneuploidy. *Nat. Rev. Genet.* **2**, 280–291 (2001).
52. Hassold, T., Hall, H. & Hunt, P. The origin of human aneuploidy: where we have been, where we are going. *Hum. Mol. Genet.* **16**, R203–R208 (2007).
53. Lekka, M. Discrimination between normal and cancerous cells using AFM. *BioNanoScience* **6**, 65–80 (2016).
54. Sant, G. R., Knopf, K. B. & Albala, D. M. Live-single-cell phenotypic cancer biomarkers-future role in precision oncology? *NPJ Precis. Oncol* **1**, 21 (2017).
55. Guck, J. et al. Optical deformability as an inherent cell marker for testing malignant transformation and metastatic competence. *Biophys. J.* **88**, 3689–3698 (2005).
56. Suresh, S. et al. Connections between single-cell biomechanics and human disease states: gastrointestinal cancer and malaria. *Acta Biomater.* **1**, 15–30 (2005).
57. Hou, H. W. et al. Deformability study of breast cancer cells using microfluidics. *Biomed. Microdevices.* **11**, 557–564 (2009).
58. Xu, W. et al. Cell stiffness is a biomarker of the metastatic potential of ovarian cancer cells. *PLoS ONE* **7**, e46609 (2012).
59. Newell-Litwa, K., AR. Horwitz, R. & Lamers, M. L. Non-muscle myosin II in disease: mechanisms and therapeutic opportunities. *Dis. Model. Mech.* **8**, 1495–1515 (2015).
60. Toyoda, Y. et al. Genome-scale single-cell mechanical phenotyping reveals disease-related genes involved in mitotic rounding. *Nat. Commun.* **8**, 1266 (2017).
61. Verlhac, M. H., Kubiak, J. Z., Clarke, H. J. & Maro, B. Microtubule and chromatin behavior follow MAP kinase activity but not MPF activity during meiosis in mouse oocytes. *Dev. Biol.* **120**, 1017–1025 (1994).
62. Reis, A., Chang, H. Y., Levasseur, M. & Jones, K. T. 2006. APCcdh1 activity in mouse oocytes prevents entry into the first meiotic division. *Nat. Cell Biol.* **8**, 539–540 (2006).
63. Manil-Ségalen, M. et al. Chromosome structural anomalies due to aberrant spindle forces exerted at gene editing sites in meiosis. *J. Cell Biol.* **217**, 3416–3430 (2018).
64. Dard, N., Louvet-Vallée, S., Santa-Maria, A. & Maro, B. Phosphorylation of ezrin on threonine T567 plays a crucial role during compaction in the mouse early embryo. *Dev. Biol.* **271**, 87–97 (2004).
65. Miyanari, Y., Ziegler-Birling, C. & Torres-Padilla, M. E. Live visualization of chromatin dynamics with fluorescent TALEs. *Nat. Struct. Mol. Biol.* **20**, 1321–1324 (2013).
66. Thanisch, K. et al. Targeting and tracing of specific DNA sequences with dTALEs in living cells. *Nucleic Acids Res.* **42**, e38 (2014).
67. Cadart, C. et al. Size control in mammalian cells involves modulation of both growth rate and cell cycle duration. *Nat. Commun.* **9**, 3275 (2017).
68. Evans, E. & Yeung, A. Apparent viscosity and cortical tension of blood granulocytes determined by micropipet aspiration. *Biophys. J.* **56**, 151–160 (1989).
69. Sbalzarini, I. F. & Koumoutsakos, P. Feature point tracking and trajectory analysis for video imaging in cell biology. *J. Struct. Biol.* **151**, 182–195 (2005).
70. Bennabi, I. & Manil-Ségalen, M. Laser ablation of microtubule–chromosome attachment in mouse oocytes. *Methods Mol. Biol.* **1818**, 153–161 (2018).
71. Andrade, J. M. & Estévez-Pérez, M. G. Statistical comparison of the slopes of two regression lines: a+ tutorial. *Anal. Chim. Acta* **838**, 1–12 (2014).

## Acknowledgements

We thank Cécile Sykes (Institut Curie, Paris, France) for allowing us to use her micro-pipette aspiration setting and for critical reading of the manuscript. We thank Clément Nizak (ESPCI), Maria Almonacid from the lab and the imaging facility of the CIRB for their input on imaging quantification. We also thank Marie Anfosso and Anthony Gagnon, master students, for their technical help, and Raphaël Voituriez (Sorbonne University, Paris, France) and the members of the Verlhac/Terret team for helpful discussions. We thank Dr. Keith T. Jones, University of Adelaide, Australia, for the MajSat-mClover construct and Greg Fitzharris, University of Montreal, Canada, for sharing his protocol of the Monastrol spreads. This work was supported by grants from the Fondation pour la Recherche Médicale (FRM Label to MHV-DEQ20150331758 then EQU201903007796), from the ANR (ANR-14-CE11 to MHV, ANR-16-CE13 to M.E.T.), and from the Labex Memolife (to M.H.V.). This work has received support from the Fondation Bettencourt Schueller, support under the program « Investissements d'Avenir » launched by the French Government and implemented by the ANR, with the references: ANR-10-LABX-54 MEMO LIFE, ANR-11-IDEX-0001-02 PSL\* Research University.

## Author contributions

I.B., M.H.V., and M.E.T. conceived and supervised the project. I.B. performed most experiments. F.C. characterized the cFH1FH2 construct, E.N. did all experiments for the revisions of the manuscript, M.M.S. did the chromosome tracking experiments at high time resolution, they both analyzed their experiments. I.B., M.H.V., and M.E.T. analyzed most experiments. G.L. quantified chromosome behavior throughout meiosis I and computed all MSDs. C. Cadart and R.A. were involved for the volume measurement experiments. C. Campillo was involved for the cortical tension measurement experiments. A.O. and A.G. were involved for the computational 3D imaging approach. A.C. did the original observation that extra-soft oocytes have misaligned chromosomes. I.B. and M.E.T. wrote the manuscript, which was seen and corrected by all authors.

## Competing interests

The authors declare no competing interests.

## Additional information

**Supplementary information** is available for this paper at <https://doi.org/10.1038/s41467-020-15470-y>.

**Correspondence** and requests for materials should be addressed to M.-H.V. or M.-E.T.

**Peer review information** *Nature Communications* thanks the anonymous reviewer(s) for their contribution to the peer review of this work. Peer reviewer reports are available.

**Reprints and permission information** is available at <http://www.nature.com/reprints>

**Publisher's note** Springer Nature remains neutral with regard to jurisdictional claims in published maps and institutional affiliations.



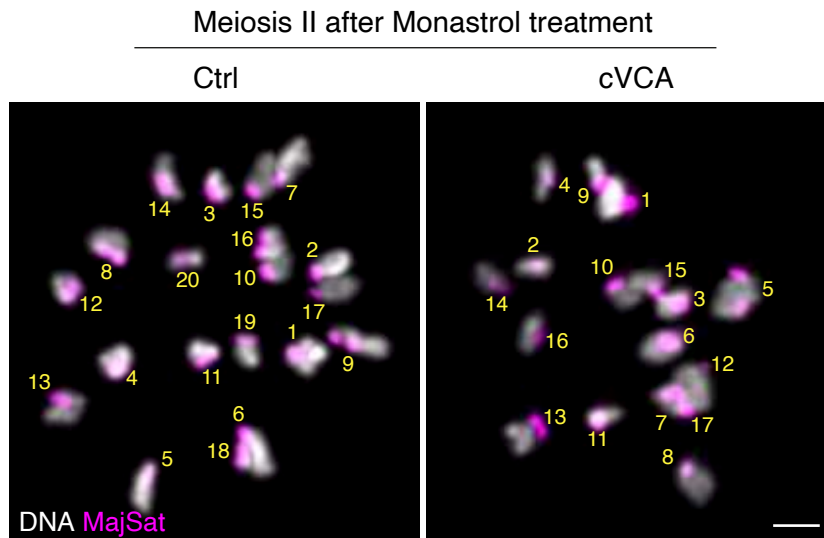
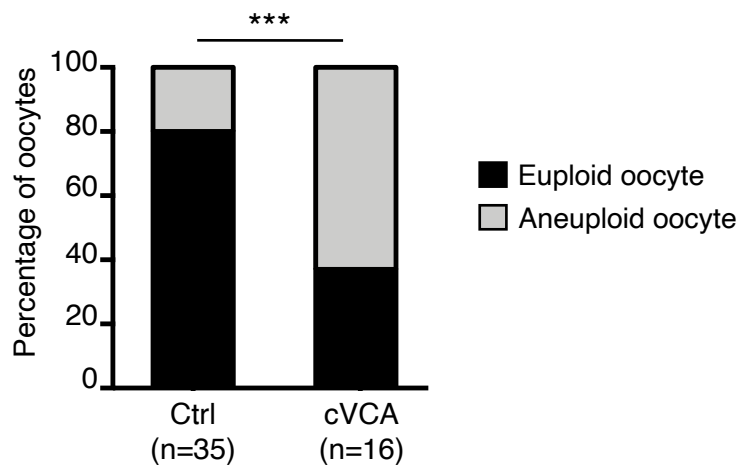
**Open Access** This article is licensed under a Creative Commons Attribution 4.0 International License, which permits use, sharing, adaptation, distribution and reproduction in any medium or format, as long as you give appropriate credit to the original author(s) and the source, provide a link to the Creative Commons license, and indicate if changes were made. The images or other third party material in this article are included in the article's Creative Commons license, unless indicated otherwise in a credit line to the material. If material is not included in the article's Creative Commons license and your intended use is not permitted by statutory regulation or exceeds the permitted use, you will need to obtain permission directly from the copyright holder. To view a copy of this license, visit <http://creativecommons.org/licenses/by/4.0/>.

© The Author(s) 2020

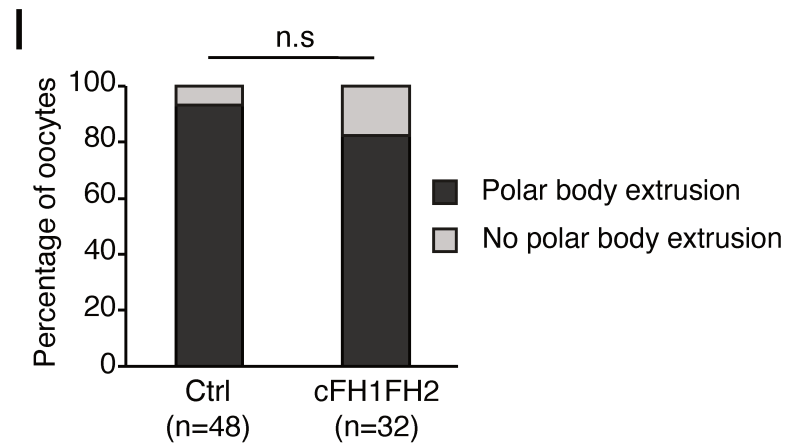
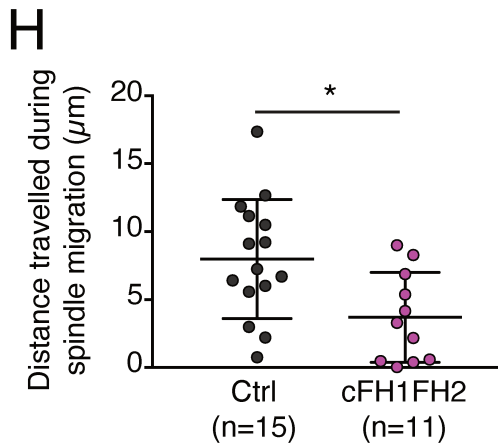
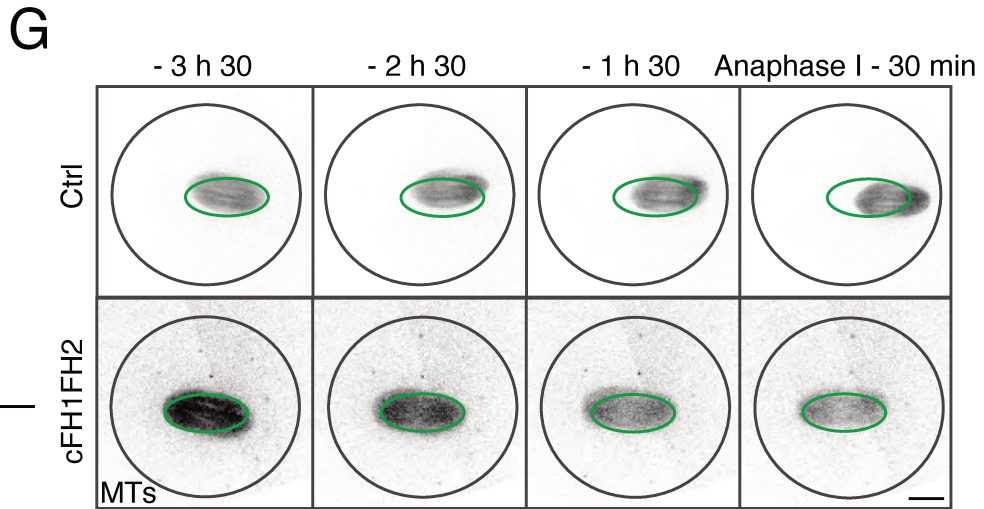
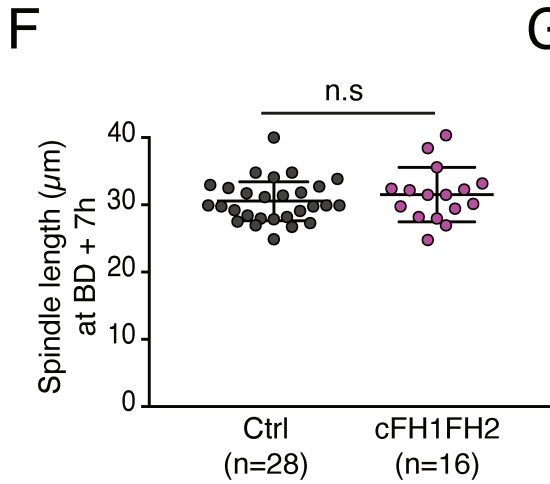
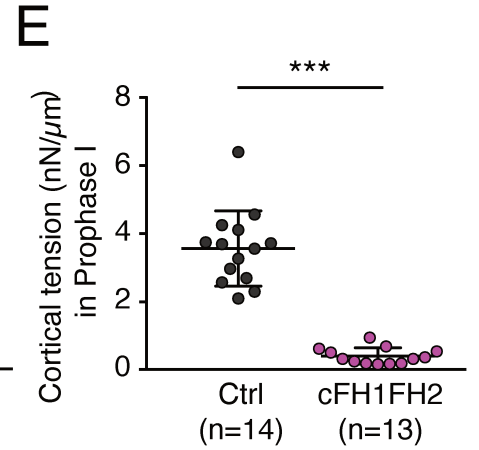
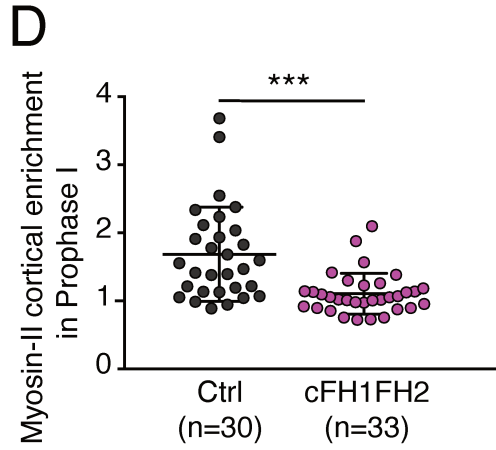
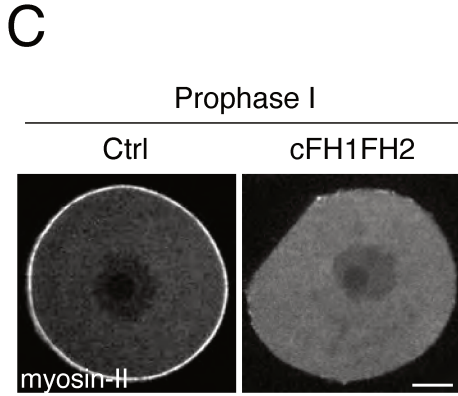
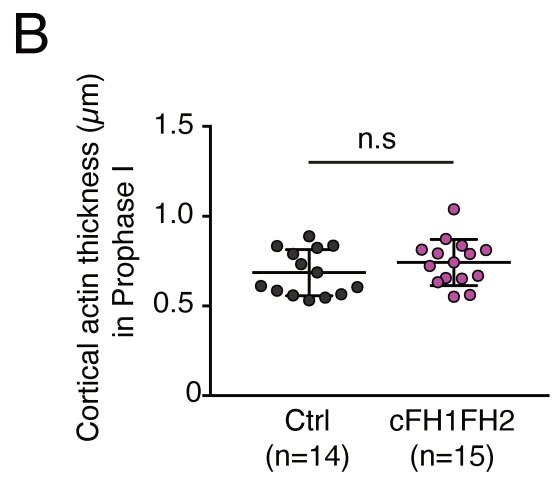
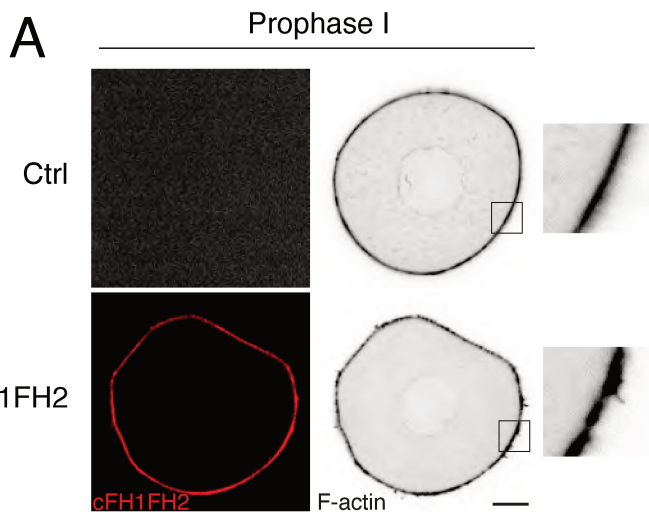
# **Supplementary Information**

**Artificially decreasing cortical tension  
generates aneuploidy in mouse oocytes**

Bennabi et al.

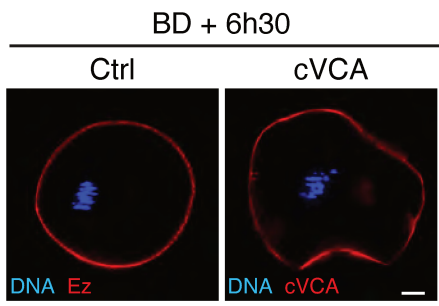
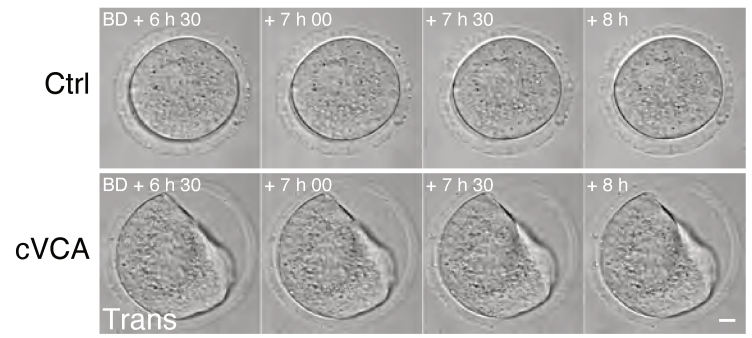
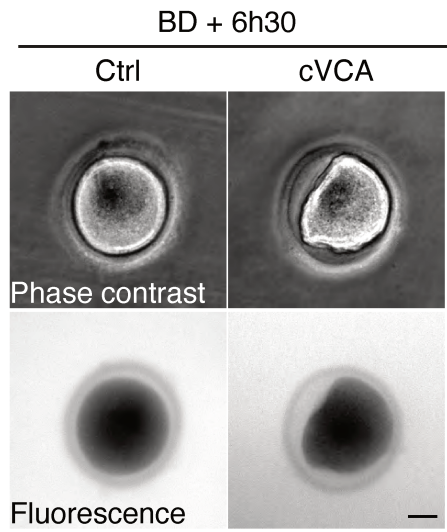
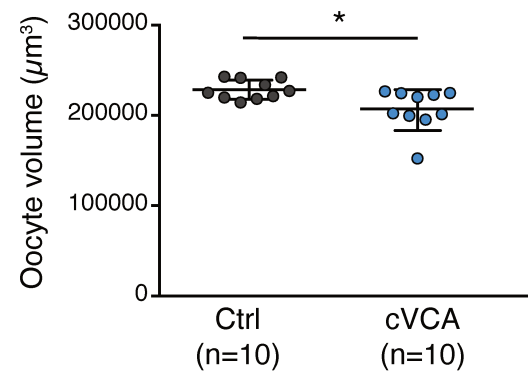
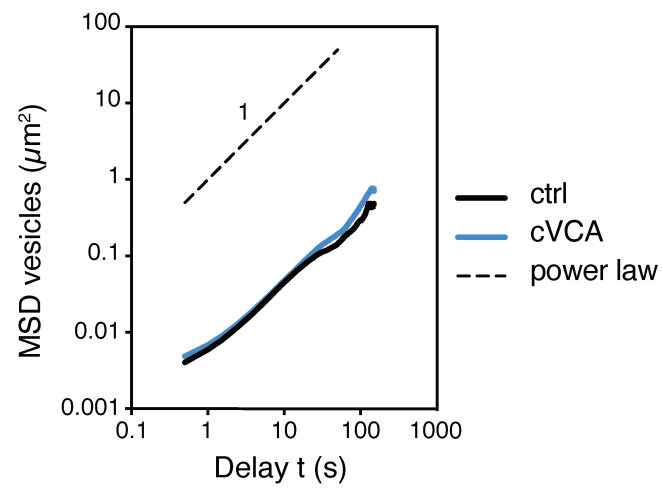
**A****B****Supplementary Figure 1: Extra-soft oocytes are aneuploid.**

(A) Z-projections from control and cVCA oocytes in meiosis II incubated 2h in 200  $\mu$ M Monastrol, expressing Histone(H2B)-GFP (grey) and MajSat-mClover (magenta). Scale bar: 5  $\mu$ m. The chromosomes are arbitrarily numbered in yellow. This experiment was repeated independently 3 times with similar results. (B) Bar graph representing the percentage of euploid oocytes (black) and aneuploid oocytes (grey) in meiosis II for controls and cVCA oocytes. (n) is the number of oocytes analyzed. Data are from 3 independent experiments. Statistical significance of differences is assessed with a Chi-square test two-sided: \*\*\*P-value<0.0001.



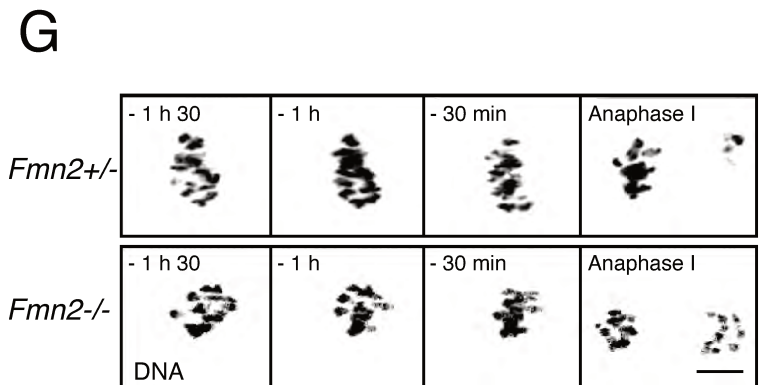
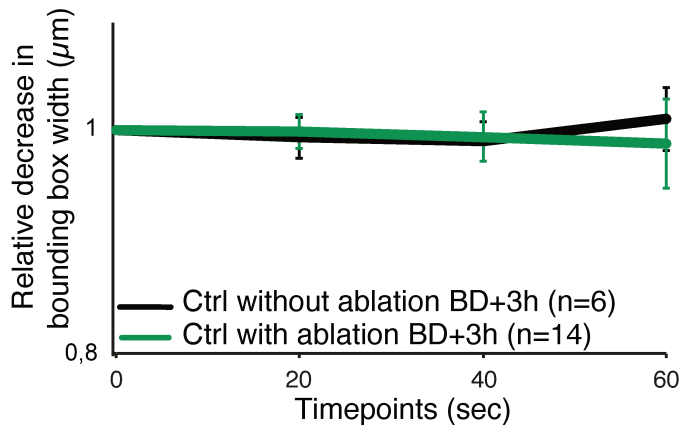
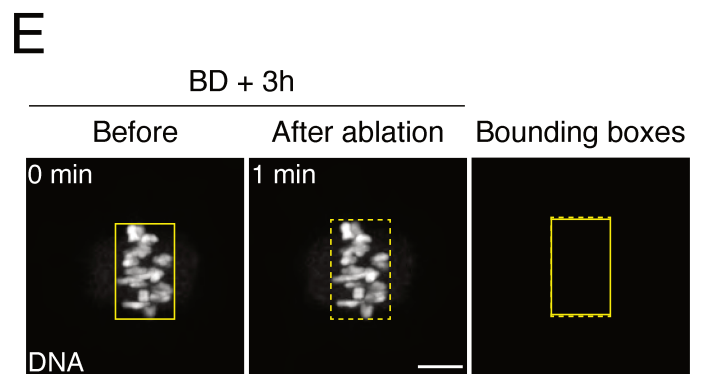
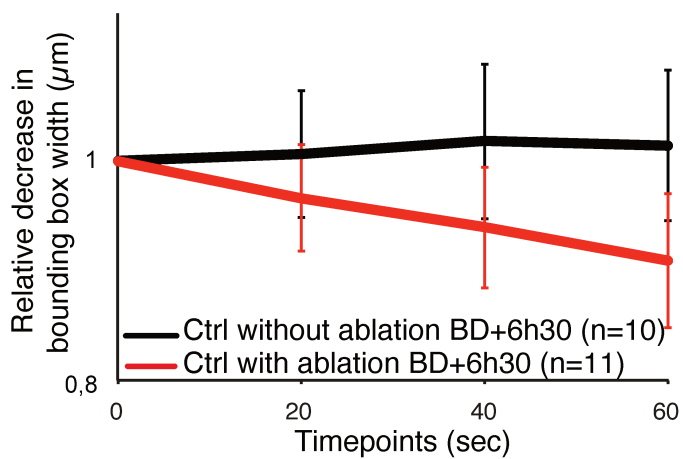
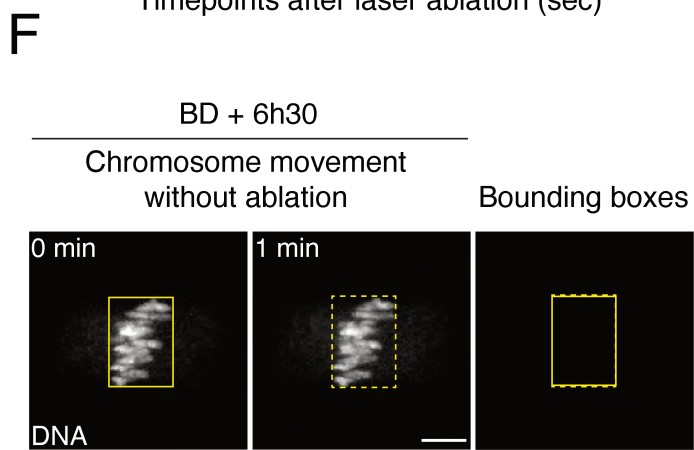
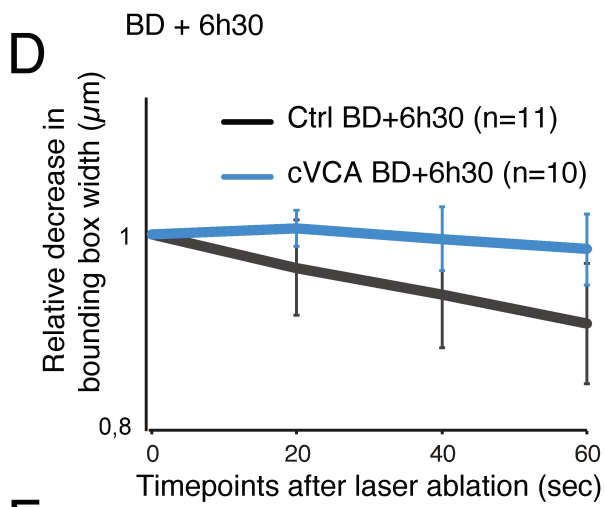
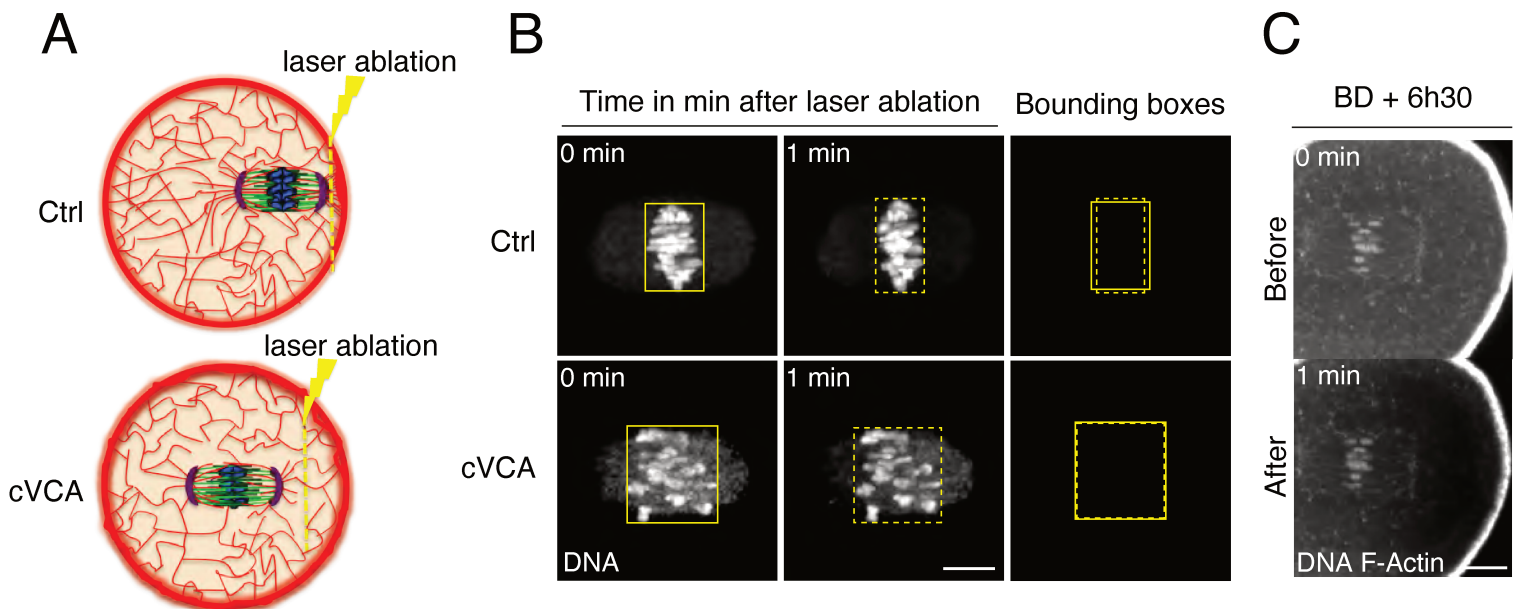
**Supplementary Figure 2: cFH1FH2 oocytes also display a decrease in cortical tension and an absence of spindle migration.**

(A) Representative images of control and cFH1FH2 (red) Prophase I oocytes expressing GFP-UtrCH (black). Right insets show magnifications of the cortex. Scale bar: 10  $\mu\text{m}$ . 2 independent experiments. (B) Cortical actin thickness in Prophase I control and cFH1FH2 oocytes. Data are from 2 independent experiments. (n) is the number of oocytes analyzed. Statistical significance was tested with a t-test two-sided: n.s P-value=0.24. (C) Representative images of control and cFH1FH2 oocytes expressing SF9-GFP (grey) in Prophase I. Scale bar: 10  $\mu\text{m}$ . 2 independent experiments. (D) Dot plot representing myosin-II cortical enrichment (see Methods) for control and cFH1FH2 oocytes. (n) is the number of oocytes analyzed. Data are from 2 independent experiments. Statistical significance of differences is assessed with a Mann-Whitney test two-sided: \*\*\*P-value<0.0001. (E) Dot plot showing cortical tension values in control and cFH1FH2 oocytes (see Methods). (n) is the number of oocytes analyzed. Data are from 3 independent experiments. Statistical significance of differences is assessed with a Mann-Whitney test two-sided: \*\*\* P-value <0.0001. (F) Spindle length for controls and cFH1FH2 oocytes 7 hours after nuclear envelope breakdown. (n) is the number of oocytes analyzed. Data are from 4 independent experiments. Statistical significance is determined with a Mann-Whitney test two-sided: n.s P-value=0.4066. (G) Representative time-lapse movies showing spindle (SiR-Tubulin, black) position in a control and a cFH1FH2 oocyte. The green ovals mark initial spindle positions. Acquisitions were taken every 30 minutes starting 3h30 before anaphase I. Scale bar: 10  $\mu\text{m}$ . 5 independent experiments. (H) Dot plot showing the distance travelled by the spindle starting 4h before anaphase I for control and cFH1FH2 oocytes. Data are from 5 independent experiments. (n) is the number of oocytes analyzed. Statistical significance of the differences was assessed with a t-test two-sided: \* P-value=0.012. (I) Rate of polar body extrusion in control and cFH1FH2 oocytes. Data are from 4 independent experiments. (n) is the number of oocytes analyzed. Statistical significance tested with a Fisher's test two-sided: n.s P-value=0.1871. For (B, D, E, F, H) black bars and whiskers represent mean and standard deviation.

**A****B****C****D****E**

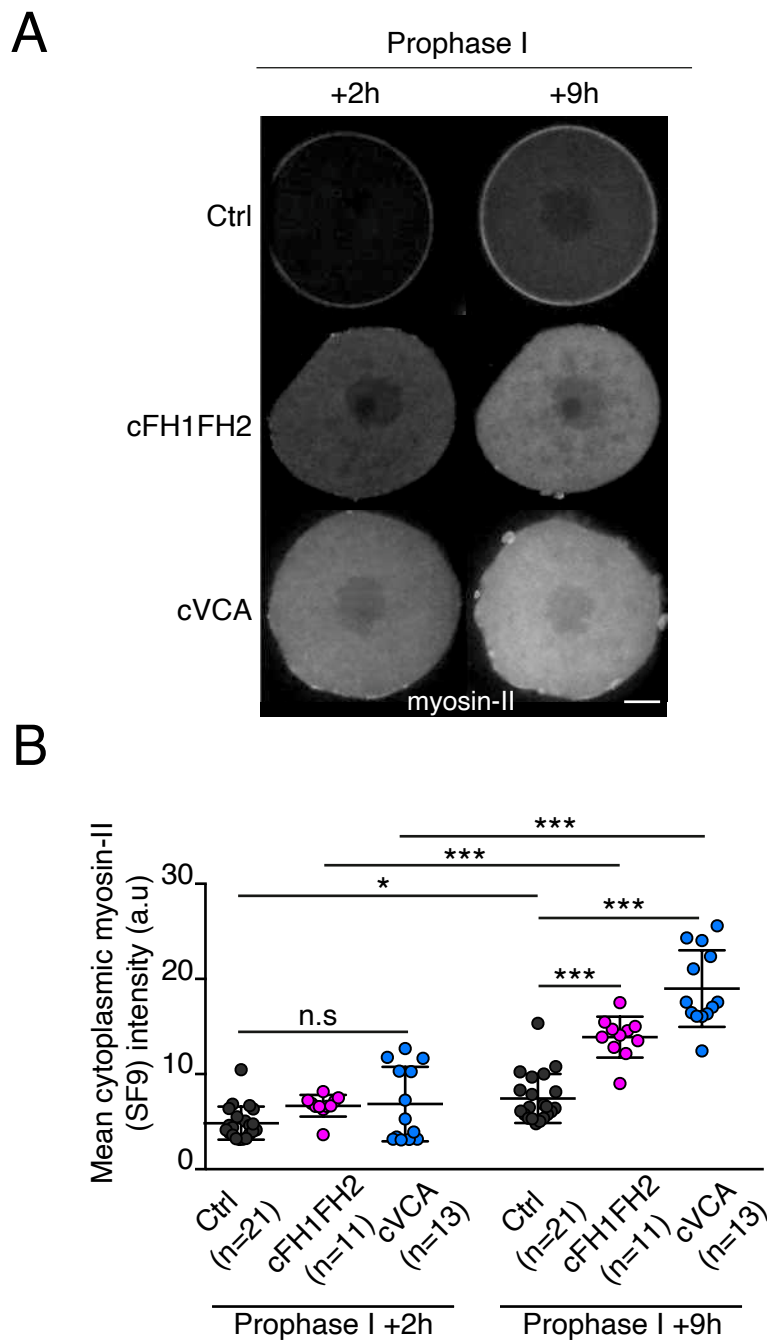
**Supplementary Figure 3: Cell volume but not cytoplasmic activity is reduced in extra-soft oocytes.**

**(A)** Confocal spinning disk images of control and cVCA oocytes at BD + 6h30. Chromosomes are labeled with Histone(H2B)-GFP (blue). The cortex is labeled with Ezrin-mCherry in control and Ezrin-mCherry-cVCA in cVCA oocytes (both red). Scale bar: 10  $\mu\text{m}$ . This experiment was repeated independently 3 times with similar results. **(B)** Representative time-lapse movies of a control and a cVCA oocyte showing that oocytes are stable in shape between BD + 6h30 and BD + 8h. Acquisitions were taken every 30 minutes. Scale bar: 10  $\mu\text{m}$ . This experiment was repeated independently 3 times with similar results. **(C)** For volume measurements, control and cVCA oocytes are in chambers filled with fluorescent dextran (bottom panels). Scale bar: 20  $\mu\text{m}$ . This experiment was repeated independently 3 times with similar results. **(D)** Oocyte volume is reduced in cVCA oocytes compared to controls. Each dot represents the volume ( $\mu\text{m}^3$ ) of one oocyte from 3 independent experiments. (n) is the number of oocytes analyzed. Black bars and whiskers represent mean and standard deviation. A Wilcoxon rank sum test two-sided was performed to compare the mean (black line) of the two conditions: \*P-value=0.0232. **(E)** The motion of Nile red-labeled vesicles is similar in cVCA oocytes compared to controls, suggesting comparable cytoplasmic activity. The dashed line represents a power law of 1. MSD data are fitted to a simple linear regression model ( $R^2 > 0.97$ ). Data are from 3 independent experiments.



**Supplementary Figure 4: The forces applied to the chromosomes are altered in extra-soft oocytes but it is not the main cause of chromosome misalignment.**

(A) Scheme of the laser ablation in control and cVCA oocytes. Actin is in red, microtubules in green, chromosomes in blue and myosin-II in purple. (B) Representative images at BD + 6h30 of oocytes expressing Histone(H2B)-GFP and EB3-GFP (grey) in control and cVCA oocytes. Bounding boxes of the metaphase I plate are represented in solid lines before and dashed lines 1 min after ablation. Scale bar: 10  $\mu$ m. 5 independent experiments. (C) Laser ablation (before and 1 minute after) of F-actin between the spindle and the closest cortex at BD + 6h30 in a control oocyte expressing Histone(H2B)-GFP (grey) and GFP-UtrCH (also in grey). Scale bar: 10  $\mu$ m. 5 independent experiments. (D) Graph representing the relative decrease of the metaphase I plate bounding boxes every 20 seconds (s) during 1 minute in control and cVCA oocytes. (n) is the number of oocytes analyzed. Data are compiled from 5 independent experiments. (E) Representative images at BD + 3h of a control oocyte expressing Histone(H2B)-GFP and EB3-GFP (grey). Bounding boxes of the chromosomes are represented in solid lines before and dashed lines 1 min after ablation. Scale bar: 10  $\mu$ m. The graph below represents the relative decrease of the chromosomes bounding boxes at BD + 3h with or without laser ablation. (n) is the numbers of oocytes analyzed. (F) Representative images at at BD + 6h30 of a control oocyte expressing Histone(H2B)-GFP and EB3-GFP (grey). Bounding boxes of the metaphase I plate are represented in solid lines and dashed lines 1 min after. Scale bar: 10  $\mu$ m. The graph below represents the relative decrease of the metaphase I plate bounding boxes at BD + 6h30 without laser ablation or following ablation (red). (n) is the numbers of oocytes analyzed. (G) Representative time-lapse movies of control and *Fmn2*<sup>-/-</sup> oocytes expressing Histone(H2B)-GFP (black). Acquisitions were taken every 30 minutes starting 1h30 before anaphase I. Scale bar: 10  $\mu$ m. 3 independent experiments. For (D, E, F), the mean and standard deviation are shown for each timepoint.



**Supplementary Figure 5: Myosin-II accumulates in the cytoplasm in extra-soft oocytes over time.**

**(A)** Confocal spinning disk images of control, cVCA and cFH1FH2 oocytes expressing SF9-GFP (myosin-II intrabody, grey). Prophase I oocytes are observed 2h and 9h after cRNA injection. Scale bar: 10  $\mu$ m. This experiment was repeated independently 3 times with similar results. **(B)** Dot plot representing the SF9-GFP cytoplasmic intensity in prophase I arrested oocytes 2h and 9h after expression of SF9-GFP alone (control) or together with cVCA or cFH1FH2. Six measurements were taken in the cytoplasm for each oocyte. (n) is the number of oocytes analyzed. Data are from 3 independent experiments. Black bars and whiskers represent mean and standard deviation. Statistical significance of differences is assessed with a One-Way ANOVA test. For the Prophase I +2h groups, all conditions (Ctrl vs. cFH1FH2, Ctrl vs. cVCA, cVCA vs. cFH1FH2) are all n.s P-value>0.9999. Regarding the evolution of SF9-GFP cytoplasmic intensity, Ctrl Prophase I +2h vs. +9h are different (\*P-value=0.0335), and cFH1FH2 Prophase I +2h vs. +9h and cVCA Prophase I +2h vs. +9h are different (\*\*\*P-values<0.0001).

Chez les femelles mammifères, les cellules germinales, appelées ovocytes, sont produites lors du développement fœtal et conservées dans l'ovaire, chacune entourée de manière individuelle par des cellules somatiques. Ces cellules somatiques, les cellules de la granulosa, travaillent en synergie avec l'ovocyte pour coordonner les grandes étapes du développement ovocytaire *post-partum*. Ce développement commence par la croissance ovocytaire, une période d'expansion en taille de l'ovocyte associée à un stockage de nutriments essentiel pour soutenir les premières étapes du développement embryonnaire. S'ensuit une étape de maturation méiotique, durant laquelle l'ovocyte effectue deux divisions cellulaires et suspend son développement en métaphase de seconde division, jusqu'à la fécondation. Ces divisions sont asymétriques en taille et produisent une cellule germinale haploïde qui a conservé un maximum de volume de cytoplasme pour permettre l'embryogénèse précoce.

Les cellules de la granulosa façonnent la qualité ovocytaire en s'engageant dans un dialogue bidirectionnel avec l'ovocyte. Le dialogue somatique est principalement établi par contact intercellulaire grâce à des protrusions émises par les cellules de la granulosa appelées projections transzonales (TZPs). Les TZPs ressemblent aux filopodes par leur forme et leur composition structurale. Ils résident dans la matrice extracellulaire qui entoure l'ovocyte, la zone pellucide. Des jonctions cellulaires sont élaborées entre l'extrémité de ces protrusions et la membrane ovocytaire, en particulier des jonctions d'adhérence permettant l'adhésion entre l'ovocyte et les cellules de la granulosa. Des jonctions gap, également présentes à cette interface, couplent l'ovocyte et les cellules somatiques sur le plan métabolique et jouent un rôle majeur dans le développement de l'ovocyte, notamment en autorisant le transfert de métabolites d'un type cellulaire à l'autre.

Durant ma thèse, j'ai étudié le rôle des TZPs, et implicitement des interactions directes ovocyte/cellules de la granulosa, dans le développement ovocytaire. En générant une lignée de souris dépourvue de manière totale de la Myosine-X, un moteur moléculaire contenu dans les TZPs et connu pour participer à la formation des filopodes, nous avons obtenu des ovocytes avec une densité réduite en TZPs à la fin de la croissance ovocytaire. Nous montrons que la réduction de la densité des TZPs n'empêche pas l'ovocyte d'atteindre une taille canonique, mais altère l'intégrité de la zone pellucide et l'adhésion ovocyte-matrice extracellulaire. Par analyse transcriptomique, nous mettons en évidence que la diminution de la densité des TZPs altère le transcriptome de l'ovocyte à la fin de la croissance ovocytaire, avec des transcrits majoritairement sur-exprimés, suggérant que le transcriptome de l'ovocyte est modulé de manière exogène par les cellules de la granulosa. Enfin, bien que présentant un fuseau de division correctement assemblé et des chromosomes bien alignés, les ovocytes dépourvus de TZPs sont enclins à arrêter leur développement en métaphase de première division méiotique. Cet arrêt méiotique n'est pas causé par la déplétion ovocytaire de la Myosine-X. En effet, des souris dépourvues de Myosine-X de manière conditionnelle dans l'ovocyte sont fertiles et produisent des ovocytes qui terminent la maturation méiotique comme les ovocytes témoins. La Myosine-X n'est donc pas requise pour le positionnement du fuseau dans l'ovocyte de souris, contrairement à son rôle établi dans plusieurs cellules mitotiques.

Nous proposons que les cellules somatiques modulent la synthèse ou la stabilité d'un sous-ensemble de transcrits ovocytaires par le biais de leurs protrusions cellulaires. Cette modulation améliore la capacité de l'ovocyte à terminer la maturation méiotique, et par extension, les chances de produire un embryon.

# Résumé/Abstract

Chez les femelles mammifères, les cellules somatiques qui entourent l'ovocyte, les cellules de la granulosa, coordonnent le développement ovocytaire *post-partum*, la croissance ovocytaire et la maturation méiotique, en dialoguant avec l'ovocyte. Ce dialogue est principalement établi par contact intercellulaire grâce à des protrusions des cellules de la granulosa, les projections transzonales (TZPs). Les TZPs ressemblent à des filopodes, résident dans la matrice extracellulaire entourant l'ovocyte, la zone pellucide, et établissent des jonctions gap et d'adhérence avec la membrane de l'ovocyte. Durant ma thèse, j'ai étudié le rôle des TZPs dans le développement ovocytaire. En générant un knockout total de la Myosine-X chez la souris, une protéine contenue dans les TZPs et participant à la formation des filopodes, nous avons obtenu des ovocytes avec une densité de TZPs réduite. Cela n'empêche pas l'ovocyte d'atteindre une taille canonique. Cependant, cela altère l'intégrité de la zone pellucide, l'adhésion ovocyte-matrice extracellulaire, et le transcriptome de l'ovocyte en fin de croissance, les transcrits dérégulés étant majoritairement sur-exprimés. Les ovocytes dépourvus de TZPs sont enclins à arrêter leur développement en métaphase de première division méiotique, bien que présentant un fuseau de division correctement assemblé et des chromosomes bien alignés. Nous proposons que les cellules somatiques modulent la synthèse ou la stabilité d'un sous-ensemble de transcrits ovocytaires par le biais de leurs protrusions cellulaires. Cette modulation améliore la capacité de l'ovocyte à terminer la maturation méiotique, et par extension, les chances de produire un embryon.

In female mammals, somatic cells surrounding the oocyte, termed granulosa cells, coordinate the critical stages of *post-partum* oocyte development, i.e. oocyte growth and meiotic maturation, by dialoguing with the oocyte. This dialogue is primarily mediated by cell-cell contact carried out by granulosa cell protrusions termed transzonal projections (TZPs). TZPs are analogous to filopodia in their snake-like shape, but also in their structural composition. TZPs are located in the *zona pellucida*, the extracellular matrix surrounding the oocyte, and their extremities establish cellular junctions with the oocyte membrane, i.e. gap and adherens junctions. In my thesis, I investigated the role of TZIP-mediated interaction between granulosa cells and the oocyte in oocyte development. By generating a total knockout of Myosin-X, a molecular motor contained in TZPs and participating in filopodia formation, we obtained mouse mutant oocytes with a reduced TZIP density at the end of oocyte growth. This reduction does not impede the oocyte from reaching a canonical size. However, it impairs *zona pellucida* integrity, oocyte-matrix adhesion, and the oocyte transcriptome at the end of oocyte growth, with a subset of transcripts mostly up-deregulated. Importantly, TZIP-deprived oocytes tend to cease their development at metaphase of the first meiotic division, despite a well-assembled division spindle and properly aligned chromosomes. We propose that somatic cells modulate the synthesis or stability of a subset of oocyte transcripts through their cellular protrusions. This modulation enhances the oocyte capacity to end meiotic maturation, and by extension, the chances of producing an embryo.